# Fortschritt-Berichte VDI

## Reihe 12

Verkehrstechnik/
Fahrzeugtechnik

Dipl.-Ing. Matthias Patrick Alexander Mrosek, Frankfurt am Main

Nr. 803

# Model-Based Control of a Turbocharged Diesel Engine with High- and Low-Pressure Exhaust Gas Recirculation

Berichte aus dem

Institut für
Automatisierungstechnik
und Mechatronik
der TU Darmstadt

*iat*

# Model-Based Control of a Turbocharged Diesel Engine with High- and Low-Pressure Exhaust Gas Recirculation

Vom Fachbereich
Elektrotechnik und Informationstechnik
der Technischen Universität Darmstadt
zur Erlangung des Grades eines Doktor-Ingenieurs (Dr.-Ing.)
genehmigte Dissertation

von

**Dipl.-Ing. Matthias Patrick Alexander Mrosek**

geboren am 8. Februar 1978 in Frankfurt am Main

D 17 · Darmstadt 2017

# Fortschritt-Berichte VDI

Dipl.-Ing. Matthias Patrick
Alexander Mrosek, Frankfurt am Main

# Model-Based Control of a Turbocharged Diesel Engine with High- and Low-Pressure Exhaust Gas Recirculation

iat

"Model-Based Control of a Turbocharged Diesel Engine with High- and Low-Pressure Exhaust Gas Recirculation" presents the complete scope for a model-based control design with regard to the control objective dynamical driving cycle emissions. A semi-physical air path model delivers system properties of the controlled system. Experimental models for stationary and dynamical engine raw emissions are the base for stationary and dynamical optimisations of emissions and engine torque and allow to motivate deviations between stationary and dynamical emission formation. The control concept directly incorporates semi-physical relationships and model parameters of the air path model for control of HP-EGR, LP-EGR and charging pressure. The control performance is rated with quantified stationary and dynamical contributions to the overall driving cycle emissions. All models and control methods have been experimentally parameterised and validated at an engine test bench.

# Preface

This dissertation is the outcome of my time as research associate at the Institute of Automatic Control and Mechatronics at Technische Universität Darmstadt. It has been supervised by Prof. Dr.-Ing. Dr. h. c. Rolf Isermann, head of the Research Group Control Systems and Process Automation.

First of all, I would like to express my sincere gratitude to Prof. Dr.-Ing. Dr. h. c. Rolf Isermann for offering me the opportunities for my research and to write this dissertation. I felt very pleased with the high degree of responsibility that Prof. Isermann granted to me. That allowed a self dependent research, which resulted in this dissertation and shaped my personal development in an entirely positive sense. In particular, I thank Prof. Isermann for the chances to present my scientific results on national and international conferences.

Furthermore, I would like to thank my secondary examiner Prof. Dr.-Ing. Ulrich Konigorski, head of the Department of Control Systems and Mechatronics at Technische Universität Darmstadt, for his interest in my research work and the assumption of the *Koreferat*.

The research for this dissertation was enabled by a doctoral scholarship funded by Technische Universität Darmstadt. As representatives I would like to thank the university presidents Prof. Dr.-Ing. Johann-Dietrich Wörner and Prof. Dr. Hans Jürgen Prömel.

Particular thanks to all colleagues at the Institute of Automatic Control and Mechatronics as well as to all technical and administrative staff. A considerable contribution to this dissertation results from the excellent working atmosphere and the creative collaboration with colleagues. Especially the close cooperation, the support and the can-do attitude in the project group internal combustion engines will remain as a lasting memory. Special thanks go to Dr.-Ing. Heiko Sequenz, with whom I claimed the topic of emission modelling and engine optimisation and compiled several publications. Furthermore, I would like to thank Dr.-Ing. Sebastian Zahn for enriching discussions about modelling and parameterisation of air path and turbocharger. I would also like to thank Dr.-Ing. Martin Kohlhase and Dr.-Ing. Karl von Pfeil for giving me good orientation at the begin of my research.

Above all, I would to express my sincere gratitude to my parents for their unconditional support during my whole education, which was the foundation for everything else. I am indebted to my wife Dr. med. dent. Friederike Mrosek, for all her patience and support during the research work.

Frankfurt am Main, March 2017
*Matthias Patrick Alexander Mrosek*

*to Friederike, Jonathan and Theodor*

# Contents

# Symbols and Abbreviations

## Symbols

### General Letter Symbols

| Symbol | Explanation |
|---|---|
| $e$ | error |
| $EM$ | extrapolation measure |
| $G$ | transfer function |
| $J$ | loss function, quality criterion |
| $k$ | discrete time |
| $k$ | factor |
| $M$ | number of local models |
| $n$ | number of data points |
| $p$ | number of model inputs |
| $q$ | number of model outputs |
| $q^{-1}$ | time delay operator: $x(k-1) = q^{-1}x(k)$ |
| $R^2$ | coefficient of determination |
| $s$ | Laplace operator |
| $T$ or $\tau$ | time constant |
| $T_\mathrm{d}$ | dead time |
| $u$ | process input, input variable |
| $\mathbf{x}$ | x-regressors |
| $y$ | process output, output variable |
| $w$ | weight |
| $\mathbf{z}$ | z-regressors |
| $\mathcal{A}$ | feasible set of regressors |
| $\Delta$ | linearised form, deviation, measurement uncertainty |
| $\phi$ | validity function |
| $\boldsymbol{\theta}$ | parameter vector |

## General Physical Quantities

| Symbol | Explanation | Unit |
|--------|-------------|------|
| $a$ | specific work | J/kg |
| $A$ | surface area | $m^2$ |
| $b$ | width | m |
| $C_D$ | orifice discharge coefficient | 1 |
| $c_p$ | heat capacity at constant pressure | J/(kg K) |
| $c_V$ | heat capacity at constant volume | J/(kg K) |
| $c$ | absolute velocity | m/s |
| $c_m$ | meridional part of the absolute velocity | m/s |
| $c_u$ | circumferential component of the absolute velocity | m/s |
| $d$ | diameter | m |
| $h$ | specific enthalpy | J/kg |
| $I$ | moment of inertia | kg $m^2$ |
| $k$ | heat transmission coefficient | W/($m^2$K) |
| $l$ | length | m |
| $\dot{m}$ | mass flow rate | kg/s or kg/h |
| $m$ | mass | kg |
| $M$ | molar mass | g/mol |
| $M$ | torque | Nm |
| $p$ | pressure | Pa |
| $P$ | power | W |
| $q$ | specific heat transfer | J/kg |
| $\dot{Q}$ | heat flow | W |
| $R$ | resistance | $\Omega$ |
| $R$ | specific gas constant | J/(kg K) |
| $t$ | time | s |
| $T$ | temperature | K or °$C$ |
| $u$ | circumferential velocity | m/s |
| $U$ | internal energy | J |
| $U$ | voltage | V |
| $v$ | velocity | km/h |
| $V$ | volume | $m^3$ |
| $\dot{V}$ | volume flow rate | $m^3$/s |
| $w$ | relative velocity | m/s |
| $w_m$ | meridional part of the relative velocity | m/s |
| $w_c$ | circumferential part of the relative velocity | m/s |
| $x$ | air content (ratio of fresh air mass to total gas mass) | 1 |

| Symbol | Explanation | Unit |
|--------|-------------|------|
| $\alpha$ | heat transfer coefficient | $W/(m^2 K)$ |
| $\alpha$ | absolute flow angle, guiding vane angle | deg |
| $\beta$ | relative flow angle, rotor blade angle | deg |
| $\delta p$ | differential pressure | Pa or bar |
| $\kappa$ | isentropic expansion factor | 1 |
| $\mu$ | slip factor | 1 |
| $\Pi$ | pressure ratio | 1 |
| $\rho$ | density | $kg/m^3$ |
| $\omega$ | angular velocity | rad/s |

## Letter Symbols for Combustion Engines

| Symbol | Explanation | Unit |
|--------|-------------|------|
| $c_{mss}$ | micro soot sensor measurement | $mg/m^3$ |
| $c_{nox}$ | $NO_x$ sensor measurement | ppm |
| $c_{opa}$ | opacity measurement | % |
| $k_{af}$ | load factor air filter | 1 |
| $k_{dpf}$ | load factor DPF | 1 |
| $L_{st}$ | stoichiometric air requirement | 1 |
| $m_{air}$ | air mass per working cycle | mg/cyc |
| $m_{mss}$ | distance related particulate emissions (micro soot sensor) | mg/km |
| $m_{nox}$ | distance related nitrogen oxide emissions | mg/km |
| $m_{pm}$ | distance related particulate emissions | mg/km |
| $\dot{m}_{air}$ | air mass flow rate | kg/s or kg/h |
| $\dot{m}_{c}$ | compressor gas mass flow rate | kg/s or kg/h |
| $\dot{m}_{eng,in}$ | gas mass flow rate entering the cylinder | kg/s or kg/h |
| $\dot{m}_{eng,out}$ | gas mass flow rate exiting the cylinder | kg/s or kg/h |
| $\hat{\dot{m}}_{f}$ | estimated injected fuel mass flow rate | kg/s or kg/h |
| $\dot{m}_{hp-egr}$ | HP-EGR gas mass flow rate | kg/s or kg/h |
| $\dot{m}_{lp-egr}$ | LP-EGR gas mass flow rate | kg/s or kg/h |
| $\dot{m}_{mss}$ | particulate mass flow rate (micro soot sensor) | mg/s |
| $\dot{m}_{nox}$ | $NO_x$ mass flow rate | mg/s |
| $\dot{m}_{t}$ | turbine gas mass flow rate | kg/s or kg/h |
| $\dot{m}_{th}$ | throttle valve gas mass flow rate | kg/s or kg/h |
| $M_{c}$ | turbocharger compressor torque | Nm |
| $M_{f}$ | turbocharger friction torque | Nm |
| $M_{eng}$ | engine torque | Nm |
| $M_{t}$ | turbocharger turbine torque | Nm |
| $n_{eng}$ | engine rotational speed | 1/min |
| $n_{tc}$ | turbocharger rotational speed | 1/s |
| $op$ | operation point | 1 |

| Symbol | Explanation | Unit |
|---|---|---|
| $p_1$ | pressure before the compressor | Pa or bar |
| $p_{2c}$ | pressure after the compressor | Pa or bar |
| $p_{2i}$ | pressure in the intake manifold | Pa or bar |
| $p_{2ic}$ | pressure after the intercooler | Pa or bar |
| $p_3$ | pressure in the exhaust manifold | Pa or bar |
| $p_4$ | pressure before the particulate filter | Pa or bar |
| $p_5$ | pressure after the particulate filter | Pa or bar |
| $p_a$ | ambient pressure | Pa or bar |
| $p_{hp-egr}$ | pressure in the HP-EGR pipe | Pa or bar |
| $p_{lp-egr}$ | pressure in the LP-EGR pipe | Pa or bar |
| $p_{rail}$ | pressure in the common rail injection system | bar |
| $P_c$ | turbocharger compressor power | W |
| $P_f$ | turbocharger friction power | W |
| $P_t$ | turbocharger turbine power | W |
| $\dot{Q}_{i,t}$ | heat transmission to state $i$ | W |
| $r_{egr}$ | EGR-rate | 1 |
| $r_{lp-egr}$ | LP-EGR-rate | 1 |
| $s_{eth}$ | exhaust throttle valve position (normalised) | 1 |
| $s_{hp-egr}$ | HP-EGR-valve position (normalised) | 1 |
| $s_{ith}$ | intake throttle valve position (normalised) | 1 |
| $s_{lp-egr}$ | LP-EGR-valve position (normalised) | 1 |
| $s_{lp-egr/eth}$ | LP-EGR-valve combined with exhaust throttle valve position | 1 |
| $s_{lp-egr/ith}$ | LP-EGR-valve combined with exhaust intake valve position | 1 |
| $s_{sa}$ | swirl actuator position (normalised) | 1 |
| $s_t$ | VGT-actuator position (normalised) | 1 |
| $s_{th}$ | throttle valve position (normalised) | 1 |
| $\tilde{s}_i$ | Actuator position $i$ (measured) | mm or % |
| $T_1$ | temperature before the compressor | $K$ or °C |
| $T_{2c}$ | temperature after the compressor | $K$ or °C |
| $T_{2ic}$ | temperature after the intercooler | $K$ or °C |
| $T_{2i}$ | temperature in the intake manifold | $K$ or °C |
| $T_3$ | temperature in the exhaust manifold | $K$ or °C |
| $T_4$ | temperature before the particulate filter | $K$ or °C |
| $T_5$ | temperature after the particulate filter | $K$ or °C |
| $T_a$ | ambient temperature | $K$ or °C |
| $T_{cl}$ | temperature cooling fluid | $K$ or °C |
| $T_{h_2o}$ | temperature engine coolant | $K$ or °C |
| $T_{hp-egr}$ | temperature in the HP-EGR pipe | $K$ or °C |
| $T_{lp-egr}$ | temperature in the LP-EGR pipe | $K$ or °C |
| $u_{icc}$ | control signal intercooler ventilator | 1 |
| $u_{inj}$ | desired injection quantity | mm$^3$/cyc |

| Symbol | Explanation | Unit |
|--------|-------------|------|
| $V_d$ | displacement volume | m$^3$ |
| $W_{eng}$ | engine work | kWh |
| $x$ | air content (ratio of fresh air mass to total gas mass) | 1 |
| $x_1$ | air content before the compressor | 1 |
| $x_{2c}$ | air content after the compressor | 1 |
| $x_{2ic}$ | air content after the intercooler | 1 |
| $x_{2i}$ | air content in the intake manifold | 1 |
| $x_{eng,in}$ | air content entering the cylinder | 1 |
| $x_{eng,out}$ | air content exiting the cylinder | 1 |
| $x_3$ | air content in the exhaust manifold | 1 |
| $x_4$ | air content before the particulate filter | 1 |
| $x_5$ | air content after the particulate filter | 1 |
| $x_{hp-egr}$ | air content in the HP-EGR pipe | 1 |
| $x_{lp-egr}$ | air content in the LP-EGR pipe | 1 |
| $z$ | number of cylinders per combustion cycle | 1 |
| $\lambda$ | air-fuel ratio | 1 |
| $\lambda_a$ | volumetric efficiency | 1 |
| $\varphi_{mi}$ | start of main injection | °CA |
| $\varphi_{Q50}$ | crank angle of 50 % mass fraction burned | °CA |
| $\xi_{hp-egr}$ | desired proportion of HP-EGR | 1 |
| $\xi_{p,st}$ | pipe volume fraction | 1 |
| $\chi_{hp-egr}$ | fraction of HP-EGR to total EGR | 1 |
| $\omega_{tc}$ | angular velocity turbocharger | rad/s |

## Subscripts

| Index | Explanation |
|---|---|
| 1 | state variables before compressor |
| 2c | state variables after compressor |
| 2ic | state variables after intercooler |
| 2i | state variables intake manifold |
| 3 | state variables exhaust manifold |
| 4 | state variables after turbine |
| 5 | exhaust pipe quantities |
| a | actuator |
| acc | acceleration |
| adi | adiabatic |
| af | air filter quantities |
| c | compressor quantities |
| cj | cold junction |
| ctl | closed-loop control |
| cyl | cylinder |

| Index | Explanation |
|---|---|
| des | desired quantity |
| dia | diabatic |
| dpf | Diesel particulate filter quantities |
| dyn | dynamical |
| eng,in | entering cylinder |
| eng,out | exiting cylinder |
| eth | exhaust throttle valve quantities |
| f | friction |
| fil | filtered |
| ffc | feedforward control |
| gas | gas |
| h2o | engine coolant liquid |
| hp-egr | HP-EGR quantities |
| icc | intercooler cooler |
| in | input, inflow |
| ise | isentropic |
| lim | limited |
| lp-egr | LP-EGR quantities |
| mair-ctl | air mass flow rate control |
| measured | measured |
| mi | main injection / mean indicated pressure |
| mi,lp | mean indicated pressure intake and exhaust stroke low pressure loop in p-V diagram |
| mi,hp | mean indicated pressure compression and power stroke high pressure loop in p-V diagram |
| min | minimum |
| mss | micro soot sensor quantities |
| nox | $NO_x$ quantities |
| opa | opacimeter quantities |
| opt | optimised quantity |
| out | output, outflow |
| p | power, pipe |
| r | receiver |
| ref | reference |
| regr-ctl | EGR-rate control |
| rsf | reference shaping filtered |
| s | shunt |
| sim | simulated |
| stat | stationary |
| t | turbine quantities |
| tc | turbocharger quantities |
| th | throttle valve quantities |

## General Abbreviations

| Abbreviations | Explanation |
|---|---|
| °CA | Unit of the Rotational Angle of the Crank Shaft |
| CAN | Controller Area Network |
| CASEM | Crank Angle Synchronous Engine Models |
| CLK | Clock Generator Oscillator |
| CO | Carbon Monoxide |
| cyc | Combustion Cycle |
| DOC | Diesel Oxidation Catalyst |
| DPF | Diesel Particulate Filter |
| ECU | Electronic Control Unit |
| EGR | Exhaust Gas Recirculation |
| EMF | Electro Magnetic Fields |
| HC | Hydrocarbons |
| HCCI | Homogeneous Charge Compression Ignition |
| HP-EGR | High-Pressure Exhaust Gas Recirculation |
| IMC | Internal Model Control |
| LOLIMOT | Local Linear Model Tree |
| LOPOMOT | Local Polynomial Model Tree |
| LP-EGR | Low-Pressure Exhaust Gas Recirculation |
| LSB | Least Significant Bit |
| MFB50 | 50 % Mass Fraction Burned |
| MVEM | Mean Value Engine Model |
| NEDC | New European Driving Cycle |
| $NO_x$ | Nitrogen Oxides |
| PM | Particulate Matter |
| PN | Particulate Number |
| PRBS | Pseudo Random Binary Signals |
| RDE | Real Driving Emissions |
| RMSE | Root-Mean-Square Error |
| RSF | Reference Shaping Filter |
| VGT | Variable Geometry Turbine |
| VVT | Variable Valve Timing |
| WLTP | Worldwide Harmonized Light-Duty Vehicles Test Procedure |

## Mathematical Abbreviations

| Abbreviations | Explanation |
|---|---|
| $f\left(\cdot\right)$ | function of $\cdot$ |
| $f_{\text{LOLIMOT}}\left(\cdot\right)$ | LOLIMOT model with the model inputs $\cdot$ |
| $\hat{\cdot}$ | modelled quantity $\cdot$ |
| $\bar{\cdot}$ | mean value of quantity $\cdot$ |
| $x$ | scalar |
| $\mathbf{x}$ | vector |

# Abstract

Modern Diesel engines fulfil challenging requirements for emission limits, fuel consumption and ride comfort by numerous modular combinable components and mechatronical actuators. These components are utilised for precondition and aftertreatment of air, fuel and exhaust gas, which is involved in the combustion process. In this dissertation a methodology for a model-based function development with semi-physical engine models for control of air path quantities of an exemplary Diesel engine with high-pressure (HP-EGR) and low-pressure exhaust gas recirculation (LP-EGR) is developed. In this framework for function development black-box models for stationary and dynamical emission formation are utilised to optimise reference values for the air path control and to rate the developed control scheme with regard to the cumulated driving cycle emissions of the new European driving cycle (NEDC).

A combination of HP-EGR and LP-EGR represents a novel approach to significantly lower the particulate and $NO_x$ emissions of Diesel engines. A semi-physical mean value engine model with lumped parameters is the base to analyse the system properties of the complex air path. In doing so, the additional LP-EGR shows only minor influences to the quantities charge air pressure and HP-EGR, while there are significant influences of these quantities on the LP-EGR mass flow rate. Furthermore, the LP-EGR is characterised by significant gas propagation times in the intake and exhaust system. These delays are modelled by a gas composition model, which is incorporated into the control scheme.

$NO_x$ and particulate emissions as well as engine torque are stationary modelled by local polynomial models with input quantities of the combustion process. These quantities are air mass flow rate, charge air pressure, intake temperature and crank angle of 50 % mass fraction burned. A bilinear interpolation between engine speed and injection quantity transforms local polynomial models into global models. Models for the dynamical emission formation are given by considering the combustion as a batch process. Consequently all dynamics are included in the quantities of the cylinder charge at intake valve closing and the emission measurement dynamics. Thus, a combination of a dynamical gas composition model, stationary emission models and models for the emission measurement dynamics yield the dynamical course of the engine emissions.

The investigated system properties and the emission models deliver the control variables charge air pressure, air content and intake temperature for the engine with VGT-turbocharger, HP- and LP-EGR. A stationary optimisation with regard to emissions and engine torque delivers reference values for the air path control and further shows the potential of the LP-EGR to lower the emissions. Due to the multi-variable characteristics of the air path with different dynamics, there are increased dynamical emissions at engine transients. These dynamical emissions are lowered by dynamical optimised reference values for the air path control.

Generally, the air path is a strongly nonlinear process and the multitude of engine variants and engine operation modes result in a trade-off between achievable control quality, control robustness and number of control parameter sets. A semi-physical feedforward control, which is based upon parameterised model relationships of the mean value engine model delivers a good response to setpoint changes. Thus, the disturbance rejection can be achieved by relatively simple controllers. This results in an significantly lower application effort of control parameters and allows by its modular structure to exchange engine components without the drawback to completely re-parameterise the control parameters. A reference value transformation with modelled states of the gas composition model compensates long gas propagation times in the intake and exhaust system and delivers an optimal air content in the cylinder charge. All control concepts are validated with measurements at the engine test bench. Finally, the derived control concepts for the LP-EGR are compared to the classical HP-EGR control with regard to the cumulated driving cycle emissions. In this investigation the proportion of stationary and dynamical emissions is clearly quantified.

In a nutshell this dissertation is an important contribution for model-based optimisation and function development for the air path control of Diesel engines. The given combination of models for dynamical emission formation, dynamically optimised reference values for the air path control and semi-physical control design are a holistic framework to master the complexity and variance of future Diesel and gasoline engines.

# Kurzfassung

Moderne Dieselmotoren erfüllen die hohen Anforderungen bezüglich Emissionen, Verbrauch und Fahrkomfort durch eine Vielzahl von modular kombinierbaren Bauteilen und mechatronischen Aktoren zur Vor- und Nachbehandlung der am Verbrennungsprozess beteiligten Stoffe Frischluft, Kraftstoff und Abgas. In dieser Dissertation wird am Beispielprozess eines aufgeladenen Dieselmotors mit Hoch- (HD-AGR) und Niederdruck-Abgasrückführung (ND-AGR) eine Methodik zur modularen modellbasierten Funktionsentwicklung für die Luftpfadregelung mit semi-physikalischen Modellen entwickelt. Black-Box-Modelle für die stationären und dynamischen Emissionen werden zur Optimierung der Sollwerte für die Luftpfadregelung und zur Bewertung des entwickelten Regelungskonzepts anhand der kumulierten Emssionen des neuen Europäischen Fahrzyklus (NEFZ) verwendet.

Eine Kombination von Hoch- und Niederdruck-Abgasrückführung ist ein neuer Ansatz, die Ruß- und Stickoxidemissionen von Dieselmotoren erheblich zu verringern. Ausgehend von einer semiphysikalischen Modellierung des Luft- und Abgaspfades mit konzentrierten Parametern werden die Systemeigenschaften des komplexen Luftpfades untersucht. Dabei zeigt das ND-AGR-System geringen Einfluss auf Ladedruck und HD-AGR, während selbige den ND-AGR-Massenstrom stark beeinflussen. Weiterhin kann die ND-AGR durch lange Gaslaufzeiten im Einlass- und Abgassystem charakterisiert werden. Diese Laufzeiten werden durch ein Gaszusammensetzungsmodell abgebildet und später in den Regelungsentwurf integriert.

Die Emissionen $NO_x$, Ruß und das Motordrehmoment werden stationär mit lokalen Polynomen mit den Eingangsgrößen Luftmasse, Ladedruck, Ladungstemperatur und Schwerpunktlage der Verbrennung modelliert. Eine bilineare Interpolation der lokalen Polynome über Motordrehzahl und Einspritzmenge liefert stationäre globale Emissionsmodelle. Betrachtet man die Verbrennung als Chargenprozess, so ergibt sich der dynamisch messbare Verlauf der Emissionen durch die dynamische Beschreibung der Zylinderfüllung beim Schließen der Einlassventile und der Messdynamik der Emissionsmessung. Durch die Kombination des Gaszusammensetzungsmodells, der stationären Emissionsmodelle und Modellen für die Messdynamik wird der dynamische Emissionsverlauf simuliert.

Aus den Systemeigenschaften und den Emissionsmodellen werden Ladedruck, Gaszusammensetzung und Einlasstemperatur als Regelgrößen für den Luftpfad mit Turbolader, HD- und ND-AGR ausgewählt. Eine stationäre Optimierung bezüglich der Emissionen und des Motordrehmoments liefert die Sollwerte für die Regelung und zeigt im Vergleich mit der HD-AGR Serienkonfiguration das Potential der ND-AGR zur Verringerung der Emissionen. Durch die unterschiedlichen Dynamiken der Regelgrößen im Luftpfad kommt es bei Arbeitspunktwechseln zu erhöhten Emissionen. Dieses Verhalten wird durch eine dynamische Optimierung der Sollwerte der Luftpfadregelung kompensiert.

Der Luftpfad ist ein stark nichtlinearer Prozess und die Vielzahl von Motorvarianten und Motorbetriebsmodi führt zu einem Zielkonflikt zwischen erreichbarer Regelgüte, Robustheit der Regelung und der dazu notwendigen Anzahl von Reglerparametersätzen. Der Einsatz einer semiphysikalischen Vorsteuerung basierend auf den parametrierten Modellgleichungen des Luftpfadmodells liefert ein sehr gutes Führungsverhalten, während das Störverhalten durch einfache Regler kompensiert werden kann. Dies verringert den Applikationsaufwand und erlaubt durch den modularen Aufbau den Austausch einzelner Motorbauteile, ohne den Nachteil einer Neuparametrierung aller Reglerkennfelder. Eine Sollwerttransformation mit modellierten Zuständen des Gaszusammensetzungsmodells kompensiert die langen Gaslaufzeiten im Einlass- und Auslasssystem des Motors und sorgt für eine optimale Gaszusammensetzung der Zylinderfüllung. Alle Regelungskonzepte werden mit Messdaten vom Motorprüfstand validiert. Abschließend werden die entwickelten Regelungskonzepte für die ND-AGR mit der klassischen Regelung einer HD-AGR anhand der kumulierten Zyklusemissionen während des NEFZ verglichen. In dieser Betrachtung wird für alle Regelungskonzepte der Anteil von dynamischen Emissionen und stationären Emissionen quantifiziert.

Zusammenfassend leistet diese Dissertation einen wichtigen Beitrag zur modellbasierten Optimierung und Funktionsentwicklung der Luftpfadregelung von Dieselmotoren. Die Kombination von dynamischen Emissionsmodellen, einer dynamischen Optimierung der Sollwerte für die Luftpfadregelung und der semi-physikalische Regelungsentwurf stellen ein ganzheitliches Vorgehen zur Beherrschung der Komplexität und Varianz von zukünftigen Diesel- und Ottomotoren dar.

# 1   Introduction

The goal of this thesis is a method for an integrated model-based framework to calibrate reference values and to develop series control functions for a turbocharged Diesel engine with high and low-pressure exhaust gas recirculation. This chapter will give an introduction and will highlight the unsolved problems in this field of research. Thereafter the thesis' content will be outlined.

Diesel engines are the motor of our modern living. Their great energy efficiency, frugality on fuel quality and reliability makes them the motor of choice in land and sea transportation and enables the modern globalisation with daily exotic fruits, consumer electronics and cheap clothing from overseas. During its more than 120 years of development, it changed from a thundering, vibrating and polluting infernal working machine to a cultivated drive for a pleasant holiday trip. This metamorphoses was driven by requirements for more comfort, lower system cost, more reliability, less fuel consumption and legislative emission limitations.

A major driver of Diesel engine development are the steadily tightening legislative emission limitations for each country. Typical restrictions for on-road applications limit the emissions components carbon monoxide (CO), hydrocarbons (HC), nitrogen oxides ($NO_x$), particulate matter (PM) and particulate number (PN) during a reference driving cycle, while prospective limitations are going to limit fuel consumption and the related carbon dioxide emissions (Regulation 443/2009/EC of the European parliament). In Europe emission standards for passenger cars are benchmarked over the *New European Driving Cycle* (NEDC), as depicted in Fig. 1.1a). The tolerated driving cycle emissions are reduced constantly since 1992 from the *EURO 1* emission standard to the *EURO 6* emission standard in 2014. Thus, Fig. 1.1b) shows the steadily decreasing emission limits in mg/km for the Diesel engine's major emission quantities particulate matter $m_{pm}$ and nitrogen oxide emissions $m_{nox}$.

These limits are given in mg/km and consequently light engines with less fuel consumption can achieve the emission limitations easier than more powerful engines. Accordingly, there is a large variety in emission lowering measures, which are tailored to each engine with regard to demanded emission targets, system cost, impact on engine efficiency and maintenance cost. Generally, the engine tailpipe emissions can be reduced by engine internal provisions and exhaust gas aftertreatment. Milestones in exhaust gas aftertreatment are the series application of oxidation catalyst, Diesel particulate filters (DPF), $NO_x$ storage catalytic converter and selective catalytic reduction with urea injection.

A main purpose of engine internal provisions is to positively influence the fuel-mixture generation to avoid local rich fuel mixtures with lack of oxygen, which lead to an incomplete combustion with

a)

b)
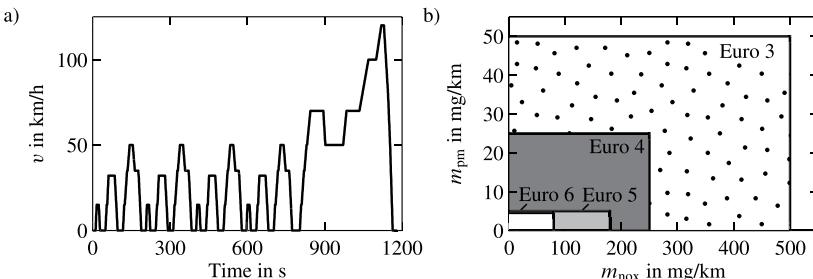
Figure 1.1: a) Velocity profile of the *new European driving cycle* NEDC b) European legis-
lative limitations for particulate and $NO_x$ emissions during the NEDC (Regulations 98/69/EC;
715/2007/EC of the European parliament)

large particulate emissions. Another often contrary target is to avoid high oxygen concentrations
in combination with high peak temperatures leading to enlarged $NO_x$ emissions. These engine
internal provisions can be separated into in-cylinder and intake and exhaust system measures.
In-cylinder measures cover the complex combustion chamber geometry, variable valve timings,
high-pressure fuel injection, injection patterns with up to eight injections for each engine working
cycle (Bischoff et al., 2012), closed-loop controlled combustion process and modern combustion
processes like homogeneous charge compression ignition (HCCI). The intake and exhaust system
has the tasks to supply the combustion process with a desired cylinder charge and to condition
the operation and regeneration of aftertreatment systems. In which turbocharging, charge cooling,
charge motion and exhaust gas recirculation (EGR) are the major measures to increase the engine
efficiency and to decrease the in-cylinder emissions.

Turbochargers have become state of the art in Diesel engines and are applied more and more in
spark ignition engines. Their working principle recuperates enthalpy from the exhaust gas to drive
a compressor, which allows higher charge-air pressures and consequently larger cylinder fillings.
On the one hand this decreases the charge cycle losses, on the other hand more fuel can be injected
at a given displacement volume. This downsizing results in smaller cylinders with less wall heat
losses, less friction, lighter engines, a higher efficiency in partial load and consequently less fuel
consumption. All measures of charge cooling increase the gas density of the cylinder charge and
are beneficial for the fuel consumption and usually result in lower $NO_x$ emissions. However, too
low gas temperatures can lead to condensation and slow down the combustion, so that the fuel does
not react completely and enlarged CO and HC emissions occur. Consequently, special measures
like switchable EGR coolers are necessary to avoid too low charge temperatures at engine warm-
up or states with low load, see Dworschak et al. (2009); Uesugi et al. (2009) and Werner et al.
(2011).

An exhaust gas recirculation is one of the most effective method to reduce the $NO_x$ emissions.
For this purpose a part of the cylinder charge is replaced by recirculated exhaust gas. This ex-
haust gas can be kept as internal EGR in the combustion chamber via valve timings or can be

fed back as external EGR from the exhaust system to the intake system. Generally, recirculated inert exhaust gas has a lower oxygen concentration and an enlarged heat capacity. This results in a slower rate of combustion and in combination with a larger heat capacity in reduced combustion peak temperatures with less $NO_x$ formation. In contrast, the resulting lower oxygen concentration results in enlarged particulate emissions and a $NO_x$ particulate tradeoff occurs. Besides the rate of recirculated exhaust gas, also charge-air pressure, intake temperature, injection and combustion characteristics determine this tradeoff. Consequently, this tradeoff has to be stationary and dynamically optimised by the engine calibration and the control strategy for the air path actuators and the injection quantities.

The external EGR can be achieved in form of a classical high-pressure exhaust gas recirculation (HP-EGR), in which the usually cooled exhaust gas is recirculated via a valve on high-pressure level from exhaust manifold to intake manifold. As a drawback this approach extracts the gas before it can drive the turbine and the turbocharger usually decelerates. At large charge-air pressures and high HP-EGR rates the compressor operation moves towards its surge line and can be operated in unstable regions of the turbocharger map (Weber et al., 2005). Consequently, in this configuration high HP-EGR rates in conjunction with large charge-air pressures are not possible. Furthermore, the pressure difference between intake and exhaust manifold limits feasible HP-EGR rates. Finally, the HP-EGR has the drawback of a short mixing section, which can lead to cylinder individual air contents between HP-EGR and fresh air.

A novel approach termed low-pressure exhaust gas recirculation (LP-EGR) recirculates the exhaust gas on low pressure side from turbine outlet to compressor inlet after it has recuperated its energy. The LP-EGR is dosed via a valve and an additional throttle valve in either the intake or the exhaust system can increase the pressure drop over the LP-EGR route to achieve higher LP-EGR rates. In contrast to a HP-EGR, the LP-EGR results in lower charge temperatures, since it is triple cooled by the turbine expansion process, a LP-EGR cooler and the charge air cooler. Due to the longer route, changes in the LP-EGR mass flow rate reach the cylinders delayed, but show compared to a HP-EGR a better mixing of exhaust gas with fresh air. This homogeneous gas mixing can be advantageous for combustion modes with large proportions of recirculated gas like HCCI. Since the LP-EGR is operated on the low pressure side of turbine and compressor, it has less couplings to the turbocharger and allows simultaneously high LP-EGR rates at large charge-air pressures. At a given air mass flow rate and pressure ratio the compressor is operated at a higher isentropic efficiency with LP-EGR (Weber et al., 2005), but also has to compress both the fresh air and the recirculated exhaust gas. In a LP-EGR configuration a Diesel particulate filter becomes obligatory to protect the fast running compressor from impact of particulates. Further precautions like a homogeneous mixture between exhaust gas and fresh air and a protective coating for aggressive condensation and particulate impact are necessary to guard the compressor wheel from wearing, see Münz et al. (2008); Brune (2009). While the HP-EGR bypasses the particulate filter and only the tailpipe emissions load the filter, the LP-EGR delivers an additional filter load, which can lead to shorter filter regeneration intervals (Maiboom et al., 2009).

Investigations showed, that especially the $NO_x$ emissions can be significantly lowered by a LP-EGR (Beatrice et al., 2009; Schöppe et al., 2009). However, a solely LP-EGR configuration leads

to too low intake temperatures at engine warm-up and cold ambient conditions. Therefore, a combination between a HP-EGR and LP-EGR seems to be a promising solution to reach future emissions limits in conjunction with other engine improvements and a moderate exhaust gas aftertreatment, especially for small to medium power engines, see Rinolfi (2008), Ertl et al. (2009); Genieser et al. (2010) and Nam et al. (2011). Also series engines with dual EGR paths fulfilling the most stringent emission limits Tier 2 Bin5 respectively EURO6 are available, see Hadler et al. (2008); Lückert et al. (2013).

Future engine trends result in more and more complex engine systems and it is foreseeable that two-stage turbochargers will become state of the art in series engines (Bischoff et al., 2012; Wartha et al., 2012). Other developments are going even further and apply three-stage turbochargers with up to 4 bar charge-air pressure in series (Eidenböck et al., 2012). If further less fuel consumption is demanded, it is likely that engine cylinder deactivation for spark ignition engines (Middendorf et al., 2012; Flierl and Lauer, 2013; Kortwittenborg and Walter, 2013) will be adapted to the Diesel engine. This rising complexity forces the manufacturer to utilise more common parts to tailor the single engines with different powers from predefined construction kits (Dworschak et al., 2009; Crabb et al., 2013; Neusser et al., 2013). A further trend in engine development shows, that market individual emission standards and engine adaptations lead to hundreds of application variants for one and the same engine (Zimmermann et al., 2015). Besides the mechanical reuse of common parts this will likely demand the reuse and interchange of models, model parameters, base calibrations, control and diagnosis algorithms between the different engine variants and engines.

## 1.1 Thesis Objective

Considering the past and future development of Diesel engines there are several tasks, which are solved in this thesis. The additional LP-EGR system increases the complexity of the intake and exhaust system and demands an investigation of the novel system properties like side-effects to other air path quantities. Another problem is to identify suitable controlled variables for a dual EGR air path configuration with turbocharger. After the controlled variables are identified and reference values are derived, a control scheme is necessary to develop the controllers. Then the derived control concept needs to be benchmarked with regard to the resulting driving cycle emissions, since the main driver for the LP-EGR system are the legislative emission limits.

Due to the system complexity these tasks can be hardly mastered manually and need support by model-based methods, which demand a modelling of the engine air path and the emission formation. In consideration of the utilisation of more and more common parts over different engine types and engine variants, the models and parameters for the engine air path should be modular and exchangeable. Models for the stationary and dynamical emissions as well as reference values for the controllers are necessary to determine the controlled variables and to rate the control concepts.

The steadily decreasing emission limits require an engine control with high demands on reference following and disturbance rejection. The trend to a further engine downsizing can benefit

from a fast charge-air pressure buildup in order to have a dynamical torque response. Especially the air path quantities are coupled and strongly nonlinear, which requires a sophisticated multi-variable control to control the single quantities to their setpoint. As a further side condition the controllers have to be capable to meet these requirements under changing engine conditions like varying ambient conditions, different particulate filter loads, several engine operation modes for exhaust gas aftertreatment system maintenance and future requirements like a cylinder deactivation. These demands preferably have to be met with a minimum of controller calibration effort and the controllers are ideally directly calibrated by flexible models in order to be able to handle the strongly rising variance of a single engine for individual market adaptations. Since there are deviations between stationary calibrated emissions and dynamical driving cycle emissions, there is a last need for a dynamically optimised control with regard to the emissions.

## 1.2   Thesis Outline and new Contributions

Diesel engines have been and are still a nutritious field of research. Their tremendously risen and rising complexity demands a deep system understanding for an efficient development and test of control and diagnosis algorithms. The model-based design methodology is an efficient approach to master this complexity and maybe its largest benefits are the capabilities to give a deep understanding of the investigated processes. However, to get even a small glimpse into the Diesel engine process a solid base of knowledge is necessary. Considering the complete process is understood, many of the arising problems often can be solved with simple solutions. Therefore, a complete methodology ranging from modelling, model analysis, model optimisation is necessary for control function development. Consequently, this publication has to be separated into a brief dissertation and an extensive version given in Mrosek (2017) to illuminate the engine interactions and the process of function development for modern engines as a holistic approach. Main contributions of this dissertation can be summarised to:

- Analysis of system properties for the turbocharged HP- and LP-EGR air path.

- Gas composition modelling with lumped parameter and pipe receiver approach. Validation and comparison of different models with test bench measurements.

- System property and emission model based determination of controlled variables for the HP- and LP-EGR air path.

Stationary and dynamical combustion and emission models are utilised to optimise stationary and dynamical reference values for the air path control. Novelties in the application of stationary and dynamical combustion and emission models are:

- Detailed investigation and separation of emission formation and emission measurement dynamics.

- Combination of experimental stationary emission and combustion models with dynamical models for the engine air path and measurement dynamics to simulate the engine behaviour.

- Investigation of the source of dynamical emission formation and comparison of different control concepts with regard to dynamical emissions.

- On-line capable optimisation of reference values for the air path control with respect to dynamical emission formation.

All knowledge is finally composed in the control concept wit the new findings:

- Modular semi-physical feedforward control for a charge-air pressure and HP-EGR mass flow rate control with consideration of ambient conditions and different engine operation modes. This masters the risen complexity of future engine control systems and allows an efficient management of engine variants. Extension to a semi-physical internal model control.

- Calibration friendly semi-physical LP-EGR mass flow rate control, which is invariant to the engine operation point.

- Dynamical reference value generation for the HP- and LP-EGR mass flow rate control, which masters the gas propagation effects introduced by the LP-EGR and is invariant to modelling and measurement uncertainties.

- Evaluation, quantification and comparison of different control concepts with respect to dynamical driving cycle emissions and quasi-stationary emissions.

All work is carried out with the exemplary process of the turbocharged Diesel engine with HP- and LP-EGR, but the shown methods are not limited to this process and can be easily applied and extended to most air path configurations. The developed methods are valid for many kinds of Diesel engine applications and not limited to automotive and truck applications. A further application of the presented methods for the development of control functions for turbocharged spark ignition engines is also possible.

**Outline**

Objective of this work is to deliver an integrated approach for function development of engine control functionalities. This approach is carried out with an exemplary engine configuration consisting of a turbocharged Diesel engine with HP- and LP-EGR.

In Chap. 2 an introduction about the engine configuration is given. Chap. 3 covers the physical relationships to model the ducts, valves, coolers, flow restrictions and the turbocharger in the intake and exhaust system, as well as a mean value model for the in-cylinder processes.

Chap. 4 deals with the analysis of stationary and dynamical influences of turbocharger, HP-EGR and LP-EGR-actuators to the intake and exhaust system quantities and the properties of different LP-EGR configurations are shown. Major differences between a HP-EGR and a LP-EGR configuration are the gas propagation effects in the intake and exhaust system, which are represented by a control-oriented model.

Chap. 5 focuses on stationary and dynamical emission formation and illustrates different sources of process and measurement dynamics. The apparent process and measurement dynamics demand a stationary measurement design to model the stationary emissions by polynomial models with the cylinder charge composition as model input. A combination of these stationary emission models with dynamical models for the cylinder charge and measurement dynamics allows to simulate the dynamical emission formation and to derive advanced control functionalities.

The stationary series HP-EGR engine calibration is compared to a given LP-EGR engine calibration in Chap. 6. Further, the dynamical emissions for different control concepts are shown and a method for the on-line optimisation of reference values for the air path control with regard to the dynamical emission formation is given.

Chap. 7 composes the gained system knowledge to derive a semi-physical feedforward control for charge-air pressure and HP-EGR mass flow rate and compares different control concepts for these quantities. A non-linear controller based on a semi-physical relationship allows to control the LP-EGR mass flow rate at all given engine operation points and different engine operation modes. These control concepts are a replacement for state of the art controllers with numerous interacting maps and are based on transparent semi-physical relationships. The modular structure of the control law, which is based on semi-physical model equations, covers most process non-liniearities and allows an efficient adaptation of the control to engine variants. Further, a reference value transformation is derived, which supplies the cylinder with a desired air content considering the current air contents in the intake and exhaust system, which is characterised by long gas propagation times of the LP-EGR. Finally, different control concepts are evaluated for the NEDC with respect to the delivered engine work and the simulated dynamical emission quantities $NO_x$ and particulates. Further, the emissions of the stationary engine calibration are quantitatively compared to the dynamical emission formation during the driving cycle. Finally, the findings are summarised in Chap. 8.

# 2 Engine Configuration and Modelling

This chapter describes the investigated HP- and LP-EGR engine with all relevant process inputs, states and outputs. Based upon the system design suitable modelling approaches to simulate the engine air path and the emissions are chosen.

## 2.1 Engine Configuration with two EGR-Systems

The engine intake and exhaust system conditions the cylinder filling for the combustion process by manipulating its pressure, temperature, air content and swirl. After an emission aftertreatment, the exhaust gas is disposed via the exhaust pipe, see Pischinger et al. (2009); Mollenhauer and Tschöke (2010); Reif (2012). Fig. 2.1 shows the system configuration of the test engine having a single stage turbocharger with variable geometry turbine (VGT) and two exhaust gas recirculation systems. Fresh air enters the intake system and an air filter prevents that dust and particulates foul the intake system and the combustion chamber and it further decreases the suction noise. Its load results in an pressure drop and is simulated via the loading factor $k_{af}$. An intake throttle valve is part of the low pressure exhaust gas recirculation and lowers the intake pressure, to allow more exhaust gas via the LP-EGR path.

The turbocharger is driven by exhaust gas and compresses the inflowing gas to larger pressures, which result in higher gas densities. Consequently, at a given displacement volume more gas can be filled in the cylinder and simultaneously more fuel can be injected and burned. This recuperation of exhaust gas enthalpy has positive influences on the charge cycle and in combination with an enlarged power per displacement volume the engine efficiency is improved. The compression process increases the charge temperature, which is afterwards cooled by an intercooler to allow higher gas densities, an improvement of the thermal engine efficiency and lower emissions. In the intake manifold the inflowing gas is mixed with cooled recirculated exhaust gas, which is dosed via a valve. Since the exhaust gas is recirculated on the high pressure level of compressor and turbine, this kind of exhaust gas recirculation is termed high pressure exhaust gas recirculation. An additional throttle valve in the intake manifold can enlarge the pressure drop over the HP-EGR-valve and increases the amount of recirculated gas on the high pressure level. Further, it has the objectives to reduce the air mass flow rate in case of a Diesel particulate filter regeneration and to prevent engine shaking at switching off.
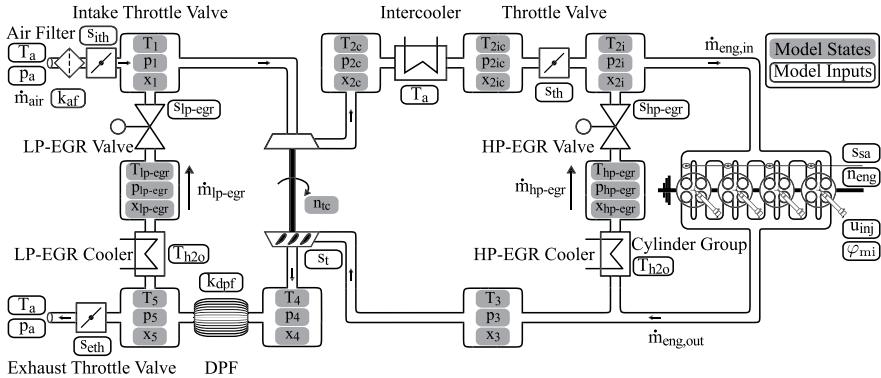
**Figure 2.1:** System configuration for the investigated turbocharged engine with HP- and LP-EGR

Before the gas enters the combustion chamber via the intake valves, a swirl actuator gives the stream a favourable motion to allow a good mixture with the injected fuel. A desired fuel quantity is injected in several pilot injections, a main injection and post injections via a common rail injection system. After the combustion has taken place in the power stroke, the gas is pushed into the exhaust manifold during the exhaust stroke. The exhaust gas is guided by the variable turbine geometry and drives the turbine, which allows to operate the turbocharger in an optimal operation mode at low and high mass flow rates. At low mass flow rates the guiding vanes of the VGT are closed, so that the gas is further accelerated and the turbine delivers more power to drive the compressor. At high mass flow rates the guiding vanes are opened to a larger surface area with a slower fluid velocity, so that the turbocharger stays within its specified speed limits. After the expansion process, the exhaust gas passes the Diesel particulate filter and is cleaned. In which the loading of the particulate filter can be simulated by the factor $k_{\text{dpf}}$. At a rather low pressure level a part of the exhaust gas is cooled and recirculated via the low pressure exhaust gas recirculation. The other part of the exhaust gas leaves the engine via the exhaust throttle valve.

For this dissertation the intake and exhaust system of the Opel DTH-Z19 common rail Diesel test engine was extended by the author with a LP-EGR path. Additional to the series configuration a Diesel particulate filter, a LP-EGR cooler, a LP-EGR-valve, an intake throttle valve and an exhaust throttle valve were mounted to the engine. The LP-EGR cooler was kindly provided by Behr and is connected to the testbed cooling system. With support of DES (Diesel Exhaust Systems GmbH) a DPF solution with electric regeneration was retrofitted.

Usually the pressure drop over the LP-EGR-valve is not large enough to drive the demanded LP-EGR mass flow rates. Consequently, the pressure over the LP-EGR-valve can be enlarged with the help of additional throttle valves, which can be mounted either at the engine intake or the exhaust. An intake throttle valve can lower the pressure after the air filter by throttling the inflowing air, while the other option is to throttle the exhaust gas and rise the pressure after the DPF. Generally,
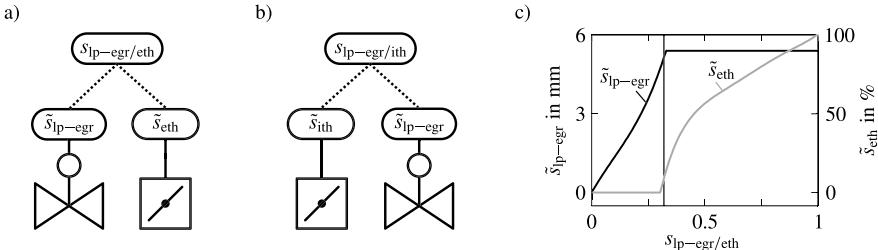
**Figure 2.2:** a) Combination of actuators intake throttle valve and LP-EGR-valve to the combined actuator position $s_{lp-egr/ith}$ b) combination of actuators exhaust throttle valve and LP-EGR-valve to the combined actuator position $s_{lp-egr/ith}$ c) mapping of the combined actuator position $s_{lp-egr/eth}$ to the single actuator positions $\tilde{s}_{lp-egr}$ and $\tilde{s}_{eth}$

a standard throttle valve can be utilised as intake throttle valve, while an exhaust throttle valve is exposed to harsh conditions with hot exhaust gas and condensates. In this installation a dynamical fast electric driven throttle valve with a sophisticated position control as given in Kopf (2014) is utilised for the intake throttle valve, while a dynamical slow thermal robust pneumatic throttle valve without position control is applied for exhaust throttling. Hence, all control results in Chap. 7 are derived with the intake throttle valve configuration.

All relevant air path actuators are equipped with a position sensor and most are position controlled. Normalised positions are given for the intake throttle valve $s_{ith}$, throttle valve after compressor $s_{th}$, swirl actuator $s_{sa}$, HP-EGR-valve $s_{hp-egr}$, VGT-actuator $s_t$, LP-EGR-valve $s_{lp-egr}$ and exhaust throttle valve $s_{eth}$. All $i$ actuator positions $s_i$ are normalised between 0 and 1 and measured positions are denoted by $\tilde{s}_i$. The HP-EGR-valve is shaped according to Appx. C to have a rather linear relationship between the normalised position and the potential controlled variables $\dot{m}_{hp-egr}$ and $\dot{m}_{air}$. Furthermore, the LP-EGR-valve is combined with either the intake throttle valve or the exhaust throttle valve. This combination results in the combined actuator positions $s_{lp-egr/ith}$ in Fig. 2.2a) and $s_{lp-egr/eth}$ in Fig. 2.2b). The combinations of the single actuators are shaped to achieve a linear actuator characteristics with regard to the quantities $\dot{m}_{lp-egr}$ and $\dot{m}_{air}$, see exemplary Fig. 2.2c) and the more detailed description in Appx. C.

Besides the air path actuators, the quantities engine speed $n_{eng}$, desired injection quantity $u_{inj}$ and start of the main injection $\varphi_{mi}$ are considered as model inputs for the air path model. Other influencing variables for the combustion process are neglected to keep the model complexity reasonable. Further, influencing quantities and model inputs are the quantities ambient pressure $p_a$, ambient temperature $T_a$, engine coolant temperature $T_{h_2o}$, loading of air filter $k_{af}$ and loading of particulate filter $k_{dpf}$. Overall this results in a model input dimensionality of 14. Further, the model states are shown in Fig. 2.1. These states are pressures $p_i$, temperatures $T_i$ and air contents (ratio of fresh air mass to total gas mass) $x_i$ in the storage elements $i$ as well as the turbocharger speed $n_{tc}$. This yields a model of order 28, if all states are modelled.

Whenever simulated or estimated quantities are mixed with measured quantities, the simulated quantities are denoted by the hat symbol. This is exemplary the case, if the HP-EGR mass flow rate is estimated via a model ($\hat{\dot{m}}_{\text{hp}-\text{egr}}$), while the other quantities are directly measured ($p_{2\text{i}}$, $\dot{m}_{\text{air}}$, . . .). When only simulated quantities are considered, the shown quantities are not necessarily marked by the hat symbol.

In this dissertation there are two modelling tasks to model the emission formation and the engine air path. The emission formation is a complex process and can only hardly be modelled by physical and chemical laws. Consequently, a black-box modelling of the emissions is a promising approach. There are various methods of statistical learning for experimental modelling, e.g. polynomials (Nelles, 2000; Isermann and Münchhof, 2011), support vector machines (Kecman, 2001; Vogt, 2008), neural networks (Nelles, 2000; Kecman, 2001) as well as fuzzy, neuro-fuzzy and local linear neural fuzzy models (Nelles, 2000; Isermann and Münchhof, 2011). Local linear neural fuzzy models of type local linear model tree (LOLIMOT), see Nelles (2000); Isermann and Münchhof (2011), showed promising results in modelling the emissions in Schüler (2001) and Hafner (2002) and the emission modelling capabilities have been improved by the local polynomial model tree (LOPOMOT) as described in Sequenz (2013). Thus, these local polynomials will be utilised to model the emission formation in Chap. 5.

# 3 Semi-Physical Mean Value Engine Model

This chapter contains the fundamental physical relationships to describe a mean value engine model. The overall mean value engine model is composed as an interconnection of several different submodels. First the intake and exhaust system with storage elements, flow restrictions and heat exchangers is modelled. Then follow the mean value cylinder model and the turbocharger model. A block diagram shows relationships and interactions between different submodels.

The proper choice of a model class depends upon the problem to be solved (Guzzella and Onder, 2010). Detailed investigations of flow phenomena in the intake and exhaust system demand *distributed parameter* models as one-dimensional models or even three-dimensional models with *computational fluid dynamics* (Merker et al., 2006). These models are computational demanding and usually not realtime-capable.

Hence, simplified models as control oriented models with *lumped parameters* are state of the art for function development. In these models the gas system is modelled by ordinary differential equations, which describe the states in the intake and exhaust system and the input-output behaviour with reasonable precision at low computational cost. These models include the stationary and the relevant dynamical characteristics of the air path and are therefore suitable for modern control methods, system analysis and engine calibration, see e.g. Heywood (1988); Guzzella and Onder (2010); Jung (2003); Ammann (2003); Eriksson (2007). The class of lumped parameter engine models can be further divided into *mean value engine models* (MVEM) and *crank angle synchronous engine models* (CASEM). Here, the accuracy of the cylinder model is the major difference between these two modelling approaches. Mean value engine models usually consist of a simplified cylinder model, where the gas mass and enthalpy flows entering and exiting the engine are modelled as their mean value during the engine working cycle. Consequently, pressure and flow pulsations in the intake and exhaust system are neglected and there is generally no detailed combustion model.

Crank angle synchronous engine models can be categorised in their complexity between lumped parameter models and one-dimensional models. Usually a simple combustion model delivers cylinder individual crank angle synchronous in-cylinder measures like the in-cylinder pressure. Also the influences of the charge cycle, like the pressure and mass flow oscillations in the intake and exhaust system are modelled crank angle synchronously (Zahn, 2012). These CASEM models are mainly necessary to design, calibrate and test the functionality of in-cylinder measurement based combustion controls. A further field of application are system analysis, calibration and function development for variable valve timing (VVT) engines. When it comes to the control of air path

quantities, most requirements for modern control methodologies and system analysis can be satisfied by a conventional mean value engine model. The following sections present the state of the art modelling of the intake and exhaust system as given in Heywood (1988); Guzzella and Onder (2010); Jung (2003); Ammann (2003); Eriksson (2007); Zahn (2012), while the parametric turbocharger power models are mainly based upon the work of Zahn and Isermann (2008). After all relevant submodels are derived, the signal flow diagram of the overall mean value engine model is given in Sect. 3.4.

## 3.1   Intake and Exhaust System

A lumped parameter approach represents the intake and exhaust system as an alternating sequence of storages (intake manifold, ducts, exhaust manifold) and throttles (valves, filter, coolers). Figure 2.1 shows the structure of the modelled elements in the mean value engine model. Only the dynamical relevant states are modelled. Small storages like the duct of the HP-EGR path are not modelled to keep the model complexity and model stiffness reasonable low (Guzzella and Onder, 2010).

**Storage Elements**

Fig. 3.1a) depicts a storage element in gas mass flow representation with its model inputs, model states and model outputs. The model inputs are given as inflowing gas mass flow rates $\dot{m}_{\text{in},i}$, outflowing gas mass flow rates $\dot{m}_{\text{out},j}$, inflow temperatures $T_{\text{in},i}$ and inflow air contents $x_{\text{in},i}$. Model states are gas mass $m_{\text{st}}$, internal energy $U_{\text{st}}$ and air content $x_{\text{st}}$ in each storage element, while the model outputs pressure $p_{\text{st}}$ and temperature $T_{\text{st}}$ follow by algebraic equations from the model states. A further quantity are the wall heat losses $\dot{Q}_{\text{w,st}}$, which are necessary to determine the internal energy. Alternatively storage elements can be represented as a block diagram in input output representation, as given in Fig. 3.1b).
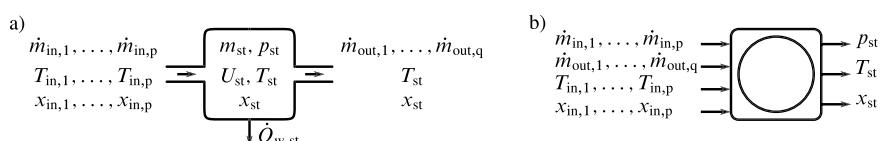


**Figure 3.1:** a) Inputs, states, and outputs of a storage element in gas mass flow representation.
b) Block diagram of a storage element in input output representation

These lumped storage elements in the gas system can be regarded as open thermodynamic systems with $p$ inflowing and $q$ outflowing mass and enthalpy flows. With the assumption that no substantial changes in the potential or kinetic energy in the flow occur, the basic equations for these storage components are the conservation laws for mass

$$\frac{dm_{st}}{dt} = \sum_{i=1}^{p} \dot{m}_{in,i} - \sum_{j=1}^{q} \dot{m}_{out,j} \qquad (3.1)$$

and energy

$$\frac{dU_{st}}{dt} = \sum_{i=1}^{p} h_{in,i} \dot{m}_{in,i} - \sum_{j=1}^{q} h_{out} \dot{m}_{out,j} - \dot{Q}_{w,st}. \qquad (3.2)$$

The change in energy is described by the wall heat losses $\dot{Q}_{w,st}$ and the enthalpy in- and outflows which are determined by the specific enthalpies

$$h_{in,i} = c_p T_{in,i} \qquad \text{and} \qquad h_{out} = c_p T_{st} \qquad (3.3)$$

and the corresponding mass flow rates $\dot{m}_{in,i}$ and $\dot{m}_{out,j}$. These specific enthalpies result from the heat capacity at constant pressure $c_p$ and the temperatures $T_{in,i}$ and $T_{st}$ of in- and outflowing mass flows. The totally stored energy in a storage element results from the storage temperature $T_{st}$, the stored gas mass $m_{st}$ and the heat capacity at constant volume $c_V$.

$$U_{st} = c_V T_{st} m_{st} \qquad (3.4)$$

In order to determine the temperature differential equation of a storage element, it follows from Eq. (3.4)

$$\frac{dU_{st}}{dt} = \frac{d\left(c_V T_{st} m_{st}\right)}{dt} = c_V m_{st} \frac{dT_{st}}{dt} + c_V T_{st} \frac{dm_{st}}{dt}. \qquad (3.5)$$

Substitution in Eq. (3.2) leads to

$$\frac{dT_{st}}{dt} = \frac{1}{c_V m_{st}} \left( \sum_{i=1}^{p} h_{in,i} \dot{m}_{in,i} - \sum_{j=1}^{q} h_{out,j} \dot{m}_{out,j} - \dot{Q}_{w,st} - c_V T_{st} \frac{dm_{st}}{dt} \right). \qquad (3.6)$$

The calculation of the internal energy $U_{st}$, as well as the specific enthalpies $h_{in,i}$ and $h_{out,j}$ are based on the simplified assumption of constant heat capacities $c_V$ and $c_p$ for air. A variable heat capacity for gas could be considered in each storage element for a more detailed model which demands more computation time. This variable heat capacity of burned gas mainly depends on the gas temperature and air-fuel ratio $\lambda$ and can be approximated by a polynomial approach (Merker et al., 2006). This approach is supposed to go back on the tables for pure gases of Justi (1938), but it is more likely based on the diagrams for combustion gases published in Lutz and Wolf (1938) which are a further development of Justi's tables. The consideration of a variable heat capacity would

further result in a variable isentropic expansion factor $\kappa$ which is given as $\kappa = c_{\mathrm{p}}/c_{\mathrm{V}}$ and form a complexer relationship Eq. (3.22).

The wall heat losses $\dot{Q}_{\mathrm{w,st}}$ are modelled by Newton's law of heat transfer

$$\dot{Q}_{\mathrm{w,st}} = k_{\mathrm{w,st}} A_{\mathrm{w,st}} \left( T_{\mathrm{st}} - T_{\mathrm{a}} \right) \tag{3.7}$$

with the overall heat transmission coefficient $k_{\mathrm{w,st}}$, the duct surface area $A_{\mathrm{w,st}}$, the gas temperature $T_{\mathrm{st}}$ and the ambient temperature $T_{\mathrm{a}}$. For model simplification an additional state with wall heat storage and wall temperature is neglected. These wall heat losses are only considered in the exhaust pipe with its large surface area in storage element 5. In all other storages the wall heat losses are not of great significance and are neglected in the storage temperature derivation. However, especially for the following turbocharger power models in Sect. 3.3.2 heat transfers will play an important role.

Afterwards the pressure in every storage element results with the ideal gas law and the solution of the mass balance (3.1) for the gas mass $m_{\mathrm{st}}$ as well as the integration of the temperature differential equation (3.6) for the storage temperature $T_{\mathrm{st}}$ as

$$p_{\mathrm{st}} = \frac{m_{\mathrm{st}} T_{\mathrm{st}} R}{V_{\mathrm{st}}}, \tag{3.8}$$

where $V_{\mathrm{st}}$ represents the lumped storage element volume and $R$ is the specific gas constant. The ideal gas law can be rearranged to yield the gas density $\rho_{\mathrm{st}}$ in each storage element

$$\rho_{\mathrm{st}} = \frac{m_{\mathrm{st}}}{V_{\mathrm{st}}} = \frac{p_{\mathrm{st}}}{T_{\mathrm{st}} R}. \tag{3.9}$$

The air content $x_{\mathrm{st}}$ in each storage element allows to investigate the dynamic impact of the two EGR-systems in the intake and exhaust system. The normalised air content can be expressed as the proportion of the fresh air mass $m_{\mathrm{st,air}}$ and the total gas mass $m_{\mathrm{st}}$ in each storage element, see also Mrosek and Isermann (2010a)

$$x_{\mathrm{st}} = \frac{m_{\mathrm{st,air}}}{m_{\mathrm{st}}} = \frac{m_{\mathrm{st,air}}}{m_{\mathrm{st,air}} + m_{\mathrm{st,f}} L_{\mathrm{st}} + m_{\mathrm{st,f}}}. \tag{3.10}$$

Furthermore, $m_{\mathrm{st}}$ can be divided into the sum of fresh air mass $m_{\mathrm{st,air}}$, the burned gas mass containing no oxygen $m_{\mathrm{st,f}} L_{\mathrm{st}}$ and the amount of fuel $m_{\mathrm{st,f}}$ in each storage element. Herein $L_{\mathrm{st}}$ represents the stoichiometric air requirement. Thus, $x_{\mathrm{st}} = 1$ represents pure fresh air, consisting of 20.9 % oxygen, while $x_{\mathrm{st}} = 0$ stands for a totally consumed amount of fresh air. The air-fuel ratio

$$\lambda = \frac{m_{\mathrm{air}}}{m_{\mathrm{f}} L_{\mathrm{st}}} \tag{3.11}$$

is globally expressed as the ratio of fresh air $m_{air}$, which enters the gas system and the amount of air $m_f L_{st}$ which is required to burn the injected fuel quantity. However, this only describes the air fuel ratio with respect to the quantities which globally enter the combustion engine. For storages after the combustion process, the global fresh air mass $m_{air}$ flowing into the engine can be divided into a remaining fresh air mass $m_{st,air}$ and a burned gas mass $m_{st,f} L_{st}$. Then the air-fuel ratio of a storage element $\lambda_{st}$ can be rewritten as

$$\lambda_{st} = \frac{m_{st,air} + m_{st,f} L_{st}}{m_{st,f} L_{st}}. \tag{3.12}$$

Accordingly the relationship between the air content (3.10) and the air fuel ratio (3.12) follows by substituting $m_{st,f}$ as

$$\lambda_{st} = \frac{m_{st,air} + \left(\frac{m_{st,air}(1-x_{st})}{x_{st}(1+L_{st})}\right) L_{st}}{\left(\frac{m_{st,air}(1-x_{st})}{x_{st}(1+L_{st})}\right) L_{st}} = \frac{x_{st} + L_{st}}{L_{st} - L_{st} x_{st}}. \tag{3.13}$$

In a lumped parameter approach the differential equation for the air content is given as derivative of (3.10)

$$\frac{dx_{st}}{dt} = \frac{\frac{dm_{st,air}}{dt} m_{st} - m_{st,air} \frac{dm_{st}}{dt}}{m_{st}^2}, \tag{3.14}$$

in which the change of stored fresh air mass can be expressed with the air contents of inflows $x_{in,i}$ and outflows $x_{out,j}$ as

$$\frac{dm_{st,air}}{dt} = \sum_{i=1}^{p} x_{in,i} \dot{m}_{in,i} - \sum_{j=1}^{q} x_{out,j} \dot{m}_{out,j}. \tag{3.15}$$

Then (3.1) and (3.15) can be inserted in (3.14) and yield

$$\frac{dx_{st}}{dt} = \frac{\left(\sum_{i=1}^{p} x_{in,i} \dot{m}_{in,i} - \sum_{j=1}^{q} x_{out,j} \dot{m}_{out,j}\right) m_{st} - m_{st,air} \left(\sum_{i=1}^{p} \dot{m}_{in,i} - \sum_{j=1}^{q} \dot{m}_{out,j}\right)}{m_{st}^2}. \tag{3.16}$$

Given that $x_{out,j} = x_{st}$ and substituting according to (3.10) $m_{st,air} = x_{st} m_{st}$ finally leads to differential equation for the air content

$$\frac{dx_{st}}{dt} = \frac{1}{m_{st}} \left[ \sum_{i=1}^{p} (x_{in,i} - x_{st}) \dot{m}_{in,i} \right]. \tag{3.17}$$
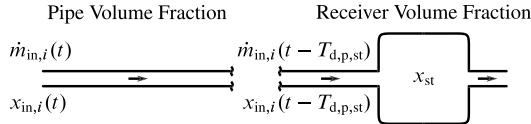
**Figure 3.2:** Pipe receiver air content model

Alternatively to the lumped parameter approach, the air content dynamics can be modelled as a plug flow via a pipe receiver model (Benz, 2010), see Fig. 3.2. Dependent on the storage geometry every lumped storage $V_{st}$ can be partitioned by the pipe volume fraction $\xi_{p,st}$ into a pipe section without storage

$$V_{p,st} = V_{st}\xi_{p,st} \tag{3.18}$$

and a subsequent receiver volume

$$V_{r,st} = V_{st}\left(1 - \xi_{p,st}\right). \tag{3.19}$$

In each pipe element the gas propagation time results as a variable dead time

$$T_{d,p,st} = \frac{\rho_{p,st}V_{p,st}}{\dot{m}_{p,st}} \tag{3.20}$$

with the pipe volume $V_{p,st}$, the mass flow rate $\dot{m}_{p,st}$ and the gas density $\rho_{p,st}$. For the receiver dynamics, temperature and pressure in every storage element are modelled by the lumped parameter approach with the complete volume $V_{st}$ and allow to determine with (3.8) and (3.19) the gas mass stored in each receiver element $m_{r,st}$. Then the receiver air content dynamics results with (3.17) and the corresponding stored gas mass in every receiver element $m_{r,st}$.

In the overall mean value engine model the air content is modelled with the lumped parameter approach which considers only a receiver proportion. In Sect. 4.4 the lumped parameter approach is compared to the pipe receiver approach and a control-oriented model for the air content based upon the pipe and receiver approach is presented.

**Flow Restrictions**

The pressure difference between two storage elements and the resistance of the connecting flow restriction cause a mass flow rate. This mass flow rate can be modelled by Bernoulli's law for incompressible fluids as

$$\dot{m}_{res} = C_D A_{ref}\sqrt{\frac{2p_{in}}{RT_{in}}}\sqrt{p_{in} - p_{out}}. \tag{3.21}$$

For compressible fluids the flow restriction can be treated as an isenthalpic throttle which yields

$$
\dot{m}_{\text{res}} = C_D A_{\text{ref}} \frac{p_{\text{in}}}{\sqrt{R T_{\text{in}}}} \sqrt{\frac{2\kappa}{\kappa-1} \left[ (\Pi)^{\frac{2}{\kappa}} - (\Pi)^{\frac{\kappa+1}{\kappa}} \right]}
$$
$$
\text{with} \qquad \Pi = \min \left[ \max \left[ \frac{p_{\text{out}}}{p_{\text{in}}}, \left( \frac{2}{\kappa+1} \right)^{\frac{\kappa}{\kappa-1}} \right], 1 \right].
$$
(3.22)

In which $C_D$ is the orifice discharge coefficient, $A_{\text{ref}}$ denotes a reference flow area and $\kappa$ is the isentropic expansion factor. $p_{\text{in}}$ and $T_{\text{in}}$ are the pressure and the temperature upstream the orifice, while $p_{\text{out}}$ is the pressure downstream the flow restriction. Orifices with a fixed flow area (filters, coolers, ducts) are characterised by low flow velocities and a small pressure drop. They are modelled by Eq. (3.21). These models have only the product $C_D A_{\text{ref}}$ as parameter, which is identified with test bench measurements. In flow restrictions with a variable cross sectional area (throttle valve, EGR-valves) large differential pressures and high flow velocities occur. Especially at high pressure differences when the reference area is very narrow, the flow reaches sonic conditions. In such cases Eq. (3.22) is applied and $C_D A_{\text{ref}}$ is modelled as a polynomial of the normalised actuator position $s$. The temperatures before and after the orifice are approximately equal.

**Heat Exchanger**

Heat exchangers like the intercooler and both EGR-coolers cool down the inflowing gas $\dot{m}_{\text{gas}}$ with the temperature $T_{\text{in}}$ by heat dissipation to a cooling fluid with the temperature $T_{\text{cl}}$ to an outflow temperature $T_{\text{out}}$, see Fig 3.3a).
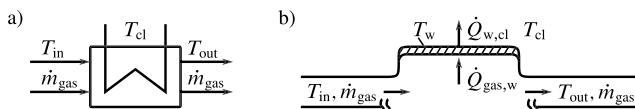


**Figure 3.3:** a) Control oriented heat exchanger model with considered quantities to model the heat transfer b) Internal dynamics in a lumped parameter heat exchanger model

For the EGR-coolers this cooling fluid is the engine coolant, while the intercooler is cooled by an air flow. These heat exchangers are modelled as flow restrictions with heat transfer, whereas the heat transfer can be represented as change in specific enthalpy

$$
h_{\text{out}} = h_{\text{in}} - \frac{\dot{Q}_{\text{gas,w}}}{\dot{m}_{\text{gas}}},
$$
(3.23)

in which $\dot{m}_{\text{gas}}$ represents the mass flow rate of the cooled gas and $\dot{Q}_{\text{gas,w}}$ the total heat transfer between gas and heat exchanger wall.

A simple lumped parameter model for heat exchangers with wall heat dynamics can be derived according to VDI-Gesellschaft Verfahrenstechnik und Chemieingenieurwesen (2010) as the com-

bination of two heat transfers, see Fig. 3.3b). The heat transfer between intake and exhaust system gas $\dot{m}_{\text{gas}}$ with inflowing temperature $T_{\text{in}}$ and heat exchanger wall is given as

$$\dot{Q}_{\text{gas,w}} = \alpha_{\text{gas,w}}(\dot{V}_{\text{gas}}) A_{\text{gas,w}} (T_{\text{in}} - T_{\text{w}}) \tag{3.24}$$

and the heat transfer between the heat exchanger wall and the cooling liquid as

$$\dot{Q}_{\text{w,cl}} = \alpha_{\text{w,cl}}(\dot{V}_{\text{cl}}) A_{\text{w,cl}} (T_{\text{w}} - T_{\text{cl}}) . \tag{3.25}$$

The averaged heat transfer coefficient between the gas and the heat exchanger wall $\alpha_{\text{gas,w}}$ and the coefficient between the wall and the cooling fluid $\alpha_{\text{w,cl}}$ both depend on the volume flow rates of the gas $\dot{V}_{\text{gas}}$ and the cooling fluid $\dot{V}_{\text{cl}}$, while the surface areas $A_{\text{gas,w}}$ and $A_{\text{w,cl}}$ are constant.[1] If no dynamical heat storage is considered both in- and outflowing heat flows become equal.

$$\dot{Q}_{\text{gas,w}} = \dot{Q}_{\text{w,cl}} \tag{3.26}$$

Then the stationary heat transfer model can be simplified by solving (3.24) for $T_{\text{w}}$ and substituting it in (3.25) to

$$\dot{Q}_{\text{gas,w}} = \frac{\alpha_{\text{gas,w}}(\dot{V}_{\text{gas}}) A_{\text{gas,w}} \alpha_{\text{w,cl}}(\dot{V}_{\text{cl}}) A_{\text{w,cl}}}{\alpha_{\text{gas,w}}(\dot{V}_{\text{gas}}) A_{\text{gas,w}} + \alpha_{\text{w,cl}}(\dot{V}_{\text{cl}}) A_{\text{w,cl}}} (T_{\text{in}} - T_{\text{cl}}) = A_{\text{cl}} k_{\text{cl}}(\dot{V}_{\text{cl}}, \dot{V}_{\text{gas}}) (T_{\text{in}} - T_{\text{cl}}) . \tag{3.27}$$

Finally, it can be rewritten with the averaged cooler surface area $A_{\text{cl}}$ and the coefficient of heat transmission $k_{\text{cl}}$. Then the specific enthalpy at the cooler outflow follows by inserting (3.27) in (3.23).

## 3.2 Mean Value Cylinder Model

A semi-physical mean value engine model is characterised by a simplified cylinder model. In this approach the mass flow rates entering $\dot{m}_{\text{eng,in}}$ and exiting $\dot{m}_{\text{eng,out}}$ the cylinder, as well as the enthalpy flow and the air content exiting the cylinder are modelled as stationary models representing their mean values during an engine combustion cycle.

The mean value of the mass flow rate entering the cylinder can be estimated utilising the model of a volumetric pump

---

[1] Note that only the cooling fluid inflow temperature is measured with the given test bench instrumentation. Hence, $T_{\text{cl}}$ has to approximated by the inflowing cooling fluid temperature. Otherwise $T_{\text{cl}} = (T_{\text{cl,in}} + T_{\text{cl,out}})/2$ would count.

$$\dot{m}_{\text{eng,in}} = \lambda_{\text{a}} \frac{p_{2\text{i}} V_{\text{d}} z}{R T_{2\text{i}}} \frac{n_{\text{eng}}}{60 \frac{\text{s}}{\text{min}}}, \tag{3.28}$$

with the displacement volume per cylinder $V_{\text{d}}$, the number of cylinders per combustion cycle $z$ and the volumetric efficiency $\lambda_{\text{a}}$ (Heywood, 1988; Jung, 2003; Guzzella and Onder, 2010). Engine speed and gas density in the intake manifold determine the theoretical cylinder filling, while the volumetric efficiency describes deviations and losses which are not covered with the model assumption of an ideal volumetric pump. These deviations include resonance effects in the intake system, characteristics of inlet and outlet valve trajectories, charge motion like a swirl flap and further nonlinearities. The volumetric efficiency is modelled as a LOLIMOT-model and shows the best modelling results with the model inputs engine speed $n_{\text{eng}}$, intake pressure $p_{2\text{i}}$ and position of the swirl actuator $s_{\text{sa}}$.

$$\lambda_{\text{a}} = f_{\text{LOLIMOT}} \left( n_{\text{eng}}, \ p_{2\text{i}}, \ s_{\text{sa}} \right) \tag{3.29}$$

Since the injected fuel mass $\hat{\dot{m}}_{\text{f}}$ is not measured, it has to be modelled from the desired injection quantity $u_{\text{inj}}$ and the engine speed. Then the mass flow rate exiting the cylinder follows directly from $\hat{\dot{m}}_{\text{f}}$ and (3.28) as

$$\dot{m}_{\text{eng,out}} = \dot{m}_{\text{eng,in}} + \hat{\dot{m}}_{\text{f}}. \tag{3.30}$$

The temperature increase due to the combustion process is given by a semi-physical stationary LOLIMOT-model. In Appx. B the significance of different model inputs is shown. Consequently, the temperature after the combustion $T_{\text{eng,out}}$ is estimated as

$$T_{\text{eng,out}} = T_{2\text{i}} + f_{\text{LOLIMOT}} \left( n_{\text{eng}}, \ u_{\text{inj}}, \ p_{2\text{i}}, \ \varphi_{\text{mi}} \right). \tag{3.31}$$

There are two advantages in modelling of $T_{\text{eng,out}}$ by the temperature rise of the combustion process and the modelled intake temperature $T_{2\text{i}}$. First a direct $T_{\text{eng,out}}$ model would require the intake temperature as additional model input, which increases the model dimensionality. Anymore, the intake temperature strongly depends on the ambient conditions. These variations have to be considered in the model parameterisation to avoid model extrapolation. Hence, this indirect $T_{\text{eng,out}}$ modelling is of lower dimensionality and it implicitly includes ambient condition influences. Therefore this model structure demands less calibration effort.

Finally, the air content after the combustion process $x_{\text{eng,out}}$ can be described with (3.10) by the fresh air mass flow rate proportion entering the cylinder $\dot{m}_{\text{eng,in}} x_{2\text{i}}$, the burned air mass flow rate $L_{\text{st}} \hat{\dot{m}}_{\text{f}}$ and the gas mass flow exiting the cylinder $\dot{m}_{\text{eng,in}} + \hat{\dot{m}}_{\text{f}}$ as

$$x_{\text{eng,out}} = \frac{\dot{m}_{\text{air,eng,out}}}{\dot{m}_{\text{eng,out}}} = \frac{\dot{m}_{\text{eng,in}} x_{2\text{i}} - L_{\text{st}} \hat{\dot{m}}_{\text{f}}}{\dot{m}_{\text{eng,in}} + \hat{\dot{m}}_{\text{f}}}. \tag{3.32}$$

Analogue to the global air-fuel ratio (3.11), also a stationary relationship between the air content in the exhaust system ($x_3$, $x_5$, $x_{\text{eng,out}}$) and the quantities $\dot{m}_{\text{air}}$ and $\hat{\dot{m}}_{\text{f}}$ entering the combustion engine can be given by inserting the mass flow rate based form of (3.11) in (3.13).

$$x_{i,\text{stat}} = \frac{\dot{m}_{\text{air,stat}} - \hat{\dot{m}}_{\text{f,stat}} L_{\text{st}}}{\dot{m}_{\text{air,stat}} + \hat{\dot{m}}_{\text{f,stat}}} \qquad i \in \{3, \ 5, \ \text{eng, out}\} \tag{3.33}$$

In this relationship the numerator is the remaining gas mass flow rate with an air content of 1, while the denominator describes the total gas mass flow rate. This corresponds to the definition of the air content in Eq. (3.10), see also (3.32). A further transformation of (3.33) gives the stationary dependency between air mass flow rate, air content and injection quantity.

$$\dot{m}_{\text{air,stat}} = \frac{(x_{i,\text{stat}} + L_{\text{st}})\hat{\dot{m}}_{\text{f,stat}}}{1 - x_{i,\text{stat}}} \qquad i \in \{3, \ 5, \ \text{eng, out}\} \tag{3.34}$$

Further, this relationship allows to determine the actual necessary dynamical air mass $\dot{m}_{\text{air,dyn}}$ at the intake valve to achieve a desired air content after the combustion.

$$\dot{m}_{\text{air,dyn}} = \frac{(x_{\text{eng,out}} + L_{\text{st}})\hat{\dot{m}}_{\text{f}}}{1 - x_{\text{eng,out}}} \tag{3.35}$$

## 3.3 Turbocharger

Adjacent to the combustion process itself, the turbocharger is one of the most complex devices in the intake and exhaust system of combustion engines. Besides the cylinders and the two EGR-paths, the turbocharger is a further connection between the intake and exhaust system and strongly influences the air path dynamics.

Fig. 3.4 shows a turbocharger schematic with the utilised model in- and outputs for the turbocharger simulation within a lumped parameter mean value engine model.[2] The demanded model outputs in the intake system are the compressor mass flow rate $\dot{m}_{\text{c}}$ and the temperature behind the compressor $T_{2c}^*$. In the exhaust system, the model outputs turbine mass flow rate $\dot{m}_{\text{t}}$ and temperature after the turbine $T_4^*$ have to be provided for the mean value engine simulation[3].

---

[2]The utilised turbocharger is oil-cooled. However, there is no measurement for the oil temperature. The only available quantities to model heat flows outside the turbocharger housing are the ambient temperature $T_{\text{a}}$ and the engine coolant temperature $T_{\text{h2o}}$.

[3]Note that especially for simulation purposes the turbocharger output temperatures $T_{2c}^*$ and $T_4^*$ dynamically differ from the temperatures $T_{2c}$ and $T_4$ in the subsequent ducts and have to be indexed separately, see also Fig. 3.5. However, in practice these dynamical fast differences cannot be measured with the given test bench temperature sensors, which possess a significant measurement delay.

$T_{2c}^*\ p_{2c}$          Measured Variables          $T_3\ p_3\ \dot{m}_t$

Thermodynamic System

$\dot{Q}_{2,t}$          $\dot{Q}_{3,t}$

$T_{2c}'$          Fluid-Dynamic System          $T_3'$

$P_c$          $P_t$

$\dot{Q}_{tc,t}$

$\dot{Q}_{tc,r}$

$P_f\ n_{tc}$

$T_1'$          $s_t$          $T_4'$          $T_a$

$\dot{Q}_{1,t}$          $\dot{Q}_{in,t}$          $\dot{Q}_{out,t}$          $\dot{Q}_{4,t}$

$T_1\ p_1\ \dot{m}_c$          $T_{h2o}$          $T_4^*\ p_4$
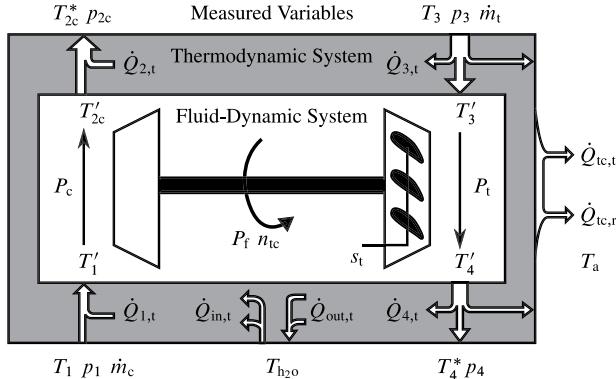
**Figure 3.4:** VGT turbocharger scheme with fluid-dynamic system, thermodynamic system, an illustration of heat flows inside the turbocharger housing and measured quantities

In order to model these quantities, the turbocharger is divided into a thermodynamic system and a fluid-dynamic system. The block diagram of the fluid-dynamic turbocharger model is given in Fig. 3.5 and comprises submodels for compressor and turbine mass flow rates as well as fluid-dynamical compressor $P_c$ and turbine power $P_t$. The turbocharger shaft is the link between compressor and turbine side and further decelerates the turbocharger via friction losses of its bearings $P_f$. Its rotational speed $n_{tc}$ is a driving input for the afore mentioned submodels and dominantly influences the overall engine air path dynamics. A further submodel applies Newton's second law of motion to the momentum balance at the shaft and delivers the turbocharger speed.

Turbocharger Shaft

$\dot{m}_c$          $P_c$          $P_f$          $(2\pi)^2 k_f$          $n_{tc}^2$          $s_t\ p_3\ T_3'$          $s_t\ p_3\ p_4\ T_3$

| Compressor Mass Flow | Compressor Power | $\dfrac{1}{4\pi^2 I_{tc} n_{tc}}$ | $\dfrac{1}{s}$  $n_{tc}$ | Turbine Power | Turbine Mass Flow |

$p_1\ p_{2c}\ T_1$          $p_{2c}\ T_{2'}$          $P_t$          $\dot{m}_t$
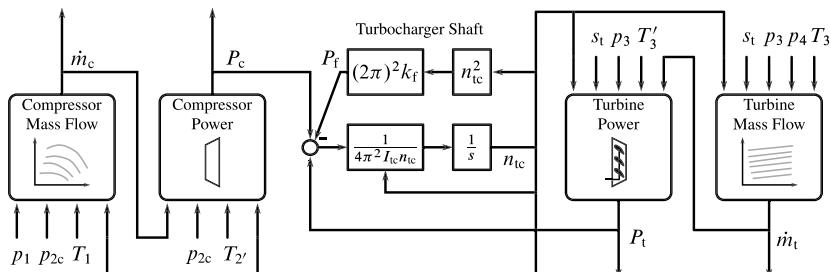
**Figure 3.5:** Block diagram of the fluid-dynamic turbocharger model

Additionally to the fluid-dynamical process with the $i$ fluid-dynamical temperatures $T_i'$ in Fig. 3.4, the heat transfers in the turbocharger housing have to be considered to model the overall thermodynamical compression and expansion process with the temperatures $T_i^{(*)}$ (Rautenberg et al., 1983; Malobabic, 1989; Shaaban, 2004). As depicted in Fig. 3.4, heat transfer occurs between com-
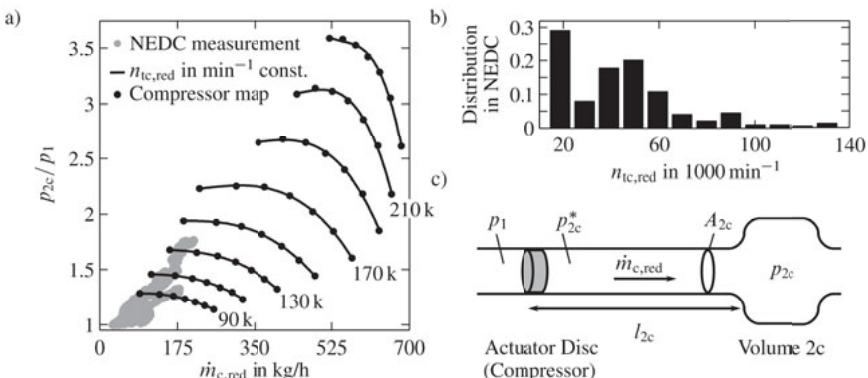
**Figure 3.6:** a) Comparison between the compressor map from the turbocharger manufacturer and the data distribution from test bench measurements of the NEDC b) Measured turbocharger speed distribution in the NEDC c) Greitzer compressor mass flow rate model

pressor, engine block, cooling oil, turbine and ambient air. Thus, these heat transfers at the states $i$ are considered with simplified stationary heat transfer models by heat transmission $\dot{Q}_{i,t}$ and radiation $\dot{Q}_{i,r}$. Finally, the thermodynamical system includes these heat transfers and relates the fluid-dynamical temperatures $T_i'$ at the compressor and turbine rotor to measurable temperatures $T_i^{(*)}$ outside the turbocharger housing.

State of the art turbocharger models are typically based on characteristic maps delivered by the turbocharger manufacturers. Usually these maps are measured separately for the compressor and the turbine on hot gas turbocharger test benches at stationary conditions. At these test benches the turbine is commonly driven with a stationary hot gas flow rate from a burner at one fixed temperature, usually 600 °C. However, the realistic gas conditions at engine operation are characterised by a pulsating engine flow, a large temperature range and rapid exhaust temperature changes (Shaaban, 2004; Berndt, 2009; Guzzella and Onder, 2010).

As a further drawback the characteristic maps cover only a limited speed range and usually turbocharger speeds above 40 % of the maximal turbocharger speed are represented. This limitation results from measurement uncertainties which prevent a reliable determination of the isentropic compressor efficiency (Shaaban, 2004; Berndt, 2009; Guzzella and Onder, 2010).

Figure 3.6a) exemplary shows a compressor mass flow rate map from the turbocharger manufacturer. In these maps mass flow rates and turbocharger speed are normalised by (3.36) and (3.37) to reference conditions. The manufacturer measures only a few data points at constant speed lines. Due to measurement uncertainties these measurements are typically carried out at large turbocharger speeds. However, in a common engine operation this considered measurement range is little covered, since most of the grey dotted data points from engine test bench measure-

ments of the NEDC are located far below the lowest measured speed line with $90000\,\mathrm{min}^{-1}$, see also Moraal and Kolmanovsky (1999); Berndt (2009). The data distribution in Fig. 3.6b) illustrates the deviation between the manufacturer's map and the typical engine conditions even more drastic. As it can be seen, only a minority of data points exceed a turbocharger speed of $90000\,\mathrm{min}^{-1}$. Therefore, some approaches try to interpolate and to extrapolate turbocharger maps into regions not provided by the turbocharger manufacturer (Moraal and Kolmanovsky, 1999; Eriksson, 2007; Guzzella and Onder, 2010). Other approaches utilise engine test bench measurements to parameterise the turbocharger maps (Jung, 2003; Sidorow et al., 2011).

Besides the poor accordance between the operation area of the manufacturer's maps and the relevant area for engine applications, the manifold heat transfers in the turbocharger housing are a further issue in turbocharger power modelling. These heat transfers have a certain effect on the assumed compression and expansion process and their slow dynamics can severely influence the temperature measurements for the model parameterisation of the fluid-dynamical turbocharger models. Especially at engine operation points with low load these heat transfers can severely deteriorate the model,  see (Mrosek and Isermann, 2010c; Mrosek, 2017).

In the following a short excursion will present map-based mass flow rate models for the compressor and the turbine. Afterwards, the focus will be set on the turbocharger power models and the effect of heat transfers. A parametric turbocharger model based upon the work of Zahn and Isermann (2008) will be presented to model the fluid-dynamical compressor and turbine power. Finally, the turbocharger modelling closes with additional stationary heat transfer models.

### 3.3.1  Mass Flow Rate

The turbocharger mass flow rates are modelled by characteristic maps which are calibrated with measurements from the engine test bench. First the compressor mass flow rate is modelled. In order to minimise the effect of temperature and pressure changes, the compressor mass flow rate model is described by the quantities reduced mass flow rate $\dot{m}_{c,red}$ and reduced turbocharger speed $n_{tc,red}$ (Malobabic, 1989; Shaaban, 2004). These reduced quantities are related by the relationships

$$n_{tc,red} = n_{tc} \sqrt{\frac{T_{ref}}{T_1}} \tag{3.36}$$

and

$$\dot{m}_{c,red} = \dot{m}_c \frac{p_{ref}}{p_1} \sqrt{\frac{T_1}{T_{ref}}} \tag{3.37}$$

to a reference pressure $p_{ref}$ and a reference temperature $T_{ref}$, which are defined as $p_{ref} = 1.013\,\mathrm{bar}$ and $T_{ref} = 288.15\,\mathrm{K}$ (Malobabic, 1989).

The reduced compressor mass flow rate $\dot{m}_{c,red}$ is usually given as a characteristic map of the pressure ratio over the compressor wheel $p_{2c}/p_1$ and the reduced compressor speed $n_{tc,red}$. However, in Fig. 3.6a) the proficient reader realises, that there is no unique functional relation between the pressure ratio $p_{2c}/p_1$ and $\dot{m}_{c,red}$ at a certain turbocharger speed. Which means that the compressor mass flow rate cannot be clearly reconstructed from a given turbocharger speed and pressure ratio. Especially at high turbocharger speeds the curves become flat and lose their monotonic characteristics, which is necessary for a well fitting mass flow rate model with the model inputs pressure ratio and turbocharger speed. This non-unique functional relationship is typical for automotive compressors and can also be observed in the compressor mass flow rate maps given in Malobabic (1989); Moraal and Kolmanovsky (1999); Eriksson (2007) and Berndt (2009).

Greitzer (1976) presents an alternative approach to overcome this issue, see also Moraal and Kolmanovsky (1999) and Guzzella and Onder (2010). In Fig. 3.6c) this compressor mass flow rate model is illustrated and will be utilised in the following. First the stationary pressure ratio over the compressor wheel

$$\frac{p_{2c}^*}{p_1} = f_{\text{LOLIMOT}}\left(\dot{m}_{c,red},\ n_{tc,red}\right) \tag{3.38}$$

is modelled with a LOLIMOT-model, in which the pressure $p_{2i}^*$ is an intermediate state. Then it is assumed, that the compressor has some inherent dynamics in the rate its mass flow can change. These dynamics are modelled with the one dimensional momentum equation and by simplifying the compressor to an *actuator disc* with the upstream pressure $p_{2c}^*$. Afterwards the volume between the compressor wheel and the subsequent storage can be formulated by the equivalent duct length $l_{2c}$ and the cross sectional area $A_{2c}$ and finally the compressor mass flow rate dynamics can be expressed as

$$\frac{d\dot{m}_{c,red}}{dt} = \frac{A_{2c}}{l_{2c}}\left(p_{2c}^* - p_{2c}\right). \tag{3.39}$$

As a large benefit this inverse mass flow rate model (3.38) overcomes the drawbacks of the non-unique relationship between pressure ratio and mass flow rate. With the model inputs reduced mass flow rate and turbocharger speed, there is a strong functional relationship to the model output pressure ratio, see Fig. 3.6a). On the other hand the overall mean value model gains one more state, which might lead to a *stiff* system when the ratio $A_{2c}/l_{2c}$ becomes too small for a given engine configuration (Moraal and Kolmanovsky, 1999).

The turbine mass flow rate $\dot{m}_t$ is modelled with the flow equation for compressible fluids (3.22). In which a stationary LOLIMOT-model with the model inputs $s_t$ and $n_{tc}$ represents the turbine's flow discharge coefficient and reference flow area $(C_D A_{ref})_t$. A more detailed investigation of the turbine mass flow model is given in Mrosek (2017).

### 3.3.2 Turbocharger Power

As a fluid-dynamical device, the turbocharger is characterised by the enthalpy difference and the pressure ratio over the turbine and the compressor wheel. Due to the large temperature gradients between the hot turbine side, the cooling oil, the ambient and the rather cold compressor side many heat transfers occur in the turbocharger housing, see Fig. 3.4. If the conventional adiabatic turbocharger compression and expansion process assumptions are made, the present heat transfers falsify the model parameterisation and the resulting models deliver unsatisfying simulation results. Hence, in recent turbocharger research these heat transfers are also incorporated in the assumed flow process extending it from adiabatic to diabatic (Rautenberg et al., 1983; Shaaban, 2004; Bohn et al., 2005; Berndt, 2009). Generally, heat transfers occur spatially over the entire flow path and become unhandy for control-oriented simulation models. Thus, these heat transfers are commonly simplified by two lumped heat transfers before and after the flow process (Shaaban, 2004; Bohn et al., 2005; Berndt, 2009; Zahn and Isermann, 2008).
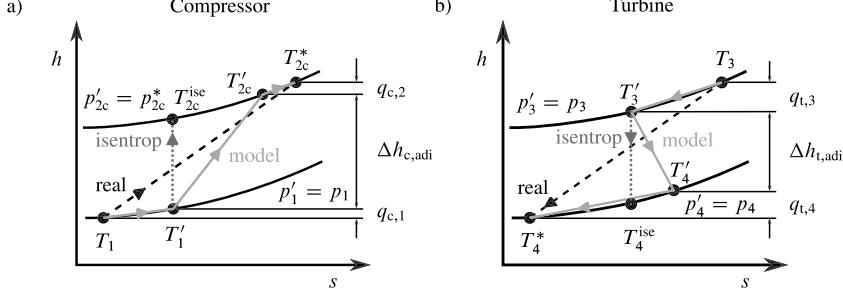


**Figure 3.7:** Schematic h-s diagram of the diabatic compression and expansion process with isentropic $T_i' \rightarrow T_j^{\mathrm{ise}}$, adiabatic $T_i' \rightarrow T_j'$ and diabatic $T_i \rightarrow T_i^*$ change of condition

Consequently, the diabatic compression process can be described by the h-s diagram in Fig. 3.7a). Then the diabatic rise of the specific enthalpy is given as

$$\Delta h_{\mathrm{c,dia}} = c_{\mathrm{p}}(T_{2\mathrm{c}}^* - T_1) \tag{3.40}$$

and can be also expressed as the result of an adiabatic irreversible compression process $\Delta h_{\mathrm{c,adi}}$ and the transfer of the specific heats $q_{\mathrm{c,1}}$ and $q_{\mathrm{c,2}}$.

$$\Delta h_{\mathrm{c,dia}} = q_{\mathrm{c,1}} + \Delta h_{\mathrm{c,adi}} + q_{\mathrm{c,2}} \tag{3.41}$$

The enthalpy difference $\Delta h_{\mathrm{c,adi}}$ can be expressed similar to (3.40) by the fluid-dynamical temperatures $T_1'$ and $T_{2\mathrm{c}}'$. Note that additionally to the isentropic compression process $\Delta h_{\mathrm{c,ise}}$ with the

isentropic temperature $T_{2c}^{ise}$ also flow and friction losses are incorporated in the adiabatic process model.

In the following the adiabatic (fluid-dynamical) portion of the flow process is modelled with a parametric turbocharger model based on the mean line theory as presented in Zahn and Isermann (2008).

**Compressor Model**

The adiabatic irreversible change in enthalpy $\Delta h_{c,adi}$ represents the energy transferred to the impeller $a_c$. It can be derived from Euler's turbine equation

$$\Delta h_{c,adi} = a_c = u_{c2}c_{c2,u} - u_{c1}c_{c1,u}. \tag{3.42}$$

$u_{c1}$ and $u_{c2}$ are the circumferential velocities at compressor inlet and outlet. $c_{c1,u}$ and $c_{c2,u}$ are the corresponding circumferential components of the flow velocities. The flow entering the impeller normally has no prewhirl ($c_{c1,u} = 0$). Hence, Eq. (3.42) simplifies to

$$a_c = u_{c2}c_{c2,u}. \tag{3.43}$$

The circumferential velocity at the compressor impeller outlet results from

$$u_{c2} = \pi d_{c2} n_{tc} \tag{3.44}$$

in which $d_{c2}$ is the impeller's outer diameter. In Fig. 3.8b) the peripheral component of the absolute velocity at the impeller outlet can be derived from the compressor velocity triangles as

$$c_{c2,u} = \mu c_{c2,u,th} = \mu \left( u_{c2} + c_{c2,m} \cot(\beta_{c2,b}) \right). \tag{3.45}$$

Using the continuity equation and neglecting blade blockage the meridional component $c_{c2,m}$ in (3.45) results in

$$c_{c2,m} = \frac{\dot{m}_c}{\rho_2' \pi d_{c2} b_{c2}}. \tag{3.46}$$

In this connection $\rho_2'$ is the fluid-dynamical gas density with the relevant temperature $T_{2c}'$ at impeller exit not incorporating the subsequent heat transfer and $b_{c2}$ is the width at impeller exit. The slip factor $\mu$ in (3.45) is a widely used method to describe deviations between the actual flow angle $\beta_{c2}$ and the theoretical blade angle $\beta_{c2,b}$. It is modelled by a classical approach proposed by Stodola (1945). The slip factor can be derived from the velocity triangles by

a)   impeller inlet                              b)   impeller outlet
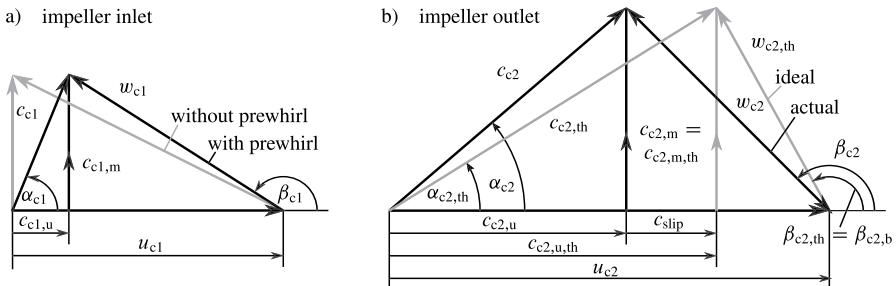


**Figure 3.8:** Compressor velocity triangles with following notation: $c$ absolute velocity, $u$ circumferential velocity, $w$ relative velocity; indices $c$ compressor, 1 impeller inlet, 2 impeller outlet, $m$ meridional part, $u$ circumferential part, $th$ theoretical

$$\mu = \frac{c_{c2,u}}{c_{c2,u,th}} = 1 - \frac{c_{slip}}{c_{c2,u,th}} \tag{3.47}$$

and

$$c_{c2,u,th} = u_{c2} + c_{c2,m} \cot\left(\beta_{c2,b}\right). \tag{3.48}$$

According to Stodola (1945) $c_{slip}$ can be expressed as $c_{slip} = k_{slip}u_{c2}$ in which $k_{slip}$ is a constant depending on the impeller geometry. Hence, applying (3.46), (3.47) and (3.48) the slip factor results in

$$\mu = 1 - \frac{k_{slip}u_{c2}}{u_{c2} + \frac{\dot{m}_c}{\rho_2'}\frac{\cot\left(\beta_{c2,b}\right)}{\pi d_{c2}b_{c2}}}. \tag{3.49}$$

Consequently, by substituting (3.44), (3.45) and (3.46) into (3.43), the fluid-dynamical power of the compressor results in

$$P_c = \dot{m}_c a_c = \mu\dot{m}_c\left(\left(\pi d_{c2}n_{tc}\right)^2 + \frac{\dot{m}_c n_{tc}}{\rho_2'}\frac{\cot(\beta_{c2,b})}{b_{c2}}\right). \tag{3.50}$$

Thus, the compressor power model can be fully parameterised with only three parameters $d_{c2}$, $\frac{\cot(\beta_{c2,b})}{b_{c2}}$ and $k_{slip}$, whereas $d_{c2}$ is usually given from the turbocharger geometry.
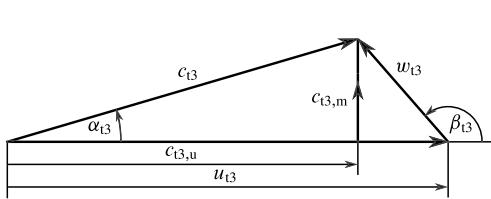
a)     rotor inlet                                  b)     rotor outlet
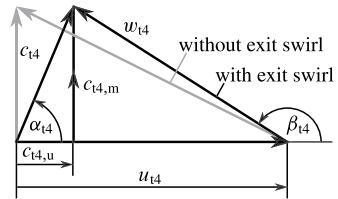


**Figure 3.9:** Turbine velocity triangles with following notation: $c$ absolute velocity, $u$ circumferential velocity, $w$ relative velocity; indices $t$ compressor, 3 rotor inlet, 4 rotor outlet, $m$ meridional part, $u$ circumferential part

**Turbine Model**

The diabatic turbine expansion process is presented in the h-s diagram in Fig. 3.7b). Similar to the compression process the diabatic change in the specific enthalpy is given as

$$\Delta h_{t,dia} = c_p \left( T_3 - T_4^* \right). \tag{3.51}$$

Further the turbine expansion process is assumed to be irreversible adiabatic $\Delta h_{t,adi}$ and two lumped specific heat transfers $q_{t,3}$ and $q_{t,4}$ before and after the expansion are introduced. Then the diabatic expansion process can be expressed as

$$\Delta h_{t,dia} = q_{t,3} + \Delta h_{t,adi} + q_{t,4}. \tag{3.52}$$

Similar to (3.51) the diabatic enthalpy difference $\Delta h_{t,adi}$ can also be expressed by the fluid-dynamical temperatures $T_3'$ and $T_4'$. Note that due to flow and friction losses the adiabatic turbine exit temperature $T_4'$ is higher than the temperature $T_4^{ise}$ of an isentropic expansion process $\Delta h_{t,ise}$.

Then the fluid-dynamical work transferred to the turbine wheel is expressed by Euler's equation

$$-\Delta h_{t,adi} = a_t = u_{t4}c_{t4,u} - u_{t3}c_{t3,u}. \tag{3.53}$$

The turbine is usually designed for no exit swirl, see Fig. 3.9b). Therefore $c_{t4,u}$ vanishes and Eq. (3.53) can be simplified to

$$a_t = -u_{t3}c_{t3,u}. \tag{3.54}$$

Consequently, only the rotor inlet velocities in Fig. 3.9a) contribute to the turbine blade work. The outer turbine inlet diameter $d_{t3}$ allows to calculate the circumferential velocity as

$$u_{t3} = \pi d_{t3} n_{tc}. \tag{3.55}$$

The swirl velocity $c_{t3,u}$ results from the trigonometrical relationship

$$c_{t3,u} = \frac{c_{t3,m}}{\tan(\alpha_{t3})} = c_{t3,m}\cot(\alpha_{t3}), \tag{3.56}$$

in which $\alpha_{t3}$ is the absolute flow angle at the rotor inlet. It is determined by the guiding vanes' angle and can be modelled as function of the VGT-actuator position $s_t$

$$\alpha_{t3} = f(s_t). \tag{3.57}$$

The meridional component $c_{t3,m}$ of the absolute velocity is given by the continuity equation

$$c_{t3,m} = \frac{\dot{m}_t}{\rho_3' \pi d_{t3} b_{t3}} \tag{3.58}$$

wherein $\rho_3'$ is the gas density with the relevant temperature $T_3'$ at the turbine wheel. Further $b_{t3}$ is the blade width at the rotor inlet. A substitution of Eqs. (3.55), (3.56) and (3.58) into (3.53) finally results in the fluid-dynamical turbine power

$$P_t = \dot{m}_t a_t = -\frac{\dot{m}_t^2 n_{tc}}{\rho_3'} \frac{\cot(\alpha_{t3})}{b_{t3}}. \tag{3.59}$$

The relation $\cot(\alpha_{t3})/b_{t3}$ characterises the turbine and has to be parameterised with geometrical data or test bench measurements. Mrosek and Isermann (2010c) showed that a simple third order polynomial of the VGT-actuator position $s_t$ in the form

$$\frac{\cot(\alpha_{t3})}{b_{t3}} = \sum_{i=0}^{3} w_{t,i} s_t^i \tag{3.60}$$

could deliver a reasonable modelling performance for the turbine model. Furthermore, Mrosek and Isermann (2010c) extended the model presented by Zahn and Isermann (2008) empirically with the consideration of the exhaust gas density $\rho_3'$ as additional model input. This could significantly improve the model quality, so that a model in the form

$$\frac{\cot(\alpha_{t3})}{b_{t3}} = \sum_{i=0}^{3} w_{t,i} s_t^i + w_{t,\rho_3',1} s_t \rho_3' + w_{\rho_3,4} \rho_3'^4. \tag{3.61}$$

will be utilised in the following.

**Turbocharger Shaft**

At the turbocharger shaft the compressor $P_c$ and the turbine power $P_t$, respectively their resulting torques aggregate and accelerate the turbocharger according to Newton's second law of motion

$$\frac{\mathrm{d}n_{tc}}{\mathrm{d}t} = -\left(\frac{1}{2\pi}\right)^2 \frac{P_t + P_c + P_f}{n_{tc}I_{tc}}. \tag{3.62}$$

The turbocharger dynamics are determined by the shaft inertia $I_{tc}$. Further the journal bearing friction losses $P_f$ contribute to the power balance at the shaft. These losses are modelled with the friction coefficient $k_f$ by a viscous friction approach as

$$P_f = (2\pi n_{tc})^2\, k_f. \tag{3.63}$$

### 3.3.3 Turbocharger Heat Transfer

Additionally to the adiabatic compression and expansion process heat transfers on the compressor side and the turbine side contribute to the diabatic compression (3.41) and expansion process (3.52) in Fig. 3.7. As it is shown in Fig. 3.4, the overall heat transfer in the turbocharger housing consists of several heat flows. In recent research these stationary heat transfers have been investigated more detailed. The field ranges from stationary heat transfer assumptions in Malobabic (1989), Shaaban (2004) and Berndt (2009) to the stationary calculation of the one- and three-dimensional heat transfer in Romagnoli and Martinez-Botas (2012) and Bohn et al. (2005). A further approach by Zahn (2012) even models the heat transfer dynamics with a simplified lumped parameter model.

In this dissertation, the heat transfer models are limited to a stationary approach to keep the overall model complexity reasonable. The heat transfer inside the turbocharger housing is modelled as heat transmission, see VDI-Gesellschaft Verfahrenstechnik und Chemieingenieurwesen (2010). All heat transfers between gas or cooling liquid and the turbocharger wall, as well as heat conduction inside the turbocharger housing are summarised in the heat transmission coefficient $k_{i \to j,\mathrm{d}}$. Thus, a heat transfer between a fluid with the temperature $T_i$ and another fluid with the temperature $T_j$ can be expressed as

$$\dot{Q}_{i \to j,\mathrm{t}} = k_{i \to j,\mathrm{t}} A_{i \to j,\mathrm{t}} \left(T_i - T_j\right), \tag{3.64}$$

in which $A_{i \to j,\mathrm{t}}$ can be regarded as averaged surface area for the heat transfer. However, the turbocharger geometry is quite complicated and it is hard to divide surface area and heat transmission coefficient into their physical meaningful proportions. Hence, the product $k_{i \to j,\mathrm{t}} A_{i \to j,\mathrm{t}}$ is treated and identified as one single parameter which describes the heat transmission. For a mored detailed investigation of the single heat transfers and their contribution to the turbocharger power refer to Mrosek and Isermann (2010c) and Mrosek (2017).

## 3.4 Mean Value Engine Model Signal Flow Diagram

All previously described submodels are combined to the overall mean value engine model of reduced order. Similar to Zahn (2012) a signal flow diagram is derived in Figure 3.5. This diagram is extended for the LP-EGR path and adapted to the chosen modelling depth. As it can be seen, the single submodels are strongly coupled. Especially the intake and exhaust system are coupled by the LP-EGR path, the HP-EGR path, the turbocharger and the combustion process in the cylinders.

In order to reduce the model complexity, all volumes between coolers (HP-EGR cooler, LP-EGR cooler, intercooler) and valves are neglected. This results in an algebraic loop, since the cooler heat transfer coefficients depend on volume flow rates, respectively mass flow rates, through the coolers. Further the subsequent flow equation which usually deliver this mass flow rate, demand the gas temperature behind the cooler as a model input. Therefore the coolers' outflow temperatures are delayed for one simulation step to omit an algebraic loop and to allow for a numerical solution of the differential algebraic equation system. For model simulation there is a dynamical difference between the temperature behind a flow restriction e.g. $T_{\text{dpf}}$ and the temperature in the subsequent storage e.g. $T_5$. Due to sensor dynamics these dynamical fast differences between these temperatures cannot be distinguished at the engine test bench, so that for the sake of simplicity the temperature quantities in the volumes are utilised instead. Furthermore, the chosen semi-physical engine model approach is capable of simulating varying ambient conditions, which come into play for the submodels air filter and intake throttle, exhaust throttle and intercooler. These ambient conditions strongly influence the stationary process behaviour (Mrosek, 2017) and should be considered in the control concept. Moreover the heat transfer in the exhaust pipe is modelled as wall heat transfer (3.7) in the component Diesel particulate filter. Finally, the chosen model structure is also capable to model the engine warm-up with the consideration of the engine coolant temperature $T_{\text{h}_2\text{o}}$ in the submodels turbocharger housing, LP-EGR cooler and HP-EGR cooler. Different loadings of the Diesel particulate filter and the air filter can be simulated with the parameters $k_{\text{dpf}}$ and $k_{\text{af}}$.

## 3.5 Summary

In this chapter the mathematical description of several submodels is presented. These submodels are composed to the overall semi-physical mean value engine model. A challenge of semi-physical models is the strongly coupled interaction of many low dimensional submodels to describe the overall process behaviour. For a satisfying model quality these interactions between single submodels demand a sophisticated method to parameterise each single submodel. For further readings on model parameterisation refer to Mrosek et al. (2009, 2010b) and Mrosek and Isermann (2010c). A more comprehensive publication for measurement design, model parameterisation and validation is given in Mrosek (2017). After a successful model parameterisation with the cited methodology, a comparison between test bench measurements and model simulation in Fig. 4.2, Fig. 4.3 and Fig. 4.5 results in a qualitatively good agreement between measured and simulated quantities and validates the overall air path model.
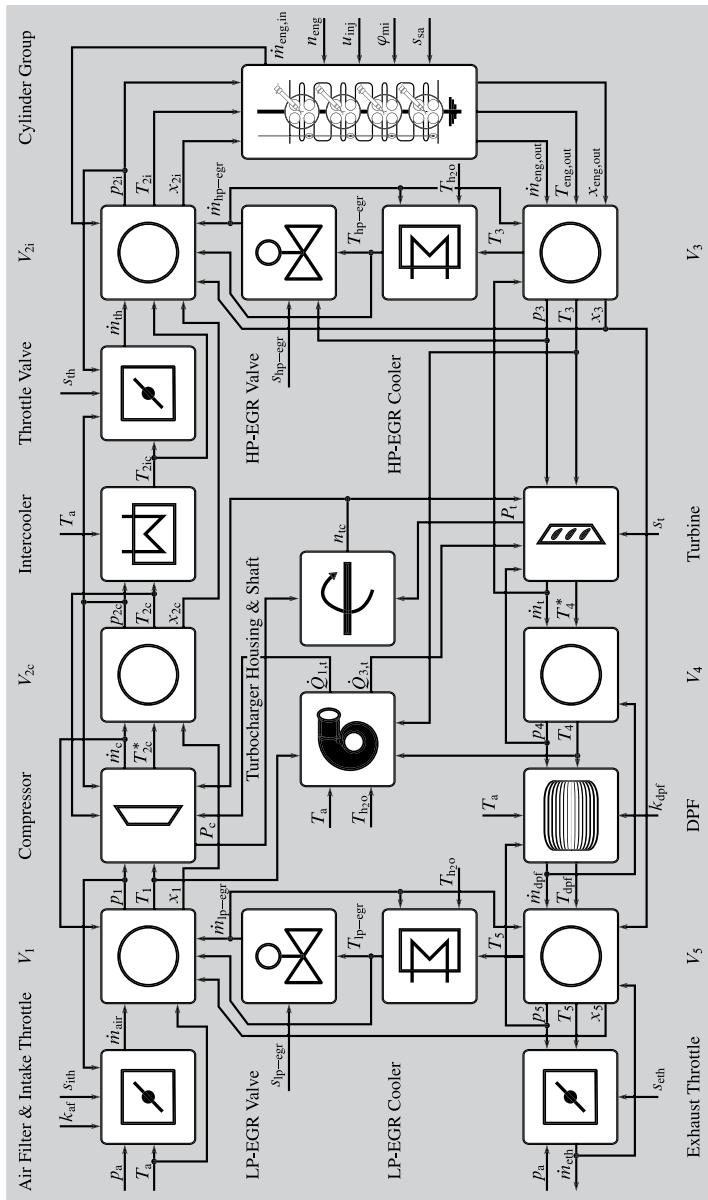
Figure 3.10: Multi-port signal flow diagram of intake system, exhaust system and combustion model

# 4   System Properties of the Air Path with HP- and LP-EGR

In this chapter the stationary and dynamical system properties of the air path with HP- and LP-EGR are analysed. The stationary system properties highlight couplings between actuators and control variables and further show the operation range benefit of the LP-EGR system. A study of the dynamical system properties shows that the major differences between HP- and LP-EGR can be seen in the gas propagation times. Then the gained insights into the process behaviour are utilised to choose the appropriate control variables and furthermore lay the foundation for the later presented control concepts.

In the following, the stationary and dynamical system properties of the air path are analysed with the purpose to identify appropriate control variables for the dual path EGR-system with a VGT turbocharger. Furthermore, the gained system insight will be utilised for the later following control concept design in Chap. 7.

First the system responses of the multivariable engine intake and exhaust system to step excitation signals of the relevant HP-EGR, LP-EGR and VGT-actuators are physically motivated. An investigation of two different LP-EGR configurations with an exhaust throttle valve and an intake throttle valve gives valuable insights into the stationary air path couplings. Finally, the gas propagation times of HP- and LP-EGR are investigated and a control-oriented model to handle these gas propagation effects for air path control and dynamical emission simulation is derived.

## 4.1   Air Path System Analysis by Step Responses

The dual EGR path control problem with VGT turbocharger can be regarded as a further extension of the classical HP-EGR and VGT control problem and is a strongly coupled nonlinear multivariable system. Thus, for a deeper understanding the complex multi-port diagram of the mean-value engine model from Fig. 3.5 is simplified to a signal flow diagram in Fig. 4.1. This simplified signal flow diagram comprises all dominant states and shows the relevant couplings to understand the interactions between HP-EGR, LP-EGR and VGT turbocharger. In the classical HP-EGR and VTG control problem the major air path dynamics can be described by interaction of the fast pressure dynamics of $p_{2i}$ and $p_3$, which are superimposed by the slow turbocharger dynamics of $n_{tc}$. These dynamics determine the output quantities like mass flow rates, which are calculated via nonlinear algebraic relationships from the process states. Note, that the fast pressure dynamics of $p_{2i}$ and $p_3$
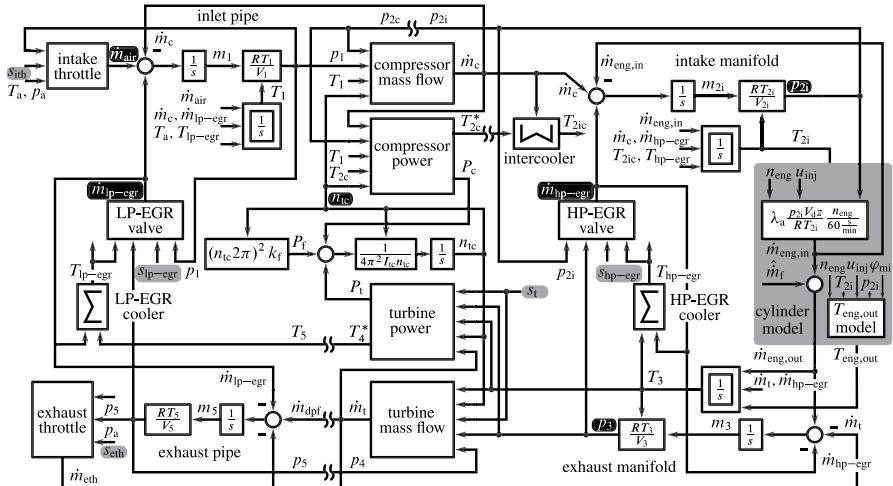
**Figure 4.1:** Simplified signal flow diagram based on the model equations from Chap. 3 and the complete model description in Fig. 3.5 to illustrate couplings between the actuators $s_{hp-egr}$, $s_{lp-egr}$ and $s_t$ and the air path quantities. All storages and flow orifices, which do no dominantly influence the air path dynamics as well as turbocharger heat transfers are neglected.

refer to the states $m_{2i}$ and $m_3$, which represent the fast transients in the HP-EGR system. These dynamics must not be be misunderstood as the slow charge air pressure build-up, which is caused by superposition with the turbocharger dynamics in $n_{tc}$ influencing $p_{2i}$ by increasing and decreasing $\dot{m}_c$, see Fig. 4.1. The LP-EGR mass flow rate $\dot{m}_{lp-egr}$ is driven by two additional pressures $p_1$ and $p_5$. Besides the pressures, also the sketched temperatures are necessary to understand the system responses in the intake and exhaust system.

While the classical HP-EGR and VTG control problem is extensively investigated by Kolmanovsky et al. (1997); Jung (2003); Wahlström (2009) and von Pfeil (2011), additional couplings are introduced by the LP-EGR path and are investigated by Mrosek and Isermann (2011). In the following, the system responses for the extended dual path EGR system are physically motivated by measured step-responses and the signal flow diagram in Fig. 4.1. Besides the already in Kolmanovsky et al. (1997); Jung (2003); Wahlström (2009) exploited stationary and dynamical properties of the single loop EGR system with a non-minimal phase characteristics in $p_{2i}$ and a sign-reversal in $\dot{m}_{air}$ also unpublished effects like an air mass flow rate overshoot will be discussed in the following. After the influences of the single air path actuators on the system quantities are motivated, the results are summarised in a block diagram in p-canonical structure in Sect. 4.1.5.

### 4.1.1  HP-EGR Actuator System Responses

First the system responses to three HP-EGR-valve $s_{hp-egr}$ excitations are given in Fig 4.2. The HP-EGR-valve is the shortest connection between intake and exhaust system and recirculates exhaust gas from exhaust manifold to intake manifold. The mass flow rate $\hat{\dot{m}}_{hp-egr}$ is the main effect of $s_{hp-egr}$, which is basically determined by the pressure ratio between $p_3$ and $p_{2i}$ and the valve orifice, see Eq.(3.22). Generally, it can be stated that the further the HP-EGR-valve $s_{hp-egr}$ is opened, the higher becomes $\hat{\dot{m}}_{hp-egr}$.

Another important influence of $s_{hp-egr}$ is $\dot{m}_{air}$. Thus, the HP-EGR-valve is typically used to control $\dot{m}_{air}$ in an air mass flow rate control concept. In Fig. 4.2 it can be observed, that for a step of $s_{hp-egr}$ the decrease of $\dot{m}_{air}$ is larger than the simultaneous increase of $\hat{\dot{m}}_{hp-egr}$. This can be motivated by the signal flow diagram in Fig. 4.1. At constant pressure $p_{2i}$ and temperature $T_{2i}$ the mass flow rate entering the engine $\dot{m}_{eng,in}$ (3.28) remains constant. Consequently, the mass flow rate through the compressor decreases for the amount $\hat{\dot{m}}_{hp-egr}$ increases. However, due to the increased HP-EGR mass flow rate the intake temperature $T_{2i}$ rises and the pressure $p_{2i}$ drops, so that in steady state the decrease in $\dot{m}_c$ and therefore the decrease in $\dot{m}_{air}$ is larger than the increase in $\hat{\dot{m}}_{hp-egr}$.

**Stationary Side-Effects of $s_{hp-egr}$ to $n_{tc}$, Respectively $p_{2i}$**

When the HP-EGR-valve opens, the portion of recirculated exhaust gas $\hat{\dot{m}}_{hp-egr}$ is missing to drive the turbine wheel with $\dot{m}_t$, see Fig. 4.1. Consequently, less turbine power $P_t$ is transferred to the compressor. On the compressor side less mass flow rate $\dot{m}_c$ has to be delivered to fill the cylinder by $\dot{m}_{eng,in}$, since it is replaced by recirculated exhaust gas. Thus, also less compressor power $P_c$ is demanded to maintain the charge-air pressure.

A comparison between the formulation of compressor power (3.50) and turbine power (3.59) shows, that the turbine power rises quadratically with the mass flow rate $\dot{m}_t$ and only linearly with the turbocharger speed $n_{tc}$, while the largest proportion of the compressor power rises quadratically with $n_{tc}$ and only linearly with $\dot{m}_c$. Anymore, Fig. 3.6 shows that the compressor mass flow rate maps are very flat in the relevant area, which means that at a lowered mass flow rate the turbocharger speed has to be maintained to achieve a fixed pressure ratio over the compressor wheel. These differences in the compressor power and the turbine power characteristics lead to a turbocharger deceleration and a negative relationship between $s_{hp-egr}$ and $n_{tc}$, respectively the charge-air pressure $p_{2i}$.

Further, the opening of $s_{hp-egr}$ widens a different flow route for the gas mass flow, which avoids the turbine flow restriction, see Fig. 4.1. Due to the lowered overall flow resistance for outflows of $V_3$ the exhaust pressure $p_3$ drops and as a consequence of the decreased compressor power the temperature after the compressor $T_{2c}$ sinks as well.
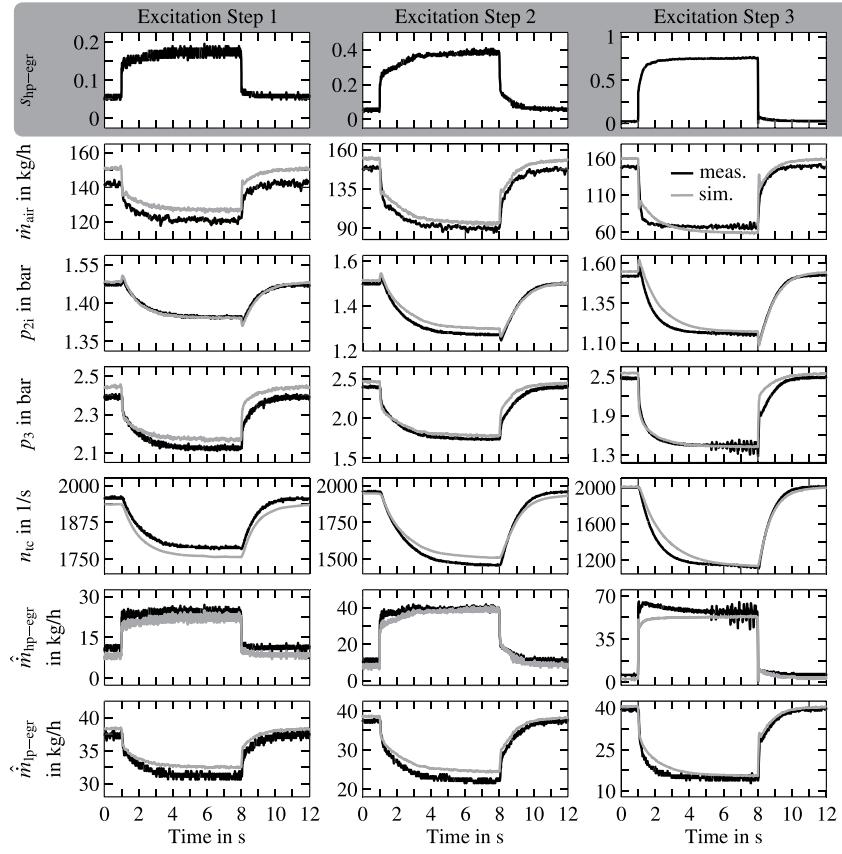
**Figure 4.2:** Measured and simulated step responses to a step input of $s_{\text{hp}-\text{egr}}$ at $n_{\text{eng}} \approx 2250\,\text{min}^{-1}$ and $u_{\text{inj}} = 15\,\text{mm}^3/\text{cyc}$ $(s_{\text{t}} = 1,\ s_{\text{lp}-\text{egr}/\text{eth}} = 0.3,\ u_{\text{icc}} = 0)$

### Stationary Side-Effects of $s_{\text{hp}-\text{egr}}$ to $\hat{\dot{m}}_{\text{lp}-\text{egr}}$

Anymore, the HP-EGR-valve opening $s_{\text{hp}-\text{egr}}$ influences the mass flow rate over the LP-EGR path $\hat{\dot{m}}_{\text{lp}-\text{egr}}$. These influences result from the opening of $s_{\text{lp}-\text{egr}}$ and the pressure before the compressor wheel $p_1$ as well as the exhaust pipe pressure $p_5$, see Fig. 4.1. If the orifices in the intake (air filter; intake throttle valve) and orifices in the exhaust pipe (pipe flow restriction; exhaust throttle valve) stay constant, these pressures depend only on mass flow rates entering $\dot{m}_{\text{air}}$ and exiting $\dot{m}_{\text{eth}}$ the engine gas system.

Hence, a rise in $\dot{m}_{\text{air}}$ is caused by lowering $p_1$. On the other end this increased $\dot{m}_{\text{air}}$ is enriched by burned fuel. This exhaust gas $\dot{m}_{\text{eth}}$ has to leave the system via a flow resistance and enlarges the pressure $p_5$. These two opposed pressure changes and the influence of recirculated HP-EGR to $\dot{m}_{\text{air}}$ and $\dot{m}_{\text{eth}}$ result in an influence of $s_{\text{hp−egr}}$ to the LP-EGR mass flow rate. Therefore $\hat{\dot{m}}_{\text{lp−egr}}$ rises and falls with the course of $\dot{m}_{\text{air}}$ and $s_{\text{hp−egr}}$ has a negative system gain to $\hat{\dot{m}}_{\text{lp−egr}}$.

**Dynamical System Responses**

After the stationary influences to $s_{\text{hp−egr}}$ have been investigated, the dynamical system responses in Fig. 4.2 are focused and motivated by the signal flow diagram in Fig. 4.1. In the HP-EGR system the pressure $p_3$ can be considered as the driving state for the fastest process dynamics. When the HP-EGR-valve suddenly opens, a high pressure difference between the states $p_{2\text{i}}$ and $p_3$ exists. This pressure difference increases the mass flow rate over the opening HP-EGR-valve almost instantaneously and the exhaust manifold empties. As a result the pressure $p_3$ abruptly sinks until a short-time equilibrium between $\dot{m}_{\text{t}}$, $\hat{\dot{m}}_{\text{hp−egr}}$, the corresponding flow orifices and their counter pressures is reached. In the intake manifold the relative high exhaust pressure $p_3$ drives $\hat{\dot{m}}_{\text{hp−egr}}$, so that $p_{2\text{i}}$ rises. Furthermore, the recirculated exhaust gas significantly increases the intake temperature, while the compressor is still delivering its mass flow rate $\dot{m}_{\text{c}}$. These effects lead to the non-minimum phase behaviour in $p_{2\text{i}}$. For the compressor the dynamical increasing counter pressure $p_{2\text{i}}$ is a resistance, so that the mass flow rate over the compressor and the dependent mass flow rate $\dot{m}_{\text{air}}$ steeply drop.

Shortly after the dynamical fast transients are settled, the slow turbocharger dynamics gets visible in $n_{\text{tc}}$. The opening of $s_{\text{hp−egr}}$ bypasses the turbine and the turbine mass flow rate $\dot{m}_{\text{t}}$ drops. As a result the turbine power drops more than the compressor power and the turbocharger decelerates until a new equilibrium between compressor and turbine power is reached. During this transient the turbocharger moment of inertia dominates the process dynamics. This dynamical slow turbocharger deceleration can be observed in the turbocharger speed and all pressures and mass flow rates in Fig. 4.2.

Similar observations can be made for the fast and the slow dynamics in case of a HP-EGR-valve closing. During the dynamical fast HP-EGR-valve closing, the decreasing amount of $\hat{\dot{m}}_{\text{hp−egr}}$ cannot be substituted by the compressor, which is still working against the relative high pressure $p_{2\text{i}}$, respectively $p_{2\text{c}}$. At the same time the engine inflow $\dot{m}_{\text{eng,in}}$ stays rather constant and $T_{2\text{i}}$ almost instantaneously drops. Consequently, the engine inflow empties the intake manifold and this results in the non-minimal phase drop of $p_{2\text{i}}$. As a result the pressure ratio over the compressor wheel sinks and larger gas flow rates $\dot{m}_{\text{c}}$ and $\dot{m}_{\text{air}}$ can be charged into the intake manifold. In the exhaust system the HP-EGR-valve closing redirects the engine outflow over the turbine and the exhaust pressure $p_3$ increases quickly due to the decreased overall flow area at constant volume flow rate. This increased turbine mass flow rate establishes a dynamical slow turbocharger acceleration via the raised turbine power.

Finally, due to the stationary relationship between the states $p_1$ and $p_5$ and $\dot{m}_{\text{air}}$, the dynamics in the LP-EGR path are directly linked to the air mass flow rate.

These stationary and dynamical couplings can be observed over the whole engine operation range and the interested reader can gain further process insights with step responses to $s_{hp-egr}$ taken at different engine operation points in Mrosek (2017). It should be noted that the stationary and dynamical influences strongly vary with the engine operation point. Especially the stationary process gain can easily vary by a factor of $3 \ldots 4$, see exemplary the coupling between $s_{hp-egr}$ and $\dot{m}_{air}$ over the engine operation range in Fig. C.1.

Summing up, $s_{hp-egr}$ positively influences $\hat{\dot{m}}_{hp-egr}$ and negatively influences $\dot{m}_{air}$, $\hat{\dot{m}}_{lp-egr}$ and $p_{2i}$. The process gains of these influences depend on the engine operation point and the position $s_{hp-egr}$. Generally, the influences to the mass flow rate quantities are dynamically fast and are superimposed by the slow dynamics of the turbocharger, which can be seen in the quantities $p_{2i}$ and $n_{tc}$.

## 4.1.2 VGT-Actuator System Responses

Next, the influences of the VGT-actuator $s_t$ to the gas system quantities are illustrated in Fig. 4.3 with step responses at three different positions of the HP-EGR-valve $s_{hp-egr}$. In the beginning the VGT-actuator is fully closed and then completely opens at a step time of 1 s. This opening increases the cross-sectional area for the turbine and decreases the swirl velocity $c_{t3,u}$, see (3.56). Consequently, less pressure is necessary to drive the turbine mass flow rate $\dot{m}_t$ and the exhaust pressure $p_3$ rapidly drops. Furthermore, the reduced swirl velocity also reduces the turbine power $P_t$ and the turbocharger decelerates its speed $n_{tc}$. The resulting consequences of the reduced turbocharger speed can be observed with the assistance of Fig. 4.1 in the shown quantities charge-air pressure $p_{2i}$ as well as in the temperatures $T_{2c}$ and $T_{2ic}$, which represent the compressor's enthalpy increase. For a closing VGT-actuator these couplings appear vice versa. Generally, the actuator $s_t$ shows a positive coupling to the charge-air pressure, which strongly varies in process gain over the engine working range. For more investigations about these varying process gains refer to (Mrosek, 2017).

### Stationary Side-effects of $s_t$ to $\hat{\dot{m}}_{hp-egr}$ and $\dot{m}_{air}$ as well as Sign-Reversal of $\dot{m}_{air}$

A special role plays the HP-EGR-valve opening $s_{hp-egr}$. When this valve is opened, the pressure $p_3$ drives the mass flow rate $\hat{\dot{m}}_{hp-egr}$. The influence of $s_t$ to $\hat{\dot{m}}_{hp-egr}$ is throughout positive, since a closing of $s_t$ ($s_t \rightarrow 1$) rises $p_3$. Interestingly the sign of the stationary process gain between $s_t$ and $\dot{m}_{air}$ depends on the opening position $s_{hp-egr}$. For a fairly closed HP-EGR-valve in the left column of Fig. 4.3 this process gain is positive and becomes almost zero at a certain position of $s_{hp-egr}$ in the middle column. Finally, for a more opened HP-EGR-valve in the right column this process gain turns into a negative direction.

This sign-reversal of $\dot{m}_{air}$ has multiple effects and can be explained as follows. First the stationary mass flow rate into the cylinder can be expressed by the balance equation

$$\dot{m}_{eng,in} = \dot{m}_{air} + \hat{\dot{m}}_{lp-egr} + \hat{\dot{m}}_{hp-egr}, \tag{4.1}$$
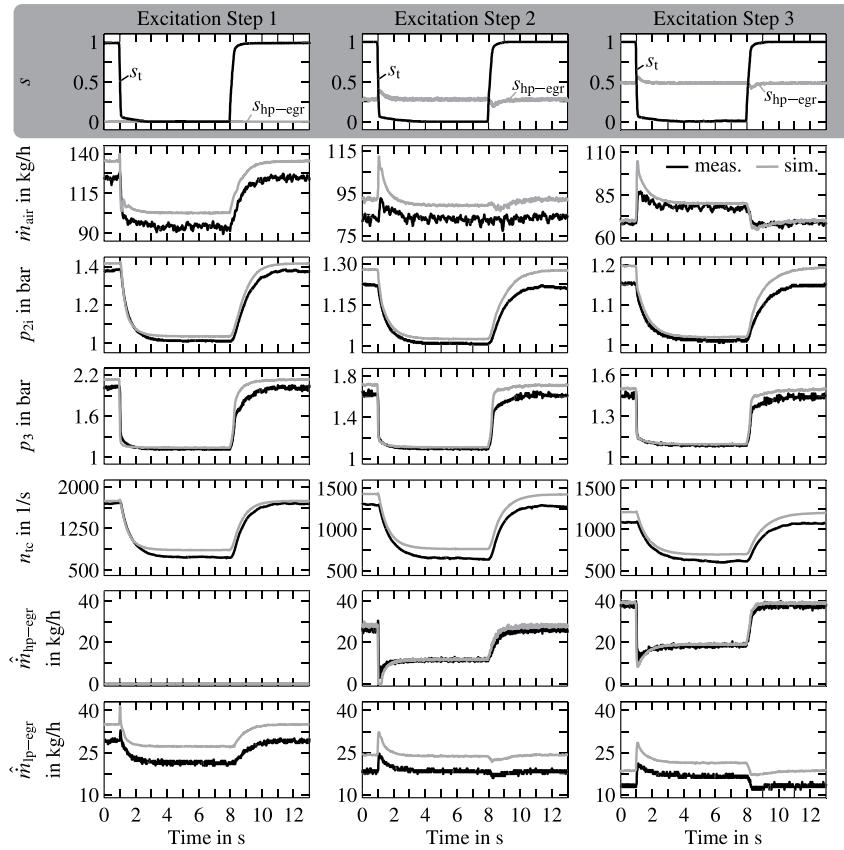
**Figure 4.3:** Measured and simulated step responses to a $s_t$-step at three different $s_{hp-egr}$ positions $\left(s_{lp-egr/eth} = 0.3,\ u_{icc} = 0,\ n_{eng} \approx 2000\,\text{min}^{-1},\ u_{inj} = 15\,\text{mm}^3/\text{cyc}\right)$

at which $\dot{m}_{eng,in}$ is roughly proportional to the gas density in the intake manifold (3.28) and therefore proportional to the charge-air pressure and reciprocal to the intake temperature, see also Fig. 4.1. For the sign-reversal of $\dot{m}_{air}$ the two quantities $\dot{m}_{eng,in}$ and $\hat{\dot{m}}_{hp-egr}$ come into play. On the one hand the closing of $s_t$ increases the swirl velocity, the pressure $p_3$, the turbine power and consequently the charge-air pressure $p_{2i}$ and as a further result the quantity $\dot{m}_{eng,in}$ rises.

On the other hand the flow restriction over the turbine gets larger and furthermore the flow orifice of $s_{hp-egr}$ has to be considered, since both orifices determine the exhaust manifold outflow. The further $s_{hp-egr}$ opens, the more gas mass flow rate can recirculate from the exhaust manifold via the HP-EGR route and less gas passes the turbine. This mass flow rate is missing at the turbine

wheel and less power is transferred to the compressor, so that the increase of $p_{2i}$ for a closing VGT-actuator becomes smaller with the opening of $s_{hp-egr}$ while $\hat{\dot{m}}_{hp-egr}$ increases. Anymore, the increasing mass flow rate $\hat{\dot{m}}_{hp-egr}$ raises the intake temperature. These changes in $p_{2i}$ and $T_{2i}$ determine the variation of the mass flow rate into the engine $\dot{m}_{eng,in}$. Hence, three cases can be considered. When $\dot{m}_{eng,in}$ rises stronger than $\hat{\dot{m}}_{hp-egr}$, a positive cross-coupling can be observed between $s_t$ and $\dot{m}_{air}$. For an equal magnitude of change this cross-coupling becomes zero and negative for a larger increase of $\hat{\dot{m}}_{hp-egr}$. Finally, the LP-EGR mass flow rate is directly coupled to $\dot{m}_{air}$ and also shows the sign-reversal characteristics.

### Dynamical System Responses

The dynamical system properties for a $s_t$ actuation are comparable to the process dynamics resulting from $s_{hp-egr}$ and show the fast process states $p_{2i}$ and $p_3$ and the dynamical slow process state $n_{tc}$ which drive the output quantities. Note, that influences on $p_{2i}$ via the HP-EGR path are dynamically fast, while the influences of $n_{tc}$ to $p_{2i}$ are dynamically slow. An excitation of $s_t$ has two dynamical effects of a fast process response via the changed turbine flow orifice and a dynamical delayed process response via the changed turbine power.

When the actuator $s_t$ moves, the flow restriction over the turbine changes first. In Fig. 4.3 an opening of $s_t$ ($s_t \rightarrow 0$) widens the turbine's cross sectional area and the pressure $p_3$ rapidly drops. This rapid pressure drop in $p_3$ drastically lowers the pressure ratio over the HP-EGR path and causes steep drops in $\hat{\dot{m}}_{hp-egr}$ which can be noticed during the excitation steps two and three in Fig. 4.3. In order to satisfy Eq. (4.1), the ebbing mass flow rate $\hat{\dot{m}}_{hp-egr}$ is taken over by the compressor and a large overshoot in the quantities $\dot{m}_{air}$ and $\hat{\dot{m}}_{lp-egr}$ can be noticed. Naturally, these overshoots have consequences for the emission formation, see Mrosek (2017). Hence, a VGT control scheme, as given in Sect. 7.4.5, should limit the opening speed of $s_t$, to avoid an overshoot of $\dot{m}_{air}$.

After the fast pressure dynamics are settled, the changed turbine power comes into play and the turbocharger decelerates, see Fig. 4.1. The slowing turbocharger decreases the charging pressure $p_{2i}$ and the mass flow rates settle to their steady state conditions. Along with $p_{2i}$ also the intake temperatures $T_{2c}$ and $T_{2ic}$ show the course of the $n_{tc}$ dynamics. Whereas the measured temperatures are further low pass filtered by the heat storage in the turbocharger and the sensors' dynamics. When $s_t$ closes ($s_t \rightarrow 1$), the pressure $p_3$ increases relatively slow compared to the pressure course during the actuator opening. For this actuator closing the dynamics in $p_3$ show a dynamical fast portion for the changed flow orifice and a dynamical slow portion which follows the charge-pressure build-up. All in all the $s_t$ actuator manipulation results in a non-linear direction dependent dynamics in the quantities $\dot{m}_{air}$, $\hat{\dot{m}}_{hp-egr}$, $\hat{\dot{m}}_{lp-egr}$ and $p_3$. One reason is that $p_3$ can be lowered almost instantaneously via the turbine's cross sectional area, while the pressure build-up is delayed by the exhaust manifold volume and the turbocharger dynamics. Another reason lies in the asymmetrical VGT-actuator dynamics, as given in Fig. 4.4a) for the actuator opening and Fig. 4.4b) for the actuator closing.

a)

b)
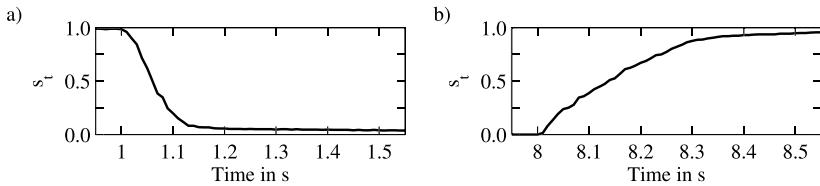


**Figure 4.4:** Direction dependent dynamics of the VGT-actuator, zoom into Fig. 4.3 excitation step 1. a) VGT-actuator opening b) VGT-actuator closing

The actuator opening takes about 100 ms, while the actuator closing process takes 300 ms. A main reason for this dynamical asymmetry lies in the design of pneumatical actuators, which are driven by the atmospheric pressure with an almost infinite volume for the opening direction and the vacuum-system with a limited volume for the closing direction. These pressures drive the actuator and result in the asymmetrical dynamics which shall not be further discussed here. For further readings about modelling and control of pneumatic actuators refer to Moraal et al. (1999); Schwarte (2007); Galindo et al. (2009). However, even if the asymmetrical dynamics will not be further investigated in this dissertation, a simplified dynamical model for the asymmetrical VGT-actuator dynamics will be utilised to achieve a better control quality in the semi-physical feed forward control in Sect. 7.4.

In a nutshell $s_t$ influences the quantities $p_{2i}$ and $\hat{\dot{m}}_{hp-egr}$ positively, while the influence to $\dot{m}_{mair}$ and $\hat{\dot{m}}_{lp-egr}$ can be negative, zero or positive. This change in sign depends on the opening of the HP-EGR-valve and the engine operation point. For step changes of the VGT-actuator a superposition of a fast and a slow dynamics can be observed in the pressures and mass flow rates. The fast dynamics are introduced via the HP-EGR path and the pressures $p_{2i}$ and $p_3$, while the slow dynamics results from turbocharger acceleration. Further, a fast opening of the VTG-actuator results in a collapse of $\hat{\dot{m}}_{hp-egr}$ and can be seen in an overshoot of $\dot{m}_{air}$.

### 4.1.3  LP-EGR/ETH Actuator System Responses

The system responses to the combined actuator $s_{lp-egr/eth}$ (Fig. 2.2a)) complete the system analysis by step responses. In Fig. 4.5 three excitation steps of $s_{lp-egr/eth}$ are shown. In the first two step responses only the LP-EGR-valve is active, whereas in the last excitation step also the exhaust throttle valve is activated.

The stationary system responses of $s_{lp-egr/eth}$ can be described by the LP-EGR-valve ($s_{lp-egr}$) flow restriction and the exhaust throttle valve ($s_{eth}$) flow restriction at the engine exhaust pipe. First the LP-EGR-valve opening determines the mass flow rate of the LP-EGR path via Eq. (3.22) mainly via the pressure difference between $p_1$ and $p_5$. These pressures are directly related to the mass flow rate entering and exiting the engine gas system, see also Sect. 4.1.1. Thus, the lower the pressure $p_1$ falls in relationship to $p_a$, the more fresh air flows via the air filter into the engine gas
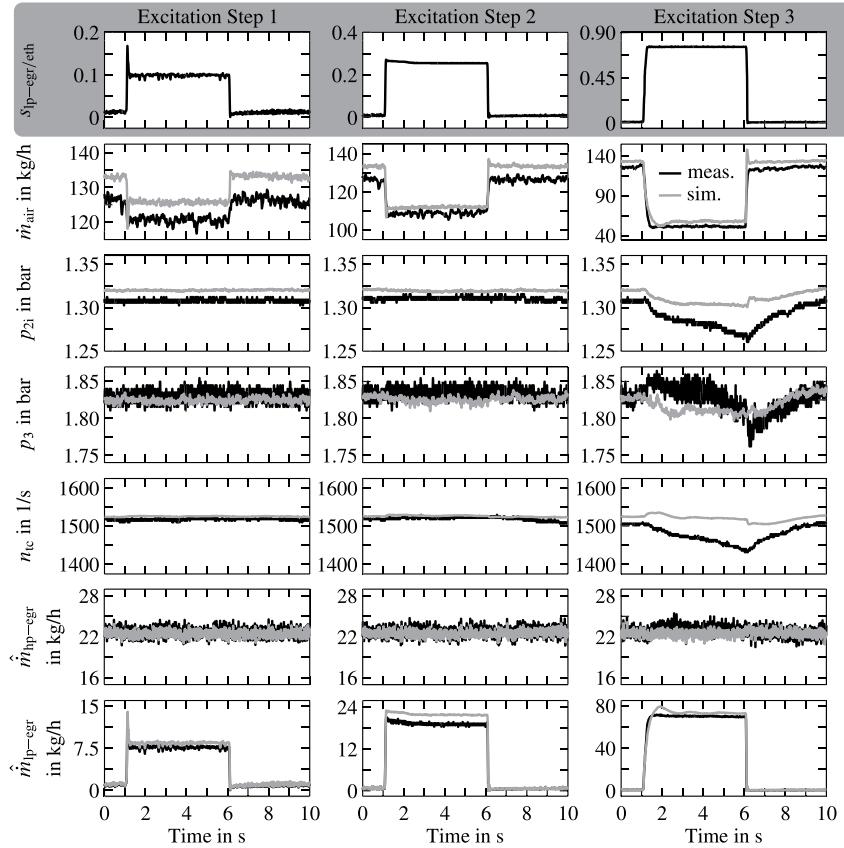
**Figure 4.5:** Measured and simulated step responses to a step input of $s_{lp-egr}$ at $n_{eng} \approx 2000\,\mathrm{min}^{-1}$ and $u_{inj} = 15\,\mathrm{mm}^3/\mathrm{cyc}$ $\left(s_t = 1,\ s_{hp-egr} = 0.2,\ u_{icc} = 0\right)$

system. This increased air mass flow rate causes a pressure rise in $p_5$ since the inflowing gas mass flow rate and the injected fuel stationary have to exit the exhaust system.

An opening of $s_{lp-egr}$ bypasses the intake and exhaust system and the pressure difference between $p_1$ and $p_5$ drives $\hat{\dot{m}}_{lp-egr}$. This mass flow rate $\hat{\dot{m}}_{lp-egr}$ results in a rise of $p_1$ and $\dot{m}_{air}$ decreases. Consequently, the actuator $s_{lp-egr/eth}$ shows a positive process gain to $\hat{\dot{m}}_{lp-egr}$ and a negative process gain to $\dot{m}_{air}$. Furthermore, the rising LP-EGR mass flow rate increases the temperatures upstream $T_1$ and downstream the compressor $T_{2c}$.

When the pressure difference over the LP-EGR path is too small to drive a desired $\hat{\dot{m}}_{lp-egr}$, the exhaust throttle valve can increase this pressure difference via an increased exhaust pressure $p_5$,

see Fig. 4.5 excitation step 3. During this operation a small coupling to the pressures $p_{2i}$ and $p_3$ can be observed. Otherwise these states and the output quantity $\hat{\dot{m}}_{\text{hp}-\text{egr}}$ show only a minor coupling to the actuator $s_{\text{lp}-\text{egr/eth}}$. Similar couplings can be observed for the alternative actuator configuration $s_{\text{lp}-\text{egr/ith}}$ with an intake throttle valve $s_{\text{ith}}$, which replaces the exhaust throttle valve $s_{\text{eth}}$.

The dynamical system properties are mainly determined by the fast transients of $p_1$ and $p_5$. Hence, there are no significant dynamics in the quantities $\dot{m}_{\text{air}}$ and $\hat{\dot{m}}_{\text{lp}-\text{egr}}$.

In summary the LP-EGR actuators positively influence $\hat{\dot{m}}_{\text{lp}-\text{egr}}$ and $\dot{m}_{\text{air}}$ dynamical fast, while there is only a weak influence to the quantities on the high pressure side of the air path.

### 4.1.4  Time Constants and Process Gains of the Air Path Model

From control perspective there is a legitimate interest to formulate the arising system properties of the mean value engine model in concrete quantities as process gains, time constants and eigenvalues of this process. For an air path control the quantities of interest are pressures and the mass flow rates. The pressures can be considered as derived states of stored mass and energy, while the mass flow rates represent output quantities.

The system dynamics in the utilised mean value engine model from Chap. 3 are modelled by the states storage of gas masses (3.1), energy (3.2) and turbocharger speed (3.62). Further states are air content of storages (3.17) and compressor mass flow rate dynamics (3.39). The measurable quantities storage temperature and storage pressure, which are closely related to the system states, follow by the relationships (3.4) and (3.8) from the stored gas masses and energy.

The differential equations for pressure changes and temperature changes in storages are given by the adiabatic formulation as

$$\frac{\mathrm{d}p_{\text{st}}}{\mathrm{d}t} = \frac{\kappa R}{V_{\text{st}}} \left( \sum_{i=1}^{p} \dot{m}_{\text{in},i} T_{\text{in},i} - \sum_{j=1}^{q} \dot{m}_{\text{out},j} T_{\text{st}} \right) \tag{4.2}$$

and

$$\frac{\mathrm{d}T_{\text{st}}}{\mathrm{d}t} = \frac{R T_{\text{st}}}{p_{\text{st}} V_{\text{st}} c_{\text{V}}} \left( c_{\text{p}} \sum_{i=1}^{p} \dot{m}_{\text{in},i} T_{\text{in},i} - c_{\text{p}} \sum_{j=1}^{q} \dot{m}_{\text{out},j} T_{\text{st}} - c_{\text{V}} \left( \sum_{i=1}^{p} \dot{m}_{\text{in},i} - \sum_{j=1}^{q} \dot{m}_{\text{out},j} \right) T_{\text{st}} \right). \tag{4.3}$$

However, due to the nonlinear process characteristics of the in- and outflowing mass flow rates and the dependency of Eq. (4.2) from Eq. (4.3), it is not trivial to derive a linear time constant for each storage element. Thus, the filling time constant of a storage element is approximated according to (Zahn, 2012) as

$$\tau_{st} \approx \frac{\rho_{st} V_{st}}{\kappa \dot{m}_{st}}, \tag{4.4}$$

in which $\dot{m}_{st}$ is the total mass flow rate passing through a storage element. In a typical engine operation the mass flow rate passing through the storages in the intake and exhaust system varies between 25 and 300 kg/h and yields with the identified storage volume $V_{st}$ the filling time constants in Tab. 4.1 for the single modelled storages.

**Table 4.1:** Approximated filling time constants of the storages in the intake and exhaust system

| Storage Element | Volume $V_{st}$ in cm$^3$ | Time Constant $\tau_{st}$ in ms |
|---|---|---|
| $V_1$ | 1400 | 12 . . . 144 |
| $V_{2c}$ | 3600 | 56 . . . 370 |
| $V_{2i}$ | 5600 | 101 . . . 461 |
| $V_3$ | 1400 | 15 . . . 144 |
| $V_4$ | 1950 | 10 . . . 120 |
| $V_5$ | 25400 | 130 . . . 1567 |

Next, the time constant of the turbocharger can be determined analytically by transforming the turbocharger speed in its angular velocity

$$\omega_{tc} = 2\pi n_{tc} \tag{4.5}$$

and replace the effective power $P_i$ at the turbocharger shaft by the acting torque $M_i$

$$P_i = 2\pi n_{tc} M_i \qquad i \in \{t, c, f\}. \tag{4.6}$$

Substituting (4.5) and (4.6) in (3.62) yields a different form of turbocharger acceleration

$$\frac{d\omega_{tc}}{dt} = -\frac{M_t + M_c + M_f}{I_{tc}}, \tag{4.7}$$

in which the friction torque $M_f$ can be replaced by (4.5), (4.6) and (3.63) as

$$\frac{d\omega_{tc}}{dt} I_{tc} + \omega_{tc} k_f = -(M_t + M_c). \tag{4.8}$$

This differential equation includes the turbocharger time constant $\tau_{tc} = I_{tc}/k_f$. With an identified shaft inertia of 1.10e-5 kg m$^2$ and an identified friction factor $k_f$ of 3.23e-6 kg m$^2$/s the time constant is given as 3.4 s. However, as it can be observed in the step responses, this time constant does not reflect the process behaviour of the nonlinear turbocharger dynamics, since both $M_c$ and $M_t$

are functions of the turbocharger speed and the resulting mass flow rates, see (3.50) and (3.59). A more reasonable time constant of the turbocharger dynamics between 0.7 s and 2.6 s can be obtained by linearising the mean value engine model with the MATLAB *linmod* command. In which the lower value refers to engine operation points with almost closed HP-EGR-valve, while the larger time constant results from engine operation points with opened HP-EGR-valve.

Besides the time constants, also the process gains give valuable insights for the later control design. Thus, the minimal and maximal values of the modelled process gains are determined at three engine operation points[1] $op_1 \ldots op_3$ by model linearisation and are summarised in Tab. 4.1.4. Since the position of the air path actuators have a significant influence on the process gains, not investigated actuators are kept at fixed positions ($s_{\text{hp−egr}} = 0.5; s_{\text{t}} = 0.5; s_{\text{lp−egr/ith}} = 0.3$), while the actuators in the columns of Tab. 4.1.4 are varied between positions of $0..05 \ldots 0.95$ to avoid a zero gain of a closed actuator. The range of process gains to the quantities $p_{2\text{i}}$, $\dot{m}_{\text{air}}$ $\dot{m}_{\text{hp−egr}}$ and $\dot{m}_{\text{lp−ger}}$ are listed in the column for each actuator.

The results in Tab. 4.1.4 confirm the investigations of the previous sections and show that the engine air path is a multi-variable system with strong interactions between actuators and the single considered quantities. The shown process gains strongly vary between single engine operation points, at a fixed operation point and with variation of the other actuators.[2] Especially the relationship $\Delta s_{\text{t}}$ to $\Delta p_{2\text{i}}$ shows a strongly varying process gain between single engine operation points, while the relationships $\Delta s_{\text{t}}$ to $\Delta \dot{m}_{\text{air}}$ and $\Delta s_{\text{t}}$ to $\Delta \dot{m}_{\text{lp−egr}}$ show the sign-reversal in the process gain.

As a consequence of these strongly varying time constants and process gains, a suitable control concept in Chap. 7 must handle these system properties and deliver a good response to setpoint changes and disturbance rejection at all engine operation points and operation modes.

### 4.1.5 Summarised Air Path Couplings in P-Canonical Structure

As a summary the air path influences of the classical $s_{\text{hp−egr}}$ and $s_{\text{t}}$ control problem (Schloßer, 2000; Rückert, 2004; von Pfeil, 2011) can be expanded in Fig. 4.6 to the dual EGR path control problem with three actuators $s_{\text{hp−egr}}$, $s_{\text{t}}$, $s_{\text{lp−egr/eth}}$ and $s_{\text{lp−egr/ith}}$ and the output quantities $\dot{m}_{\text{hp−egr}}$, $\dot{m}_{\text{lp−egr}}$, $\dot{m}_{\text{air}}$ and $p_{2\text{i}}$ (Mrosek and Isermann, 2011). In which simplified system transfer functions are given in linearised form ($\Delta$) and p-canonical structure with their corresponding step responses.

In order to describe the complete system behaviour, both possible LP-EGR-actuator configurations with exhaust throttle valve $\Delta s_{\text{lp−egr/eth}}$ and intake throttle valve $\Delta s_{\text{lp−egr/ith}}$ are given as inputs for the $i$ transfer functions $G_{3i}$. These process gains are of the same sign for both actuators. Further, the output quantities $\Delta \dot{m}_{\text{air}}$ and $\Delta \dot{m}_{\text{lp−egr}}$ are shown as the same process output. The process gains between actuators and output quantities only differ for the LP-EGR transfer function $G_{33}$, where

---

[1] $op_1$ : $n_{\text{eng}} = 1000\,\text{min}^{-1}, u_{\text{inj}} = 10\,\text{mm}^3/\text{cyc}$, $op_2$ : $n_{\text{eng}} = 2000\,\text{min}^{-1}, u_{\text{inj}} = 15\,\text{mm}^3/\text{cyc}$, $op_3$ : $n_{\text{eng}} = 3000\,\text{min}^{-1}, u_{\text{inj}} = 20\,\text{mm}^3/\text{cyc}$

[2] For simplification a variation of other actuators is not considered in Tab. 4.1.4.

**Table 4.2:** Minimal and maximal process gain of the linearised mean value engine model with actuators in normalised position (dimensionless) at the engine operation points $op_1 : n_{eng} = 1000\,\text{min}^{-1}, u_{inj} = 10\,\text{mm}^3/\text{cyc}, op_2 : n_{eng} = 2000\,\text{min}^{-1}, u_{inj} = 15\,\text{mm}^3/\text{cyc}, op_3 : n_{eng} = 3000\,\text{min}^{-1}, u_{inj} = 20\,\text{mm}^3/\text{cyc}$. Not investigated actuators are kept at fixed positions $s_{hp-egr} = 0.5; s_t = 0.5; s_{lp-egr/ith} = 0.3$

| $i \in \{_{t,\ hp-egr,\ lp-egr/eth,\ lp-egr/ith}\}$ | | | $\Delta s_t$ | $\Delta s_{hp-egr}$ | $\Delta s_{lp-egr/eth}$ | $\Delta s_{lp-egr/ith}$ |
|---|---|---|---|---|---|---|
| $\Delta p_{2i}/\Delta s_i$ | in bar | $op_1$ | 0.01...0.06 | -0.06...-0.02 | -0.04...0.02 | -0.01...0.001 |
| $\Delta p_{2i}/\Delta s_i$ | in bar | $op_2$ | 0.2...0.5 | -0.4...-0.1 | -0.2...0.02 | -0.06...0.02 |
| $\Delta p_{2i}/\Delta s_i$ | in bar | $op_3$ | 0.9...2.0 | -0.3...-0.1 | -0.4...0.2 | -0.35...0.2 |
| $\Delta \dot{m}_{air}/\Delta s_i$ | in kg/h | $op_1$ | -18...-3 | -50...-20 | -50...-40 | -50...-24 |
| $\Delta \dot{m}_{air}/\Delta s_i$ | in kg/h | $op_2$ | -30...20 | -100...-20 | -115...-100 | -95...-70 |
| $\Delta \dot{m}_{air}/\Delta s_i$ | in kg/h | $op_3$ | 60...140 | -150...-33 | -260...-200 | -200...-150 |
| $\Delta \dot{m}_{hp-egr}/\Delta s_i$ | in kg/h | $op_1$ | 5...20 | 15...60 | 0.2...4 | 0.2...2 |
| $\Delta \dot{m}_{hp-egr}/\Delta s_i$ | in kg/h | $op_2$ | 20...32 | 15...115 | -0.5...5 | -0.5...5 |
| $\Delta \dot{m}_{hp-egr}/\Delta s_i$ | in kg/h | $op_3$ | 20...50 | 20...250 | -10...1 | 1...6 |
| $\Delta \dot{m}_{lp-egr}/\Delta s_i$ | in kg/h | $op_1$ | -8...-1 | -18...-5 | 38...50 | 24...38 |
| $\Delta \dot{m}_{lp-egr}/\Delta s_i$ | in kg/h | $op_2$ | -12...8 | -40...-11 | 72...100 | 62...100 |
| $\Delta \dot{m}_{lp-egr}/\Delta s_i$ | in kg/h | $op_3$ | 21...51 | -70...-20 | 50...250 | 126...210 |

the process gain between the LP-EGR-actuators and $\Delta \dot{m}_{lp-egr}$ is positive, while it is negative for $\Delta \dot{m}_{air}$. The weak LP-EGR process gains $G_{31}$ and $G_{32}$ are displayed in a dashed line. Finally, $G_{23}$ denotes the transfer function between $\Delta s_t$ and the two output quantities $\Delta \dot{m}_{air}$ and $\Delta \dot{m}_{lp-egr}$. For these influence the sign of the process gain depends on the engine operation point and the opening of $s_{hp-egr}$, see Sect. 4.1.2.

In anticipation of Chap. 7 the influence of the different actuators to the output quantities will be handled by two separate control concepts. A first control concept handles the actuation of HP-EGR-valve and VGT-actuator, while a second control concept controls the LP-EGR-actuator and handles all disturbances via $G_{13}$ and $G_{23}$ of the first control concept.

## 4.1.6 Summary

An investigation of the step responses to steps of the actuators $s_{hp-egr}$, $s_t$ and $s_{lp-egr/eth}$ showed, that measurements and simulations of the mean value engine model agree well. Consequently, the model is capable to simulate the relevant engine air path quantities. The engine air path is a nonlinear process with strongly varying stationary process gains and dynamics. These quantities vary with the engine operation point and the position of the air path actuators. While there are strong influences of the HP-EGR-valve and VGT-actuator to the air path quantities, there are only weak influences of the LP-EGR-actuators to the quantities on the high-pressure side of the air path ($\dot{m}_{hp-egr}$, $p_{2i}$, $p_3$, $n_{tc}$). Thus, in Chap. 7 two separate control concepts will control the
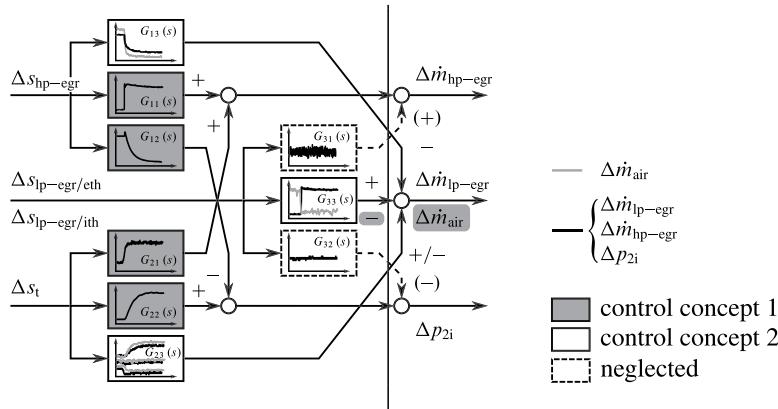
**Figure 4.6:** Signal flow and step responses between the actuators for the two EGR paths, the VGT-actuator and the resulting output variables HP-EGR mass flow rate, LP-EGR mass flow rate, air mass flow rate and charging pressure in linearised p-canonical structure.

nonlinear engine process, while the first control concept handles the actuation of HP-EGR-valve and VGT-actuator, the second controls the LP-EGR-actuator.

## 4.2 Stationary System Properties

After the system couplings have been investigated by means of step responses, in the following a special attention will be paid to stationary differences between different EGR configurations. Due to this dissertation's compactness some stationary system properties have to be briefly summarised in the following. The interested reader can find further readings about these stationary system properties in Mrosek (2017)

### HP- and LP-EGR Operation Range

HP- and LP-EGR operation show large differences in the feasible operation range in $\dot{m}_{air}$ and $p_{2i}$. While a HP-EGR operation substantially decreases the charging pressure there are only small influences of a LP-EGR operation in the charging pressure, see Fig. 4.2 and Fig. 4.5. Further, a LP-EGR operation with exhaust throttle valve is favourable to an operation with intake throttle valve with respect to the feasible operation area in the $\dot{m}_{air}/p_{2i}$-plane (Mrosek, 2017).

**HP- and LP-EGR Charge Cycle Losses**

A comparison between $s_{\text{lp}-\text{egr/eth}}$ and $s_{\text{lp}-\text{egr/ith}}$ in in Mrosek (2017) shows, that at a constant air mass flow rate and charging pressure the exhaust throttle valve is advantageous over the intake throttle valve configuration with respect to the charge cycle losses. At rather low charging pressures $s_{\text{hp}-\text{egr}}$ is advantageous over the LP-EGR configurations, while this benefit turns to a disadvantage when a rather high charging pressure needs to be maintained during a simultaneous HP-EGR or LP-EGR-operation.

**Influence of the Ambient Conditions**

Ambient conditions have a strong effect on the air path quantities (Mrosek, 2017). Therefore the ambient conditions should be incorporated in the engine model to reliably simulate the engine during the current present ambient conditions. Otherwise a test bench conditioning with a defined air pressure and a defined gas temperature can help to get reproducible measurements and simulation results. In order to get improved feedforward control signals, these ambient conditions are incorporated into the semi-physical feedforward control scheme in Chap. 7.

### 4.2.1 Properties of the Combined LP-EGR Actuators

Next, the influences of the combined actuators $s_{\text{lp}-\text{egr/ith}}$ and $s_{\text{lp}-\text{egr/eth}}$ are investigated in the following with simulations of the mean value engine model at four exemplary engine operation points $op_1 \ldots op_4$, as given in Tab. C.1. In Fig. 4.7a) the stationary characteristics of the combined actuator $s_{\text{lp}-\text{egr/ith}}$ with regard to the quantities $\dot{m}_{\text{air}}$, $p_1$, $p_5$ and the low pressure EGR-rate

$$r_{\text{lp}-\text{egr}} = \frac{\dot{m}_{\text{lp}-\text{egr}}}{\dot{m}_{\text{lp}-\text{egr}} + \dot{m}_{\text{air}}} \tag{4.9}$$

are shown. The topmost plot in Fig. 4.7a) shows a strong increase in $\dot{m}_{\text{air}}$ for operation points with a higher load and engine speed. Furthermore, it can be seen, that the actuator shaping in Appx. C gives a quite linear relationship between actuator position and $\dot{m}_{\text{air}}$. Obviously the stationary gain between actuator position and air mass flow rate depends highly on the engine operation point and varies by factor 4 between $op_1$ and $op_4$.

In the middle plot of Fig. 4.7a) the influences of $s_{\text{lp}-\text{egr/ith}}$ on exhaust pressure $p_5$ and intake pressure $p_1$ are investigated. These influences can be divided into two regions. At $s_{\text{lp}-\text{egr/ith}} \in [0, 0.28]$ only the LP-EGR-valve is active, while otherwise the intake throttle valve is actuated. When the LP-EGR-valve opens, the pressure in the intake system rises, since the exhaust excess pressure routes the exhaust gas mass flow rate into the intake manifold. This results in a decreased mass flow rate through the air filter and therefore in an increase of $p_1$. Anymore, less of the remaining gas has to pass the exhaust pipe, which results in the decrease of $p_5$. For a higher LP-EGR mass flow rate, the pressure drop over the LP-EGR-valve has to be enlarged. This is
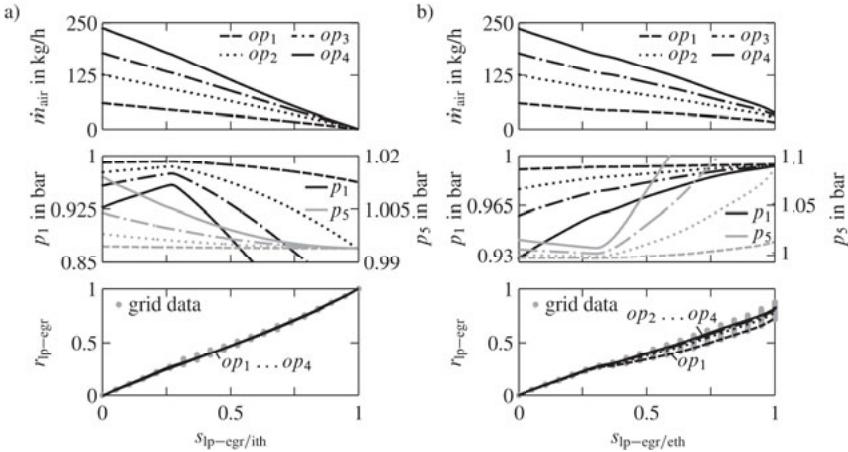
**Figure 4.7:** Mean value engine model simulations at four engine operation points $op_1 \ldots op_4$, as given in Tab. C.1. The further simulated grid data points show that the LP-EGR-rate is fairly invariant to the engine operation point and mainly depends on the positions of a) $s_{lp-egr/ith}$ and b) $s_{lp-egr/eth}$.

achieved with the intake throttle valve for $s_{lp-egr/ith} \in\ ]0.28, 1]$, which throttles the intake system after the air filter by closing $s_{ith}$. Then the cylinder and the compressor suction generate a partial vacuum $p_1$, which drives the LP-EGR mass flow rate and results in a further decrease of $p_5$. Especially at engine operation points with high LP-EGR mass flow rates ($op_3$, $op_4$) the pressure $p_1$ becomes very low. Hence, the system's pressure tolerances to $p_1$ give the limitations for this LP-EGR configuration and will determine the amount of LP-EGR which can be recirculated at engine operation points with high gas mass flow rates entering the engine.

The bottom graph in Fig. 4.7a) shows the relationship between the actuator position $s_{lp-egr/ith}$ and the low pressure EGR-rate (4.9). It can be clearly seen, that $r_{lp-egr}$ is fairly invariant to the engine operation point. For all four engine operation points the curves overlap and the single curves are hard to distinguish. For a further analysis the LP-EGR-rate is simulated in the whole modelled engine operation range ($n_{eng}, u_{inj}$), considering a large full factorial set of combinations between $s_{lp-egr/ith}$, $s_t$ and $s_{hp-egr}$. These simulations are added as grid data points to the bottom graph and confirm the $r_{lp-egr}$ invariance from the engine operation point.

Interestingly, $r_{lp-egr}$ almost exclusively depends on the position of the combined actuator $s_{lp-egr/ith}$. This is mainly caused by the relationship between the air mass flow rate and the pressures $p_1$ and $p_5$ and can be described by the couplings between $\dot{m}_{lp-egr}$ and the actuators $s_{hp-egr}$ and $s_t$, see Sect. 4.1. Anymore, a more detailed explanation for this largely operation point invariant characteristics between $r_{lp-egr}$ and $s_{lp-egr/ith}$ is given in the following. The mass flow rate through the LP-EGR-valve (3.22) is mainly determined by the flow coefficient $(C_D A_{ref})_{lp-egr}$ and the pressure drop over the valve itself. The gas temperature plays also a role, but this can be considered as minor,

since on the one hand the model sensitivity to the gas temperature is rather small (Mrosek et al., 2010b) and on the other hand the gas is cooled, so that temperature variations after the LP-EGR cooler are moderate.

A change in the engine operation point or the air path actuators result in a change of $\dot{m}_{\text{air}}$. In order to satisfy Eq. (3.22) this mass flow rate entering the gas system results from an altered pressure $p_1$. Furthermore, in stationary engine conditions the inflowing gas flow has to leave the system via the exhaust pipe, being enriched by the injected fuel mass. A change in the outflowing exhaust gas flow rate also changes the exhaust pressure $p_5$. Fortunately, the pressures $p_1$ and $p_5$ are influenced in opposite directions by $\dot{m}_{\text{air}}$. For a rise in $\dot{m}_{\text{air}}$ the pressure $p_1$ decreases and the pressure $p_5$ increases and vice versa. These characteristics also influence the pressure drop over the LP-EGR-valve, so that $\dot{m}_{\text{lp-egr}}$ changes in the same direction as $\dot{m}_{\text{air}}$. This means that also $r_{\text{lp-egr}}$ is fairly invariant to the engine operation point, since all external changes of $\dot{m}_{\text{air}}$ result in a change of $\dot{m}_{\text{lp-egr}}$. In the later following Sect. 7.7 this coherence will be utilised to derive a semi-physical control scheme for the LP-EGR path.

A combination between a LP-EGR-valve and an exhaust throttle valve gives the second option for a LP-EGR system. Similar to the previous analysis the actuator $s_{\text{lp-egr/eth}}$ is analysed in Fig. 4.7b). In the topmost plot the relationship between the air mass flow rate and the actuator position shows a comparable operation point dependent stationary gain between the actuator position and $\dot{m}_{\text{air}}$. In the middle plot first differences between the intake throttle valve and the exhaust throttle valve can be observed. When the exhaust throttle valve is in operation for $s_{\text{lp-egr/eth}} \in \,]0.28, 1]$ a rise in $p_1$ and $p_5$ can be observed. Also in this configuration the strong rising pressure $p_5$ seems to be a limiting factor for high LP-EGR mass flow rates at engine operation points with a high air mass flow rate, e.g. $op_3$ and $op_4$.

In the bottom plot of Fig. 4.7b) the relationship between $r_{\text{lp-egr}}$ and the actuator position $s_{\text{lp-egr/eth}}$ is shown. Also for this sensor configuration $r_{\text{lp-egr}}$ is quite dependent on the actuator position. Further, the simulations over the whole engine operation range with the full factorial actuation of the other air path actuators confirm this dependency in the grid data points. In comparison to the other curves only the curve for $op_1$ shows small variations. These variations become larger for a further closed exhaust throttle valve ($s_{\text{lp-egr/eth}} \rightarrow 1$) and very high LP-EGR-rates. Investigations have shown, that the exhaust gas temperature $T_5$ is the main reason for these deviations. Contrary to the intake throttle valve configuration the flow orifice of the exhaust throttle valve is exposed to the rather hot tailpipe temperatures. A strong change in the exhaust temperature in Eq. (3.22) changes the gas density and also the necessary pressure drop between $p_5$ and $p_a$ to maintain a defined mass flow rate through the flow orifice $(C_D A_{\text{ref}})_{\text{eth}}$. This temperature dependency gets even larger for an orifice with a small effective diameter and larger pressure drops, see Mrosek et al. (2010b) and Mrosek (2017). At $op_1$ the engine is operated with no injection, so that the exhaust temperature is comparable low. This readjusts the pressure relationship between $p_1$ and $p_5$ and results in small variations to the other curves.

However, the deviations between the actuator position and $r_{\text{lp-egr}}$ are comparable small and occur mostly in engine overrun state with no demand for an air path control. Further, the deviations are

only significant for large LP-EGR-rates. Thus, also the $r_{lp-egr}$ invariance to the exhaust throttle valve position can be utilised for a control scheme as presented in Sect. 7.7.

## 4.3 Air Content Dynamics

After the system properties of the dual path EGR system have been investigated by means of step functions and stationary system properties, the air content dynamics will be investigated in the following. The main differences between the HP- and LP-EGR system can be seen in different operation ranges in charging pressure and air mass flow rate, different charge temperature and gas propagation times in the intake and exhaust system. The fastest way to influence the cylinder charge is given via the charge cycle by the internal EGR. Then follows the HP-EGR which directly connects the intake and exhaust manifold. Finally, the gas propagation through the LP-EGR path gives the dynamical slowest option to influence the cylinder charge, since the gas has to circle around almost the whole intake and exhaust system.
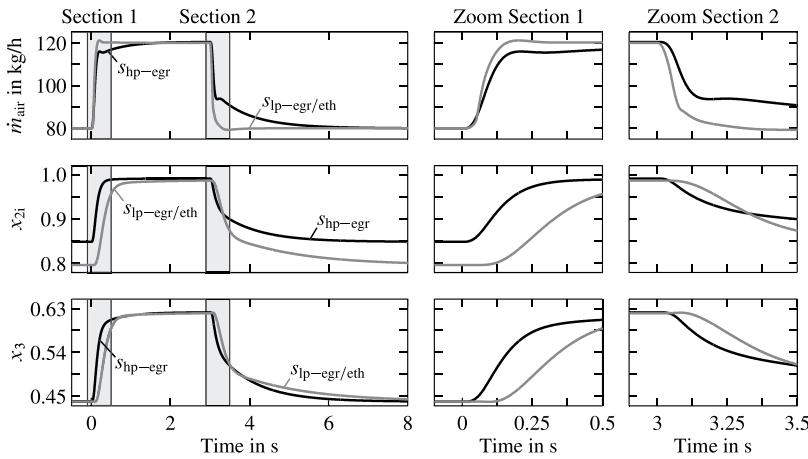


**Figure 4.8:** Mean value engine model simulation of the dynamical impact for step excitations of $s_{hp-egr}$ and $s_{lp-egr/eth}$ to the air mass flow rate $\dot{m}_{air}$, the air contents (ratio of fresh air mass to total gas mass) in the intake $x_{2i}$ and exhaust manifold $x_3$ ($n_{eng} = 2000\,min^{-1}$, $u_{inj} = 15\,mm^3/cyc$)

Fig. 4.8 illustrates the air content dynamics of the HP- and LP-EGR system with step excitations of $s_{hp-egr}$ and $s_{lp-egr/eth}$ which result in step responses of equal size in $\dot{m}_{air}$. At a time of 0 s the HP-EGR-valve closes and the air mass flow rate increases in the first milliseconds from 80 kg/h to 117.5 kg/h. Then the slow turbocharger acceleration further increases the air mass flow rate to its stationary end value of 120 kg/h. For the valve opening at a time of 3 s a similar course of $\dot{m}_{air}$ can be observed. In comparison to the $s_{hp-egr}$ response, the response to the step in $s_{lp-egr/eth}$

shows a significant faster dynamics in $\dot{m}_{air}$, as it can be seen more detailed in the zoomed sections. This is due to the direct injection of $\dot{m}_{lp-egr}$ behind the air mass flow rate sensor, see Fig. 2.1. In contrast, the influence of the HP-EGR has to propagate through the whole intake volume and is filtered by the intake system states. Hence, the air mass flow rate dynamics of the LP-EGR system is significantly faster than the HP-EGR step response. Further, the LP-EGR system influences the turbocharger dynamics less.

When the air content step responses in the intake manifold $x_{2i}$ and the exhaust manifold $x_3$ are investigated, the fast and the slow system dynamics are opposite. With regard to these quantities, the HP-EGR system has the faster system dynamics, since the HP-EGR path is a short connection between the exhaust manifold and the intake manifold. For the LP-EGR path, the exhaust gas has to pass the whole exhaust and intake system until it is recirculated into the intake manifold. Furthermore, the air content dynamics is direction dependent. A total EGR-valve closing directly disconnects the intake manifold from the exhaust system and the intake system is directly flushed with fresh air. On the other hand an EGR-valve opening first recirculates exhaust gas with a larger proportion of oxygen to the intake system and lowers the intake air content. Then this gas has to pass the cylinder before it can lower the air content in the exhaust system to be recirculated into the intake system again. Due to this recirculation process it usually takes a longer time until all transients are settled and an equilibrium is reached for the EGR-valve opening. A further comparison between the air mass flow rate and the air content dynamics shows that especially in the LP-EGR configuration the air content dynamics settles much slower than the $\dot{m}_{air}$ dynamics.

In Fig. 4.8 it can be further observed, that a fixed air mass flow rate in conjunction with a fixed injection quantity generally results in a fixed air content after the combustion process $x_3$. This observation corresponds to the definition of the air-fuel ratio (3.11) and its relationship to the air content (3.13). However, at a constant $\dot{m}_{air}$ and $x_3$ the air content in the intake manifold varies with the charging pressure and the intake temperature in a way that $x_{2i}$ differs for HP- and LP-EGR operation. This means that at a constant $\dot{m}_{air}$, a lowered intake temperature or an increased charging pressure demand a larger EGR mass flow rate to fill-up the increasing engine inflow $\dot{m}_{eng,in}$, see (3.28). Consequently, the air content $x_{2i}$ in the intake manifold sinks. These changes in $\dot{m}_{eng,in}$ and $x_{2i}$ compensate each other so that stationary the air contents $x_{eng,out}$ and $x_3$ stay constant for an equal injection quantity and a constant $\dot{m}_{air}$.

In summary the air content shows an inherent dynamics, which can not be expressed by the air path quantities mass flow rate and pressure. Thus, in the following section these inherent system states are modelled by a air content model.

## 4.4   Air Content Model

The main dynamical difference between the HP- and the LP-EGR system stays hidden from most series sensors in the air content dynamics in the intake and exhaust system. These dynamics determine the oxygen concentration in the cylinder charge and it will be later shown that the air content influences the emission formation. Hence, it is advisable to derive a simplified control-oriented model for these air content dynamics. Later it will be applied for the dynamical emission simulation in Sect. 5.4 and to consider the air content dynamics in the air path control scheme in Sect. 7.8. This model will utilise measured quantities to determine the air contents in the intake and exhaust system.

The air content dynamics have been longer in the interest of research. Diop et al. (1999) model the intake and exhaust air content for a turbocharged Diesel engine with HP-EGR with a lumped parameter approach and a two volume air path discretisation. Wang (2009) further extends this lumped parameter model for a HP- and LP-EGR system, discretises the air path into four volumes and determines the air content dynamics with measurements of pressure and temperature in each volume, an air mass flow rate measurement and the EGR mass flow rate determination via the flow equation (3.22) for both EGR paths. Bessai et al. (2011) model the intake oxygen concentration with dead times for the HP- and LP-EGR path.
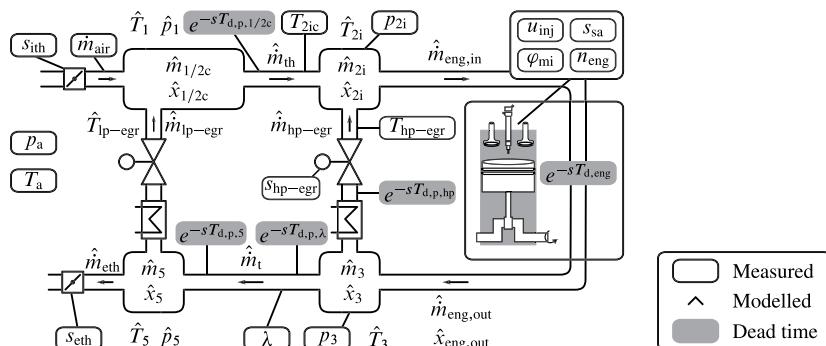


**Figure 4.9:** Control-oriented model for the air content in the intake ($\hat{x}_{1/2c}$, $\hat{x}_{2i}$) and exhaust system ($\hat{x}_3$, $\hat{x}_5$).

In the following a lumped parameter and a pipe receiver model for the air content dynamics with a minimal sensor configuration will be described and validated with measurements from the engine test bench according to Mrosek and Isermann (2010a). The lumped parameter and pipe receiver model differ only by the pipe volume fraction $\xi_{p,st}$, which turns zero for the lumped parameter model, see Eq. (3.18), Eq. (3.19) and Eq. (3.20).

Fig. 4.9 gives the model structure with four volumes and explicitly separates measured from modelled quantities. The measured quantities are ambient pressure $p_a$ and temperature $T_a$, air mass flow rate $\dot{m}_{air}$, temperature after the intercooler $T_{2ic}$ and temperature after the HP-EGR cooler

$T_{\text{hp}-\text{egr}}$, charging pressure $p_{2i}$ and exhaust pressure $p_3$. A similar temperature measurement structure with a $T_{2ic}$ and a $T_{\text{hp}-\text{egr}}$ sensor are also utilised in Schommers et al. (2008) and Ertl et al. (2009). Anymore, the position of the HP-EGR-valve $s_{\text{hp}-\text{egr}}$ and either the exhaust throttle valve position $s_{\text{eth}}$ or the intake throttle valve $s_{\text{ith}}$ position need to be measured. Anymore, the ECU contributes the series measurements $u_{\text{inj}}$, $s_{\text{sa}}$, $\varphi_{\text{mi}}$ and $n_{\text{eng}}$. At last, the measured air-fuel ratio $\lambda$ will only be used to validate the air content model with the test bench measurements.

The air path dynamics is modelled via the system states for the stored gas masses $\hat{m}_{\text{st}}$ and the air contents $\hat{x}_{\text{st}}$ in the volumes $V_{\text{st}}$. Generally, the estimated gas mass in each volume can be determined via the ideal gas law (3.8) from pressure, temperature and storage volume. Whereas the storage volume is given by the air path geometry and follows by the pipe volume fraction $\xi_{\text{p,st}}$ and Eq. (3.19) as the receiver volume. The pipe volume (3.18) contributes to the gas transport delay time $T_{\text{d,p},i}$, as given in (3.20). Setting the pipe volume fraction $\xi_{\text{p,st}}$ of all storages to zero results in the lumped parameter model. Next, the differential equation for the storage air content dynamics (3.17) can be rewritten with the consideration of the single transport delays $T_{\text{d,p},i}$ in each pipe element $i$ as

$$\frac{\mathrm{d}}{\mathrm{d}t} x_{\text{st}}(t) = \frac{1}{m_{\text{st}}(t)} \left[ \sum_{i=1}^{p} \left( x_i \left( t - T_{\text{d,p},i} \right) - x_{\text{st}}(t) \right) \dot{m}_{\text{in},i} \left( t - T_{\text{d,p},i} \right) \right], \qquad (4.10)$$

where both the inflowing mass flow rates $\dot{m}_{\text{in},i}$ and the inflowing air contents $x_{\text{in},i}$ are delayed by the gas propagation time. When the pipe receiver approach turns to the lumped parameter approach these gas propagation times become zero. Note that both the inflowing air contents and the inflowing mass flow rates have to be delayed by the same dead time $T_{\text{d,p},i}$, since the delay is modelled at receiver inflow, see Fig. 3.2. If the mass flow rate would not be delayed, an exemplary opening of the HP-EGR-valve would instantaneously change the air content of the intake manifold, instead being delayed by its gas propagation time through the HP-EGR-pipe. All considered dead times are shown in Fig. 4.9, in which an additional dead time $T_{\text{d,p},\lambda}$ considers the gas propagation time to the $\lambda$-sensor. A further dead time $T_{\text{d,eng}}$ is caused by the engine cycling time and considers the delay of the four stroke engine working cycle for both modelling approaches.

The single volumes $V_{\text{st}}$ interact via their air contents $x_{\text{st}}$ and the mass flow rates in the pipes. In this connection the cylinder is a driving force in the system and delivers the burnt air content $\hat{x}_{\text{eng,out}}$ (3.32) and the estimated mass flow rates entering $\hat{m}_{\text{eng,in}}$ (3.28) and exiting $\hat{m}_{\text{eng,out}}$ (3.30) the cylinders. As a further simplification the estimated exhaust temperature $\hat{T}_3$ is set equal to the temperature at engine exit $\hat{T}_{\text{eng,out}}$ (3.31). Then the HP-EGR mass flow rate can be determined from the measured quantities via the flow equation (3.22) as

$$\begin{aligned}
\hat{m}_{\text{hp}-\text{egr}} &= \min\left( \text{Eq.}(3.22), \text{Eq.}(4.12) \right) \\
&= \min\left( \left( (C_D A_{\text{ref}})_{\text{hp}-\text{egr}} \frac{p_{\text{in}}}{\sqrt{R T_{\text{in}}}} \sqrt{\frac{2\kappa}{\kappa-1} \left[ (\Pi)^{\frac{2}{\kappa}} - (\Pi)^{\frac{\kappa+1}{\kappa}} \right]} \right), \hat{m}_{\text{hp}-\text{egr,max}} \right)
\end{aligned} \qquad (4.11)$$

and is further limited by the maximal possible additional mass flow rate into the engine system by the intake system balance equation

$$\hat{m}_{hp-egr,max} = \hat{m}_{eng,in} + \frac{dp_{2i}}{dt}\left(\frac{V_{2c}}{T_{2ic}R} + \frac{V_{2i}}{\hat{T}_{2i}R}\right) - \dot{m}_{air}. \tag{4.12}$$

Besides the mass flow rates entering and exiting the system, also the dynamical gas storage via pressure changes in the intake manifold are considered according to Eq. (D.1). Further, the gas storage dynamics is dived into the two volumes $V_{2c}$ and $V_{2i}$ with their distinct temperatures $T_{2ic}$ and $\hat{T}_{2i}$. This limitation of $\hat{m}_{hp-egr}$ to the balance equation (4.12) is necessary, since there is a certain degree of measurement uncertainty in the estimated quantities and otherwise the later estimated $\hat{m}_{lp-egr}$ would tend to have negative values for some uncertainty distribution. Accordingly the LP-EGR mass flow rate can be determined with the balance equation

$$\hat{m}_{lp-egr} = \hat{m}_{eng,in} - \dot{m}_{air} - \hat{m}_{hp-egr} + \frac{dp_{2i}}{dt}\left(\frac{V_{2c}}{T_{2ic}R} + \frac{V_{2i}}{\hat{T}_{2i}R}\right). \tag{4.13}$$

Due to the limitation of $\hat{m}_{hp-egr}$ via (4.11) usually no negative LP-EGR mass flow rates (4.13) occur. However, when the engine is operated without any EGR it can happen that the measured value of $\dot{m}_{air}$ is greater than the estimated value of $\hat{m}_{eng,in}$. In this special case the estimated LP-EGR mass flow rate will become negative and the intake air content will reach values greater than 1. Contrary to the other publications in the field of air content models the truncation of the estimated HP-EGR mass flow rate and the possible air contents larger than one are the key to master the existing measurement uncertainties. It will be proven in Sect. 7.8.2, that these precautions lead to an stationary correct estimated $\hat{x}_3$ and a measurement uncertainty tolerant reference value generation for the air path control. Further, the estimated mass flow rate through the intake throttle valve

$$\hat{m}_{th} = \hat{m}_{eng,in} - \hat{m}_{hp-egr} + \frac{dp_{2i}}{dt}\frac{V_{2i}}{\hat{T}_{2i}R} \tag{4.14}$$

and the mass flow rate through the turbine

$$\hat{m}_{t} = \hat{m}_{eng,out} - \hat{m}_{hp-egr} \tag{4.15}$$

follow by means of balance equations. For the turbine mass flow rate the effect of gas storage can be neglected, since the exhaust manifold volume $V_3$ is rather small. The mass flow rates (4.11) and (4.14) as well as the measured temperature after the intercooler $T_{2ic}$ and the HP-EGR temperature $T_{hp-egr}$ allow a dynamical fast model of the intake gas temperature.

$$\hat{T}_{2i} = \frac{\hat{m}_{th}T_{2ic} + \hat{m}_{hp-egr}T_{hp-egr}}{\hat{m}_{th} + \hat{m}_{hp-egr}} \tag{4.16}$$

In contrast to a temperature measurement in the intake manifold, this model is less affected by the significant temperature sensor dynamics, since the major dynamics of the temperature $\hat{T}_{2i}$ is caused by the proportion of the dynamical fast estimated mass flow rates $\hat{m}_{th}$ and $\hat{m}_{hp-egr}$. Afterwards $\hat{T}_5$ at the end of the exhaust pipe is modelled in two steps. First a simplified polynomial model

$$\hat{T}_4 = w_{\hat{T}_3,0} + w_{\hat{T}_3,1}\hat{T}_3 + w_{p_3,1} p_3 \tag{4.17}$$

describes the temperature $\hat{T}_4$ after the turbocharger with the exhaust manifold temperature $\hat{T}_3$ and the exhaust pressure $p_3$ as model inputs. Then the exhaust pipe heat transfer model (3.23) and (3.27) models the temperature $\hat{T}_5$ from $\hat{T}_4$, $T_a$ and $\hat{m}_t$.

The stored gas mass in the exhaust pipe is modelled with the differential equation

$$\frac{d\hat{m}_5}{dt} = \hat{m}_t - \hat{m}_{lp-egr} - \hat{m}_{eth}, \tag{4.18}$$

in which $\hat{m}_t$ and $\hat{m}_{lp-egr}$ are given by (4.15) and (4.13). With the estimated gas mass $\hat{m}_5$ and $\hat{T}_5$ the pressure $\hat{p}_5$ can be estimated by the ideal gas law (3.8). Then the mass flow rate $\hat{m}_{eth}$ can be determined via the flow equation for compressible fluids (3.22).

Finally, the states in the combined volume $V_{1/2c}$ are determined. The estimated gas mass proportion, which is stored upstream the compressor is determined with the quantities $T_{2ic}$ and $p_{2i}$. The stored gas mass proportion downstream the compressor can be given by the estimated temperature $\hat{T}_1$ and the estimated pressure $\hat{p}_1$. $\hat{T}_1$ follows similar to (4.16) from ambient temperature, LP-EGR gas temperature $\hat{T}_{lp-egr}$ and corresponding mass flow rates. In which $\hat{T}_{lp-egr}$ is estimated via the LP-EGR cooler model (3.23) and (3.27). For the pressure $\hat{p}_1$ the flow equation for compressible fluids (3.22) cannot be easily solved. However, $s_{ith}$ should throttle the mass flow rate only moderate. Hence, the flow equation for incompressible fluids (3.21) is rearranged to estimate the intake pressure $\hat{p}_1$ as

$$\hat{p}_1 \approx p_a - \left(\frac{\dot{m}_{air}}{C_D A_{ref}}\right)^2 \frac{R T_a}{2 p_a} \quad \text{with} \quad C_D A_{ref} = f(s_{ith}). \tag{4.19}$$

After the air content has been modelled with a lumped parameter model and a pipe receiver model, these two models are validated with test bench measurements in Fig. 4.10. In the topmost plot the mass flow rates for the measured air mass flow rate $\dot{m}_{air}$ and the step excitation signals $\hat{m}_{hp-egr}$ and $\hat{m}_{lp-egr}$ are shown. During the operation without any EGR it can be seen, that the estimated LP-EGR mass flow rate (4.13) compensates some of the model and measurement uncertainties in $\hat{m}_{eng,in}$. At this time both the HP- and LP-EGR-valve are closed and the apparent value of $\hat{m}_{lp-egr}$ compensates these accumulated modelling uncertainties. This compensation ensures that the air content after the combustion process stationary corresponds to the value which would be reached with the currently measured air mass flow rate and injection quantity, see Sect. 7.8.2.
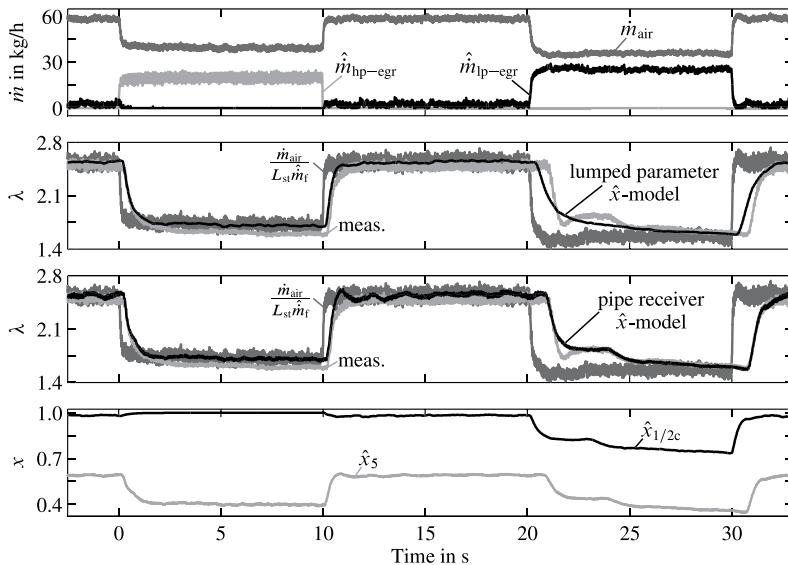
**Figure 4.10:** Model validation with HP- and LP-EGR step responses for two air content models with a lumped parameter and a pipe receiver modelling approach ($n_{\text{eng}} \approx 1000\,\text{min}^{-1}$, $u_{\text{inj}} = 16\,\text{mm}^3/\text{cyc}$)

In the next plot the system response is given by two estimates of the air-fuel ratio (3.11) and the measured air-fuel ratio $\lambda$ in the exhaust system, see Fig. 4.9. One estimate for the air fuel ratio is determined by (3.11) from the injection quantity and the measured air mass flow rate. The second estimate results from the air content model in lumped parameter form and is transformed to the air-fuel ratio via Eq. (3.13). The air-fuel ratio, which is based on the pure air mass flow rate measurement represents the effect of a classical air mass flow rate control scheme and hurries ahead of the real air content dynamics. For both steps in HP- and LP-EGR the measured air-fuel ratio is dynamically much slower than the $\dot{m}_{\text{air}}$ based one which is $\approx 0.3\,\text{s}$ ahead of the measured HP-EGR response and precedes the LP-EGR response for $\approx 1\,\text{s}$. Then the lumped parameter air content model is shown. It meets the intake and exhaust system dynamics much better and fits well for the HP-EGR step response and delivers satisfying results for the LP-EGR system response. During the LP-EGR response a distinctive dead time can be observed, which posses a further step in the $\lambda$-signal at a time between 21 s and 24 s. The simulation results for the lumped parameter $\hat{x}$-model average this measured dead time afflicted $\lambda$-signal with satisfying results.

Better validation results can be reached with the pipe and receiver model, which separates the air content dynamics into a transport delay pipe contribution and afterwards filters the signal in a subsequent receiver. The third plot shows the validation results for the pipe receiver $\hat{x}$-model. It

gets obvious, that this model fits both the HP- and the LP-EGR step response well and also models the λ-signal step between 21 s and 24 s.

This step is caused by the inherent dynamics in the intake and exhaust system and can be explained by the plotted air contents $\hat{x}_{1/2c}$ and $\hat{x}_5$ in the bottom plot. At an intake and exhaust system equilibrium with $\hat{x}_5 \approx 0.55$ and $\hat{x}_{1/2c} \approx 1$ the LP-EGR-valve is opened at a time of 20 s. Then exhaust gas $\hat{x}_5$ is recirculated into the intake system and lowers the intake system air content to $\hat{x}_{1/2c} \approx 0.85$. This changed air content first has to propagate through the whole intake system, is further lowered by the combustion process and has to pass the whole exhaust system until it further lowers $\hat{x}_5$. Then the recirculation loop through the intake and exhaust system begins again and stepwise lowers the air contents towards an equilibrium state. When the LP-EGR-valve is fully closed at a time of 30 s only the intake system needs to be flushed with fresh air and the stationary condition is reached after the intake gas propagation time is settled.

This inherent air content dynamics is existent in the whole engine operation range and can be observed in delay and step effects in the measured air-fuel ratio λ. For more measurements with these effects, which also contain their influence on the emission formation refer to Mrosek (2017).

In a nutshell the inherent dynamics of the air contents in the intake and exhaust system show a major difference between the HP-EGR and the LP-EGR system. These dynamics can be successfully modelled by a pipe receiver air content model, which also reflects the long dead times of more than 2.5 s and the step wise change in the air contents for step responses of LP-EGR. The dynamics for a pure HP-EGR configuration are in the range of 150 ms and can be neglected for standard engines. When it comes to combustion modes, which demand the dynamical precise control of large EGR-rates like homogeneous charge compression ignition (HCCI) or dual path EGR system where the gas propagation times become large, it is advisable to consider these dynamics in the air path control scheme.

Consequently the air content model and the related knowledge about the internal air content states will be incorporated in the reference value generation for the air path control in Sect. 7.8. Contrary to a reactive feedback control strategy of the air content in the intake or exhaust manifold this reference value generation will allow a preemptive intervention in the dead time system. Anymore, the pipe receiver air content model will be utilised for the simulation of the dynamical emissions in Sect. 5.4.

## 4.5   Summary

This chapter analyses the stationary and dynamical system properties of the dual path EGR system. In this multi-variable system the actuation of one single actuator results in system responses of many output quantities and process states. Besides the system responses of the classical HP-EGR system, there are novel interactions with the additional LP-EGR path. These effects and the engine operation point dependent process gains should be incorporated in an appropriate air path control structure to achieve a good quality of control.

A LP-EGR system can be achieved with an intake throttle valve and an exhaust throttle valve.  In both LP-EGR configurations the achieved LP-EGR-rate is fairly invariant to the engine operation point and mostly depends on the actuator position. This insight will later be incorporated to derive the LP-EGR control scheme.

Finally, the air content dynamics are a main difference between a LP-EGR system and a HP-EGR system. These dynamics can been modelled with a lumped parameter model and a pipe receiver model. Both models are capable to describe the dynamic characteristics of the process, whereas the more detailed pipe receiver model is more accurate in simulating the gas transport delays. Finally, the intake air content could be identified as controlled variable for the HP-EGR and LP-EGR air path.

# 5 Emission and Combustion Models

Stationary and dynamical models for the $NO_x$ and particulate emissions as well as the combustion quantities are given in this chapter. At first, sources of dynamics in the intake and exhaust system as well as emission measurement dynamics are highlighted. Stationary global-local emission and combustion models are introduced and finally extended to models for the dynamical emission formation.

Emission and combustion models are widely used in the engine development process and there exist a wide range of model classes, which differ in their complexity and their application for different tasks. Stiesch (2003) gives an overview of models with a high complexity, which model the combustion process by computational fluid dynamics, multi-zone or single-zone models. These models utilise chemical reaction kinetics or phenomenological models to describe the emission formation. Depending on the model complexity these models allow to simulate the *rate of heat release* and the emission formation for different injection patterns and combustion chamber geometries in spatial and temporal resolution before the engine physically exists. However, these models require a high modelling effort and they can be computationally demanding.

Besides these physically motivated models, experimental black-box models can be applied to model the emissions and the combustion characteristics. They usually demand less modelling effort and computational cost, but have to be trained with measurements from existing engines. Limitations in model extrapolation capabilities can demand a new model training whenever the engine configuration is modified. Therefore, black-box models are generally utilised quite late in the engine development process, but their universal approximation of complex chemical kinetics in the emission formation makes them a powerful instrument in the development phase. Especially in the stationary engine calibration process black-box emission and combustion models can be considered as state of the art, see Isermann (2010); Röpke et al. (2009).

In this chapter, black-box models are utilised to model the stationary and the dynamical emission formation as well as the engine torque. Modelled emission quantities are the $NO_x$ emissions $c_{nox}$ measured by a NGK $NO_x$ sensor and the particulate emissions $c_{mss}$, which are measured by a micro soot sensor. One objective of these models is to find a suitable control variable for the LP-EGR path. Furthermore, these models will be utilised to optimise the engine control in stationary and dynamical engine operation. In the following a comprehensive methodology to model the stationary and dynamical emission formation and the engine torque will be given. It is based upon several publications by Sequenz and Mrosek. At first, the process and measurement dynamics in the intake and exhaust system are investigated (Mrosek et al., 2010a). Based on an algorithm

for local polynomial regression and subset selection (Sequenz et al., 2009) a global-local[1] model structure is introduced and stationary global models for the emissions and the combustion process are given (Sequenz et al., 2010a,b). Finally, these combustion models are utilised to model the dynamical emission formation (Mrosek et al., 2010a).

The emission measurement dynamics are detailed investigated in   Mrosek et al. (2011b) and Mrosek (2017). In a nutshell these dynamics depend on engine speed, gas volume flow in the exhaust system and the sensor itself. The micro soot measurement shows a dead time $T_{d,tot,mss}$ between 2 s and 3.5 s and a first order lag with a time constant in the range of 0.8 s, while the $NO_x$ measurement posses a dead time $T_{d,tot,nox}$ between 0.25 s and 0.55 s and is second order filtered with time constants in the range of 0.2 s and 0.45 s. Finally, an extensive description of the innovative measurement design and preprocessing of measurement data is given in Mrosek (2017).

## 5.1   Intake and Exhaust System Dynamics

There are various sources for process and sensor dynamics, which affect the emission formation and the emission measurement in the intake and exhaust system (Mrosek et al., 2010a, 2011b). Regarding these continuous dynamics, the combustion process can be simplified as a batch process, in which the outcome of each combustion cycle is determined by the cylinder charge at intake valve closing and the injection characteristics. Furthermore, the combustion outcome can be influenced by the conditions in the cylinder, like the cylinder wall temperature. In order to achieve a good model quality, the emission model parameterisation demands a detailed investigation of sensor and process dynamics. Since the cylinder charge composition is important for the emission formation it needs to be determined without being corrupted by process or sensor dynamics. Consequently, Fig. 5.1 gives an overview of the different sources of process and sensor dynamics.

The fastest process dynamics are gas transport and mixing delays in the intake and the exhaust system, see Sect. 4.3. Then the turbocharger acceleration and the much slower heat storage dynamics of turbocharger housing, coolers, engine block and ducts influence the cylinder charge. These dynamics are additionally superimposed by significant measurement dynamics of temperature sensors in the intake and exhaust system, while pressures and mass flow rate can be measured without significant measurement dynamics (Mrosek et al., 2010b; Mrosek, 2017). In order to determine the cylinder charge dynamically correct, the states $x_{2i}$, $p_{2i}$ and $T_{2i}$ in the intake manifold are chosen, because these states contain the most relevant information about the gas in the combustion chamber. Note that in the following the air content $\hat{x}_{2i}$ is estimated by the pipe receiver air content model of Sect. 4.4 and the intake temperature $\hat{T}_{2i}$ is estimated by Eq. (4.16) to reduce the temperature sensor delay.

---

[1]In this context global-local stands for the interpolation of local models at a constant engine operation point ($n_{eng}$, $u_{inj}$) to describe the global engine behaviour by superimposing local models over the dimensions $n_{eng}$ and $u_{inj}$.
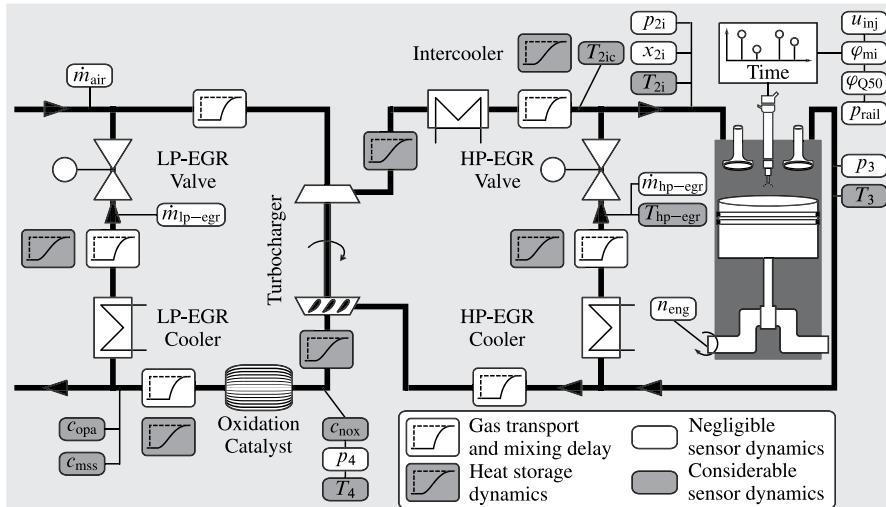
**Figure 5.1:** Process and measurement dynamics in the intake and exhaust system

Besides the cylinder charge also the injection characteristics influence the combustion and the emission formation. Quantities of the combustion characteristics are desired injection quantity $u_{inj}$, start of main injection $\varphi_{mi}$, pressure on the common rail injection system $p_{rail}$ and crank angle of 50 % mass fraction burned $\varphi_{Q50}$. These are discrete time quantities at each injection event and can be determined without any significant measurement dynamics. The engine speed $n_{eng}$ has also an influence on the emission formation can be measured dynamically fast.

All dynamics from the instant of emission formation to the moment of measurement are considered as measurement dynamics. These dynamics consist of engine cycling time, gas transport and mixing delay as well as sensor dynamics and are investigated in Mrosek et al. (2011b); Mrosek (2017).

## 5.2 Measurement Design

In order to eliminate process and measurement dynamics, a grid based fast stationary measurement with holding times of 15 s is carried out to generate data points for emission and combustion modelling. At fixed engine operation points in $n_{eng}$ and $u_{inj}$ the quantities $\dot{m}_{air}$, $p_{2i}$, $\varphi_{Q50}$ and $T_{2i}$ are closed-loop controlled[2] to reference values of a *full factorial design*. In this measurement design the data points are reduced to the feasible engine operation space, which is essentially

---

[2]In order to control the intake temperature, the desired air mass flow rate is transformed by Eq. (7.40) into a reference value for $\dot{m}_{hp-egr}$ and by Eq.(7.43) into a reference value for $\dot{m}_{lp-egr}$, see Sect. 7.8. The controllers for the air path quantities $p_{2i}$ and $\dot{m}_{hp-egr}$ are according to Sect. 7.3 decentralized PI(D)-controllers, while $\dot{m}_{lp-egr}$ is

determined by the mean-value engine model from Chap. 3. This closed-loop control results in faster settling air path quantities and consequently allows shorter holding times for each data point. A summer ($T_a = 22 \ldots 52°C$) and a winter ($T_a = 4 \ldots 16°C$) measurement delivered 4543 data points for model training and 2264 data points for model validation. In Mrosek (2017) a more detailed description of measurement design and data preprocessing is given.

## 5.3 Stationary Emission and Combustion Models

The emission formation is a highly nonlinear process and can either be modelled by chemical kinetic reactions and phenomenological laws (Stiesch, 2003) or by black-box models. Compared to the complex and computational demanding chemical and phenomenological models, the here applied black-box models are based on measured data and describe the unknown relations with a relatively small amount of process knowledge.

In several publications the $NO_x$ are modelled, but only a few publications show models for the particulate emissions. Schüler (2001) presents stationary LOLIMOT models for a stationary engine optimisation with the optimised quantities EGR actuator $u_{hp-egr}$, VGT-actuator $u_t$ control signals and $\varphi_{mi}$. Validation results of a $NO_x$ model and a fuel consumption model with the air path actuator control signals as model inputs are shown. Then the validation results of an opacity model and a HC model with air path quantities as model inputs are given. Furthermore, dynamical emission models are parameterised with step functions and holding times of 5-10 s. Hafner (2002) excites the engine with an *amplitude-modulated pseudo-random binary signal* (APRBS) with 500 input combinations and an average holding time of 7 s to obtain global stationary and dynamical $NO_x$, opacity and torque models. Stationary models with air path actuator control signals and the start of the injection as model inputs are trained. First the models are trained by stationary data points which are generated by averaging the dynamically excited measurements. Other stationary emission models are derived from the stationary process gain of identified dynamical models with external dynamics.

In Benz (2010) the $NO_x$ emission, the particulate emissions and the engine torque are modelled. The utilised model structure is based on a base map which describes the model outputs at stationary engine operation and multiplicative correction terms which model the deviations from these stationary conditions. Model inputs for the deviation model are gas system quantities and combustion characteristics. Appropriate low order input transformations are identified with a generic algorithm by a symbolic regression approach. Wenzel (2006) presents models based on a power series with multiplicative and exponential coefficients for the filter smoke number and the $NO_x$ emissions. The utilised model inputs are mainly based on characteristic values from the rate of heat release. Since these model inputs are hard to excite, a D-optimal measurement design with 200 data points for model training and 28 data points for model validation is generated with a candidate set of air path quantities and injection quantities.

---

controlled by a semi-physical controller as described in Sect. 7.7. A cylinder-individual closed-loop control controls the location of mass fraction burned 50 %, see Kohlhase (2011).

### 5.3.1 Suitable Model Inputs and Outputs

The task of the emission and combustion model restricts the set of feasible model inputs, the model dimensionality and the modelled quantity. In this dissertation models for simulation of measured quantities and models to optimise reference values for the air path control are considered.

Models for simulation of measured quantities are relatively unrestricted to type and number of utilised model inputs and the chosen model inputs can freely vary for each modelled quantity. On the other hand models for an engine optimisation have to be restricted to adjustable model inputs and engine states. These model inputs have to correspond to the sum of manipulatable variables and the number of quantities describing the engine state, e.g. engine speed and injection quantity for the engine state and air mass flow rate and charging pressure for the manipulated variables. An exemplary reference value optimisation for a control of $\dot{m}_{air}$ and $p_{2i}$ can utilise only these two manipulate variables as model inputs, even if better models can be achieved by considering more influences with a higher model complexity.

After considering the model inputs, also suitable model outputs have to be chosen, since the quantities of the emission measurement and the legislative standards for engine approval can differ. Statutory provisions for driving cycles can be defined as g/km, g/s, g/kWh, while the sensors deliver usually an emission concentration in the exhaust gas. These concentrations can be measured as volume fraction like parts per million, or as mass per volume like kg/m$^3$. A volume fraction for the emission component $x$ can be transformed by the ratio of molar masses and the exhaust gas mass flow rate into the single emission component's mass flow rate by

$$\dot{m}_x = c_x 10^{-6} \frac{M_x}{M_{exh}} \dot{m}_{exh}. \tag{5.1}$$

| | | | |
|---|---|---|---|
| $\dot{m}_x$ | emission component mass flow rate | in | kg/s |
| $c_x$ | emission component in volume fraction | in | ppm |
| $M_x$ | molar mass emission component | in | g/mol |
| $M_{exh}$ | molar mass exhaust gas | in | g/mol |
| $\dot{m}_{exh}$ | exhaust gas mass flow rate | in | kg/s |

Commonly the emission components $NO_x$, carbon monoxide and the hydrocarbons are measured in parts per million or a similar volume fraction. The molar mass of the exhaust gas can be simplified to the molar mass of air (28.96 g/mol) (Sequenz et al., 2011b). The molar mass of $NO_x$ is given as $NO_2$ equivalent (46.01 g/mol) for the European emission limits (European Commission, 2007). Other emission components like the particulate concentration of the micro soot sensor are measured as mass per volume. In this case the gas density at the measurement cell is the determining factor to transform the measured concentration into a mass flow rate. The emission mass flow rate can be derived from the mass per volume measurement by

$$\dot{m}_x = c_x \frac{\dot{m}_{\text{exh}}}{\rho_{\text{meas}}} \tag{5.2}$$

| | | | |
|---|---|---|---|
| $\dot{m}_x$ | emission component mass flow rate | in | kg/s |
| $c_x$ | emission component in mass per volume | in | kg/m$^3$ |
| $\rho_{\text{meas}}$ | exhaust gas density at the measuring cell | in | kg/m$^3$ |
| $\dot{m}_{\text{exh}}$ | exhaust gas mass flow rate | in | kg/s |

As the emission models shall be used for the simulation of the emission formation, the emissions should be modelled in the same quantity as they are measured. For optimisation purpose the favoured model output is an emission mass flow rate. After the modelling approach is presented in the following, the utilised model in- and outputs for the emission and combustion models are motivated in Sect. 5.3.4.

### 5.3.2 Global-Local Polynomial Model Approach

All following stationary quantities are modelled with a global-local polynomial approach (Sequenz et al., 2010b; Sequenz, 2013), which is summarised in the following. In this approach a global model output is superimposed of several local polynomial models (LPMs). Local engine operation points are defined by the engine speed $n_{\text{eng}}$ and the desired injection quantity $u_{\text{inj}}$. At these operation points *local* polynomial models are trained and composed to a *global* model by means of a bilinear interpolation. This model structure is motivated by the working principle of common ECUs, where control parameters and reference values are generally stored in grid map structures. Inputs for the grid map structures are often defined by the engine operation point and the output is derived as a bilinear interpolation between the grid points.
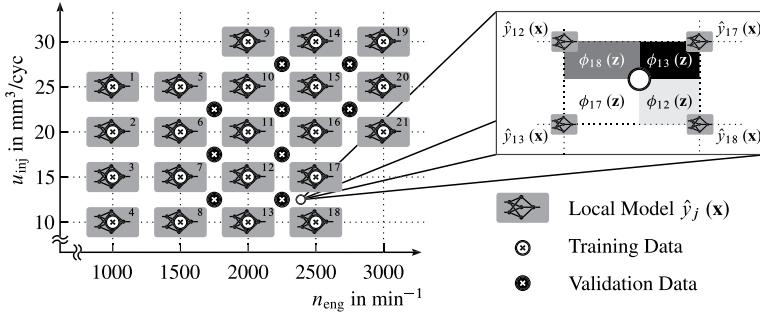


**Figure 5.2:** Global-local model structure with bilinear interpolation between the local models

Fig. 5.2 illustrates the global-local model structure with bilinear interpolation. The local polynomial models are located in the $n_{\text{eng}}$/ $u_{\text{inj}}$ plane. The training data is centred at each local polynomial

model and the placement of the validation data has been chosen with a maximal distance to the local models. A bilinear interpolation between the $j$ local model outputs $\hat{y}_j(\mathbf{x})$ results in the global model output $\hat{y}$. The model input is divided into the *x-regressors* $\mathbf{x}$ and the *z-regressors* $\mathbf{z}$. The z-regressors are defined by the engine operation point $\mathbf{z} = \left(n_{\text{eng}}\, u_{\text{inj}}\right)$ and determine the validity $\phi_j(\mathbf{z})$ for each local model. The x-regressors contain the local model inputs, e.g. $\mathbf{x} = \left(\hat{x}_{2i}\ p_{2i}\ \hat{T}_{2i}\ \varphi_{Q50}\right)$. Thus, the stationary global model is a weighted summation of the $M$ local polynomial models and is given as

$$\hat{y}(\mathbf{z}, \mathbf{x}) = \sum_{j=1}^{M} \phi_j(\mathbf{z})\, \hat{y}_j(\mathbf{x}). \tag{5.3}$$

The local model $\hat{y}_j(\cdot)$ is a polynomial in $\mathbf{x}$ with dimension $p$ and the regressors of these local models are derived by a Taylor series up to order three, which means that the sum of exponents in each regressor is limited to a maximum of three.

$$\hat{y}_j(\mathbf{x}) = w_{0,j} + w_{1,j}x_1 + w_{2,j}x_1^2 + w_{3,j}x_1x_2 + w_{4,j}x_2^2 + w_{5,j}x_1x_2^2 + \ldots + w_{(|\mathcal{A}|-1),j}x_p^3 \tag{5.4}$$

Cross terms are limited to a maximum of two inputs $\left(x_1x_2, x_1x_2^2, \ldots\right)$. Then the feasible set of regressors $\mathcal{A}$ for a four dimensional local model has 31 potential regressors.

$$\mathcal{A} = \{1, x_1, x_1^2, x_1x_2, x_2^2, x_1x_2^2, \ldots, x_4^3\} \qquad |\mathcal{A}| = 31 \tag{5.5}$$

The significant regressors from that set are selected by an algorithm composed of forward selection, backward selection and replacement of regressors, see Sequenz (2013). [3] The weights for the local models are calculated by a normalised pyramidal validity function

$$\mu_j(\mathbf{z}) = \prod_{i=1}^{n_z} \left(1 - \frac{\Delta z_i}{d_{j,i}}\right) \tag{5.6}$$
$$\text{with } \Delta z_i = \min\left(|z_i - z_{0,j,i}|, d_{j,i}\right)$$

and are normalised to unit sum

$$\phi_j(\mathbf{z}) = \frac{\mu_j(\mathbf{z})}{\sum_{j=1}^{M} \mu_j(\mathbf{z})}. \tag{5.7}$$

---

[3] Note that the number of chosen regressors depends on the training data distribution and differs for each modelled quantity and each local model. An overview about the total number of regressors for the emission and combustion models can be found in Appx. E.

In which $d_{j,i}$ is the width and $z_{0,j,i}$ is the centre coordinate of the $j$-th local model in the $z_i$-th dimension. $n_z$ is the number of z-regressors. For equidistant operation points this weighting can be interpreted as a bilinear interpolation of the local models. Note that the training data has not necessarily to be centred in local models, since the weighting functions (5.7) determine the membership to each local model. With this membership the local model regressors can be determined as the weighted least squares solution, see Sequenz (2013). Anymore, due to the bilinear interpolation between the models in the $n_{eng}/u_{inj}$ plane, no more than four local polynomial models have to be evaluated at once to obtain the global model output.

Fig. 5.3a) shows the network structure of the static global-local model structure. The z-regressors $n_{eng}$ and $u_{inj}$ determine the validity of the local polynomial models with a pyramidal weighting function. Polynomial models with the x-regressors as local model inputs derive the local models' outputs. In this example, the x-regressors are given as $\mathbf{x} = \begin{pmatrix} \hat{x}_{2i} & p_{2i} & \hat{T}_{2i} & \varphi_{Q50} \end{pmatrix}$. Then the global model output $\hat{y}$ results from the superposition of the weighted local models $\phi_j \hat{y}_j$. In this example three global-local models for the quantities $\hat{c}_{nox}$, $\hat{c}_{mss}$ and $\hat{M}_{eng}$ are shown. In comparison to the well established LOLIMOT modelling approach, the novel modelling approach increases the model complexity with local polynomials and it can reach a comparable model quality with less parameters (Sequenz, 2013). This is especially advantageous for emission and combustion models, where a stationary measurement is recommended and the number of data points for model training is limited to a low quantity.
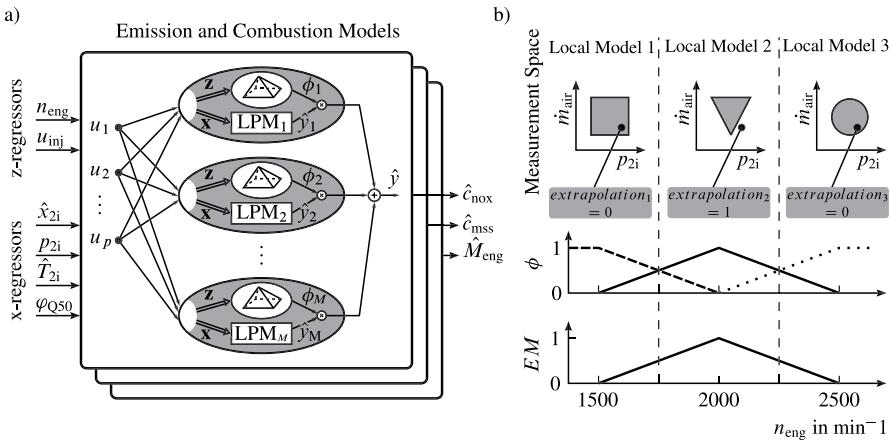


**Figure 5.3:** a) Network structure of the static global-local model structure with $M$ local polynomial models, $p$ model inputs divided into z-regressors and x-regressors and a pyramidal weighting function. b) Exemplary extrapolation measure estimation for a bilinear interpolation between three polynomial models with only $n_{eng}$ as z-regressor and the local x-regressors $\dot{m}_{air}$ and $p_{2i}$.

### 5.3.3  Extrapolation Measure

Black-box models like neural networks, characteristic maps, support vector machines and polynomials can model the training space well, but generally show poor model extrapolation capabilities outside the training area. Especially high order polynomial models tend to plus and minus infinity if the model input leaves the model training space. Therefore, measures shall be taken to avoid this undesired model behaviour. The output of each local polynomial model is bounded between the maximal and minimal output value in the training data. Furthermore, the model input is limited to the *minimum bounding box* of the training data. This input constraint is widened for 10 % to allow some model extrapolation.

These input and output limitations are an easy to implement and a computationally fast to calculate measure to avoid model extrapolation. However the feasible model input space shape differs considerably from the minimum bounding box. Especially for a model based engine optimisation, a more detailed knowledge of the feasible model input space is necessary to limit the optimiser to physical reachable quantities. Otherwise offline optimised reference values may not be reachable at the engine test bench if they are outside the drivability space. Hence, an extrapolation measure is introduced in the following (Mrosek et al., 2010a; Sequenz et al., 2010b).

A *convex hull* determines the training space for each local polynomial model and it is stored with the model. Thus, it can be tested whether a local data point $\mathbf{x}$ is within the $j$th local hull ($extrapolation_j = 0$) or outside the local convex hull ($extrapolation_j = 1$). Consequently, the global extrapolation measure $EM$ of a data point for all $M$ local models follows as

$$EM(\mathbf{z}) = \sum_{j=1}^{M} extrapolation_j(\mathbf{x}) \, \phi_j(\mathbf{z}), \qquad (5.8)$$

with $\phi_j(\mathbf{z})$ being the membership function for the local model $j$. The calculation of the extrapolation measure is clarified in Fig. 5.3b).[4] Three exemplary convex hulls at $n_{\text{eng}} = 1500\,\text{min}^{-1}$, $n_{\text{eng}} = 2000\,\text{min}^{-1}$ and $n_{\text{eng}} = 2500\,\text{min}^{-1}$ are shown. These hulls surround the training space in the input dimensions $\dot{m}_{\text{air}}$ and $p_{2\text{i}}$. An extrapolation for the data point can be observed at the local model 2. For the other two models there is no extrapolation, since these data points are within the local convex hulls. Further the membership functions for the three local models and the global extrapolation measure $EM$ are shown. There is no extrapolation for engines speeds below $1500\,\text{min}^{-1}$ and above $2500\,\text{min}^{-1}$. In case the validity of local model 2 rises, the extrapolation measure rises concurrently with its maximum at $n_{\text{eng}} = 2000\,\text{min}^{-1}$. At this point the model is in pure extrapolation.

This model extrapolation measure will be later utilised to indicate the model confidence region for models of the dynamical emissions in Sect. 5.4. Anymore, in Sect. 6.1 the possible parameter space for a stationary reference value optimisation is restricted by the extrapolation measure.

---

[4]As a simplification the $\mathbf{z}$-regressor consists only of $n_{\text{eng}}$, while the $\mathbf{x}$-regressor has the inputs $\dot{m}_{\text{air}}$ and $p_{2\text{i}}$.

### 5.3.4 Model Results

In the global-local model structure the engine operation point in $n_{eng}$ and $u_{inj}$ determines the validity of each local model to superimpose the local model outputs to the global model output. The local model inputs describe the cylinder charge and the combustion characteristics. One important variable to describe the combustion is a measure for the oxygen concentration or the oxygen mass. This could be the air mass flow rate $\dot{m}_{air}$, the estimated air content in the intake manifold $\hat{x}_{2i}$ or the estimated air content after the combustion $\hat{x}_{eng,out}$, see Sect. 4.4.

The air contents are dynamically advantageous, since they implicitly include the gas propagation times in the intake and exhaust system, see Sect. 4.4. On the other hand, the air mass flow rate can be directly measured and it is free from modelling errors. Besides an information about the oxygen mass or concentration, the cylinder charge is determined with (3.28) by the charge-air pressure $p_{2i}$ and the estimated intake temperature $\hat{T}_{2i}$. Alternatively to $\hat{T}_{2i}$ the cylinder charge can be described with the total EGR-rate

$$r_{egr} = \frac{\dot{m}_{hp-egr} + \dot{m}_{lp-egr}}{\dot{m}_{hp-egr} + \dot{m}_{lp-egr} + \dot{m}_{air}} \qquad (5.9)$$

as an additional model input, since it implicitly includes the mass flow rate entering the engine in stationary conditions

$$\dot{m}_{eng,in} = \dot{m}_{hp-egr} + \dot{m}_{lp-egr} + \dot{m}_{air}. \qquad (5.10)$$

Other potential variables like the fraction of HP-EGR to the total EGR mass flow rate

$$\chi_{hp-egr} = \frac{\dot{m}_{hp-egr}}{\dot{m}_{hp-egr} + \dot{m}_{lp-egr}} \qquad (5.11)$$

or the fraction $\dot{m}_{hp-egr}/\dot{m}_{lp-egr}$ are not suitable as model inputs, since they become singular at engine operation points without EGR. Additionally to the states in the intake system, the start of the main injection $\varphi_{mi}$ and the MFB50 $\varphi_{Q50}$ are considered as local model inputs to describe the combustion characteristics.

The possible local model inputs shall model the local nonlinearities in different emission and combustion quantities and shall further be capable to model the global engine behaviour. In Sequenz et al. (2010a) suitable model inputs are investigated for global emission models and it is shown that suitable model inputs for local emission models do not necessarily give good validation results for global validation data. Especially the air mass flow rate $\dot{m}_{air}$ in kg/s is disadvantageous compared to the air mass per working cycle $m_{air}$ in mg/cyc. In comparison to $\dot{m}_{air}$ the air mass flow rate working cycle is more independent of $n_{eng}$ since it describes the cylinder charge. Further investigations in Sequenz et al. (2011a) show that the model input $\hat{x}_{eng,out}$ is advantageous for model regularisation of the particulate emission models and it allows to predict the

particulate validation dataset more accurate. Additionally to $\dot{m}_{air}$ the model input $\hat{x}_{eng,out}$ also contains information about the remaining oxygen concentration after the combustion and it implicitly considers the injection quantity. This information improves the global model validation in the $u_{inj}$ direction. Thus, the set of investigated local inputs $x_i$ for the local polynomial models with four inputs $x_1 \dots x_4$ is given as

$$\mathbf{x} = [x_1, x_2, x_3, x_4] \qquad \text{with}$$
$$x_1 \in \{m_{air}, \hat{x}_{2i}, \hat{x}_{eng,out}\} \qquad x_2 \in \{p_{2i}\} \qquad x_3 \in \{\hat{T}_{2i}, r_{egr}\} \qquad x_4 \in \{\varphi_{mi}, \varphi_{Q50}\}. \tag{5.12}$$

Models for a stationary engine optimisation are given for the emission mass flow rates $\dot{m}_{mss}$ and $\dot{m}_{nox}$ as well as the engine torque $M_{eng}$. For simulation purposes the measured particulate and $NO_x$ concentrations $c_{mss}$ and $c_{nox}$ are modelled. Furthermore, the global-local modelling approach is applied to the combustion characteristics $p_{mi,lp}$, $p_{mi,hp}$, $\varphi_{Q50}$ and $\varphi_{mi}$. In which $p_{mi,lp}$ is the mean indicated pressure of the charge cycle loop and $p_{mi,hp}$ is the mean indicated pressure of the power stroke.

The particulate emissions $c_{mss}$ and $\dot{m}_{mss}$ rise extremely steep when a critical cylinder charge is reached. Therefore Sequenz et al. (2010a) present a logarithmic output transformation for the measured particulate emissions $y_{mss}$

$$y_{mss}^* = ln\,(y_{mss} + 0.5) \qquad y_{mss} \in \{\dot{m}_{mss}, c_{mss}\}. \tag{5.13}$$

A subsequent local polynomial modelling of $y_{mss}^*$ enhances the model quality especially for low particulate emissions and it is used for the following particulate models.

Tab. 5.1 shows the model qualities for stationary emission and combustion models for simulation and engine optimisation tasks with the best suitable model inputs. The first three rows show the model qualities for simulation purposes, for which the emissions are modelled as concentrations. Then models for the engine optimisation are shown, where the emissions are modelled as emission mass flow rates. These models either use the air mass flow rate or the air content $\hat{x}_{eng,out}$ as model input, depending which of those leads to better model qualities. For every modelled quantity $y$ the chosen x-regressors are displayed. The model quality is evaluated by the coefficient of determination $R^2$ and the root mean square error (RMSE). These quality criteria are given for the training dataset ($R^2_{train}$, $RMSE_{train}$), for a 10-fold cross-validation on the local training data ($R^2_{cval}$, $RMSE_{cval}$) and for a global validation with the validation dataset ($R^2_{val}$, $RMSE_{val}$).

The cross-validation denotes the prediction quality of local models, while the global engine behaviour is reflected by global model validation. Generally, the quality of the local model validation is in the same range as the model training, while the global model validation throughout shows a decrease in the achievable model quality. The $NO_x$ emissions and the engine torque can be modelled with a high model quality, while the qualities of the particulate models are worse. In comparison to the $NO_x$ emissions, it is well known that the particulate emissions are hard to model, see e.g. Benz (2010). If the measured model input $\varphi_{Q50}$ is replaced by the control signal $\varphi_{mi}$, the model quality

**Table 5.1:** Emission and combustion model quality of the chosen models for simulation and engine optimisation purpose

| $\hat{y}$ | x-regressors | | | | training | | local validation | | global validation | |
|---|---|---|---|---|---|---|---|---|---|---|
| | $x_1$ | $x_2$ | $x_3$ | $x_4$ | $R^2_{\text{train}}$ | $\text{RMSE}_{\text{train}}$ | $R^2_{\text{cval}}$ | $\text{RMSE}_{\text{cval}}$ | $R^2_{\text{val}}$ | $\text{RMSE}_{\text{val}}$ |
| model structure for simulation | | | | | | | | | | |
| $c_{\text{nox}}$ | $\hat{x}_{2\text{i}}$ | $p_{2\text{i}}$ | $\hat{T}_{2\text{i}}$ | $\varphi_{\text{Q50}}$ | 0.992 | 23.1 ppm | 0.991 | 24.8 ppm | 0.978 | 35.8 ppm |
| $c_{\text{mss}}$ | $\hat{x}_{\text{eng,out}}$ | $p_{2\text{i}}$ | $\hat{T}_{2\text{i}}$ | $\varphi_{\text{Q50}}$ | 0.949 | 2.49 mg/m³ | 0.945 | 2.67 mg/m³ | 0.912 | 1.77 mg/m³ |
| $M_{\text{eng}}$ | $\hat{x}_{2\text{i}}$ | $p_{2\text{i}}$ | $\hat{T}_{2\text{i}}$ | $\varphi_{\text{Q50}}$ | 0.997 | 1.51 Nm | 0.997 | 1.55 Nm | 0.978 | 3.05 Nm |
| model structure for optimisation | | | | | | | | | | |
| $\dot{m}_{\text{nox}}$ | $m_{\text{air}}$ | $p_{2\text{i}}$ | $\hat{T}_{2\text{i}}$ | $\varphi_{\text{Q50}}$ | 0.996 | 1.49 mg/s | 0.995 | 1.59 mg/s | 0.987 | 2.21 mg/s |
| $\dot{m}_{\text{mss}}$ | $\hat{x}_{\text{eng,out}}$ | $p_{2\text{i}}$ | $\hat{T}_{2\text{i}}$ | $\varphi_{\text{Q50}}$ | 0.968 | 1.85 µg/s | 0.960 | 2.29 µg/s | 0.902 | 1.59 µg/s |
| $M_{\text{eng}}$ | $m_{\text{air}}$ | $p_{2\text{i}}$ | $\hat{T}_{2\text{i}}$ | $\varphi_{\text{Q50}}$ | 0.997 | 1.47 Nm | 0.997 | 1.52 Nm | 0.979 | 2.94 Nm |

of most quantities gets slightly worse, see Sect. E. However, at test benches applied for engine optimisation, an indicating system measurement of $\varphi_{\text{Q50}}$ is usually existent. Therefore $\varphi_{\text{Q50}}$ is a suitable model input. For the interested reader a full overview about the reachable model qualities with various model inputs is given in Appx. E. Furthermore, the model qualities of the stationary combustion characteristics $p_{\text{mi,hp}}$, $p_{\text{mi,lp}}$, $\varphi_{\text{Q50}}$ and $\varphi_{\text{mi}}$ are given in Appx. E.

Fig. 5.4 visualises the achieved model qualities of the models with simulation purpose ($c_{\text{nox}}$, $c_{\text{mss}}$, $M_{\text{eng}}$ [5]) in the measured versus predicted plot with training and validation data. Also the distribution of the training and the validation error is shown for each modelled quantity. In Fig. 5.4a) the $c_{\text{nox}}$ data have similar distributed training and validation errors. The validation data shows some outliers at $c_{\text{nox}}$ emissions near to zero, which might be due to model extrapolation. The error distribution in Fig. 5.4b) has the shape of a normal distribution. Especially for high emissions in the training and the validation data, the model for the $c_{\text{mss}}$ emissions scatters. However, Fig. 5.4d) exhibits that many data points have an error close to zero and only a few data points deteriorate the model quality. This behaviour reflects the high nonlinearity of the particulate emissions. Finally, the engine torque model quality is shown in Fig. 5.4e) and f). The training data is met well, but there are some model inaccuracies in the validation data above 105 Nm. This inaccuracy in the validation data can also be seen as an asymmetry in the error distribution shown in Fig. 5.4f). A similar illustration with measured versus predicted plots and error distribution of the models for engine optimisation can be found in Appx. E.

---

[5] $\hat{M}_{\text{eng}} = f(n_{\text{eng}}, u_{\text{inj}}, \hat{x}_{2\text{i}}, p_{2\text{i}}, \hat{T}_{2\text{i}}, \varphi_{\text{Q50}})$
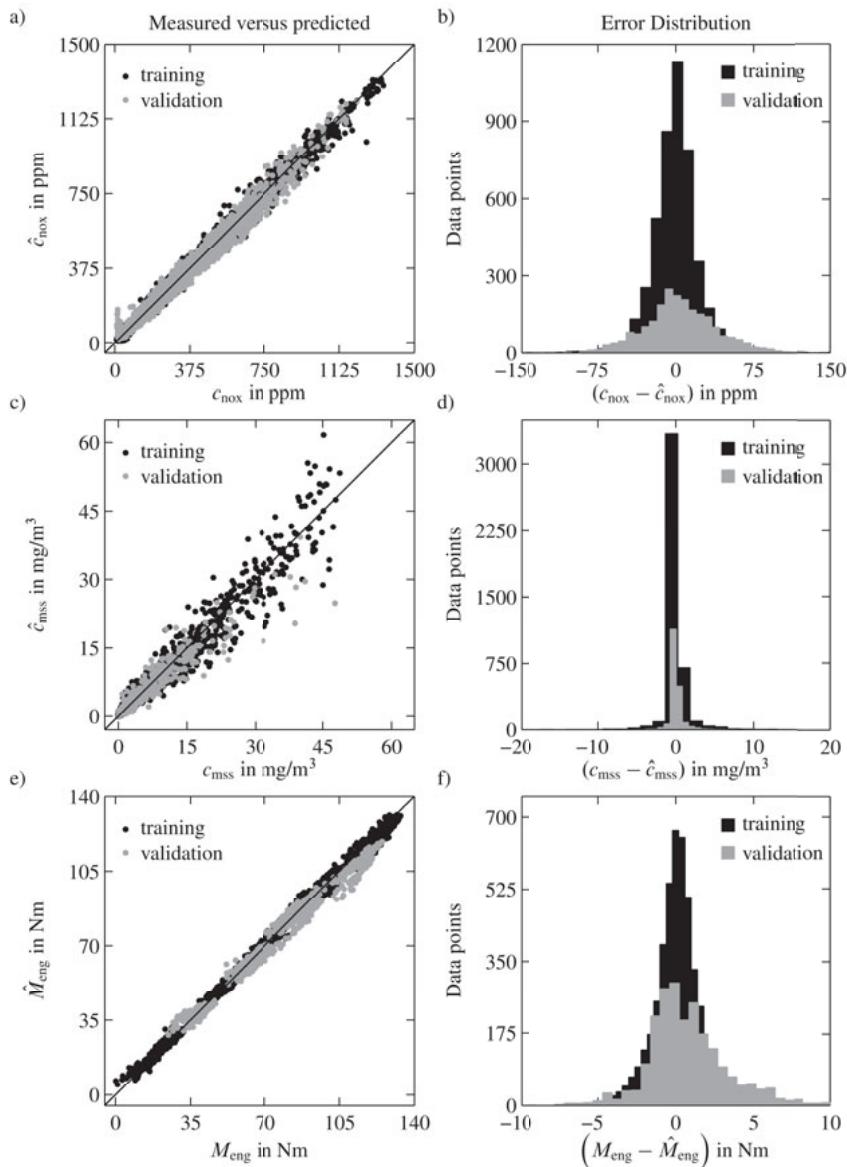
**Figure 5.4:** Measured versus predicted plots and error distributions for the modelled quantities $c_{\mathrm{nox}}$, $c_{\mathrm{mss}}$ and $M_{\mathrm{eng}}$. $\hat{c}_{\mathrm{nox}} = f(n_{\mathrm{eng}}, u_{\mathrm{inj}}, \hat{x}_{2i}, p_{2i}, \varphi_{Q50}, \hat{T}_{2i})$; $\hat{c}_{\mathrm{mss}} = f(n_{\mathrm{eng}}, u_{\mathrm{inj}}, \hat{x}_{\mathrm{eng,out}}, p_{2i}, \varphi_{Q50}, \hat{T}_{2i})$; $\hat{M}_{\mathrm{eng}} = f(n_{\mathrm{eng}}, u_{\mathrm{inj}}, \hat{x}_{2i}, p_{2i}, \varphi_{Q50}, \hat{T}_{2i})$

In summary, the global-local modelling approach is capable to model the emission and combustion quantities well. Two different sets of models for simulation and engine optimisation purpose are given in Tab. 5.1 and will be utilised in the following. All quantities and especially the demanding particulate emissions can be modelled satisfactorily. In contrast to a professional industrial test bench environment, the assessment of the model quality has to consider the side conditions at the engine test bench. The engine test bench at the institute of automatic control is not conditioned and it is directly ventilated with the ambient air. That implies that the measurements are taken at largely differing ambient pressures, ambient temperatures and humidity. Especially the measurements at summer and winter time, during dry periods and rainy days show a great variance in the side conditions. Furthermore, the fuel quality and temperature differ between summer and winter measurement, see DIN EN 590 (2010).

One remaining issue is to choose either $r_{egr}$ or $\hat{T}_{2i}$ as an additional control variable for the LP-EGR system. The models in Tab. 5.1 show that the estimated intake temperature is a suitable model input to model the engine emissions and the combustion characteristics. The choice of this model input is mainly motivated by the summarised model qualities for the particulate emissions in Tab. 5.2.

With regard to the training data there is no significant difference between the two possible model inputs $r_{egr}$ and $\hat{T}_{2i}$. In contrast the model input $\hat{T}_{2i}$ shows a large improvement in the model quality for the model validation. For the other modelled quantities in Sect. E there is no significant difference whether $r_{egr}$ or $\hat{T}_{2i}$ is chosen as a model input. Due to the better model validation results in the particulate emissions, $\hat{T}_{2i}$ is selected as an additional control variable for the LP-EGR system. Furthermore, the quantity $r_{egr}$ cannot consider the dynamical effects of gas propagation in the intake and exhaust system and it is therefore not suitable as controlled variable for an LP-EGR air path, see Sect. 4.3.

**Table 5.2:** Comparison of the potential model inputs $\hat{T}_{2i}$ and $r_{egr}$

| | x-regressors | | | | | | | |
|---|---|---|---|---|---|---|---|---|
| $\hat{y}$ | $x_1$ | $x_2$ | $x_3$ | $x_4$ | $R^2_{train}$ | RMSE$_{train}$ in mg/s | $R^2_{val}$ | RMSE$_{val}$ in mg/s |
| $c_{mss}$ | $x_{eng,out}$ | $p_{2i}$ | $\varphi_{Q50}$ | $\hat{T}_{2i}$ | 0.94958 | 2.4873 | 0.91239 | 1.7652 |
| $c_{mss}$ | $x_{eng,out}$ | $p_{2i}$ | $\varphi_{Q50}$ | $r_{egr}$ | 0.95477 | 2.2311 | 0.78939 | 4.2434 |
| $\dot{m}_{mss}$ | $x_{eng,out}$ | $p_{2i}$ | $\varphi_{Q50}$ | $\hat{T}_{2i}$ | 0.96809 | 0.0018544 | 0.90223 | 0.0015898 |
| $\dot{m}_{mss}$ | $x_{eng,out}$ | $p_{2i}$ | $\varphi_{Q50}$ | $r_{egr}$ | 0.96275 | 0.0021646 | 0.85322 | 0.0023867 |

### 5.3.5 Intersection Plots of the Emission Model

In order to get a deeper insight into the emission formation, Fig. 5.5 depicts the influence of the different local model inputs to the modelled particulate $\hat{c}_{mss}$ and $NO_x$ concentrations $\hat{c}_{nox}$. In each plot the quantity of the abscissa and either the air mass flow rate or the charge-air pressure are varied within the feasible limits denoted by the extrapolation measure (5.8). The intersection lines of the corresponding $\dot{m}_{air}$ and $p_{2i}$ quantities are given in the left box below the plot, while the other quantities are kept constant as denoted in the right box with the side conditions. For a better understanding and as a reference to previously shown plots, the air mass flow rate instead of the intake air content is applied as model input.
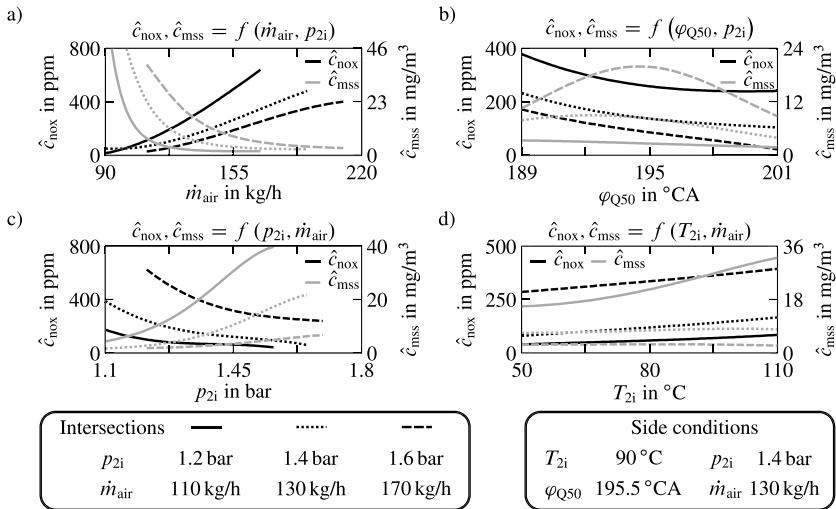


**Figure 5.5:** Simulated $\hat{c}_{nox}$ and $\hat{c}_{mss}$ intersection plots with the model input quantities $\dot{m}_{air}$, $\varphi_{Q50}$, $p_{2i}$ and $T_{2i}$ at $n_{eng} = 2500\,min^{-1}$ and $u_{inj} = 20\,mm^3/cyc$

In Fig. 5.5a) the dependency of the emissions to $\dot{m}_{air}$ is shown at three different values of $p_{2i}$. This plot reveals the trade-off between soot and $NO_x$ with changes in the air mass flow rate and the charging pressure, whereas a decrease in one emission quantity usually results in the increase of the other one. The $NO_x$ emissions are lowered almost linear with a lowered quantity $\dot{m}_{air}$, while there is a strong nonlinear increase in $\hat{c}_{mss}$ for low air mass flow rates. At a fixed value of $\dot{m}_{air}$ the $NO_x$ emissions decrease with a rising charge-air pressure, while the particulate emissions rise. This enlarged charging pressure increases the gas mass in the cylinder and results in more recirculated exhaust gas. Consequently, the local oxygen concentration within the combustion chamber drops. On the one hand this lowered oxygen concentration results in a rise of the particulate emissions, on the other hand the $NO_x$ emissions are decreased. The strong increase of $\hat{c}_{mss}$ for low air mass flow rates at $p_{2i} = 1.2\,bar$ is a key problem of the particulate emission modelling. At this critical point,

small deviations in $\dot{m}_{air}$ lead to a tremendous increase of the particulate emissions. Especially at these critical points even small deviations of EGR-distributions or injection quantities between the single cylinders can lead to great deviations in the particulate emissions and make the particulate modelling a demanding task.

Fig. 5.5b) highlights the dependency of the single emission components on $\varphi_{Q50}$ and $p_{2i}$, all other quantities are kept constant. The $NO_x$ emissions increase with $\varphi_{Q50}$ moving in direction to the top dead centre (180 °CA), while the particulate emissions show a maximum around a $\varphi_{Q50}$ of 195 °CA and they tend to be lower with late $\varphi_{Q50}$. However, a combustion process with a late $\varphi_{Q50}$ where both emission components are simultaneously lowered is not of practical relevance since also the generated torque strongly decreases. These influences on the generated torque will be subject of the next investigations in Fig. 5.6. Finally, $\hat{c}_{nox}$ also falls with a rising charge-air pressure, while $\hat{c}_{mss}$ rises.

The results in Fig. 5.5c) are comparable with Fig. 5.5a). The charge-air pressure is varied continuously while three intersections at different air mass flow rates of 110 kg/h, 130 kg/h and 170 kg/h are shown. Fig. 5.5d) reveals the influence of the intake temperature to the emissions at three different air mass flow rates. For the $NO_x$ emissions the influence of $\hat{T}_{2i}$ is almost affine and a lowered intake temperature results in lowered $NO_x$ emissions. With regard to the particulate emissions a rise in the intake temperature results in a rise of $\hat{c}_{mss}$. As it can be seen for the air mass flow rate of 110 kg/h indicated by the solid line, this relationship becomes strongly nonlinear for low air mass flow rates. In wide areas the quantities $\dot{m}_{air}$, $p_{2i}$ and $\varphi_{Q50}$ result in a trade-off between $NO_x$ and particulate emissions, while solely a lowered intake temperature $T_{2i}$ gives the possibility to simultaneously lower both emission quantities $\hat{c}_{nox}$ and $\hat{c}_{mss}$.

Besides the influences of the air path ($\dot{m}_{air}$, $p_{2i}$, $T_{2i}$) and combustion quantities ($\varphi_{Q50}$) on the emission formation, these quantities also show an influence on the generated torque. First of all the influence of $\dot{m}_{air}$ on the modelled torque $\hat{M}_{eng}$ is shown in Fig. 5.6a) at three different charge-air pressures. When the air mass flow rate is lowered, the generated torque first increases and decreases after a maximum is reached. This torque generation is a complex process and it depends on the course of the charge cycle losses as well as the combustion speed which usually is decreased for low air mass flow rates and larger amounts of recirculated exhaust gas. In this engine configuration, an increased charging pressure usually results in a loss of generated engine torque, since at a larger pressure $p_{2i}$ and a constant $\dot{m}_{air}$ more inert exhaust gas is mixed to the cylinder charge. This inert gas decreases the combustion speed and efficiency. Furthermore, an enlarged charging pressure demands a closed VGT-actuator, which rises the exhaust pressure and consequently the necessary work during during the exhaust stroke rises.

Next the influence of $\varphi_{Q50}$ on $\hat{M}_{eng}$ is shown for three pressures $p_{2i}$ in Fig. 5.6b). The torque rises with $\varphi_{Q50}$ moving towards the top dead centre (180 °CA) and depending on the wall heat losses would reach a maximum some degrees after the top dead centre (Pischinger et al., 2009). Locations of $\varphi_{Q50}$ close to the top dead centre generally result in a major $NO_x$ formation and large combustion pressure peaks inside the cylinder. Thus, operation points with an early $\varphi_{Q50}$ should be avoided for mechanical stability reasons (Pischinger et al., 2009). Hence, only locations of MFB50
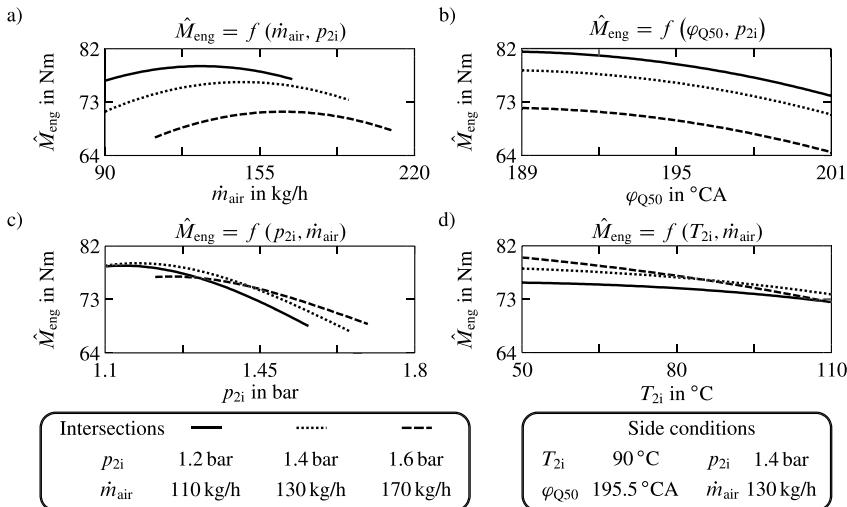
**Figure 5.6:** Simulated $\hat{M}_{\text{eng}}$ intersection plots with the model input quantities $\dot{m}_{\text{air}}$, $\varphi_{\text{Q50}}$, $p_{2\text{i}}$ and $T_{2\text{i}}$ at $n_{\text{eng}} = 2500\,\text{min}^{-1}$ and $u_{\text{inj}} = 20\,\text{mm}^3/\text{cyc}$

between 189 °CA and 201 °CA have been measured and modelled. Further it can be observed, that a larger charging pressure is disadvantageous for the torque generation which further gets obvious in the next plot Fig. 5.6b) with variations of $p_{2\text{i}}$ and $\dot{m}_{\text{air}}$. In the last plot Fig. 5.6d) it can be seen, that the torque increases with a lowered intake temperature. Consequently, a lowered intake temperature is favourable for the engine torque and the emission formation, see Fig. 5.5.

Note that engine torque and the $\text{NO}_x$ formation show a comparable course over the varied quantities in Fig. 5.5 and Fig. 5.6. Consequently the course of engine torque can be implicitly considered in a quality criteria for a multi-criteria optimisation by considering the $\text{NO}_x$ emissions, see Sect. 6.2.2.

Stationary emission and combustion models are important to analyse the stationary engine behaviour and to optimise stationary reference values for the air path control systems. However, a stationary engine operation is rather rare in commonly used driving cycles for engine certification and in real life driving cycles. A large proportion of these driving cycles consists of transients in engine speed and torque demand. Hence, in the following stationary emission models for simulation and optimisation purpose from Tab. 5.1 are extended to model the dynamical emission formation.

## 5.4   Models for the Dynamical Emissions

The steadily tightening emission standards and the large proportion of transients during certification and real life driving cycles demand the consideration of dynamical emissions in the engine development process. Thus, models for the dynamical particulate and $NO_x$ emissions, as well as models for the engine torque are necessary. The modelling of these quantities can be roughly divided into two groups. A first approach utilises dynamical models which incorporate the intake and exhaust system dynamics, as well as the sensor dynamics to model the overall process from the emission formation to the emission measurement. Thompson et al. (2000) model the emission components CO, $CO_2$, $NO_x$, opacity the particulate matter with a neural network and external dynamics. The presented models utilise eight to ten model inputs which are states in the intake and exhaust system, the engine speed, the acceleration pedal position, the injection pressure and the start of the injection. A similar approach based upon LOLIMOT neural networks with external dynamics is presented in Schüler (2001) and Hafner (2002), see also Hafner et al. (2000). Schüler (2001) identifies dynamical models from a step excitation with holding times of 5-10 s. Model inputs are the control signals of the air path actuators $u_{hp-egr}$, $u_t$ and the start of the main injection $\varphi_{mi}$. Hafner et al. (2000) excite the engine with an amplitude modulated pseudo random binary signal. Dynamical emission models with either air path states or actuator control signals as model inputs are presented.

Instead of modelling all dynamics together in one overall engine model, a second approach separates the various dynamical effects by simplifying the combustion as a batch process (Brace, 1998). That implies that the emission formation is predictable when the conditions within the combustion chamber are known. Accordingly, the quality of knowledge about the cylinder charge and the combustion determines the quality of the modelled emissions. Since the combustion is regarded as a batch process, all dynamics in the emission formation are included in the cylinder charge at intake valve closing. Further dynamics in the measured emissions are caused by the gas transportation delay in the exhaust system and the emission measurement (Mrosek et al., 2011b; Mrosek, 2017). This approach has the advantage, that the emission formation is dynamically separated from the system and sensor dynamics. Furthermore, stationary emission models, which are necessary for stationary engine optimisation, are also applied to simulate the dynamical emission formation using the dynamical correct model inputs for the cylinder charge.

In Brace (1998) a neural network is utilised to model the emissions from stationary data. Dynamical validation results are shown for a simultaneous step in engine speed and injection quantity for the modelled quantities $NO_x$, particulates and hydrocarbons. Hirsch and del Re (2009) utilise stationary polynomial emission models with air path quantities as model inputs. Dynamical data is used for the training of stationary opacity and $NO_x$ emission models. Validation results for these models are shown with data from the NEDC. Schilling (2008), Benz (2010) and Tschanz et al. (2010) model the dynamical emissions with stationary emission models and external dynamics. Model inputs are dynamical data quantities, which describe the cylinder charge and the injection, respectively the combustion process. These models utilise a base map for the emissions at a sta-
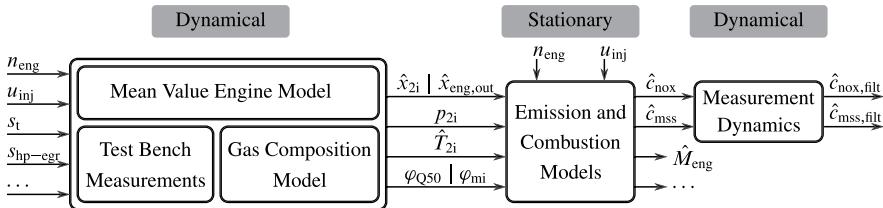
**Figure 5.7:** Model structure to simulate dynamical emission and combustion quantities with the separation of dynamical and stationary models. Chap. 3 mean value engine model, Sect. 4.4 pipe and receiver air content model, Sect. 5.3 stationary emission and combustion model with description of model structure in Tab. 5.1, emission measurement dynamics model (Mrosek et al., 2011b; Mrosek, 2017)

tionary calibrated engine operation point. Deviations from the standard conditions are modelled by correction terms.

**Modelling Approach**

In the following stationary emission models for simulation purpose, as given in Tab. 5.1, are utilised to model the dynamical emissions and the combustion characteristics. Possible dynamics of the recirculated emissions in the exhaust gas are neglected and it is further assumed that the cylinder wall temperature has no significant dynamics (Mrosek et al., 2010a). In the following a detailed separation of the single dynamics is made and their source is clearly stated.

Fig. 5.7 gives an overview about the model structure for dynamical emission and combustion models. One objective in emission modelling is the dynamical correct estimation of the cylinder charge. For simulation purposes, the dynamical cylinder charge is estimated by a mean value engine model, as presented in Chap. 3. When the engine's combustion outcome shall be predicted at a test bench or in a car, the cylinder charge can be determined by measurements of the intake manifold and the pipe receiver air content model from Sect. 4.4. Especially in a LP-EGR configuration with significant dynamics in the air content it is important to model or measure the intake air content for the cylinder charge estimation dynamically correct. In a solely HP-EGR configuration it might be sufficient to neglect some of the air content dynamics and utilise the measured air mass flow rate instead of the intake air content.

In this approach all dynamics from air path actuators are included in the quantities which describe the cylinder charge. With the dynamical characteristics of the intake manifold quantities, the engine speed and the injection parameters, the stationary emission and combustion models from Sect. 5.3 allow to predict the dynamical engine raw emissions. These emissions are further filtered by models for measurement dynamics as given in Mrosek et al. (2011b) and Mrosek (2017) to dynamical agree with the measured quantities. Note that all models except the particulate model are simulated with the cylinder intake air content $\hat{x}_{2i}$, while the air content at engine

exit $\hat{x}_{\text{eng,out}}$ is utilised as model input for the particulate models, since this results in a significantly improved model quality, see Tab. 5.1. As long as no in-cylinder pressure indicating is available, $\varphi_{\text{mi}}$ can be utilised as alternative model input to $\varphi_{\text{Q50}}$.

**Model Validation**

In the following, the model structure of Fig. 5.7 to simulate the dynamical emission formation and combustion quantities is validated with measurements of the NEDC in series calibration. First, the urban part of the NEDC is shown in Fig. 5.8. The first four plots represent the engine operation point in $n_{\text{eng}}$ and $u_{\text{inj}}$ as well as the series controlled variables $\dot{m}_{\text{air}}$ and $p_{2i}$. Further, the cylinder charge describing quantities $\varphi_{\text{Q50}}$, $\hat{T}_{2i}$, $\hat{x}_{2i}$ and $\hat{x}_{\text{eng,out}}$ are shown. In which the quantities $\hat{x}_{2i}$ and $\hat{x}_{\text{eng,out}}$ are determined by the pipe receiver air content model from Sect. 4.3, while $\hat{T}_{2i}$ is determined by Eq. (4.16).

In the subsequent plots the simulated raw emissions and combustion quantities (sim.) are compared to the measurements (meas.). According to Fig. 5.7 the quantities $\hat{c}_{\text{nox}}$ and $\hat{c}_{\text{mss}}$ are filtered (filt.) by the measurement dynamics model as given in Mrosek et al. (2011b) and Mrosek (2017) to the quantities $\hat{c}_{\text{nox,filt}}$ and $\hat{c}_{\text{mss,filt}}$. The measurement dynamics model consists of a lowpass filter and a variable dead time. For the micro soot measurement the dead time $T_{\text{d,tot,mss}}$ ranges between 2 s and 3.5 s and the first order lag has a time constant in the range of 0.8 s, while the NO$_x$ measurement posses a dead time $T_{\text{d,tot,nox}}$ between 0.25 s and 0.55 s and is second order filtered with time constants in the range of 0.2 s and 0.45 s.

The results for the filtered simulated NO$_x$ emissions fit the measurements well. A further zoom inside the section between 725 s and 745 s reveals, that the measurement dynamics is smoothing the simulated raw emissions. In the simulated raw emissions, peaks are much larger than in measured and filtered quantities. Further the zoomed section shows, that the combination of the air content model, the stationary emission model and the measurement dynamics model is capable to model the dynamical NO$_x$ measurement well.

The next plot in Fig. 5.8 illustrates the validation results of the measured micro soot concentration. Compared to the simulated NO$_x$ emissions, the particulate emissions are harder to model, see also Tab. 5.1. Consequently, larger deviations between measured and simulated particulate emissions can be observed. In the zoomed section the large dead time of the micro soot measurement gets obvious, which is met by the measurement dynamics model. Only the dead time for the second peak seems to be overcompensated. This peak is also not met exactly in its full height by the $c_{\text{mss}}$ model. Generally, the simulated raw emission peaks are smoothed by the measurement dynamics model. These measurement delays decrease the magnitude of the simulated raw emission peaks almost by factor two. Hence, based on the assumption of a smoothing measurement dynamics, the measured particulate emissions are supposed to have a similar magnitude at engine exit.

Next the validation results for the engine torque $M_{\text{eng}}$ are illustrated. The torque sensor has no significant measurement dynamics and is mounted at the shaft connecting combustion engine with test bench induction engine. The engine torque model agrees well with the measured data.
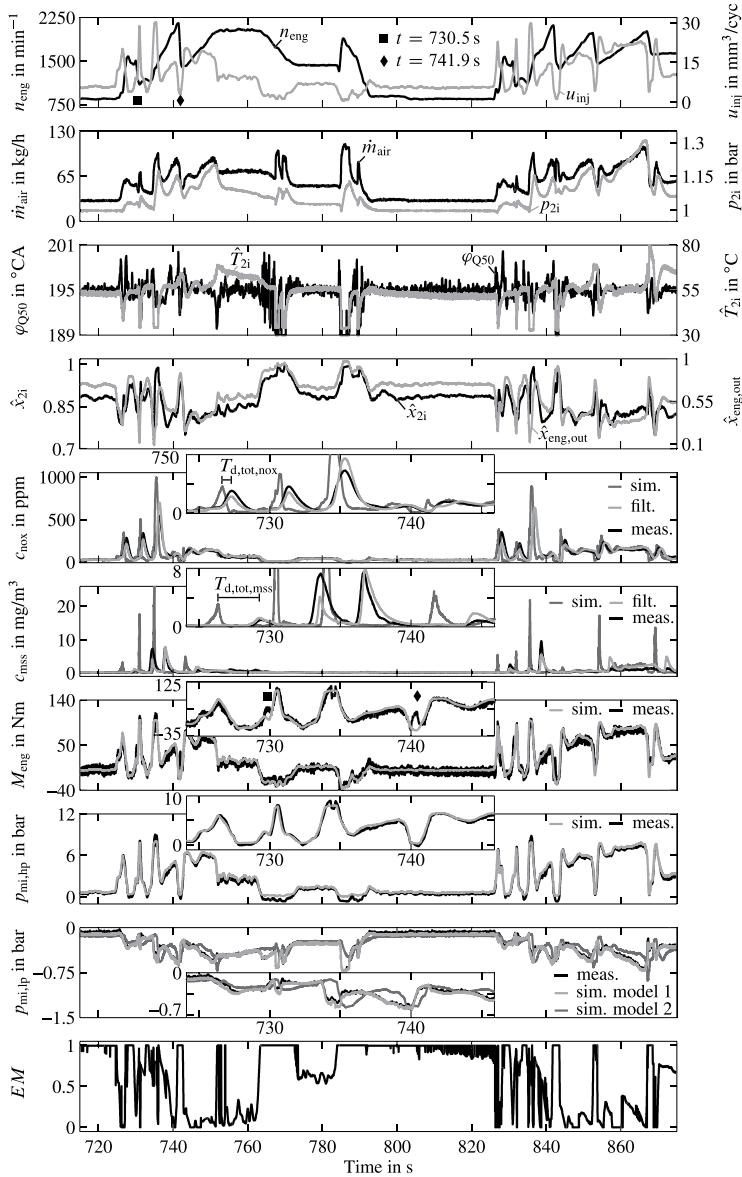
**Figure 5.8:** Urban part of the NEDC for dynamical emission and combustion model validation

However, this model reflects only the torque which is contributed by the combustion engine, acceleration and deceleration of the engine result in inertia torques of the drive train, which are measured as additional torque decrease or torque increase from the sensor. This gets obvious at the marked time stamps 730.5 s (■) and 741.9 s (♦) in the $n_{eng}$ plot. At these times the engine is strongly decelerated. In the zoomed engine torque section, deviations between measurement and model can be observed. Consequently, the engine torque cannot be parameterised with dynamical engine measurements as long as large variations in the engine speed are apparent.

Alternatively to the shaft torque, the mean indicated pressure represents a measure for the engine work (Mrosek, 2017). The mean indicated pressure of compression and expansion stroke $p_{mi,hp}$ is illustrated in the plot below the torque. This quantity is calculated without significant delay by an indicating system. The modelled and the measured $p_{mi,hp}$ fit well and there are no effects of engine deceleration at the times 730.5 s and 741.9 s. The mean indicated pressure of the charge cycle $p_{mi,lp}$ is shown next. Two models are utilised to model the quantity $p_{mi,lp}$. The first model (model 1) describes the charge cycle losses as a function of engine operation point ($n_{eng}$, $u_{inj}$), swirl actuator position $s_{sa}$, charging pressure $p_{2i}$ and exhaust pressure $p_3$ (Mrosek, 2017). With these two pressures, the model is capable to model the influence of the intake and exhaust system transients to the measured indicated pressure of the charge cycle well. The second model (model 2) with the local model inputs $\hat{x}_{2i}$, $p_{2i}$, $\hat{T}_{2i}$ and $\varphi_{Q50}$ meets the stationary engine behaviour well, but fails on the dynamical transients. For dynamical $p_{mi,lp}$ models, the influence of the pressure before and after the cylinder are essential for a good model quality and they have to be included as model inputs. Finally, the extrapolation measure $EM$ is shown for the given models and it reveals that there is a large proportion of model extrapolation ($EM>0$). The cause for this model extrapolation will be discussed after the model validation with the extra-urban part of the NEDC.

Fig. 5.9 shows the performance of the dynamical emission and combustion models with measurements of the extra-urban part of the NEDC. This part covers a large range of engine operation points in $n_{eng}$ and $u_{inj}$ but contains less dynamics than the previously investigated urban part from Fig. 5.8. The local model inputs $p_{2i}$, $\varphi_{Q50}$, $\hat{T}_{2i}$ and $\dot{m}_{air}$, respectively $\hat{x}_{2i}$ and $\hat{x}_{eng,out}$ are depicted. For all modelled quantities a section between 1005 s and 1015 s is zoomed. The $NO_x$ emissions are modelled well, while there are some deviations in the more demanding particulate models $c_{mss}$. However, the particulate model qualitatively agrees with the measurement and it can be regarded as satisfying. The $M_{eng}$, $p_{mi,hp}$ and $p_{mi,lp}$ (model 1) models show almost no deviations from the measurements, while the $p_{mi,lp}$ model (model 2) shows the afore mentioned deviations between simulation and measurements during transients.
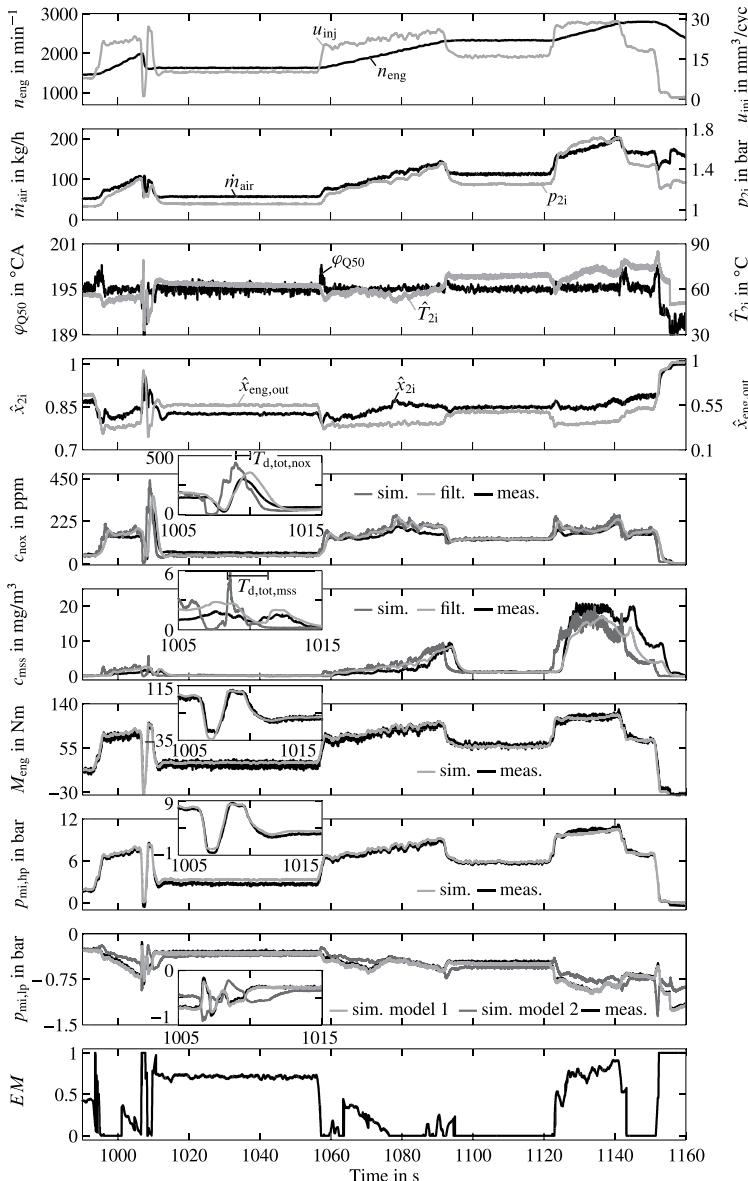
**Figure 5.9:** Extra-urban part of the NEDC for dynamical emission and combustion model validation

Model extrapolation can become a severe problem in black-box model evaluation. Especially at dynamical engine operations it is difficult to decide whether deviations result from a poor model quality or from model extrapolation. Provided that input data is situated in a model's extrapolation region, the model quality can be improved with measurement of additional data in the affected regions of the input space and by re-training the model with the refined dataset. Therefore the extrapolation measure (5.8) is an important tool to analyse the performance of black-box models.
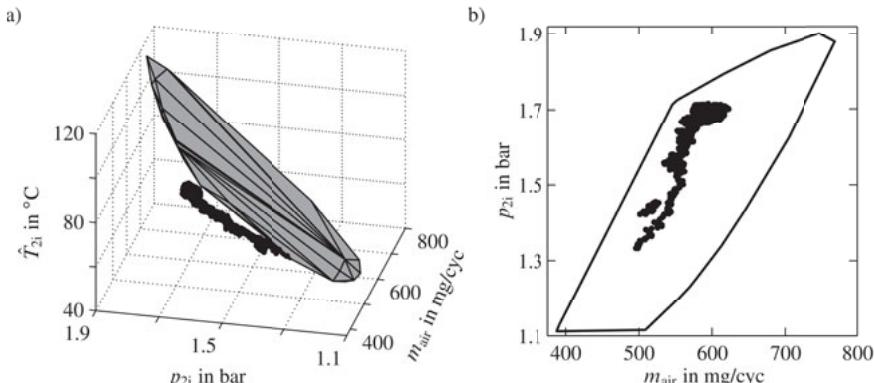


**Figure 5.10:** a) Local convex hull ($n_{eng} = 2500\,min^{-1}$, $u_{inj} = 30\,mm^3/cyc$) indicating the model training space and the dynamical data from the NEDC showing extrapolation in the intake temperature $\hat{T}_{2i}$ dimension. b) Corresponding convex hull and dynamical data in the $p_{2i}$ and $m_{air}$ dimension

In Fig. 5.8 and Fig. 5.9 the extrapolation measure $EM$ often indicated a model extrapolation. One reason for this extrapolation is the insufficiently covered area of engine operation points in $n_{eng}$ and $u_{inj}$. Further model extrapolation can be attributed to the intake temperature. The stationary training of the summer measurement was measured at hot summer days, while the NEDC measurement was undertaken at a chilly summer day. All global data points without a corresponding winter measurement show model extrapolation then. Fig. 5.10a) evaluates a local convex hull, which determines the training space. The corresponding NEDC data points which contribute to this local model with a local validity (5.7) larger than 0.1 are depicted as dots. The measurements leave the input space in the dimension of the intake temperature. A projection of the input dimensions $p_{2i}$ and $m_{air}$ in Fig. 5.10b) clarifies this. Hence, this method allows to analyse the weaknesses of the utilised models in respect of model extrapolation and thus identifies the relevant regions for model improvement. However, even with model extrapolation in the temperature dimension, the combination of stationary global-local emission models with dynamical estimates of the cylinder charge and measurement dynamics models allows to simulate the dynamical emission formation and combustion quantities satisfactory.

## 5.5 Summary

Emission and combustion modelling is a challenging task in the field of engine modelling. Largely varying system dynamics in the intake and exhaust system are superimposed by significant measurement dynamics. Anymore, the emission formation process is strongly nonlinear. Therefore small modifications in the influencing variables can lead to large changes in the emissions. Furthermore, small cylinder individual differences in air contents, injection quantities, cylinder wall temperature and others can lead to a great variance of the single cylinder emissions. Especially the rise in the particulate emissions is very steep, if the air mass flow rate, respectively the local oxygen concentration, reaches a critical value. Further the soot formation is strongly dependent on the dynamical slow intake temperature and the particulate measurement possesses the largest measurement dynamics.

First different sources of dynamics in the intake and exhaust system, as well as the measurement dynamics are identified and especially the emission measurements possess significant dynamics. Stationary emission and combustion models are modelled with a global-local polynomial modelling approach. At local engine operation points in $n_{eng}$ and $u_{inj}$, polynomial models for the emission and combustion quantities are trained. Afterwards these models are superimposed to model the global engine behaviour. Models are given for $NO_x$ and particulate emissions, engine torque, start of the main injection, MFB50 and mean indicated pressure. Based upon the validation quality of different model inputs, the intake temperature $T_{2i}$ is chosen as an additional controlled variable for the air system with HP-EGR and LP-EGR, since it describes the particulate emissions best.

Finally, the air content model, the stationary emission models and the measurement dynamics models are coupled to model the dynamical measured emissions of the engine test bench. The comparison between simulated and measured emissions reveals a good agreement in stationary and dynamical parts of the NEDC. This proves the assumption, that the combustion process can be simplified as a batch process, which implies that the combustion outcome can be mainly described by the cylinder charge at intake valve closing and the injection characteristics. Models of the dynamical emissions are given as the combination of the dynamical quantities describing the cylinder charge and the injection, a stationary emission model and a subsequent filtering with a measurement dynamics model. Especially for the dynamical simulation, the extrapolation measure gives important information about room for model improvement with regard to the utilised training data and helps to separate effects of model extrapolation from model weaknesses.

The stationary emission models are applied in Sect. 6.1 to optimise stationary reference values for the air path control. In Sect. 6.2 models for the dynamical emissions motivate the dynamical emission course of different control concepts and are utilised to derive optimised reference values for engine transients. Finally in Sect. 7.9, the driving cycle emissions of different control concepts are rated by models for the dynamical emissions and allow to compare the classical HP-EGR with the dual loop EGR consisting of HP-EGR and LP-EGR.

# 6 Optimisation of the Reference Values for the Air Path Control

Subject of this chapter are deviations of stationary and dynamical reference values for the air path control. First, optimised stationary reference values are given for a dual EGR air path control. These optimised reference values are compared to the HP-EGR series calibration and the emission lowering potential of a LP-EGR engine configuration is highlighted. Afterwards, the dynamical emission formation and deviations between the courses of different control concepts' dynamical emissions are illustrated. Finally, a dynamical optimised reference value trajectory for the air mass flow rate, respectively the air content, is derived based on local polynomial emission models.

Generally, the reference values for the engine air path control and combustion control can be considered as process inputs for the combustion process and aim to give a desired engine characteristics. On the one hand these engine characteristics are demanded by legislation as emission and fuel consumption limits, on the other hand the car manufacturer has the possibility to tailor the engine behaviour to its desired vehicle characteristics, e.g. torque response and noise. The first objective for reference values can be easily described by numerical quantities, while the second objective is mainly based on brand individual expert knowledge. This expert knowledge is usually not published and consequently the reference value derivation in this dissertation will be limited to the objectives emission limits and fuel consumption. In this chapter stationary reference values for the dual EGR engine configuration are given. These reference values are utilised to compare the potential of the additional LP-EGR path with the series calibration of a solely HP-EGR configuration. The second part of this chapter is about the dynamical emission formation at engine transients. Investigations with three different control concepts ($\dot{m}_{air}$-control, $r_{egr}$-control, $x_{2i}$-control) illustrate the deviations between stationary and dynamical engine emission course. Based on this knowledge reference values for the air mass flow rate, respectively the air content, are dynamically optimised.

## 6.1 Stationary Reference Value Optimisation

This section briefly presents the stationary reference value optimisation results of Sequenz (2013), which are necessary to finally evaluate the results of the control concepts in Sect. 7.9. A more detailed discussion of the optimisation and its results with regard to the emission lowering potential of a LP-EGR can be found in Mrosek (2017).
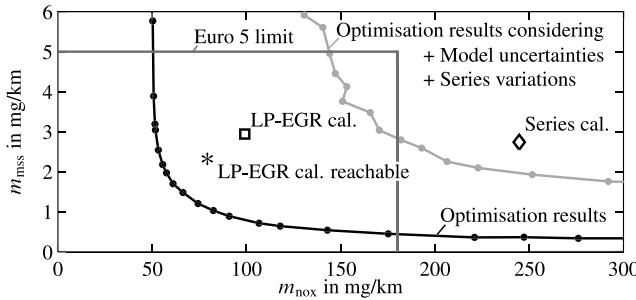
**Figure 6.1:** Cycle emissions for the NEDC from accumulated local multi-criteria optimisations (black) with additional consideration of series variations and model uncertainties (grey), as given in Sequenz (2013) by using stationary models. Regularised robust global optimisation results for the LP-EGR engine configuration (□) (Sequenz, 2013), reachable LP-EGR calibration (∗) and series HP-EGR calibration (◇).

In Fig. 6.1 the optimisation results of Sequenz (2013) are given. Two curves present the local optimisation results summed for the considered 21 engine operation points and the emission area allowed by the Euro 5 emission limits. The black curve is the *Pareto optimum* and displays the maximal potential to simultaneously lower $NO_x$ and particulate emissions. The grey curve also considers model uncertainties and series variations.

After a local optimisation determines the initial values for a subsequent global engine optimisation, Sequenz (2013) gets a globally optimised robust LP-EGR calibration. This calibration is further postprocessed for a smooth curvature and results as LP-EGR cal. (□) in Fig. 6.1. In comparison to the Euro 4 series calibration (◇) with only a HP-EGR system, these optimised reference values for the dual path EGR show a large potential to reduce the $NO_x$ emissions into the Euro 5 emission window. The consideration of robustness constraints and the dynamical emission increase leave some safety margin to the legislative emission limits. However, the calibrated reference values of Sequenz (2013) are too stringent limited, since the emission models for many operation points have been parameterised with the same data sets as utilised in Chap. 5. These data points have been partly measured during hot summer days at the unconditioned test bench. Consequently, the temperature limitations of the engine optimisation are too large, why there is further potential to lower to emissions for the ambient temperatures as defined in the legislation. Therefore, the optimised temperature reference values are manually decreased to a feasible range (∗ LP-EGR cal. reachable) and show the further lowered emission level. These reference values are the base for all following investigations.

| | $m_{nox}$ in mg/km | $m_{mss}$ in mg/km | $W_{eng}$ in kWh |
|---|---|---|---|
| HP-EGR series | 244.8 | 2.74 | 1.53 |
| LP-EGR (Sequenz, 2013) | 99.2 | 2.94 | 1.61 |
| LP-EGR reachable | 79.3 | 2.32 | 1.64 |

Tab. 6.1 quantitatively summarises the global optimisation results of Sequenz (2013) and the reachable LP-EGR calibration and compares these results to the series HP-EGR calibration with respect to the $NO_x$ and particulate emissions as well as the delivered engine work $W_{eng}$.

$$W_{eng} = \frac{1}{1000 \cdot 3600\frac{s}{h}} \sum_{j=1}^{M} k_j \omega_{eng,j} \hat{M}_{eng,j}(\mathbf{x}_j) \quad \text{in kWh} \tag{6.1}$$

It can be seen, that the additional LP-EGR path has a large potential to lower the $NO_x$ emissions, while the particulate emissions stay almost at a constant level. Furthermore, the delivered engine work during the driving cycle increases at constant injection quantity for more than 5 %.

## 6.2 Dynamical Reference Value Optimisation

A main objective of air path control systems is to positively influence the emission formation. State of the art air path control systems work well in stationary engine operation. But there are deviations to the stationary calibrated emissions during engine transients. In this section a brief analysis of the existing work on the field of dynamical emissions is given, then the discrepancy between transient and stationary emissions is analysed and a real-time capable solution, which generates dynamical optimised reference values for the air path control is presented. These dynamical optimised reference values are optimal to any trajectory in engine speed and the driver's torque demand and can be calculated online by analytical solution of the quality criterion.

A deep understanding of the dynamical emission formation is rather new in the field of engine control and there are only a few approaches which address this topic. Basically there are three approaches to improve the transient emission behaviour, which can be separated into the groups emission control, alternative control concepts and optimisation of engine transients.

Some approaches focus on the direct emission control. Alfieri (2009) presents a first step towards the fully emission controlled engine. A $NO_x$-sensor and the measured air-fuel ratio as a substitute for the particulate emissions are the controlled variables. The manipulated variables are HP-EGR-valve and start of the injection. The charge-air pressure is controlled independently. Objective of this work is to compensate manufacturing tolerances, ageing and the drift of engine components. Further researches in Tschanz (2012) use the combination of stationary emission

models, emission measurements and a *Kalman filter* to estimate the current emissions as controlled quantities. In this approach the Kalman filter compensates measurement dynamics of the sensors and model uncertainties of the emission models. The particulate and $NO_x$ emissions are controlled decentralised. A PI-controller controls the particulate emissions via the swirl actuator, while the $NO_x$ emissions are controlled by proportionally manipulating the start of the injection. Furthermore, an integral controller adapts the reference values of a burned gas rate controller to maintain the desired $NO_x$ emissions. Stölting et al. (2008) utilise an in-house control concept to control more manipulated variables than controlled variables. The $NO_x$ emissions are manipulated with $s_{hp-egr}$ and the crank angle of mass fraction burned 50 %, while the particulate emissions are controlled by the charge-air pressure and the pressure of the common rail system. A further development would be a direct emission control of the dynamical emissions. However, the emission formation is highly nonlinear and strongly coupled with the air path states. Anymore there is a tradeoff between $NO_x$ and particulate emissions, which deteriorates one emission component when the other one is improved. Besides the question for the optimal reference values for an emission control, the emission sensors involve additional costs and are dynamical not well suited for an air path control (Mrosek et al., 2011b; Mrosek, 2017).

The emissions lowering potential of different control concepts is investigated in the following publications. Nakayama et al. (2003) compare a $\dot{m}_{air}$ and $p_{2i}$ control scheme to a control of intake manifold air content $x_{2i}$ and $p_{2i}$. The $\dot{m}_{air}$ control scheme shows larger dynamical $NO_x$ emissions, while a control of $x_{2i}$ decreases these $NO_x$ emissions on the cost of larger particulate emissions. Herrmann (2005) investigates the influence of different air path control concepts to simulated qualitative characteristics of the transient $NO_x$ and soot emissions. The investigated air path consists of a VGT-turbocharger and a HP-EGR system. At a controlled charge-air pressure, the differences between a HP-EGR-rate control, a HP-EGR mass flow rate control, an air mass flow rate control and a $NO_x$ control are compared. With respect to the transient emissions the air mass flow rate control results in dynamical high $NO_x$ but low soot emissions. The results for the HP-EGR-rate control, the HP-EGR mass flow rate and the $NO_x$ control are vice versa. The $NO_x$ control concept has the dynamical best results. In test bench results the $NO_x$ control suffered from sensor dead time and the slow sensor dynamics. In comparison to the air mass flow rate the $NO_x$ control required 2 s longer to reach steady state. Therefore, the air mass flow rate is chosen as second control variable besides the charge-air pressure. Schöppe et al. (2009) choose the air fuel ratio and the HP-EGR-rate as control variables. The main influence of the HP-EGR-rate are the $NO_x$ emissions and the air fuel ratio mainly influences the particulate emissions. In comparison to the controlled variables charge-air pressure and air mass flow rate the cross couplings are supposed to be smaller, which simplifies the engine calibration process. Further, the HP-EGR-rate control yields lower dynamical $NO_x$ emissions during transient engine operation. Naber et al. (2011) compare the dynamical $NO_x$ and soot emissions of an air mass flow rate control scheme with a HP-EGR-rate control. A load step is applied and the activated smoke limitation results in two different injection characteristics. The injection quantity has a step shape with an air mass flow rate control, while the HP-EGR-rate control gets a ramp shaped injection quantity with a rise time of approximately 6 s. In the shown transient the air mass control scheme is favourable with respect to soot emissions but causes large $NO_x$ emissions, while the HP-EGR-rate control scheme results in low $NO_x$ emis-

sions at larger soot emissions. The engine management system is extended to include transient corrections to the air mass flow rate setpoints. These dynamical corrections are block shaped and added or subtracted from the calibrated stationary setpoints and have to be calibrated depending on the behaviour of the dynamic engine operation. Anymore, the impact of the start of the main injection on the dynamical $NO_x$ emissions and the torque generation is investigated.

A first step in the optimisation of the transient emissions behaviour is a smoke limitation. Usually a smoke limitation restricts the maximal injection quantity, so that the engine does not undershoot a certain air fuel ratio. Hence, the particulate emissions are limited. However, the limiting of the fuel quantity during the smoke limitation can lead to an undesired torque response. Therefore, von Pfeil (2011) optimises control variables for the transient engine operation in the smoke limitation, see also Renninger et al. (2006). Optimised variables are a maximal HP-EGR-valve position, the begin of the injection and the limit for the air fuel ratio during the smoke limitation operation mode. These can be considered as stationary enhancements and are capable to calibrate a more favourable operation point in the particulate-$NO_x$ tradeoff. A further step towards a dynamical optimised engine control is presented in Hafner (2002). Dynamical LOLIMOT-models for the emissions and the engine torque of a Diesel engine are identified. An offline optimisation delivers dynamical enhancements for the feed-forward control of HP-EGR-valve, wastegate turbocharger and start of injection. These dynamical enhancements are in form of derivative lag elements (DT1 elements) and are calibrated depending on the engine operation point. These dynamical corrections significantly improve the dynamical emission formation for a feed-forward controlled air path. However, with the uprising closed-loop control of air path quantities this approach becomes obsolete.

Other publications examine the offline optimisation of air path actuator trajectories with a priori knowledge of the demanded torque and engine speed. Alberer and del Re (2009) optimise piecewise affine trajectories of $s_t$, $s_{hp-egr}$ and $u_{inj}$ for one single load step with respect to $\hat{c}_{nox}$, $\hat{c}_{opa}$ and $\hat{M}_{eng}$. The optimisation is model-free with test bench measurements as objective function, which means that for every objective function call at least one trajectory has to be measured at the engine test bench. Then the summed $\hat{c}_{nox}$, $\hat{c}_{opa}$ and $\hat{M}_{eng}$ measurements give the effectiveness criterion for each optimisation step. Benz (2010) optimises the emissions offline with the combination of a dynamical semi-physical air path model and stationary emission models for three example transients. Considered are a load step case, a load drop case and a drivability case. The first case considers the injection quantity shaped by the series smoke limitation, which leads to a moderate increase of engine torque during the transient. Different input trajectories are optimised for several combinations of the air path inputs $s_t$ and $s_{hp-egr}$ with the injection system inputs $p_{rail}$ and start of the injection. Considered emissions are $NO_x$ and particulates. In order to reduce the complexity of the optimisation problem the chronological sequences of input trajectories are discretised. For the load step a significant reduction of particulate emissions could be reached on cost of increased $NO_x$ emissions. Regarding the load drop test case the optimisation results are vice versa. Sequenz et al. (2011b) follow a similar approach with comparable results. Besides discretised actuator trajectories also splines are utilised to reduced the complexity of the actuator trajectories. Both approaches show the potential of optimised actuator trajectories for transient

engine operation. However, a priori knowledge of engine speed and torque demand is necessary to optimise these trajectories. Further the optimisation is computational demanding and the integration of these optimised trajectories into commonly used air and fuel path control systems is still unsolved.

### 6.2.1  Dynamical Emissions of Different Air Path Control Concepts

The dynamical emissions contribute to the overall emissions during a transient engine driving cycle. In order to find appropriate measures to reduce dynamical emissions the cause of their formation needs to be investigated, see also (Mrosek et al., 2011a,c).

A direct closed-loop control of the engine emissions and torque should be the major objective of the Diesel engine air path control system. Though, a direct control of these quantities is costly, since $NO_x$ and particulate sensors bear additional costs and measure the quantities delayed. Instead air path quantities are commonly used as controlled variables and represent the emission formation sufficiently at stationary engine conditions. Fig. 6.2a) shows a general air path control structure with the controlled variables air mass flow rate $\dot{m}_{air}$ and charge-air pressure $p_{2i}$. In this general structure the stationary reference values are stored in characteristic maps and a control system manipulates the variables $s_{hp-egr}$ and $s_t$, which influence the air path quantities $\dot{m}_{air}$ and $p_{2i}$. These air path quantities determine the cylinder charge and with the injection parameters the formation of emissions and the torque response, see Sect. 5.4. Consequently, the closed-loop control of air path quantities can be considered as a feed-forward emission control, since the course of the emissions is not fed back and the emissions are only open-loop controlled by the course of the air path quantities. Anymore, this consideration is also valid for alternative controlled variables and complexer control systems with two-stage turbochargers or low-pressure EGR. These control systems can have additional reference values, air path actuators and controlled variables.

Further, the air path control is a multivariable system with different dynamics in the controlled variables. These different dynamics usually result in an unsatisfying transient emission formation. Fig. 6.2b) depicts a transition between two stationary engine operation points at constant engine speed. During the engine transient the quantity $u_{inj}$ is changed almost instantaneously, while the controlled variable $\dot{m}_{air}$ reaches its calibrated reference value relatively fast and $p_{2i}$ follows delayed. These dynamical characteristics of the cylinder charge affect the emission formation during the combustion process. Due to the different dynamics of the injection parameters and the single air path quantities, the dynamical emission formation differs from the stationary optimised emission level, in the same as shown in the right plot of Fig. 6.2b), where a particulate and a $NO_x$ peak arise.

Thus, the selected controlled variables for the air path quantities directly influence the chronological sequence of the dynamical emission formation. In the following the influences of three control concepts on the emission formation are compared. An air mass flow rate control $\dot{m}_{air,ctl}$ in combination with a charge-air pressure control $p_{2i}$ is a common control concept (Schloßer, 2000; Jung, 2003; von Pfeil, 2011). Alternatively to $\dot{m}_{air}$, an EGR-rate control $r_{egr,ctl}$ or an intake air con-

a) Closed-loop control of air path quantities
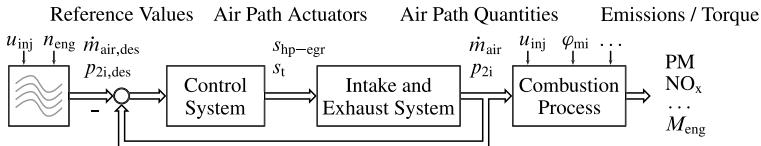


b) Schematic transition between two stationary optimal setpoints
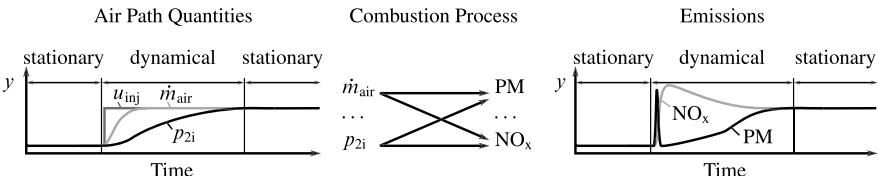


**Figure 6.2:** a) General structure of an air path control with air mass flow rate and charge-air pressure as exemplary controlled variables and open-loop controlled emission formation b) Schematic deviations between stationary emissions and dynamical emissions due to the multivariable control of the air path quantities $\dot{m}_{air}$ and $p_{2i}$ and the injection parameter $u_{inj}$ for an injection step at constant engine speed

tent control $x_{2i,ctl}$ can be used, see Nakayama et al. (2003); Wang (2009); Mrosek and Isermann (2010a). Also other combinations of controlled variables might be suitable, but for simplification the following analysis is limited to these three concepts.

Fig. 6.3 compares three control concepts $\dot{m}_{air,ctl}$, $r_{egr,ctl}$ and $x_{2i,ctl}$ with simulations of a load step in $u_{inj}$ at constant engine speed. In this multivariable control the second controlled variable is $p_{2i}$. In the following comparison all control concepts are realised with PI(D)-controllers similar to Sect. 7.3. Besides the controlled variables $\dot{m}_{air}$, $r_{hp-egr}$ and $x_{2i}$ additionally the air path quantities $x_{eng,out}$ and $\dot{m}_{hp-egr}$ are shown. The emission quantities are given in the concentration measures $\hat{c}_{nox}$ and $\hat{c}_{mss}$ as well as in the emission mass flow rates $\hat{\dot{m}}_{nox}$ and $\hat{\dot{m}}_{mss}$. Anymore, the engine torque $\hat{M}_{eng}$ is presented.

The reference values for all illustrated control concepts result stationary in equal values for air path quantities, emissions and torque. Also the charge-air pressure shows a similar dynamical characteristic for all control concepts. Though, there are considerable deviations in the course of the air mass flow rate related quantities and the emissions between the different control concepts in the transient responses. In the first 150 ms all control concepts have strongly increased particulate emissions $\hat{c}_{mss}$ ($\hat{\dot{m}}_{mss}$). This soot-peak results from the steep rise in the injection quantity and the limited dynamics of the HP-EGR-valve and the gas system. It can be reduced by a low-pass filtered injection quantity or a limited injection quantity based on a smoke limitation as e.g. given by the model-based approach in Sequenz et al. (2011a). However, a limitation of the injection quantity will not be considered and the first 150 ms of time containing the soot-peak are neglected in the

following discussion, since the soot-peak arises from the limited air path dynamics of HP-EGR-valve closing and flushing the intake manifold with fresh air, which is similar for all compared control concepts.

In comparison to the other control concepts the air mass flow rate control $\dot{m}_{air,ctl}$ reduces the mass flow rate through the HP-EGR-valve $\dot{m}_{hp-egr}$ the most. This yields to a large fresh air content in the intake manifold $x_{2i}$ and consequently large NO$_x$ emissions can be observed $\hat{c}_{nox}$ ($\hat{\dot{m}}_{nox}$). On the other hand, the dynamical particulate emissions $\hat{c}_{mss}$ ($\hat{\dot{m}}_{mss}$) are the lowest. The mass flow rate of recirculated exhaust gas $\dot{m}_{hp-egr}$ first decreases and then slowly rises with the dynamics of the charge-air pressure $p_{2i}$. During the engine transient the simulated exhaust components $\hat{c}_{nox}$ ($\hat{\dot{m}}_{nox}$) and $\hat{c}_{mss}$ ($\hat{\dot{m}}_{mss}$) converge from different directions to their stationary calibrated value. It can further be seen, that the air mass flow rate control can be stationary considered as an air content control at engine exit $x_{eng,out}$ or with (3.11) as an air-fuel ratio control, since the quantity $x_{eng,out}$ reaches its stationary value as fast as $\dot{m}_{air}$. In summary, the fast controlled air mass flow rate results in large dynamical NO$_x$ emissions, while the transient particulate emissions are clearly below their calibrated stationary value in the considered time range after the soot-peak.

In contrast the EGR-rate control $r_{egr,ctl}$ results in the lowest air content in the intake manifold $x_{2i}$. The lowered oxygen concentration of the cylinder charge results in dynamical increased particulate emissions, while the transient NO$_x$ emissions are the lowest of all shown control concepts. In the $r_{egr,ctl}$ control concept the EGR-rate reaches its calibrated reference value fast. On the other hand the air mass flow rate displays a dynamical characteristic similar to $p_{2i}$. Next, the control of $x_{2i}$ can be considered as a compromise between the afore mentioned control concepts. The dynamical $\hat{c}_{nox}$ concentration ($\hat{\dot{m}}_{nox}$) is moderately higher than its stationary concentration, whereas the dynamical $\hat{c}_{mss}$ concentration ($\hat{\dot{m}}_{mss}$) is below its stationary value. In respect of the engine torque $\hat{M}_{eng}$ the air mass flow rate control shows slight advantages followed by the $x_{2i}$ control concept and the $r_{egr}$ control. However, the differences in engine torque between the different control systems are small. Compared to the emission concentrations $\hat{c}_{mss}$, $\hat{c}_{nox}$, the tailpipe emission mass flow rates $\hat{\dot{m}}_{mss}$, $\hat{\dot{m}}_{nox}$ have dynamical a similar characteristics.

The comparison between the three control concepts $\dot{m}_{air,ctl}$, $r_{egr,ctl}$ and $x_{2i,ctl}$ shows, that the dynamical emissions during an engine transient differ from the stationary emissions. In anticipation of the following section, the interested reader can find the quantitative rating of the different control concepts and the results of the following optimisation in Tab. 6.2. Depending on the controlled variables dynamically either the NO$_x$ or the particulate emissions are favoured, while the other component is deteriorated. During transients the NO$_x$ emissions and the particulate emissions reach their final value from different directions with the dynamics of the charge-air pressure. Consequently, the course of charge-air pressure dynamics determines the time course of the emission formation. In the following trajectories for $x_{eng,out}$, respectively $\dot{m}_{air}$ are optimised with respect to $\hat{c}_{nox}$ and $\hat{c}_{mss}$. This optimisation utilises global-local emission models from Sect. 5.3.
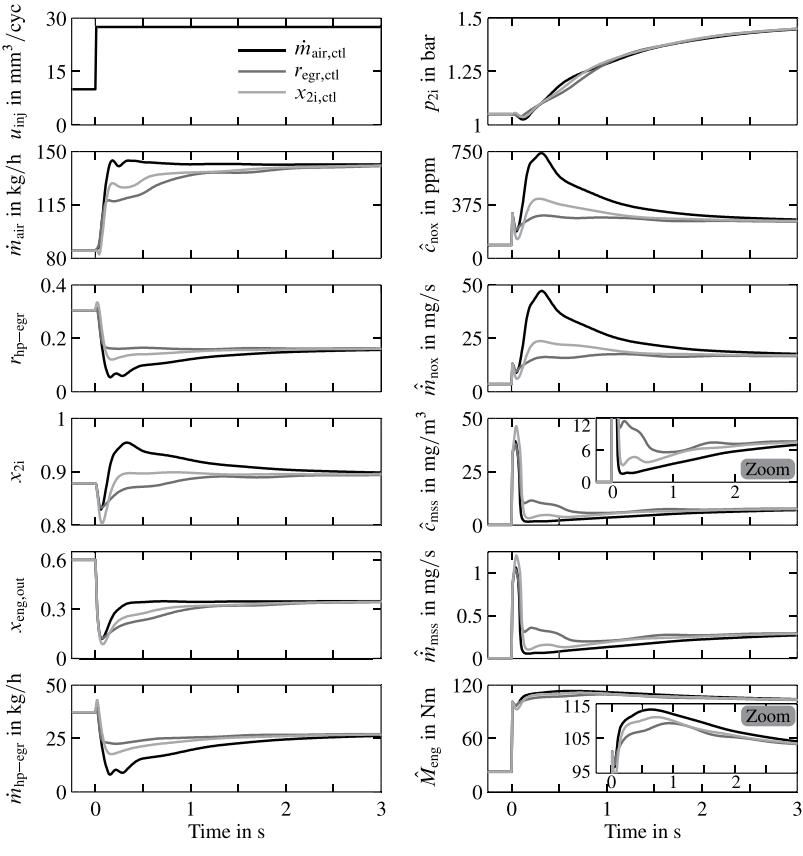
**Figure 6.3:** Comparison of different control concepts with regard to the simulated air path quantities, emissions and torque. The control concepts for the air mass flow rate $\dot{m}_{air,ctl}$, the EGR-rate $r_{egr,ctl}$ and the intake air content $x_{2i,ctl}$ are compared for a load step from $u_{inj} = 10\,\mathrm{mm^3/cyc}$ to $u_{inj} = 27\,\mathrm{mm^3/cyc}$ at $n_{eng} = 2250\,\mathrm{min^{-1}}$

### 6.2.2  Multi-Criteria Optimisation of Dynamical Reference Values

A comparison of different control concepts shows, that during engine transients the dynamical course of the cylinder air content determines the dynamical emissions. Representative quantities describing the cylinder air content can be the air mass flow rate $\dot{m}_{air}$, the EGR-rate $r_{egr}$, the air content before $x_{2i}$ or after the combustion $x_{eng,out}$. With regard to the air path, these quantities can be manipulated dynamical fast, while the charge-air pressure dynamics is delayed by the turbocharger's inertia and the gas volume in the intake system.

In the following optimised reference values for an air mass related quantity ($\dot{m}_{air}$, $r_{egr}$, $x_{2i}$ or $x_{eng,out}$) are generated based on polynomial emission models, see Eq. (5.3). A special transformation drastically reduces the model order of the polynomials and achieves an analytical real-time capable optimisation for one single quantity. This approach demands emission models with the same set of model inputs, which directly model the emission quantities $NO_x$ and particulates.

As a result of the model quality in Tab. E.1 and Tab. E.3, the air content after the combustion $x_{eng,out}$ is chosen as variable for dynamical optimised reference values. At stationary engine operation this quantity is a direct transformation of air mass flow rate and injection quantity, allows a good interpolation of the particulate emissions (Sect. 5.3.4) and since it is a transformation of air mass flow rate and injection quantity it is not affected by effects like engine ageing, engine misfire and so forth. In comparison to $r_{egr}$ or $\dot{m}_{air}$ this variable comprises most dynamical effects in the intake and exhaust system, see Sect. 4.4. $x_{eng,out}$ can be either controlled by a dynamical reference value generation as given in Sect. 7.8 or it acts as an intermediate control variable, which can be transformed into a reference value for an air mass flow rate control, see Eq. (6.9). Anymore, $\varphi_{mi}$ is utilised as model input for utilised models, since most series engines are currently not equipped with in-cylinder pressure indication.

**Multi-Criteria Optimisation Criterion**

In order to optimise reference values for $x_{eng,out}$, a multi-criteria optimisation criterion of the form

$$J_{dyn}(\mathbf{z}, \mathbf{x}) = w_{nox}(\mathbf{z})\,\hat{c}_{nox}(\mathbf{z}, \mathbf{x}) + w_{mss}(\mathbf{z})\,\hat{c}_{mss}(\mathbf{z}, \mathbf{x}) \tag{6.2}$$

with

$$\mathbf{z} = [n_{eng}(t),\, u_{inj}(t)] \quad \text{and} \quad \mathbf{x}(t) = [x_{eng,out}(t),\, p_{2i}(t),\, \hat{T}_{2i}(t),\, \varphi_{mi}(t)] \tag{6.3}$$

can be defined as loss function for the engine transient at each point in time $t$. The loss function $J_{dyn}$ depends on the z-regressors, which denote the engine operation point and the x-regressors which are the local inputs of the stationary global-local emission models, see Eq. (5.3) and Fig. 5.3a). Due to the dynamic model inputs in the z-regressors and x-regressors the emission models predict the dynamical engine emissions, see Sect. 5.4. Consequently the quality criterion $J_{dyn}$ describes the dynamical loss function of the engine transient. At each engine operation point the modelled emissions $\hat{c}_{nox}$ and $\hat{c}_{mss}$ are weighted by the weights $w_{nox}$ and $w_{mss}$ and determine the loss function $J_{dyn}$.

As discussed in Sect. 5.3.5, the $NO_x$ emissions and the engine torque have a similar dependency to the model inputs in the x-regressors, see Fig. 5.5 and Fig. 5.6. Consequently, the consideration of the engine torque in the loss function is implicitly included with the $NO_x$ emission model. Furthermore, the engine torque differs not too much with different courses of the air mass flow rate, respectively the cylinder air content, see Fig. 6.3. Thus, in a first step the quality criterion (6.2)

is limited to the quantities $NO_x$ emissions and particulate emissions, but this global loss function could be further extended to consider influencing variables like engine torque, hydrocarbon emissions or engine noise.

**Analytical Solution of the Optimisation Criterion**

Both emission models $\hat{c}_{nox}$ and $\hat{c}_{mss}$ are bilinear interpolated polynomials of order 3, see Eq. (5.3). Consequently, the loss function $J_{dyn}$ is also such a stationary polynomial function. When all model inputs except $x_{eng,out}$ are given, Eq. (6.2) can be rewritten as

$$J_{dyn}\left(x_{eng,out}(t)\right)\big|_{(\mathbf{z},\mathbf{x}')} = a\left(\mathbf{z},\mathbf{x}'\right)x_{eng,out}^3(t) + b\left(\mathbf{z},\mathbf{x}'\right)x_{eng,out}^2(t) + c\left(\mathbf{z},\mathbf{x}'\right)x_{eng,out}(t) + d\left(\mathbf{z},\mathbf{x}'\right) \tag{6.4}$$

with

$$\mathbf{z} = [n_{eng}(t),\, u_{inj}(t)] \quad \text{and} \quad \mathbf{x}' = [p_{2i}(t),\, \hat{T}_{2i}(t),\, \varphi_{mi}(t)]. \tag{6.5}$$

The dynamical inputs $\mathbf{z}$ and $\mathbf{x}'$ allow to express the third order polynomial loss function $J_{dyn}\left(x_{eng,out}(t)\right)$ at every instant of time during a transient. Its coefficients $a$, $b$, $c$ and $d$ are determined by the engine operation point $\mathbf{z}$ and the remaining air path and injection quantities $\mathbf{x}'$. The composition of the coefficients $a \dots d$ in (6.4) can be clarified as follows. The extracting of $x_{eng,out}$ alias $x_1$ out of the set of model inputs in Eq. (6.3) shifts all other quantities $x'_i$ in Eq. (6.5) by 1

$$x'_i = x_{i+1} \quad \text{for} \quad i = 1 \dots 3. \tag{6.6}$$

The local coefficients $a_j \dots d_j$ are determined by the structure of the local polynomial models (5.4) and they are subsequently superimposed (5.3) by their global validity (5.7) to the global coefficients $a \dots d$. The weighting of the local $NO_x$ and particulate model according to (6.2) can by given for instance for the local coefficient $c_j$ by (5.4) as

$$c_j\left(\mathbf{x}'\right) = w_{nox}\left(w_{1,j,nox} + w_{3,j,nox}x'_1 + w_{3,j,nox}x'^2_1 \dots\right) + $$
$$w_{mss}\left(w_{1,j,mss} + w_{3,j,mss}x'_1 + w_{5,j,mss}x'^2_1 \dots\right). \tag{6.7}$$

Next, the weights of this relationship are summarised to one weight per regressor, e.g. $w_{1,j} = w_{nox}w_{1,j,nox} + w_{mss}w_{1,j,mss}$. Further, the feasible set $\mathcal{A}$ of 31 regressors for a four dimensional local model (5.5) can be separated into feasible sets of regressors for the single coefficients $a \dots d$.

$$|\mathcal{A}_a| = 1 \qquad |\mathcal{A}_b| = 4 \qquad |\mathcal{A}_c| = 7 \qquad |\mathcal{A}_d| = 19 \qquad (6.8)$$

Thus, the maxima and minima of the loss function (6.4) can be solved analytically, as the roots of its derivative with respect to $x_{\mathrm{eng,out}}$. In which maxima and minima are assigned to the roots with help of it the second derivative with respect to $x_{\mathrm{eng,out}}$.

These derivatives with respect to $x_{\mathrm{eng,out}}$ is are achieved offline and eliminate the coefficient $d$ with its 19 feasible regressors for the first derivative and the coefficients $c$ and $d$ for the second derivative. Thus, the first derivative contains only 12 remaining regressors, while 5 regressors remain for the second derivative.

Having dynamical model inputs in $\mathbf{z}$ and $\mathbf{x}'$, the determined minima for each time step is the dynamical optimal reference value $x_{\mathrm{eng,out,opt}}$ with respect to the loss function (6.2). In comparison to other optimisations, where a complex loss function similar to (6.2) has to be calculated several times to optimise a single time step, this ingenious approach utilises the properties of the polynomial models for an analytical optimisation and reduces the computation demand dramatically. This gets obvious in the comparison of the set of feasible regressors. A single calculation of (6.2) demands the calculation of the $NO_x$ model and particulate model with 31 feasible regressors, while the analytical optimisation method depends on the calculation of the derived loss function with 12 and 5 regressors for the first and second derivative.

**Control Concept with Optimised Reference Values**

According to the control concept $x_{\mathrm{eng,out,opt}}$ can be controlled directly by a dynamical reference value generation as given in Sect. 7.8 or it can be transformed to a demanded air mass flow rate $\dot{m}_{\mathrm{air,opt}}$. This reference value consists of a dynamical air mass flow rate at the intake valve $\dot{m}_{\mathrm{air,dyn,opt}}$ (3.35) and compensates gas storage in the intake volumes $V_{2\mathrm{i}} + V_{2\mathrm{c}}$ by the partial derivative of the ideal gas law, see Eq. (D.1).

$$\dot{m}_{\mathrm{air,des,opt}} \approx \dot{m}_{\mathrm{air,dyn,opt}} + \frac{\mathrm{d}p_{2\mathrm{i}}}{\mathrm{d}t} \frac{V_{2\mathrm{i}} + V_{2\mathrm{c}}}{R\hat{T}_{2\mathrm{i}}} = \frac{(x_{\mathrm{eng,out,opt}} + L_{\mathrm{st}})\hat{\dot{m}}_{\mathrm{f}}}{1 - x_{\mathrm{eng,out,opt}}} + \frac{\mathrm{d}p_{2\mathrm{i}}}{\mathrm{d}t} \frac{V_{2\mathrm{i}} + V_{2\mathrm{c}}}{R\hat{T}_{2\mathrm{i}}} \qquad (6.9)$$

A special emphasis should be placed on the appropriate choice of the loss function weights $w_i$ in (6.2). Generally, the engine calibration process results in optimised stationary reference values for the controlled variables. These reference values can be optimal with regard to an objective mathematical quality criterion or optimal with respect to the subjective objective criterion of the calibration engineer. Thus, the major objective of a dynamical optimisation should be to reach the calibrated stationary reference values in steady state. For this reason the weights $w_i$ are chosen in every engine operation point $\mathbf{z}$, such that a local minimum occurs in (6.4) with the stationary calibrated reference values of $\mathbf{x}$. Consequently, the optimisation of (6.4) delivers the stationary calibrated reference value of $x_{\mathrm{eng,out}}$, if the quantities $n_{\mathrm{eng}}$, $u_{\mathrm{inj}}$, $p_{2\mathrm{i}}$, $\hat{T}_{2\mathrm{i}}$, $\varphi_{\mathrm{mi}}$ are in steady state.
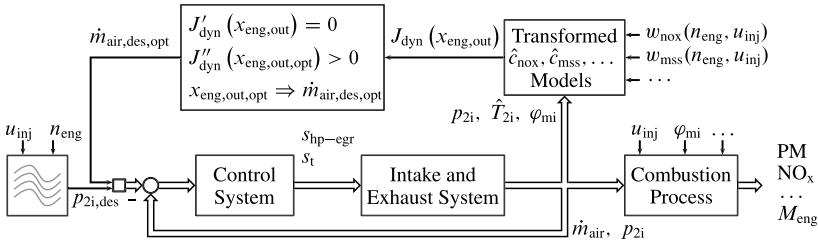
**Figure 6.4:** Control structure considering the dynamics of air path quantities to obtain optimised reference values for the air mass flow rate control

Fig. 6.4 shows the control concept to generate transient optimised reference values for an air mass flow rate control. The measured air path quantities $p_{2i}$ and $\hat{T}_{2i}$ in the intake manifold as well as $\varphi_{mi}$ are inputs for the stationary emission models. The weights $w_i$ superimpose the emission models and form the multi-criteria loss function (6.2). With the given air path and injection quantities, this loss function can be reduced to an one-dimensional polynomial of order 3 with the input $x_{eng,out}$ (6.4). The local minima $x_{xeng,out,opt}$ of (6.4) can be determined analytically from its first and second derivative under the conditions $J_{dyn}\left(x_{eng,out}\right)' = 0$ and $J_{dyn}\left(x_{eng,out,opt}\right)'' > 0$. This optimised reference value $x_{eng,out,opt}$ can be transformed with (6.9) to an optimised reference value for an air mass flow rate control. The use of measured air path quantities for reference value generation can be considered as partial optimisation of the dynamical air path control. At each instant of time during an engine transient an optimal reference value to control the quantities $\dot{m}_{air}$, respectively $x_{eng,out}$ is derived. In the following comparison of results, this control structure with optimised reference values from Fig. 6.4 is termed $x_{opt,ctl}$.

### Dynamical Optimised Versus Stationary Optimised Reference Values

Sect. 6.2.1 compared the course of air path, emission and combustion quantities for the control concepts $\dot{m}_{air,ctl}$, $r_{egr,ctl}$, $x_{2i,ctl}$. Next, this comparison is expanded for the course of dynamical optimised reference values $x_{opt,ctl}$ and follows the same engine transient as given in Fig. 6.3. In Fig. 6.5a) the excitation signal $u_{inj}$ and the time behaviour of the air path quantities $x_{eng,out}$ and $\dot{m}_{air}$, as well as the emission quantities $\hat{c}_{nox}$ and $\hat{c}_{mss}$ are shown. The time marks ($\star, \square, +, *, \times$) connect the emission time responses chronologically with their projection on the particulate-NO$_x$ tradeoff in Fig. 6.5b). During the first 0.75 s of the time response $x_{opt,ctl}$ delivers reference values for $x_{eng,out}$ which are between the references for $r_{egr,ctl}$ and $x_{2i,ctl}$. Subsequently, the optimised reference values have a similar characteristics as the results of the EGR-rate control. The different characteristics of the control concepts in $x_{opt,ctl}$ can also be transferred by (6.9) to the air mass flow rate $\dot{m}_{air}$. In terms of the emissions' time responses the control concept with optimised reference values has dynamical emissions, which are almost settled after 0.5 s to their stationary quantity and only a small decreasing trend in the $\hat{c}_{nox}$ concentration remains. For the conventional control concepts, the dynamical emissions are settled after 2 s, see also Fig. 6.3. A projection of the time responses to the particulate-NO$_x$ tradeoff in Fig. 6.5b) distinguishes the differences between the

control concepts with respect to the particulate $\hat{c}_{mss}$ and $NO_x$ emissions $\hat{c}_{nox}$. The marker symbols define equal instants of time. Since the engine operation point is stationary in $n_{eng}$ and $u_{inj}$, the air mass flow rate control $\dot{m}_{air,ctl}$ proceeds near a *Pareto optimum* with low accumulated emissions. Disadvantageous are the long-lasting high $NO_x$ emissions, which result on the other hand in lower particulate emissions. The control concept $x_{2i,ctl}$ has less dynamical $NO_x$ emissions and after 1 s an emission level is reached, for which $\dot{m}_{air,ctl}$ takes more than 1.5 s. Though, the dynamical particulate emissions are larger than these of an air mass flow rate control. Among the three conventional control concepts, the EGR-rate control results in the lowest dynamical $NO_x$ emissions at the expense of higher particulate emissions.
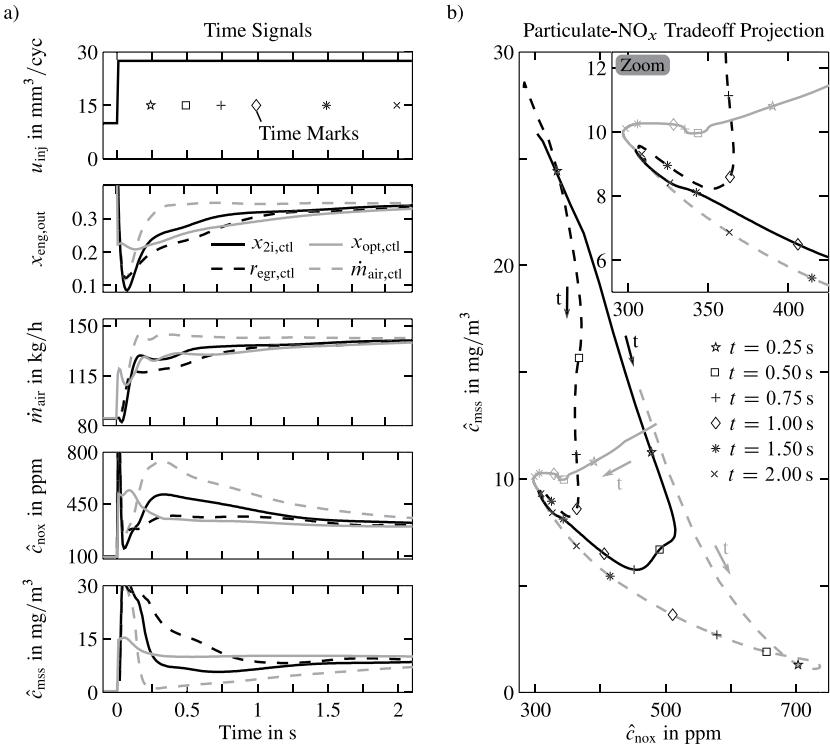


**Figure 6.5:** a) Time signals of the air path quantities and the emissions with different control concepts (Sect. 6.2.1) and dynamical optimised reference values for a load step from $u_{inj} = 10 \, mm^3/cyc$ to $u_{inj} = 27 mm^3/cyc$ at $n_{eng} = 2250 \, min^{-1}$. b) Projection of the time signals to the Particualte-$NO_x$ tradeoff

The trajectory for the optimised reference values $x_{opt,ctl}$ points straight towards the stationary emission level. Enlarged particulate and $NO_x$ emissions are optimised with respect to the quality criterion (6.2) in approximately equal proportions. As opposed to conventional control concepts, this

control concept favours neither of the emission components. A zoom in the section of the equilibrium indicates, that the dynamical emissions are almost at a level of the stationary emissions after 0.5 s with $x_{opt,ctl}$. The conventional control concepts reach a similar emission level after 1 s ($r_{egr,ctl}$), 1.5 s ($x_{2i}$) and 2 s ($\dot{m}_{air,ctl}$).

**Table 6.2:** Normalised and accumulated quantities for emissions and torque with different control concepts

| Emission Concentrations | $\dot{m}_{air,ctl}$ | $r_{egr,ctl}$ | $x_{2i,ctl}$ | $x_{opt,ctl}$ |
|---|---|---|---|---|
| $\overline{c}_{nox,dyn}/\hat{c}_{nox,stat}$ | 1.633 | 1.114 | 1.294 | 1.078 |
| $\overline{c}_{mss,dyn}/\hat{c}_{mss,stat}$ | 0.467 | 1.244 | 0.854 | 1.076 |
| $\overline{M}_{eng,dyn}/\hat{M}_{eng,stat}$ | 1.083 | 1.053 | 1.065 | 1.073 |
| Accumulated Tailpipe Emissions | | | | |
| $m_{nox}$ in mg | 64.68 | 40.67 | 48.40 | 39.04 |
| $m_{mss}$ in mg | 0.33 | 0.82 | 0.58 | 0.73 |

Tab. 6.2 summarises the dynamical characteristics of emissions and engine torque for the considered load step. The mean value of all quantities is normalised to their stationary value at the load step end. Furthermore, the accumulated tailpipe emissions are given for the different control concepts. Due to the limited air path and actuator dynamics the optimised reference values of $x_{opt,ctl}$ cannot be reached within the first 150 ms after the load step. Consequently, this would result in too small emissions during this period of time. For a fair comparison mean values and accumulated emissions are therefore estimated between 150 ms and 2 s. The quantitative analyse reflects the visual impressions from Fig. 6.3 and Fig. 6.5. For the investigated load step $\dot{m}_{air,ctl}$ has increased NO$_x$ emissions on the benefit of lowered particulate emissions. A $r_{egr}$ control has slightly deteriorated NO$_x$ emissions and significantly enlarged particulate emissions, while $x_{2i,ctl}$ can be regarded as a compromise between both control concepts. The dynamically optimised reference values $x_{opt,ctl}$ result in an emission level, which neither favours one of the emission components and can be regarded as rather neutral. Regarding the delivered engine torque, there are no significant deviations between the control concepts. Also the given tailpipe emissions reflect the observations of the emission concentrations. Generally, dynamical emissions of different control concepts differ from stationary calibrated emissions and disarrange the stationary calibrated emission level. Such a dynamical shifting of the particulate-NO$_x$ tradeoff can be considered in the optimisation by penalising $\Delta m_{nox,dyn}$ and $\Delta m_{mss,dyn}$ in the optimisation constraints. Or it can be avoided by dynamical optimised reference values $x_{opt,ctl}$. For these dynamical optimised reference values no additional calibration effort is necessary, since they are derived from the stationary engine calibration. The chosen analytical optimisation is low on computational demand, since the number of feasible regressors of the quality criterion is drastically reduced from 31 to 12 by the utilised derivative of the polynomial emission models. Further investigations and a rating of the dynamical emission formation of $\dot{m}_{air,ctl}$, $r_{egr,ctl}$ and $x_{opt,ctl}$ during the complete driving cycle are given in Sect. 7.9.

## 6.3   Summary

This chapter focuses on the optimisation of reference values for the air path control and the injection timing. The dual EGR path optimisation results of Sequenz (2013) are compared in Fig. 6.1 to the series HP-EGR calibration and show the potential of a LP-EGR system to further lower the engine's raw emissions.

An analysis of the dynamical emission formation lays the foundation to derive a dynamical reference value optimisation with respect to the emissions. The raw emissions of an air mass flow rate control, an EGR-rate control and an intake air content control are compared during a load step. It is shown, that the dynamical emission formation deviates from the stationary calibrated emission level. Anymore, the transient emissions differ significantly from control concept to control concept. These deviations result from the different dynamics in the intake and exhaust system and are mainly driven by the slow charge-air pressure dynamics and the faster cylinder air content. As consequence the air mass flow rate control has larger $NO_x$ emissions at lower particulate emissions, the EGR-rate control emissions are vice versa and the air content control has equally enlarged emissions. Based on these researches optimised reference values for the air path control are derived. In this optimisation the charge-air pressure is controlled conventional and the fast adjustable cylinder charge is optimised with respect to the current influencing variables $p_{2i}$, $\hat{T}_{2i}$ and $\varphi_{mi}$. The optimisation is carried out analytically by superimposing a polynomial loss function of order three with respect to the weighted $NO_x$ and particulate emissions. The key feature of this optimisation is the analytical solution of the optimisation problem given by the roots of the loss function's first derivative. The first derivative of polynomials can be analytically determined in advance and notably reduces the number of regressors. This simplified model can be implemented in an ECU and a real-time capable optimisation can be carried out. These optimised reference values neither favour $NO_x$ nor particulate emissions and result in a dynamical emission level close to a stationary engine calibration.

In the next chapter the control structure with stationary and dynamical optimised reference values is presented in Fig. 7.1. Afterwards in Sect. 7.9 the contribution of the dynamical emissions on the accumulated driving cycle emissions is evaluated and discussed.

# 7 Air Path Control Design and Dynamical Reference Value Generation

After the control variables of the dual EGR path system have been identified, this chapter covers the control design. First an overview about state of the art air path control structures is given. Then different classical PID and novel semi-physical motivated control structures for the air path quantities are derived and validated with test bench measurements. The final part of this chapter is devoted to the reference value generation for the LP-EGR control with consideration of the gas propagation dynamics. This chapter closes with a combination between reference value generation and air path control scheme and rates different control concepts by their dynamical emissions during the driving cycle. As a final result the increase of the accumulated driving cycle emissions by dynamical engine operation is compared to the stationary engine operation for all considered control concepts.

The air path control of Diesel engines with HP-EGR and turbocharger has been an intensive field of research and many control concepts have been developed to control the strongly coupled gas system quantities. A first overview of general design methods and application areas for the control of Diesel engines is given in Guzzella and Amstutz (1998). In the beginning of air path control with HP-EGR and manipulable turbocharger it was mostly sufficient to have a closed-loop control for only one air path quantity. Isermann et al. (2000) show a model-based approach for a gain scheduled charge-air pressure control with stationary feedforward control. A further map-based PID-control scheme for the charge-air pressure control of truck engines is given in Schaffnit (2002). van Nieuwstadt et al. (2000) compare different multi-variable control strategies with de-centralised PI-controllers, a control Lyapunov function and a rank one controller with regard to the tailpipe emissions.

Schloßer (2000) introduces an attempt for a decoupling multi-variable control of the air mass flow rate and the charge-air pressure. Decentralised decoupling PID-controllers are parameterised with a simplified linearised process model with fixed time constant and operation point dependent process gain. Furthermore, the potential of a model predictive control is shown with simulation results. Rückert (2004) simplifies the coupled system of air mass flow rate and charge-air pressure to a system of operation point varying first order lag elements and derives a gain-scheduled model predictive control for these quantities. Richert (2006) optimises the air path actuator trajectories with a model predictive control, which is based upon a step-wise linearisation of a semi-physical air path model. Ortner and del Re (2007) present a further model predictive control approach based on linear parameter varying models. Even more applications of model predictive control can be found in Herceg et al. (2006) and Drews et al. (2009).

Several control concepts for the multi-variable control of air mass flow rate and charge-air pressure are presented and compared in von Pfeil (2011). The basis for most of these control concepts are local linear engine models which are either parameterised by an experimental engine identification or by linearisation of a mean value engine model. The shown control concepts are gain scheduled decentralised PID-controllers, gain scheduled PID-controllers with additional decoupling controllers, state-space controllers with partial decoupling and a state-space based internal model control. Also Kohlhase (2011) utilises gain scheduled decentralised PID-controllers with stationary coupling terms to control the quantities $r_{egr}$ and $\dot{m}_{air}$. Jung (2003) presents a $H_\infty$ robust multi-variable control, while a further $H_\infty$ gain schedule control approach based on linear parameter varying models is given in Wei (2006). Another approach in Rajamani (2005) utilises an observer-based nonlinear feedback control to control the air path quantities air-fuel ratio and air content in the intake manifold. A further nonlinear control based on a control Lyapunov function is shown in Jankovic et al. (2000) and further extended with integral action in Wahlström (2009).

First approaches for a physical motivated control scheme use a reference value transformation of the air mass flow rate and the charge-air pressure into intermediate controlled variables. Schwarte et al. (2007) and von Pfeil (2011) propose to control the exhaust back pressure $p_3$ as intermediate control variable for the charge-air pressure $p_{2i}$. With this $p_3$-control a VGT-trajectory results from an inverted turbine mass flow rate model. A control signal for the HP-EGR-valve is given by model inversion of the HP-EGR flow equation for compressible fluids (3.22). Ammann (2003) presents a semi-physical air management system, which controls the measured quantities exhaust back pressure $p_3$, charge-air pressure $p_{2i}$ and air mass flow rate $\dot{m}_{air}$. The $p_3$-controller provides a fast turbine power build up in an inner cascade, while the charge-air pressure controller corrects the reference value for the $p_3$-controller in an outer control-loop. In this control structure several control-oriented models of the turbocharger power and the gas system quantities adapt the reference values for the controllers.

**Semi-Physical Control Law**

A further development in physical control results in the inversion of the turbocharger power balance to determine a nonlinear control law for the turbocharger actuator. Schopp et al. (2009) present the combination of an inverse control of the stationary turbocharger power balance with nonlinear PID-controllers to control the charge-air pressure. Youssef et al. (2007) motivates the inversion of the turbocharger power balance with the flatness methodology and utilises $n_{tc}^2$ as the flat model output to obtain a control law for the VGT-actuator. In a similar manner Schwarzmann (2008) derives a flatness based internal model control with a model inversion of the turbocharger maps to solely control the charge-air pressure. In Moulin and Chauvin (2011) the turbocharger power balance approach of Youssef et al. (2007) is simplified with a *singular perturbation method* to a first order reference system with the compressor pressure ratio as state variable. A dynamical inversion of this simplified model results in a feedback linearisation and an additional integral term is added to compensate model uncertainties. An extension of this turbocharger model inversion control scheme also accounts for disturbances from either HP- or LP-EGR on the turbocharger power balance in Moulin et al. (2010). Zimmermann et al. (2015) show that a single engine can

lead to hundreds of application variants tailored for individual market applications and propose to replace conventional engine map-based approaches by physical model-based approaches. In this approach physically-oriented equations master the complexity of the coupled nonlinear air path with a global approximation of the system behaviour. Due to the modular structure of the physically-oriented model, single components are easily interchangeable for different market applications.

**Feedforward Control**

The closed-loop air path control of Diesel engines with various control concepts has attracted much attention in the research community, while the development of appropriate feedforward control structures has been neglected. State of the art feedforward control structures for the air path control are mainly restricted to stationary characteristic maps, which usually correspond to the actuator control signals during stationary engine operation (Isermann et al., 2000; Nitzke and Rebohl, 2000). Some approaches extend these stationary feedforward controllers by a $PDT_1$-element to achieve a dynamical feedforward control (Hafner, 2002; Isermann, 2010; von Pfeil, 2011). However, there is no method for a systematic calibration of these $PDT_1$-elements for all possible engine transients in a map based control structure yet (Isermann, 2010; von Pfeil, 2011).

Further advantages in the feedforward control of Diesel engines are made in Kohlhase (2011) and von Pfeil (2011), who utilise a model follow-up control structure for the control of the air path quantities. Their control structure combines a feedforward control with filtered reference values, which both result from the state feedback control of a linear-parameter varying model. This dynamical feedforward control also partly decouples the air path quantities and further accounts for actuator saturation. Furthermore, the controlled outputs of this model act as filtered reference values for underlying controllers, which only have to compensate the deviations between the feedforward model and the engine process.

**LP-EGR Control**

Various control concepts are applied for turbocharged Diesel engines with HP-EGR, but only a few publications consider the recent development towards turbocharged Diesel engines with two EGR paths. In Mueller et al. (2005) a model-based predictive controller consisting of a state observer, a prediction and an optimisation algorithms is used to control the two path EGR-system. An optimised actuator position of two controlled variables $\dot{m}_{air}$ and $p_{2i}$, respectively $\dot{m}_{air}$ and $r_{egr}$ is determined by a heuristic algorithm. Another approach in Heuck et al. (2008) presents a predictive air management system with the LP-EGR fraction of the collective EGR-mass flow rate as a calibration parameter. The desired position of the air path actuators are determined by a predictive model-based method. Non-measured states are modelled by a real time air path model. In the latter approach the charge-air pressure is not controlled. Both approaches require high computation time and the algorithms to calculate the values of the manipulated variable are not trace-

able. Another nonlinear approach based on model inversion of a semi-physical model is presented in Chauvin et al. (2011). Either HP-EGR or LP-EGR and the charge-air pressure are controlled. However, to reach future emission limits both EGR-paths should be controlled simultaneously.

## 7.1 Air Path Control Scheme

Based on the findings of the previous chapters, a control scheme for the air path with HP- and LP-EGR is derived in the following and depicted in Fig. 7.1. In the LP-EGR system there are significant dynamics of the air content with dead times of up to 2.5 s for one cycle through the intake and exhaust system, which are caused by long gas transportation times, see Sect. 4.4. Further, the air content between single storages has the characteristics of a plug flow, which results in abrupt changes in the air content of single storages. The air content model with a pipe receiver approach from Sect. 4.4 is capable to model these air content dynamics and utilises measured quantities as model inputs. The air content shows inherent dynamics, which can't be described by standard control variables like the air mass flow rate or EGR-rate. Thus, the air content can be either closed-loop controlled or considered by a feedforward control.
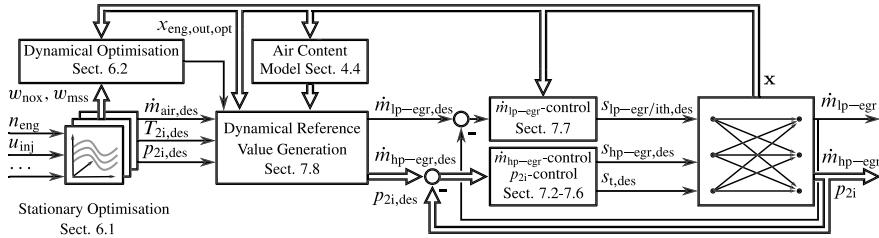


**Figure 7.1:** Air path control scheme

A closed-loop control is always reacting to compensate disturbances and it is assumed that it reacts too slow on the abrupt changes in the approaching air contents. Furthermore, these sudden air content changes are strong changes in the gain of the controlled process, which complicate a control design with good disturbance rejection and necessary robustness. Thus, the modelled air content is utilised in a feedforward control. In Fig. 7.1 this feedforward control is termed dynamical reference value generation. It utilises the modelled air contents of several storages from Sect. 4.4 as intermediate control variables to transform stationary optimised reference values for the air mass flow rate and intake temperature from Sect. 6.1 into reference values for a LP-EGR and a HP-EGR mass flow rate controller. On demand, the dynamical reference value generation can replace the setpoint of the air mass flow rate by dynamical optimised reference values $x_{eng,out,opt}$, as given in Sect. 6.2.

As a result of the system analysis from Sect. 4.1, it is shown that the LP-EGR-actuators have only minor interactions to the quantities $\dot{m}_{hp-egr}$ and $p_{2i}$, while there is a strong interaction between HP-EGR-valve, VGT-actuator and the quantities $\dot{m}_{lp-egr}$, $\dot{m}_{hp-egr}$ and $p_{2i}$. Hence, the controllers

for LP-EGR can be designed independently from the controllers of HP-EGR and charge-air pressure, see Fig. 7.1. In which the derived LP-EGR controller implicitly incorporates all interactions from HP-EGR-valve and VGT-actuator, while the $\dot{m}_{hp-egr}$ and $p_{2i}$ controller design decouples the interactions between HP-EGR-valve and VGT-actuator.

After the air path control scheme is motivated, follows an outline of the succeeding chapter. At first a control structure to control the quantities $\dot{m}_{hp-egr}$ and $p_{2i}$ is presented in Sect. 7.2. The control structure contains of a feedforward control and a decentralised PI(D)-control.[1] These PI(D)-controller are designed in Sect. 7.3. Next in Sect. 7.4, the semi-physical relationships of the parameterised mean value engine model from Chap. 3 are converted into a novel semi-physical feedforward control, which decouples the controlled quantities. This feedforward control is transformed in Sect. 7.5 to a nonlinear semi-physical internal model control of $\dot{m}_{hp-egr}$ and $p_{2i}$. Afterwards in Sect. 7.6, the controllers and feedforward control are evaluated with measurements of the engine test bench.

In Sect. 7.7 the LP-EGR mass flow rate is controlled separately by a semi-physical control, which utilises the dependency of the LP-EGR rate on the actuator position and its invariance to other air path quantities as control law, see Sect. 4.2.1. This coherence copes for changes in the engine operation point, compensates influences from the HP-EGR-valve and VGT-actuator and simplifies the resulting controller.

Later in section 7.8 a dynamical reference value generation is motivated. This reference value generation transforms stationary $\dot{m}_{air,des}$ and $T_{2i,des}$ reference value maps from Sect. 6.1 or dynamical optimised reference values for $x_{eng,out,opt}$ (Sect. 6.2) into reference values for the HP- and LP-EGR controllers. By considering the states of the air content model from Sect. 4.4, the air contents act as intermediate control variables and the inherent air content dynamics of the singles storages are incorporated into the reference value generation.

Finally, in Sect. 7.9 the different control concepts are rated with regard to their driving cycle emissions and generated engine torque. In this comparison the contribution of dynamical and stationary driving cycle parts are separated and compared to the emissions expected from a stationary engine operation in the operation points covered by the driving cycle.

## 7.2 Control Structure for HP-EGR and Charge-Air Pressure

The main purpose of the air path control is to supply the combustion process with the optimal air content, so that the driver's torque demand can be met while the emissions stay within their calibrated limits. In this context, the dynamical rather slow charge-air pressure control loop seems to be the limiting factor to reach a fast torque response. This slow turbocharger dynamics is also a reason for the deviations between the stationary and the dynamical emission formation, see Sect. 6.2. In order to improve this behaviour, a dynamical fast and accurate reference following

---

[1] $\dot{m}_{hp-egr}$ is controlled by a PI-controller and $p_{2i}$ is controlled by a PID-controller. The PI-controller is chosen, to avoid a noise amplification in the rather disturbed signal $\dot{m}_{hp-egr}$ by the derivative characteristics of a PID-controller

for the control loops of all controlled air path quantities is demanded. However, there is usually a trade-off between the controller's reachable reference following performance and the controller's robustness to nonlinearities, model uncertainties and disturbances so that the reachable controller performance has to be limited (Föllinger, 1994).

In state of the art engine control systems the nonlinear process behaviour is generally taken into account by gain-scheduled PID-controllers, whose parameters are stored in engine operation point and operation mode dependent characteristic maps (van Nieuwstadt et al., 2000; Isermann, 2010). Indeed this practice gets limited in its applicability, when the number of controlled variables, influencing quantities like ambient conditions and engine operation modes increase, since simultaneously the number of control parameters for the engine calibration rises. For modern engines the number of engine operation modes can count up to ten (Hadler et al., 2008) and will probably rise in the further engine development. Furthermore, the reachable controller performance with these PID-controllers stays limited. Hence, a novel control structure which can handle different engine operation modes with a moderate calibration effort and simultaneously good control performance is desirable.



$$\mathbf{y}_{des} = \begin{bmatrix} \dot{m}_{hp-egr,des} & p_{2i,des} \end{bmatrix} \qquad \mathbf{u}_{ffc} = \begin{bmatrix} s_{hp-egr,ffc} & s_{t,ffc} \end{bmatrix} \qquad \tilde{\mathbf{s}}_{des} = \begin{bmatrix} \tilde{s}_{hp-egr,des} & \tilde{s}_{t,des} \end{bmatrix}$$

$$\mathbf{y}_{rsf} = \begin{bmatrix} \dot{m}_{hp-egr,rsf} & p_{2i,rsf} \end{bmatrix} \qquad \mathbf{u}_{ctl} = \begin{bmatrix} s_{hp-egr,ctl} & s_{t,ctl} \end{bmatrix} \qquad \mathbf{y} = \begin{bmatrix} \dot{m}_{hp-egr} & p_{2i} \end{bmatrix}$$
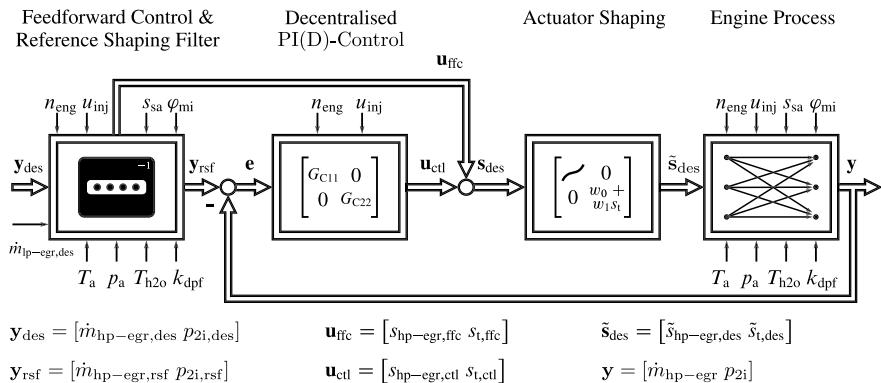
**Figure 7.2:** Two-degree of freedom control structure for the multivariable control of the air path quantities $\dot{m}_{hp-egr}$ and $p_{2i}$, consisting of a feedforward control with reference shaping filter (Sect. 7.4), a decentralised PI(D)-control (Sect. 7.3) and an actuator shaping (Appx. C). $\dot{m}_{lp-egr}$ is controlled separately, but considered in the feedforward control via $\dot{m}_{lp-egr,des}$.

In comparison to a reactive closed-loop control, a preemptive feedforward control can actuate the process with a good performance and is not affected by feedback effects of model uncertainties and disturbances. Assuming a rather accurate feedforward control, only a minor control effort has to be spent by a closed-loop control to ensure that the process meets a given reference following and the closed-loop controller can be designed rather simple for disturbance rejection. Hence, the combination between a sophisticated feedforward control and a simple closed-loop control is promising, see von Pfeil (2011).

Fig. 7.2 illustrates the control structure to control the quantities HP-EGR and charge-air pressure. It consists of a *two-degree of freedom* control structure (Horowitz, 1963; Kreisselmeier, 1999) with a semi-physical feedforward control and decentralised PI(D)-controllers ($G_{C11}$; $G_{C22}$). The non-linear model-based feedforward control utilises the reference value vector $\mathbf{y}_{des}$ to simultaneously derive a feedforward actuation $\mathbf{u}_{ffc}$ and filtered reference values $\mathbf{y}_{rsf}$ for the engine operation point dependent PI(D)-controllers. This filtering avoids an overcompensation by the PI(D)-controllers, which shall only account for deviations between feedforward control and process. The normalised control signal $\mathbf{s}_{des}$ consists of a contribution from the feedforward control $\mathbf{u}_{ffc}$ and the closed-loop control $\mathbf{u}_{ctl}$ and is transformed by an inverse actuator shaping, as given in Appx. C, to the setpoint $\mathbf{s}_{des}$ for the actuator position controllers. These position controllers and the actuator shaping can be seen as an integral part of the engine process and are not further considered in the following. The engine process delivers the controlled variables $\mathbf{y}$ dependent on engine operation point, engine operation mode, ambient conditions and actuation of the air path actuators.

The realisation of this control structure is an enhancement of Kohlhase (2011) and von Pfeil (2011), with a novel feedforward control based on model inversion of a semi-physical mean value engine model, see Sect. 7.4. Kohlhase (2011) and von Pfeil (2011) realise the feedforward control with identified local affine models, which are state space controlled to generate control signals and filtered reference values. However, with a rising engine complexity the dimensionality of models describing the engine process rises. While the input dimensionality rises linear, the volume of the model space rises exponentially, which is known as *curse of dimensionality* (Hastie et al., 2011). Consequently, the amount of training data and the model complexity have to rise exponentially with the dimensionality of the input space, if a constant coverage of the input volume is desired. This fact can limit experimental models to problems with a rather low input dimensionality (Mrosek, 2017). Consequently, a future-proof concept for a feedforward control is necessary, which can also handle the rising complexity of future combustion engines.

Further, given the trends for a modular engine development, at which engines are constructed from equal parts of construction kits, an easy exchange of models and parameters between engine types is preferable. Especially, when one and the same engine has to meet hundreds of application variants tailored for individual market applications (Zimmermann et al., 2015), it is no longer feasible to model each single engine variant by a black-box identification. In that case a semi-physical approach, where only single submodels have to be replaced or parametrised for each engine variant seems to be more productive. Thus, a feedforward control consisting of semi-physical relationships, as given in the model derivation in Chap. 3, seems to be a promising approach. In this approach additional model inputs can be easily introduced by usually low dimensional physical relationships and models can be adapted to different engine variants by replacing the parameters and models for the differing components without the need to parametrise a complete engine model for every change of a component.

Such a novel feedforward control based on model inversion of the semi-physical mean value engine model is illustrated in Fig. 7.2. Contrary to the limited input dimensionality of von Pfeil (2011) with engine speed, injection quantity, HP-EGR-valve and VGT-actuator as model inputs, this feedforward control is capable to include further influences of the decentralised LP-EGR-
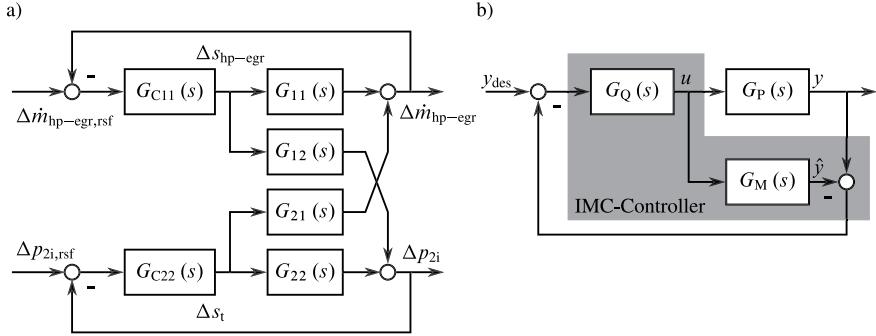
**Figure 7.3:** a) Decentralised control structure for the air path quantities in linearised form b) Internal model control structure

control ($\dot{m}_{\text{lp}-\text{egr,des}}$) and varying ambient conditions $p_a$ and $T_a$ (Mrosek, 2017) into the feedforward signals. Further, the engine conditions $T_{\text{h2o}}$ and $k_{\text{dpf}}$ as well as influences of special engine operation modes, which exemplary result in different swirl actuator positions $s_{\text{sa}}$ and injection timings $\varphi_{\text{mi}}$, are included in the feedforward actuation.

## 7.3 Decentralised PI(D)-Controllers for HP-EGR and Charge-Air Pressure

In this section the parameterisation of the decentralised PID-controllers for the quantities $\dot{m}_{\text{hp}-\text{egr}}$ and $p_{2i}$, which follows directly after the method proposed in von Pfeil (2011), is briefly summarised.

Decentralised PI(D)-controllers can be utilised for the control of multi-variable processes, when the couplings between the single actuators and the controlled variables are not too strong. In that case the multi-variable control problem is reduced to several single-input single-output (SISO) systems with rather simple controllers. Especially the industrial widespread PI(D)-controllers are easy to implement and to understand. They offer the calibration engineer the possibility for a later fine tuning at the engine test bench. Since in the control scheme from Fig. 7.2 most of the response to setpoint changes and the decoupling of the controlled variables $\dot{m}_{\text{hp}-\text{egr}}$ and $p_{2i}$ are undertaken by the semi-physical feedforward control, a simple control structure like the decentralised PI(D)-controllers is sufficient for the compensation of the remaining model inaccuracies and process disturbances.

Fig. 7.3a) shows the linearised block diagram of the decentralised control for $\dot{m}_{\text{hp}-\text{egr,rsf}}$ and $p_{2i,\text{rsf}}$ with the linearised quantities $\Delta$. In this control structure the HP-EGR-valve governs $\Delta\dot{m}_{\text{hp}-\text{egr}}$ and the VGT-actuator controls $\Delta p_{2i}$. The transfer functions are derived by operation point dependent

linearisation of the mean value engine model and the controllers are parameterised in the continuous frequency-domain. For the later implementation these continuous controllers are transformed into discrete form. In case of this coupled system, both controllers $G_{C11}$ and $G_{C22}$ influence each other via the coupling terms $G_{12}$ as well as $G_{21}$ and complicate the decentralised control. Hence, these influences have to be incorporated into the process model for the controller design. Accordingly, the process transfer function $G_{P1}$ for the HP-EGR mass flow rate control

$$\frac{\Delta \dot{m}_{\text{hp-egr,rsf}}(s)}{\Delta s_{\text{hp-egr}}(s)} = G_{P1}(s) = G_{11}(s) \left( 1 - \kappa(s) \frac{G_{C22}(s) G_{22}(s)}{1 + G_{C22}(s) G_{22}(s)} \right) \tag{7.1}$$

is also influenced by the controller $G_{C22}$ via the coupling factor

$$\kappa(s) = \frac{G_{12}(s) G_{21}(s)}{G_{11}(s) G_{22}(s)}. \tag{7.2}$$

This coupling factor (Isermann, 1991) is a quantity for the coupling between the different control loops and it quantifies the interaction between both controllers. Analog to (7.1) also the charge-air pressure process can be expressed as

$$\frac{\Delta p_{2i,\text{rsf}}(s)}{\Delta s_t(s)} = G_{P2}(s) = G_{22}(s) \left( 1 - \kappa(s) \frac{G_{C11}(s) G_{11}(s)}{1 + G_{C11}(s) G_{11}(s)} \right). \tag{7.3}$$

The controller design is performed according to the *sequential loop closing method*, in which the single control loops are closed sequentially (Knapp, 1993; Mayne, 1973). In this procedure the dynamical fastest control loop is closed at first and considers only its main coupling. Then the second control loop is designed and incorporates the first controller. In order to achieve a higher control quality, the sequential closing can be repeated iteratively with the consideration of the afore designed controllers (Huang et al., 2003). This iterative procedure is repeated until all control parameters have converged.

The controller parameterisation is achieved by an *internal model control* (IMC) design with subsequent model reduction approach. Fig. 7.3b) shows the block diagram of the IMC controller (Morari and Zafiriou, 1989), where a plant model $G_M$ is calculated parallel to the controlled process $G_P$. In contrast to a standard control loop, the controller $G_Q$ has only to compensate deviations between the modelled $\hat{y}$ and the measured process output $y$, so that in case of an ideal model this controller yields a pure feedforward control. Generally this IMC-controller shows no control deviation, when the stationary gain of the IMC-filter $G_Q$ is equal to the inverse stationary gain of the plant model $G_M$ (Morari and Zafiriou, 1989). Anymore, the complete IMC-control structure is stable, if both the controller $G_Q$ and the process $G_P$ are stable (Morari and Zafiriou, 1989).

Analog to a feedforward control the IMC-filter is designed as

$$G_Q = (G_{\tilde{M}})^{-1} G_F, \tag{7.4}$$

where $G_{\tilde{M}}$ is the stable invertible part of the plant model $G_M$ and $G_F$ is usually a lowpass filter. In case that the plant model is exact, this yields the reference action of the control loop

$$G_W = G_M G_Q = G_M (G_{\tilde{M}})^{-1} G_F. \tag{7.5}$$

Generally the filter

$$G_F = \frac{1}{(T_W s + 1)^r} \tag{7.6}$$

can be chosen as a lowpass filter with the only calibration parameter $T_W$, which can be tuned as a compromise between control performance and control robustness. The order $r$ has to be chosen such that $G_Q$ can be realised, which means that the degree of the nominator has to be at least as large as the degree of the denominator. For the design of the IMC-filter (7.4) it is necessary to invert the plant model $G_M$. In case that the plant model has non-minimum phase characteristics this inverse is unstable. Hence, most common practice is to mirror the non-minimum phase zeros (positive) at the imaginary axis and replace them by their negative counterparts, which results in the stable invertible part of the plant model $G_{\tilde{M}}$.

This IMC-based controller design yields a compensator with the order of the controlled plant, which is not suitable for a series implementation and a later fine tuning at the engine test bench. Hence, these high-order controllers for HP-EGR and charge-air pressure are according to Lee and Edgar (2004) reduced to PI(D)-controllers with the parameters $k_P$, $k_I$, $k_D$, so that the squared deviation between the IMC-controller step response $y_{IMC}$ and the PID-controller step response $y_{PID}$ gets minimal

$$\min_{(k_P, k_I, k_D)} J(k_P, k_I, k_D) = \int_0^\infty (y_{IMC} - y_{PID})^2 \, dt. \tag{7.7}$$

The HP-EGR mass flow rate signal is rather noisy. Consequently, this controller is designed as a PI-controller. Further, the derivative part of the charge-air pressure PID-controller is low pass filtered, in order to be less sensitive to measurement noise. After the PI(D)-controller parameterisation has been covered, the derivation of the semi-physical feedforward control follows in the next section.
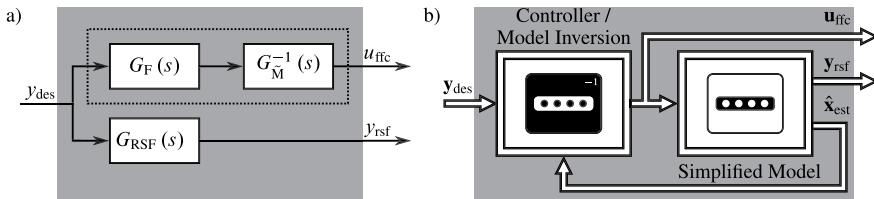
**Figure 7.4:** a) Classical feedforward control with invertible inverse plant model $G_{\bar{M}}^{-1}$, calibrated filter function $G_F$ and reference shaping filter $G_{RSF}$ to avoid overcompensation of feedforward signal by closed-loop controller b) Semi-physical nonlinear model inversion with simplified mean value model for feedforward control and reference value shaping

## 7.4 Semi-Physical Feedforward Control for HP-EGR and Charge-Air Pressure

In this section a feedforward control for the HP-EGR-valve and the VGT-actuator is derived based on the semi-physical relationships of the mean value engine model as described in Chap. 3. This feedforward control directly utilises the identified parameters of the engine model and generates its control signals by model inversion. Thus, it can implicitly account for all uprising applications variants resulting from a change of air path components, which can be modelled by the mean value engine model. Further, it comprises the nonlinearities of the engine process, decouples the quantities $\dot{m}_{hp-egr}$ and $p_{2i}$ and contributes to most of the reference action of the control loop. Consequently, the relatively simple PI(D)-controllers from last section are used for disturbance rejection and to compensate for modelling uncertainties of the feedforward control.

A closed-loop control with one degree of freedom is generally not capable to simultaneously attain a desired reference following and a sufficient rejection of disturbances and process parameter variations (Horowitz, 1963). However, for processes with two access points (process input and process output) there are exactly two degrees of freedom to design the desired reference following and disturbance rejection (Horowitz, 1963; Kreisselmeier, 1999). Generally the closed-loop control is utilised for disturbance rejection and to cope for process variations, while the feedforward control provides the reference following, see also Fig. 7.2. A common structure of a SISO feedforward controller is given in Fig. 7.4a), in which the feedforward controller is composed of the transfer functions $G_F(s)G_{\bar{M}}^{-1}(s)$ and $G_{RSF}(s)$ (Åström and Hägglund, 2005). This structure generates the feedforward control signal $u_{ffc}$ for setpoint changes of $y_{des}$ and applies it to the process, see Fig. 7.2, where feedforward control, closed-loop control and process form the overall control structure. Furthermore, setpoint changes are filtered by a reference shaping filter to $y_{rsf}$, which represents the remaining dynamics. Consequently, under ideal conditions the feedforward control perfectly matches the process and the control deviation $e = y_{rsf} - y$ in Fig. 7.2 becomes zero. However, under real conditions with modelling errors, process nonlinearities, plant variations and disturbances this error is apparent and has to be compensated by a subsequent closed-loop control.

The filters for a classical feedforward control are usually designed comparable to the IMC-filter design (7.4) as a combination of the stable invertible part of the plant model $G_{\bar{M}}$ and a filter $G_F$, so that the resulting transfer function $G_F(s)G_{\bar{M}}^{-1}(s)$ is realisable. The reference shaping filter $G_{RSF}$ avoids an overcompensation of the feedforward signal by the subsequent closed-loop controller and can be designed separately, but is often chosen with the same dynamics as $G_F$. The achievable quality of such a linear SISO feedforward control structure is limited, especially if the process becomes nonlinear and multivariable with strong couplings between the controlled quantities. As a further drawback, this structure cannot consider input saturation in the derivation of the control signal $u_{ffc}$, since there is no information feedback that a control signal has been limited. Therefore, the influence of input saturation can have negative effects on the response to setpoint changes with this feedforward structure and cannot be compensated sufficiently. Especially if a fast feedforward action is demanded, a physically truncated actuation signal can lead to an undesired slow setpoint response, see Kohlhase (2011) and von Pfeil (2011). A better reference action of the control loop under actuator saturation can be achieved with the structure in Fig. 7.4b), where a model of the plant is controlled by a closed-loop control of the model internal states $\hat{\mathbf{x}}_{est}$ and the implicitly generated actuator signals $\mathbf{u}_{ffc}$ act as feedforward signals. Such a feedforward control which implicitly results from a closed-loop controlled model is called *model follow-up control* (Hippe, 2006; Wurmthaler and Kühnlein, 2009; Roppenecker, 2009). A similar control structure with multivariable decoupling state space controllers and local affine models is successfully applied as a feedforward control for the air path of Diesel engines in Kohlhase (2011) and von Pfeil (2011).

When it comes to the recent and future Diesel engine development, the system complexity steadily rises and the air path control has to fulfil stricter requirements. These requirements demand an increased number of influencing variables and engine operation modes which all should be incorporated into the control structure. At this point the local affine models seem not to be manageable anymore with a reasonable effort, since the input dimensionality and the amount of measurements for a reliable model calibration rapidly grows. Hence, a semi-physical engine model can be the key to keep the modelling and parameterisation effort manageable and consequently the control structure from Kohlhase (2011) and von Pfeil (2011) is modified for a semi-physical feedforward control scheme. This control scheme is based on a model inversion of the semi-physical mean value engine model with a decoupling of the quantities charge-air pressure and HP-EGR mass flow rate. In that case the controller in Fig. 7.4b) has to be replaced by the model inversion control and the simplified model represents a control-oriented mean value model.

The derivation of the semi-physical feedforward control is structured as follows. First the turbocharger power balance inversion is derived. Then follows the combination of the turbocharger model inversion with a control-oriented engine model to a model follow-up control. Afterwards a feedforward scheme for the HP-EGR actuation signal is derived and the overall semi-physical feedforward control functionality is analysed with simulations. Then some further aspects on the charge-air pressure control are solved. Finally, the control is validated with engine test bench measurements.

### 7.4.1 Turbocharger Model Inversion

Fig. 7.5 illustrates the scheme for the feedforward control of the VGT-actuator position $s_{\mathrm{t,ffc}}$ with regard to the two controlled variables compressor mass flow rate $\dot{m}_{\mathrm{c,des}}$ and $p_{\mathrm{2i,des,fil}}$. The fundamental idea of this model-based control is an inversion of the turbocharger power balance (Schopp et al., 2009; Youssef et al., 2007). As novelties a turbocharger model based upon Euler's equation for turbomachinery is utilised, the VGT-actuator transfer function $G_{\mathrm{a,t}}(s)$ is considered and a limitation of the VGT-actuator control signal $s_{\mathrm{t,lim}}$ is introduced. Furthermore, the previous publications implemented the inverted turbocharger model in the form of a closed-loop control. In the following, this turbocharger model inversion is implemented into a *model follow-up control* structure with the objective to generate a feedforward control for the VGT-actuator. Then this control signal is not affected by feedback of modelling uncertainties and measurement noise and can generate a better response to setpoint changes. Anymore, this feedforward control scheme considers the $\dot{m}_{\mathrm{hp-egr}}$ controller couplings, derives a feedforward signal for the HP-EGR-valve with a novel control strategy and decouples the two quantities charge-air pressure and $\dot{m}_{\mathrm{hp-egr}}$. Note that in the following all gas system quantities are estimated quantities and denoted with the hat symbol.
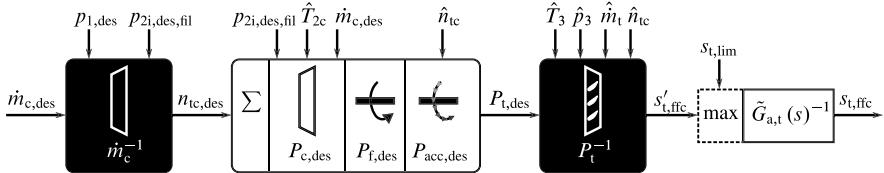


**Figure 7.5:** Model inversion to achieve a control signal for the VGT-actuator by inverting the compressor mass flow rate model and the turbo charger power balance

According to Fig. 7.5 a trajectory for the VGT-actuator $s'_{\mathrm{t,ffc}}$ is given dependent on the reference values for the mass flow rate through the compressor $\dot{m}_{\mathrm{c,des}}$ and the filtered desired charge-air pressure $p_{\mathrm{2i,des,fil}}$. The filtering of $p_{\mathrm{2i,des}}$ determines the response to setpoint changes and is motivated later in Eq. (7.21). However, in a two EGR-loop configuration the quantity $\dot{m}_{\mathrm{c,des}}$ is not directly controlled. In this configuration the controlled variables are the quantities $\dot{m}_{\mathrm{hp-egr,des}}$ and $\dot{m}_{\mathrm{lp-egr,des}}$. Hence, the desired value for $\dot{m}_{\mathrm{c,des}}$ has to be determined by the stationary mass flow rate balance in the intake system

$$\dot{m}_{\mathrm{c,des}} = \dot{m}_{\mathrm{eng,in,des}} - \dot{m}_{\mathrm{hp-egr,des,lim}} \tag{7.8}$$

from the estimated desired mass flow rate entering the cylinder $\dot{m}_{\mathrm{eng,in,des}}$ (7.9) and the currently feasible HP-EGR mass flow rate reference value $\dot{m}_{\mathrm{hp-egr,des,lim}}$ (7.11). The desired mass flow rate entering the cylinder $\dot{m}_{\mathrm{eng,in,des}}$ follows with the filtered desired charge-air pressure $p_{\mathrm{2i,des,fil}}$ and (3.28) as

$$\dot{m}_{\text{eng,in,des}} = \lambda_{\text{a}} \left( n_{\text{eng}}, \ p_{\text{2i,des,fil}}, \ s_{\text{sa}} \right) \frac{p_{\text{2i,des,fil}} n_{\text{eng}} V_{\text{d}} z}{R \hat{T}_{\text{2i}}}. \tag{7.9}$$

At fully opened HP-EGR-valve $(C_{\text{D}}A_{\text{ref}})_{\text{hp-egr,max}}$, the currently maximum mass flow rate $\hat{\dot{m}}_{\text{hp-egr,max}}$ can be determined with Eq. (3.22) and the estimated quantities $\hat{p}_{2\text{i}}$, $\hat{p}_3$ and $\hat{T}_{\text{hp-egr}}$ by

$$\hat{\dot{m}}_{\text{hp-egr,max}} = (C_{\text{D}}A_{\text{ref}})_{\text{hp-egr,max}} \ \frac{\hat{p}_3}{\sqrt{R\hat{T}_{\text{hp-egr}}}} \sqrt{\frac{2\kappa}{\kappa-1} \left[ (\Pi)^{\frac{2}{\kappa}} - (\Pi)^{\frac{\kappa+1}{\kappa}} \right]}$$
$$\text{with} \qquad \Pi = \min \left[ \max \left[ \frac{\hat{p}_{2\text{i}}}{\hat{p}_3}, \left( \frac{2}{\kappa+1} \right)^{\frac{\kappa}{\kappa-1}} \right], 1 \right] \tag{7.10}$$

and gives the limitation for the currently feasible desired HP-EGR mass flow rate

$$\dot{m}_{\text{hp-egr,des,lim}} = \min \left( \dot{m}_{\text{hp-egr,des}}, \hat{\dot{m}}_{\text{hp-egr,max}} \right). \tag{7.11}$$

In order to determine a reference value for the turbocharger speed $n_{\text{tc,des}}$, the compressor model (3.38) is inverted to

$$n_{\text{tc,des}} = f_{\text{LOLIMOT}} \left( \dot{m}_{\text{c,des}}, \ p_{\text{2i,des,fil}} / p_{\text{1,des}} \right) \tag{7.12}$$

and the input quantities are replaced by the demanded reference values $\dot{m}_{\text{c,des}}$, $p_{\text{2i,des,fil}}$ and $p_{\text{1,des}}$. Contrary to the compressor model from (3.38) this model directly incorporates the pressure drop over the charge air cooler by considering the pressure $p_{\text{2i,des,fil}}$. Further, this simplified reference value generation utilises no normalised quantities (3.36) and (3.37) to determine the desired turbocharger speed. A further model input is the expected pressure before the compressor $p_{\text{1,des}}$. It can be determined in two steps. First the expected air mass flow rate $\tilde{\dot{m}}_{\text{air,des}}$ can be determined by a balance equation and the reference value for the LP-EGR mass flow rate controller $\dot{m}_{\text{lp-gr,des}}$ as

$$\tilde{\dot{m}}_{\text{air,des}} = \dot{m}_{\text{c,des}} - \dot{m}_{\text{lp-egr,des}}. \tag{7.13}$$

Then, the desired pressure before the compressor $p_{\text{1,des}}$ can be approximated by rearranging the flow equation (3.21) for incompressible fluids as

$$p_{\text{1,des}} \approx p_{\text{a}} - \left( \frac{\tilde{\dot{m}}_{\text{air,des}}}{(C_{\text{D}}A_{\text{ref}})'_{\text{ith}}} \right)^2 \frac{R T_{\text{a}}}{2 p_{\text{a}}}, \tag{7.14}$$

with the flow parameter[2] for the intake throttle valve $(C_{\text{D}}A_{\text{ref}})'_{\text{ith}}$, the ambient pressure $p_{\text{a}}$ and the ambient temperature $T_{\text{a}}$ as model inputs. In which this approximation only holds for relative

---

[2]Note that $(C_{\text{D}}A_{\text{ref}})'_{\text{ith}}$ is the identified flow parameter for Eq. (3.21) and $(C_{\text{D}}A_{\text{ref}})_{\text{ith}}$ corresponds to the identified parameter of Eq. (3.22). The quantity of both flow parameters is a function of the cross sectional area, which is determined by $s_{\text{ith}}$.

small pressure drops over the intake throttle valve. After the desired turbocharger speed (7.12) has been determined, one can calculate the demanded compressor power $P_{c,des}$ from (3.44), (3.49) and (3.50) to reach the demanded pressure rise $p_{2i,des,fil}/p_{1,des}$ with the desired compressor mass flow rate $\dot{m}_{c,des}$.

$$P_{c,des} = \dot{m}_{c,des} \left( 1 - \frac{k_{slip}\pi d_{c2}n_{tc,des}}{\pi d_{c2}n_{tc,des} + \frac{\dot{m}_{c,des}}{\rho_{2,des}}\frac{\cot(\beta_{c2,b})}{\pi d_{c2}b_{c2}}} \right) \left( (\pi d_{c2}n_{tc,des})^2 + \frac{\dot{m}_{c,des}n_{tc,des}}{\rho_{2,des}}\frac{\cot(\beta_{c2,b})}{b_{c2}} \right) \tag{7.15}$$

In which the desired gas density $\rho_{2,des}$ demands the estimated temperature after the compressor $\hat{T}_{2c}$ as a further model input

$$\rho_{2,des} = \frac{p_{2i,des,filt}}{R\hat{T}_{2c}}. \tag{7.16}$$

Furthermore, the expected friction losses $P_{f,des}$ (3.63) contribute to the stationary power balance. So far only the stationary contributions of $P_{c,des}$ and $P_{f,des}$ to the turbocharger power balance have been regarded. This is sufficient to reach the reference values with the given system dynamics, but the system dynamics are not significantly increased. Thus, also a proportion of the desired turbocharger acceleration $P_{acc,des}$ can be considered in the power balance to increase the dynamics of the controlled system. According to Newton's second law of motion, the shaft acceleration results with the shaft inertia from (3.62) and a power balance unequal to zero. Hence, the desired power for the turbocharger acceleration can be approximated by replacing the derivative $\dot{n}_{tc}$ with the finite difference $(n_{tc,des} - \hat{n}_{tc})\,k_{tc,acc}$ as

$$P_{acc,des} = 4\pi^2 I_{tc}\hat{n}_{tc}(n_{tc,des} - \hat{n}_{tc})\,k_{tc,acc}. \tag{7.17}$$

In this equation $k_{tc,acc}$ is a tuning parameter, which allows to speed up the turbocharger by penalising deviations between the desired turbocharger speed and the modelled turbocharger speed. Suitable values for $k_{tc,acc}$ are $0 \ldots 5\,\text{s}^{-1}$. Finally, the summation of all stationary (7.15), (3.63) and dynamical (7.17) power demands gives the power, which is demanded from the turbine

$$P_{t,des} = -(P_{c,des} + P_{f,des} + P_{acc,des}). \tag{7.18}$$

This desired power can be transformed with (3.59) and the quantities $\hat{T}_3$, $\hat{p}_3$, $\hat{m}_t$ and $\hat{n}_{tc}$ to

$$\left( \frac{\cot(\alpha_{t3})}{b_{t3}} \right)_{des} = -\frac{\hat{\rho}_3}{\hat{m}_t^2\hat{n}_{tc}}P_{t,des}. \tag{7.19}$$

Note that the fraction term before the desired turbine power $P_{t,des}$ characterises the currently available quantities to drive the turbine and therefore does not contain any desired quantities. Anymore,

the effects of heat transfer are not incorporated into the determination of $\hat{\rho}_3$ in this control-oriented model. Finally, an inversion of the simplified VGT-model (3.60) by a look-up table results in the desired trajectory of the VGT-actuator $s'_{t,ffc}$.

$$s'_{t,ffc} = f\left(\left(\frac{\cot(\alpha_{t3})}{b_{t3}}\right)_{des}\right) \tag{7.20}$$

The final control signal $s_{t,ffc}$ is then derived after a further signal limitation with the signal $s_{t,lim}$ and a partly compensation of the actuator dynamics $\tilde{G}_{a,t}(s)^{-1}$. This further limitation prevents the charge-air pressure control from lowering the pressure drop over the HP-EGR path, so that it becomes inoperative. These further actions to finally derive the feedforward signal $s_{t,ffc}$ will be discussed later on in Sect. 7.4.5.

So far the generation of $s'_{t,ffc}$ is similar to the semi-physical turbocharger controls in Schopp et al. (2009) and Youssef et al. (2007) and differs only in the utilised turbocharger model. However, there are some issues in this approach which will be improved in the following. Due to model simplifications and model inaccuracies this semi-physical turbocharger control will most likely show a steady-state error. Consequently, Youssef et al. (2007) introduce a parallel working integral controller into the control scheme. Schopp et al. (2009) eliminate this control-deviation with an additional PID-controller. On the one hand these additional controllers eliminate the control-deviation, on the other hand they can show a poor performance for set point changes. For sudden reference value changes both the semi-physical controller and the additional controller will try to eliminate the control-deviation. Therefore, large control-deviations can tend to be overcompensated by these two parallel working controllers. This effect could be reduced by an appropriate reference shaping filtering or a weaker tuning of the additional controller. However, these structural deficits demand some fiddling to coordinate the semi-physical turbocharger control and the parallel working linear controller. Hence, another way to overcome steady-state deviations and performance limitations of a closed-loop control is chosen.

## 7.4.2 Model-Inversion Model Follow-Up Control

For the semi-physical control by model-inversion many quantities are necessary ($\hat{T}_{2c}, \hat{n}_{tc}, \hat{T}_3, \hat{p}_3, \hat{m}_t$) and have to be either modelled or measured. Assuming that only a few additional quantities are simulated, one can obtain a control-oriented mean value model for the major system dynamics. Thus, the control by model-inversion can be applied to the control-oriented model in form of a model follow-up control, as shown in Fig. 7.2 and Fig. 7.4b). Then all feedback loops to the engine intake and exhaust system are disconnected and the nonlinear control turns into a feedforward control. Further, the control-oriented model acts as a reference shaping filter for the charge-air pressure control and generates the set points for the underlying PI(D)-controllers in Fig. 7.2, which only has to compensate the deviations between the model and the process quantities.
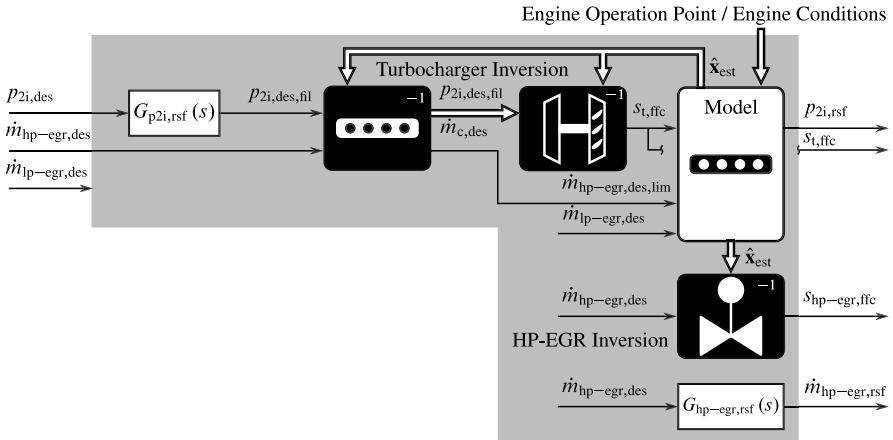
**Figure 7.6:** Block diagram of the model-inversion model follow-up control, which generates the feedforward control signals $s_{hp-egr,ffc}$, $s_{t,ffc}$ and the filtered reference values $\dot{m}_{hp-egr,rsf}$, $p_{2i,rsf}$ for the subsequent closed-loop controllers.

Fig. 7.6 illustrates the overall structure of the model follow-up control based on model-inversion. It basically consists of the four parts reference shaping filters, turbocharger inversion, HP-EGR inversion and a control-oriented model. This feedforward control considers the couplings between HP-EGR, LP-EGR and the turbocharger and generates control signals and reference values for the underlying charge-air pressure and HP-EGR controllers. The functionality of the HP-EGR-valve inversion and the separate LP-EGR control will be discussed later in Sect. 7.4.3 and Sect. 7.7.

In this structure the quantities $p_{2i,des}$ and $\dot{m}_{hp-egr,des}$ are filtered by $G_{p2i,rsf}$ and $G_{hp-egr,rsf}$. The HP-EGR filter $G_{hp-egr,rsf}$ is designed to adjust the reference value for the subsequent PI-controller to the feedforward action process response. So that the PI-controller does only compensate deviations between feedforward control and engine process. It is designed as a first-order lag element with the time constant $T_{hp-egr,rsf}$. Next, the charge-air pressure filter $G_{p2i,rsf}$ determines the desired reference value trajectory for the turbocharger model inversion. The dynamics of the charge-air pressure are of higher order and are determined by the VGT-actuator dynamics (see Fig. 4.4) and the turbocharger momentum of inertia. Hence, a second order reference shaping filter

$$G_{p2i,rsf}(s) = \frac{p_{2i,des,fil}(s)}{p_{2i,des}(s)} = \frac{1}{\left(T_{p2i,rsf}s + 1\right)^2} \tag{7.21}$$

with the time constant $T_{p2i,rsf}$ is applied to give the trajectory $p_{2i,des,fil}$ for the turbocharger power model-inversion in Fig. 7.5. Afterwards, $\dot{m}_{hp-egr,des}$ is transformed by (7.8) to (7.11) into $\dot{m}_{c,des}$ and the inverted turbocharger power balance from Fig. 7.5 results in the control signal $s_{t,ffc}$. This control signal, the reference values $\dot{m}_{lp-egr,des}$ and $\dot{m}_{hp-egr,des,lim}$ as well as the engine operation

Feedforward Control and Reference Shaping Filter
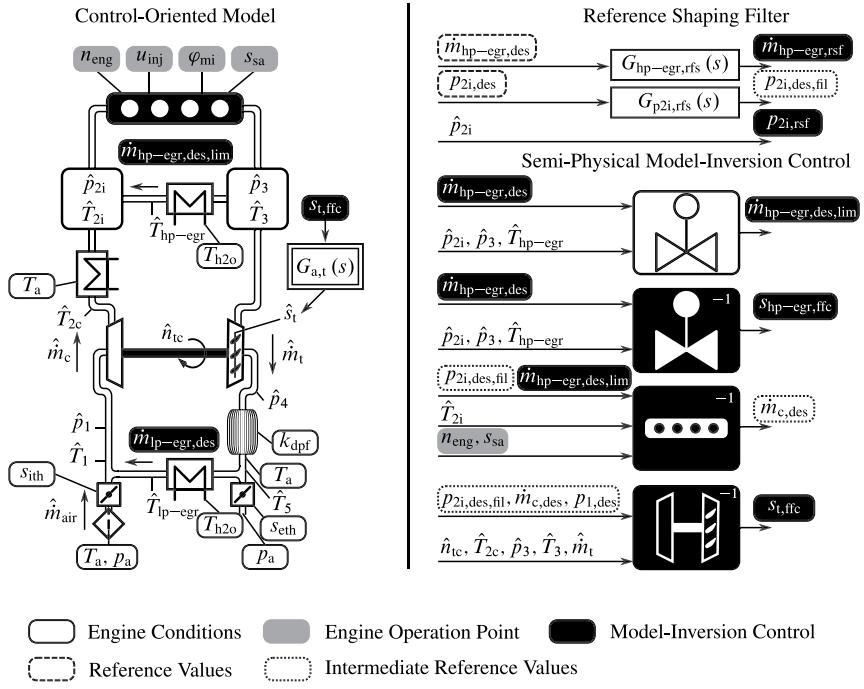


**Figure 7.7:** Model structure of the semi-physical model-based feedforward control and the reference shaping filter

point quantities and the engine conditions are inputs for a mean value engine model, which simulates the necessary quantities $\hat{\mathbf{x}}_{est}$ for the turbocharger model-inversion and the HP-EGR inversion. Furthermore, this controlled model also yields the reference value $p_{2i,rsf}$ for the underlying PID charge-air pressure control.

A more detailed view of this feedforward control and the control-oriented model is given in Fig. 7.7. The model delivers all quantities to derive the control signals $s_{t,ffc}$ and $s_{hp-egr,ffc}$ as well as a feasible course of the charge-air pressure $p_{2i,rsf}$. With the aim that the resulting feedforward signals also implicitly consider the engine operation mode and the engine conditions, these quantities are utilised as further model inputs for the control-oriented model. The engine conditions cover coolant temperature $T_{h2o}$, ambient pressure $p_a$, ambient temperature $T_a$ and load of the Diesel particulate filter $k_{dpf}$. Different engine operation modes are characterised by engine speed $n_{eng}$, desired injection quantity $u_{inj}$, start of the main injection $\varphi_{mi}$, position of the swirl actuator $s_{sa}$ and actual intake or exhaust throttling of the LP-EGR system. This LP-EGR throttling depends on the system configuration and can be either implemented as intake throttle valve $s_{ith}$ or as exhaust

throttle valve $s_{eth}$. With the consideration of these additional influences no more additional calibration of the feedforward control for engine warm-up or strongly varying process gains resulting from changes in the ambient conditions is necessary (Mrosek, 2017).

As a special feature the mass flow rates in both EGR-paths are not modelled with the flow equation for compressible fluids. Instead, the mass flow rates corresponding to the reference values $\dot{m}_{hp-egr,des,lim}$ and $\dot{m}_{lp-egr,des}$ are directly impressed into the model. This has mainly two advantages. First it is possible to compensate the feedback loop for the later derived model inversion of the HP-EGR-valve, see Sect. 7.4.3. Second the necessary states to model the mass flow rate before and after the LP-EGR-valve have not to be modelled as states and can be alternatively described with algebraic expressions. This reduces the modelling effort for the control-oriented model. Nevertheless, this simplified model can still consider couplings between LP-EGR system, HP-EGR system and charge-air pressure in the feedforward control signals. Given the states pressures and temperatures, the LP-EGR path mainly influences the gas temperature before the compressor as well as the pressures $\hat{p}_1$ and $\hat{p}_5$. The estimated mixing temperature $\hat{T}_1$ can be approximated by the balance equation

$$\hat{T}_1 \approx \frac{\dot{m}_{air} T_a + \dot{m}_{lp-egr,des} \hat{T}_{lp-egr}}{\dot{m}_{air} + \dot{m}_{lp-egr,des}} \tag{7.22}$$

and (7.13) by replacing the variable of the desired value $\dot{m}_{c,des}$ with the simulated quantity $\hat{\dot{m}}_c$. The effect of the LP-EGR on the pressure $\hat{p}_1$ can be estimated similar with (7.13) and (7.14). If the LP-EGR is manipulated with an exhaust throttle valve, one only has to consider the fixed air filter orifice in Eq. (7.14). The pressure $\hat{p}_5$ can be approximated analogue to $\hat{p}_1$ with the modified flow orifice $(C_D A_{ref})'_{eth}$ by solving Eq. (3.21) for the upstream pressure[3] as

$$\hat{p}_5 = \frac{p_a}{2} + \sqrt{\left(-\frac{p_a}{2}\right)^2 + \frac{R\hat{T}_5 \left(\hat{\dot{m}}_t - \dot{m}_{lp-egr,des}\right)^2}{2\left((C_D A_{ref})'_{eth}\right)^2}}, \tag{7.23}$$

where the mass flow rate through the exhaust pipe follows as the difference between $\hat{\dot{m}}_t$ and $\dot{m}_{lp-egr,des}$. Then, the pressure upstream the DPF can be determined accordingly as

$$\hat{p}_4 = \frac{p_5}{2} + \sqrt{\left(-\frac{\hat{p}_5}{2}\right)^2 + \frac{R\hat{T}_5 \hat{\dot{m}}_t^2}{2\left((C_D A_{ref})_{dpf} k_{dpf}\right)^2}}. \tag{7.24}$$

Supposing that no exhaust throttle valve is used, Eq. (7.23) becomes obsolete and the pressure $\hat{p}_5$ in Eq. (7.24) can be approximated by $p_a$. All other quantities in Fig. 7.7 are modelled similar to the

---

[3]Note that solving Eq. (3.21) for the upstream pressure has two solutions, in which only one is physically meaningful.

mean value engine model in Chap. 3. As a final feature the VGT-actuator has a dynamics, which depends on the direction of actuation, see Fig. 4.4. This dynamical characteristics is approximated in the control-oriented model in Fig. 7.7 by the nonlinear transfer function

$$G_{a,t}(s) = \frac{\hat{s}_t(s)}{s_{t,ffc}(s)} = \frac{1}{T_{a,t}s + 1} \qquad \text{with } T_{a,t} = \begin{cases} \acute{T}_{a,t}, & \text{for } s_{t,ffc}(t) - \hat{s}_t(t) \geq 0 \\ \grave{T}_{a,t}, & \text{for } s_{t,ffc}(t) - \hat{s}_t(t) < 0 \end{cases} \qquad (7.25)$$

and incorporated into the feedforward control scheme.

Contrary to the turbocharger model-inversion control schemes in the literature, this approach does not need an additional controller to achieve stationary accuracy. Instead of an uncertain process, this model-inversion approach controls the exactly known model. Thus, no noteworthy control-deviations between model and model inversion can be observed, since the significant maps for VGT-actuator (3.60) and compressor mass flow rate (7.12) are used in their original and inverse form. Hence, the inversion control can manipulate its exact counterpart, the control-oriented model, in a way that all reachable reference values can be achieved within the numerical precision and no additional parallel controller is necessary. Furthermore, in this structure almost[4] all feedback loops to the process are broken. Thus, this feedforward control scheme can be designed for a high-performance response to setpoint changes.

### 7.4.3  HP-EGR Model-Inversion

The second controlled variable in the model-inversion approach is the HP-EGR mass flow rate. In recent literature about semi-physical HP-EGR control, a HP-EGR mass flow rate control based on a feedback inversion is commonly suggested (Wahlström and Eriksson, 2007; Schwarte et al., 2007; von Pfeil, 2011). Such a feedback approach is depicted in Fig. 7.8, where the reference value $\dot{m}_{hp-egr,des}$ and the fed back quantities[5] $\hat{\mathbf{x}}_{est}$ are inserted into Eq. (3.22) to derive $(C_D A_{ref})_{hp-egr,des}$. Then a further inversion of the valve's characteristic curve delivers the desired actuator position $s_{hp-egr,ffc}$. The achievable position $\hat{s}_{hp-egr,ffc}$ follows delayed by the actuator transfer function $G_{a,hp-egr}$.
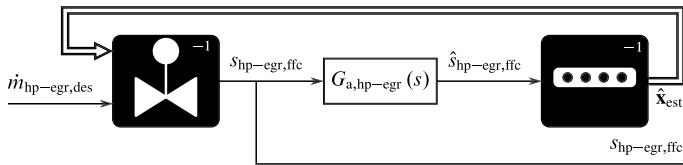


**Figure 7.8:** Structure of the HP-EGR model inversion control by feedback inversion

---

[4] $s_{ith}$, $s_{eth}$ and in case of a closed-loop combustion control $\varphi_{mi}$ feedback some process signals into the feedforward control.

[5] Depending on the utilised approach $p_3$, $p_{2i}$ and $T_{hp-egr}$ are directly measured or modelled quantities.
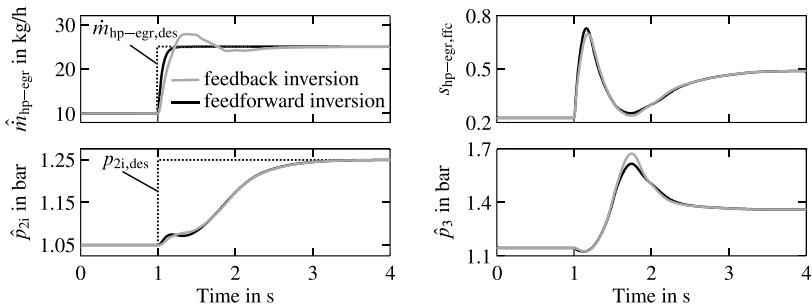
**Figure 7.9:** Simulated comparison of the HP-EGR feedforward control by feedback model-inversion and feedforward model-inversion structure at $n_{eng} = 2250\,\text{min}^{-1}$ and $u_{inj} = 15\,\text{mm}^3/\text{cyc}$ for a step of $\dot{m}_{hp-egr,des}$ and $p_{2i,des}$

This approach comes with several issues, which are introduced via the feedback loop. First for an ideal model-inversion the reference value $\dot{m}_{hp-egr,des}$, the system states $\hat{\mathbf{x}}_{est}$ and the actuator position $\hat{s}_{hp-egr,ffc}$ have to chronologically match. However, due to the apparent actuator dynamics this cannot be achieved and the achievable actuator position $\hat{s}_{hp-egr,ffc}$ follows delayed to the ideal position $s_{hp-egr,ffc}$. Secondly the HP-EGR actuator position has a strong and dynamical fast impact on the pressures $p_{2i}$ and $p_3$, see Fig. 4.2 and Sect. 4.1.1. These dynamical fast influences are fed back to the signal generation of $s_{hp-egr,ffc}$ and result in not fully satisfactory control results.

In this dissertation the model follow-up control structure offers novel possibilities to break the feedback loop of the HP-EGR-valve model inversion and allows to rearrange it to a pure feedforward control. Fig. 7.6 and Fig. 7.7 show the structure of the feedforward model inversion. In the model follow-up mean value model the HP-EGR-valve is not modelled by the flow equation for compressible fluids. Instead the limited mass flow rate $\dot{m}_{hp-egr,des,lim}$ is directly impressed into the mean value model and the quantities $\hat{p}_{2i}$, $\hat{T}_{hp-egr}$ and $\hat{p}_3$ result from this impressed mass flow rate, see Fig. 7.7. In Fig. 7.6 these quantities are part of the vector $\hat{\mathbf{x}}_{est}$, which allows to invert the flow equation (3.22) for the feedforward signal $s_{hp-egr,ffc}$. This approach allows to eliminate the feedback loop and creates a pure feedforward control.

The differences between the commonly utilised feedback inversion and the novel feedforward inversion approach are illustrated in Fig. 7.9 with simulations of the model follow-up model for the reference value followings of a simultaneous step in $p_{2i,des}$ and $\dot{m}_{hp-egr,des}$. In case of the feedback inversion approach the HP-EGR mass flow rate is modelled by the flow equation. It can be clearly noticed, that the feedback inversion approach from Fig. 7.8 shows an overshoot and undershoot behaviour in $\hat{\dot{m}}_{hp-egr}$ until the stationary reference value can be reached. This unsatisfying response to setpoint changes is caused by the finite actuator dynamics and the feedback effects of the quantities $\hat{p}_{2i}$, $\hat{p}_3$ and $\hat{T}_{hp-egr}$.

The novel feedforward model inversion approach has a smooth response to setpoint changes and the controlled variable $\hat{\dot{m}}_{hp-egr}$ reaches its setpoint significantly faster. However, both approaches
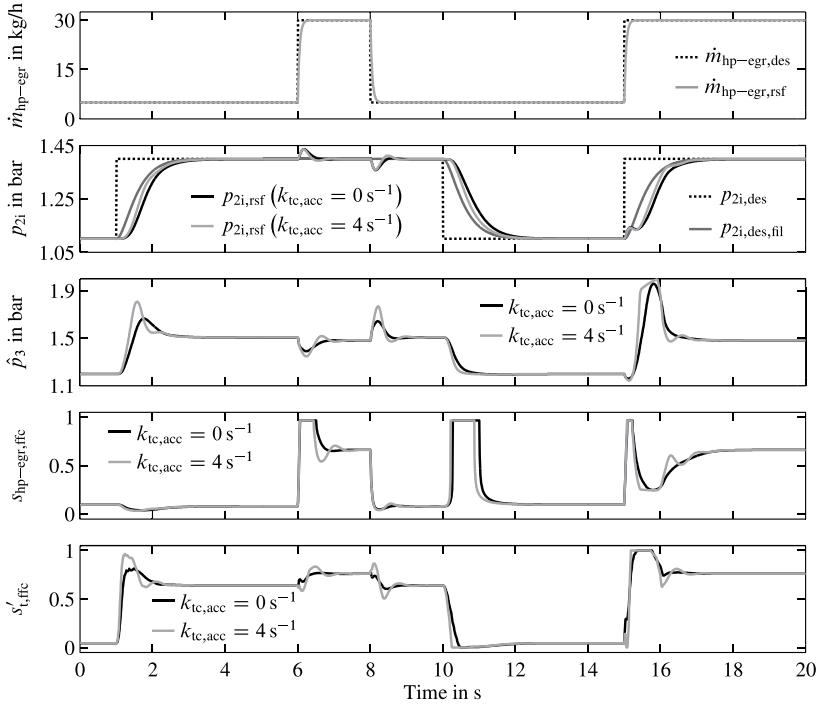
**Figure 7.10:** Model-inversion control $k_{tc,acc} = 0\,s^{-1}$, $k_{tc,acc} = 4\,s^{-1}$, $n_{eng} = 2250\,min^{-1}$ $u_{inj} = 20\,mm^3/cyc$

show a comparable actuation of $s_{hp-egr,ffc}$. Hence, in the case of a feedforward control where an additional controller compensates the deviations between the feedforward controller and the setpoint also the conventional feedback inversion approach can deliver reasonable feedforward signals. Nevertheless, this counts only for feedforward signals for the HP-EGR control variable. In the multivariable case with a concurrent charge-air pressure control, the over- and undershoots of the HP-EGR feedback approach disturb the feedforward control of the coupled charge-air pressure control. Thus, one should prefer the novel feedforward model inversion approach since it delivers more accurate control signals and does not disturb the charge-air pressure control loop with unnecessary disturbances.

### 7.4.4 Model Follow-Up Control Simulation

Fig. 7.10 reveals an example to clarify the principle of the model follow-up control scheme from Fig. 7.6 to derive the feedforward control signals $s_{hp-egr,ffc}$ and $s'_{t,ffc}$. Several reference value steps

are applied to the quantities HP-EGR mass flow rate and charge-air pressure. Besides these quantities also the exhaust pressure $\hat{p}_3$ and the corresponding actuator signals $s_{hp-egr,ffc}$ and $s'_{t,ffc}$ are shown. Note that in Fig. 7.10 only the functionality of the inverse turbocharger power balance from Fig. 7.5 for the signal $s'_{t,ffc}$ is investigated. All further aspects to derive the final control signal $s_{t,ffc}$ are motivated in the subsequent section.

At first a step on $p_{2i,des}$ is applied at a time of 1 s. The step signal is filtered by the reference shaping filter (7.21) and yields the reference $p_{2i,des,fil}$ for the turbocharger model inversion control from Fig. 7.5. Depending on the intake and exhaust system conditions the turbocharger model inversion control derives the control signals for the VGT-actuator. This control scheme can be configured by the reference shaping filter time constant $T_{p2i,rsf}$ and the acceleration factor $k_{tc,acc}$. The time constant in (7.21) solely determines the response to setpoint changes, while the parameter $k_{tc,acc}$ in (7.17) acts as a proportional controller, which reduces deviations between the desired and the estimated turbocharger speed. Hence, this parameter influences both, the reference action of the control loop and the disturbance rejection of the model inversion control. In Fig. 7.10 the control results are shown for the control with no additional turbocharger acceleration ($k_{tc,acc} = 0\,\mathrm{s}^{-1}$) and a moderate turbocharger acceleration ($k_{tc,acc} = 4\,\mathrm{s}^{-1}$). In the response to setpoint changes it can be noticed, that the acceleration factor brings the controlled signal $p_{2i,rsf}$ closer to its reference value $p_{2i,des,fil}$, but results in a larger actuation of the control signal $s'_{t,ffc}$. Furthermore, with a larger factor $k_{tc,acc}$ the influences to the exhaust pressure $\hat{p}_3$ and consequently the HP-EGR feedforward control signal $s_{hp-egr,ffc}$ becomes larger. Hence, the factor $k_{tc,acc}$ should be limited to achieve a reasonable demand of control energy and moderate couplings to the other control variables.

The control signal for the HP-EGR-valve is derived by impressing the filtered HP-EGR mass flow rate into the control oriented model. Then the feedforward position $s_{hp-egr,ffc}$ can be calculated from the resulting air path states, see Fig. 7.6. The achieved control signals can be seen in Fig. 7.10. Anymore, it gets obvious that the novel combination of the charge-air pressure and the HP-EGR mass flow rate control in the model follow-up control structure implicitly compensates the strong couplings between these two quantities and the corresponding control signals. Only minor couplings remain in the charge-air pressure at a time of 6 and 8 s. These couplings are caused by the non-minimum phase characteristics of the HP-EGR-valve and can be hardly compensated by the VGT-actuator with its limited actuation speed.

### 7.4.5  Further Aspects on Charge-Air Pressure Control

In the derivation of the turbocharger control signal $s_{t,ffc}$ in Sect. 7.4.1 some aspects in the charge-air pressure control have been left open. So far only the derivation of the control signal $s'_{t,ffc}$ in Fig. 7.5 has been covered. This control signal is further limited to keep the HP-EGR control loop operable and a further inverse filtering can partly compensate actuator dynamics.

First the limitation with regard to an operable HP-EGR control is motivated. The previous investigations of the VGT-actuator couplings in Sect. 4.1.2 showed, that a too fast opening of the VGT-actuator dynamically decreases the pressure $p_3$ so fast, that the pressure drop over the HP-

EGR-valve rapidly decreases and even a negative pressure drop ($p_{2i} > p_3$) can occur. In this case the HP-EGR mass flow rate drops and can even change direction, while an overshoot in $\dot{m}_{air}$ can be observed. As a consequence the HP-EGR-valve is not capable to drive the desired mass flow rate anymore and a $NO_x$ overshoot can be observed (Mrosek, 2017). The scenario of an opening VGT-actuator with a decreasing charge-air pressure occurs mainly during a load drop, when the injection quantity is decreased. During this transient it is more important to recirculate a large amount of exhaust gas to maintain low $NO_x$ emissions than to quickly decrease the charge-air pressure. Thus, in the following the opening of the VGT-actuator is limited in a way, such that the pressure drop over the HP-EGR-valve is large enough to drive the desired mass flow rate.
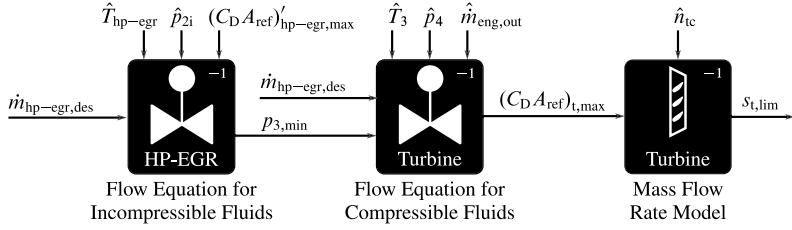


**Figure 7.11:** Limitation of the VGT-actuator to avoid an insufficient pressure ratio to maintain a desired mass flow rate through the HP-EGR-valve

Fig. 7.11 shows the scheme to keep the HP-EGR-valve operational via a limitation of the VGT-actuator position $s_{t,lim}$. At first the minimal necessary pressure to drive the desired HP-EGR mass flow rate $p_{3,min}$ is derived. It is approximated by modelling the flow restriction as incompressible and rearranging Eq. (3.21) as

$$p_{3,\mathrm{min}} \approx \frac{\hat{p}_{2i}}{2} + \sqrt{\left(\frac{\hat{p}_{2i}}{2}\right)^2 + \left(\frac{\dot{m}_{\mathrm{hp-egr,des}}}{(C_D A_{\mathrm{ref}})'_{\mathrm{hp-egr,max}}}\right)^2 \frac{R\hat{T}_{\mathrm{hp-egr}}}{2}}. \tag{7.26}$$

The input quantities are given as the currently demanded mass flow rate $\dot{m}_{\mathrm{hp-egr,des}}$, the estimated states in the air path $\hat{p}_{2i}$ and $\hat{T}_{\mathrm{hp-egr}}$ and the product of flow coefficient and reference area for a maximal opened valve $(C_D A_{\mathrm{ref}})'_{\mathrm{hp-egr,max}}$, which is parameterised by the flow equation for incompressible fluids. Next, the turbine flow equation (3.22) is solved for the currently allowed maximal turbine opening $(C_D A_{\mathrm{ref}})_{\mathrm{t,max}}$, in which the turbine mass flow rate is estimated via (4.15) from $\dot{m}_{\mathrm{hp-egr,des}}$ and $\hat{\dot{m}}_{\mathrm{eng,out}}$. Afterwards, the minimal VGT-actuator opening $s_{t,lim}$ can be determined by an inverted mass flow rate model for the turbine, see Sect 3.3.1. Finally, this VGT-actuator limitation can be implemented into the turbocharger model inversion from Sect. 7.4.1.

In Fig. 7.12 the effectiveness of the VGT-actuator limitation is compared to a conventional charge-air pressure control. Both approaches are implemented into the model follow-up control scheme to generate the feedforward signals $s_{t,ffc}$ and $s_{hp-egr,ffc}$. At a time of 1 s the desired injection quantity is decreased. This typically results in a decreased demand of charge-air pressure $p_{2i,des}$ and an
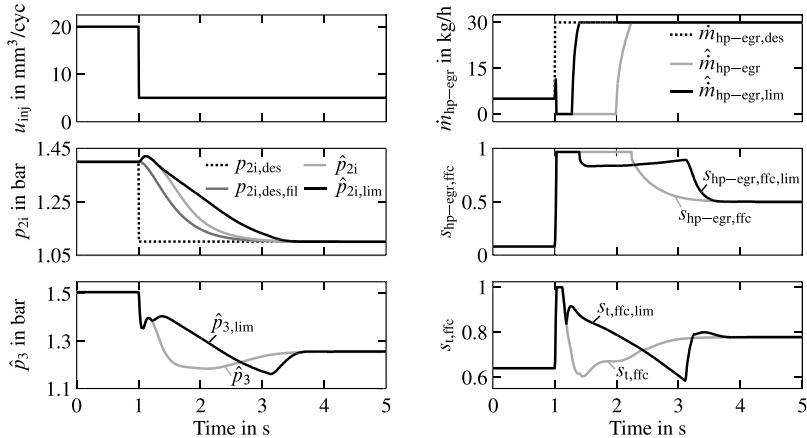
**Figure 7.12:** Effect of the VGT-actuator limitation on the model inversion control for a typical simultaneous step in injection quantity, HP-EGR and charge-air pressure at $n_{\text{eng}} = 2250\,\text{min}^{-1}$)

increased demand of HP-EGR mass flow rate. In case the charge-air pressure is controlled conventionally ($\hat{p}_{2i}$), the controller opens the VGT-actuator ($s_{\text{t,ffc}} \to 0$) to lower the turbine power and to decrease the charge-air pressure as it is desired. This controller action also decreases the pressure $\hat{p}_3$ in the exhaust manifold. At the same time the HP-EGR-valve $s_{\text{hp-egr,ffc}}$ widely opens in order to maintain the desired increase in mass flow rate. However, due to the charge-air pressure controller action the pressure drop over the HP-EGR-valve is not large enough to drive any mass flow rate $\hat{m}_{\text{hp-egr}}$. Only after $\hat{p}_{2i}$ has fallen below $\hat{p}_3$ at a time of 2 s the quantity $\hat{m}_{\text{hp-egr}}$ begins to rise and after it reaches its reference value at a time of 2.2 s the HP-EGR-valve becomes capable to control again and slowly closes.

In comparison to the conventional control, the novel introduced limitation of the VGT-actuator control signal $s_{\text{t,ffc,lim}}$ keeps the HP-EGR-valve operational over most of the transient. In Fig. 7.12 this limitation results in a delayed opening of $s_{\text{t,ffc,lim}}$ and consequently the pressures $\hat{p}_{2i,\text{lim}}$ and $\hat{p}_{3,\text{lim}}$ are slower decreasing. At the same time the HP-EGR-valve is still operational and can deliver the demanded mass flow rate, as it can be seen in the quantities $s_{\text{hp-egr,ffc,lim}}$ and $\hat{m}_{\text{hp-egr,lim}}$. Only at the beginning, this limitation is not capable to handle the non-minimum phase effects in $\hat{p}_{2i,\text{lim}}$, which result in an inoperative HP-EGR-valve for the first 200 ms of this setpoint change (1 . . . 1.2 s). During the remaining transient a small control reserve prevents the HP-EGR-valve from being fully opened (1.2 . . . 3.1 s). This control reserve is situated in Eq. (7.26) and can be calibrated by the factor $(C_D A_{\text{ref}})'_{\text{hp-egr,max}}$. It is necessary to allow the complete valve operation at the real process with apparent modelling uncertainties. In contrast to the conventional charge-air pressure control this limitation extends the necessary time for the charge-air pressure drop, but keeps the HP-EGR path operational.

As a second aspect a partial compensation of the VGT-actuator dynamics $\tilde{G}_{a,t}(s)^{-1}$ is applied to derive the final feedforward control signal in Fig. 7.5. This actuator compensation shows derivative characteristics. Due to the absence of fed back measurement noise it can be applied to the feedforward control scheme. For this reason the limited signal $s'_{t,ffc,lim}$ is inverse filtered by the transfer function

$$\tilde{G}_{a,t}(s)^{-1} = \frac{s_{t,ffc}(s)}{s'_{t,ffc,lim}(s)} = \frac{0.5\left(\acute{T}_{a,t} + \grave{T}_{a,t}\right)s + 1}{\tilde{T}_{a,t}s + 1}, \qquad (7.27)$$

in which numerator roots compensate the averaged poles of (7.25). The time constant $\tilde{T}_{a,t}$ is a tuning parameter and allows to calibrate the trade-off between actuator compensation and actuating energy. Typical values for $\tilde{T}_{a,t}$ are $0.25 \ldots 0.5$ times the numerator roots.

### 7.4.6 Signal Flow Diagram

In a nutshell Fig. 7.13 shows the interaction between semi-physical feedforward control by model inversion and control-oriented mean value engine model to generate the actuation variables $s_{t,ffc}$ and $s_{hp-egr,ffc}$ as well as filtered reference values $p_{2i,rsf}$ and $\dot{m}_{hp-egr,rsf}$ for the subsequent closed loop controllers. Note the special model inversion of the HP-EGR-valve, in which the feedback loop of an inverted flow equation and the engine model is avoided by impressing the desired mass flow rate $\hat{\dot{m}}_{hp-egr,des,lim}$ directly into the engine model. Afterwards, the model reaction to the impressed mass flow rate is utilised to derive the actuation signal $s_{hp-egr,ffc}$ by model inversion, compare to Fig. 7.8 and Fig.7.9. Furthermore the incorporation of modelled quantities in the model inversion allows to derive control signals, which consider a decoupling of charge-air pressure and HP-EGR mass flow rate.

### 7.4.7 Conclusions on the Semi-Physical Feedforward Control

In summary, this feedforward control derives the control signals $s_{t,ffc}$ and $s_{hp-egr,ffc}$ to control the quantities $p_{2i}$ and $\dot{m}_{hp-egr}$. It is achieved as model follow-up control, where a control oriented mean value model is controlled by a model inversion of the turbocharger power balance and a novel HP-EGR mass flow rate inversion strategy. A decoupling between the strongly interacting turbocharger and HP-EGR-valve and actuator saturation are implicitly included into this control scheme. Anymore the model follow-up control structure delivers feasible trajectories as reference values for the subsequent PI(D)-controllers. These controllers are only utilised to compensate the minor deviations between the feedforward control and the measured quantities. Hence, in this two degree of freedom structure the feedforward control can be designed for a good response to setpoint changes without considering modelling and measurement disturbances, while rather conservatively tuned controllers cope for the compensation of the remaining deviations. This semi-physical feedforward control approach is the consequent continuation of a model-based design
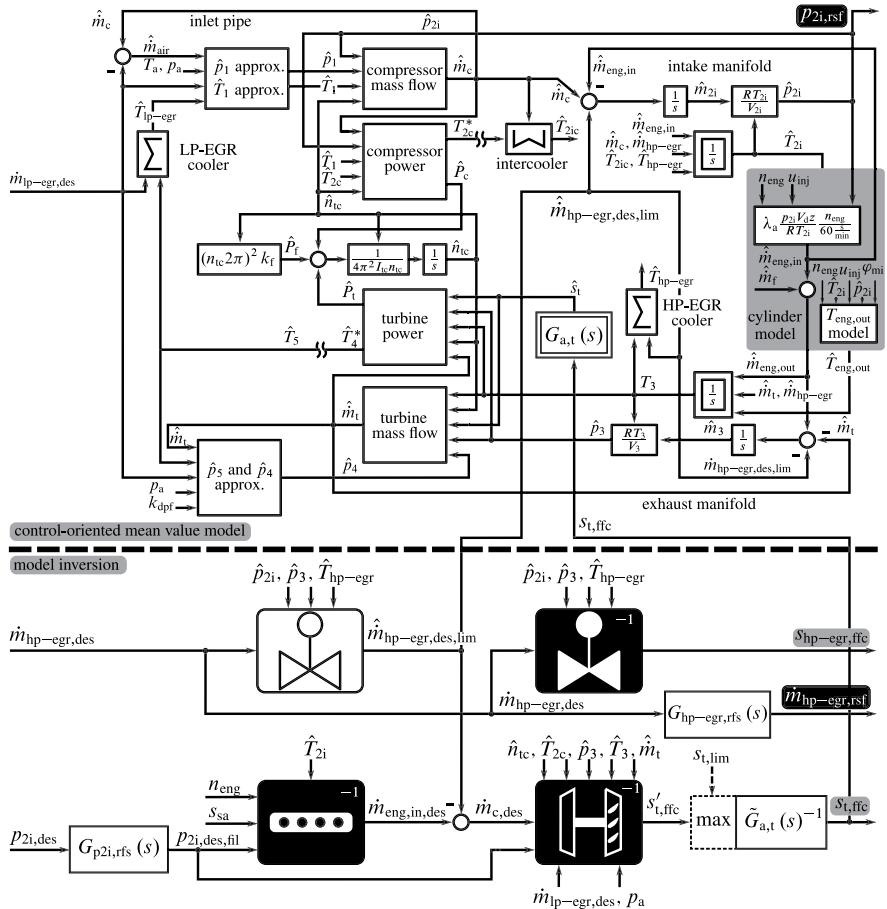
**Figure 7.13:** Signal flow diagram of the semi-physical feedforward control of $p_{2i}$ and $\dot{m}_{hp-egr}$ as model follow up control with a control-oriented mean value engine model

and allows to reuse the mean value engine model for controller implementation. The feedforward approach offers the opportunity to easily tune the control with only three major parameters $(T_{p2i,rsf}, k_{tc,acc}, \tilde{T}_{a,t})$ for the charge-air pressure control and one parameter $(T_{hp-egr,rsf})$ for the HP-EGR control. All further influences like changing ambient conditions, a loaded particulate filter and different engine operation modes are implicitly covered by the control oriented model and its corresponding model inversion. Hence, the often laborious tuning of a multitude of control parameters can be omitted with this approach. As a further benefit the feedforward control can

solely provide the combustion process with a fairly sufficient charge composition in case of detected sensor faults and a switched off closed-loop control. After the extension to a semi-physical internal model control the presented controllers will be evaluated with engine test bench measurements.

## 7.5 Semi-Physical Internal Model Control for HP-EGR and Charge-Air Pressure

In the previous section a control structure with two degrees of freedom is designed. A semi-physical model inversion controls a simplified process model, which generates feedforward signals and reference values for PI(D) closed-loop controllers. This feedforward control consists of a model inversion and a simplified controlled plant model. Referring to Fig. 7.3b), the IMC-filter $G_Q(s)$ can be replaced by the semi-physical model inversion and the plant model $G_M(s)$ can be substituted by the simplified mean value engine model. This yields a semi-physical internal model control, as given in Fig. 7.14. Note, that the IMC charge-air pressure reference value is $p_{2i,des,fil}$, which gives a smooth response to setpoint changes and fast disturbance rejection. A comparable IMC-control scheme, which is based on local linear state space models and state space controllers is utilised in von Pfeil (2011) to control the quantities $\dot{m}_{air}$ and $p_{2i}$. Other state space based IMC-controllers with a similar structure are called *model-state feedback control* and are given in Mhatre and Brosilow (2000) and Wright and Kravaris (2000).



$$\mathbf{y}_{des} = [\dot{m}_{hp-egr,des}\ p_{2i,des,fil}] \qquad \mathbf{u}_{ffc} = [u_{hp-egr,ffc}\ u_{t,ffc}]$$
$$\mathbf{y}_{rsf} = [\dot{m}_{hp-egr,rsf}\ p_{2i,rsf}] \qquad \mathbf{y} = [\dot{m}_{hp-egr}\ p_{2i}]$$
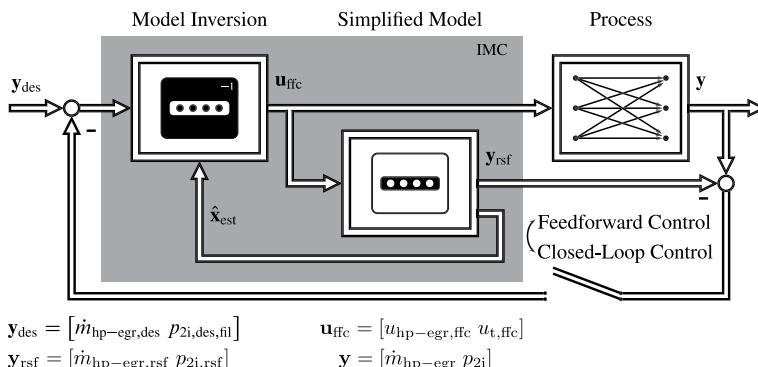
**Figure 7.14:** Model-inversion model follow-up control internal model control scheme

The semi-physical internal model control structure easily extends the feedforward control scheme to a closed-loop control and makes additional controllers superfluous. In comparison to linear PI(D)-controllers this IMC-controller is nonlinear and covers all modelled process nonlinearities. On condition the model inversion is stationary exact, no control deviation occurs. Comparable to von Pfeil (2011) this IMC-control structure in Fig. 7.14 can be switched into a pure feedforward control to actuate the air path in case of sensor faults.

## 7.6   Engine Test Bench Control Results for HP-EGR and Charge-Air Pressure

In the following different control structures to control the quantities $\dot{m}_{\mathrm{hp-egr}}$ and $p_{2\mathrm{i}}$ are validated at the engine test bench. The investigated control structures are decentralised PI(D)-controllers without feedforward control (Sect. 7.3), two degree of freedom control structure with a semi-physical model follow-up control and PI(D)-controllers (Sect. 7.4) and semi-physical internal model control (Sect. 7.5). Test signals are a series of reference value steps in the quantities $p_{2\mathrm{i,des}}$ and $\dot{m}_{\mathrm{hp-egr,des}}$ at an engine operation point of $n_{\mathrm{eng}} \approx 2250\,\mathrm{min}^{-1}$ and $u_{\mathrm{inj}} = 15\,\mathrm{mm}^3/\mathrm{cyc}$.

**PI(D)-Controllers without Feedforward Control**

First, validation results of decentralised PI(D)-controllers without feedforward control are illustrated in Fig. 7.15. In this case the control has only one degree of freedom and the decentralised PI(D)-controllers have to handle both reference action of the control loop and disturbance rejection. Consequently, the feedforward control in Fig. 7.2 is switched off, which yields $\mathbf{y}_{\mathrm{rsf}} = \mathbf{y}_{\mathrm{des}}$ and $\mathbf{u}_{\mathrm{ffc}} = 0$. In the two topmost plots of Fig. 7.15 the controlled variables charge-air pressure and HP-EGR mass flow rate are shown. The positions of the manipulated actuators $s_{\mathrm{t}}$ and $s_{\mathrm{hp-egr}}$ are displayed below. In the topmost plot the filtered reference value $p_{2\mathrm{i,des,fil}}$ for the subsequent semi-physical model inversion is further shown, to allow a better comparison to the other control concepts, see Eq. (7.21) with $T_{\mathrm{p2i,rsf}} = 0.45\,\mathrm{s}$. In this subplot the charge-air pressure $p_{2\mathrm{i}}$ has some problems to follow the reference value at the steps at 5 s and 20 s and the integral part of the PID-controller slowly adjust the VGT-actuator, which can be seen in the position $s_{\mathrm{t}}$. In this multi-variable control the couplings of $\dot{m}_{\mathrm{hp-egr}}$ act as disturbances to the decentralised $p_{2\mathrm{i}}$-controller. These couplings are compensated rather well at the times 0 s and 25 s, while there are significant control deviations between $p_{2\mathrm{i,des}}$ and $p_{2\mathrm{i}}$ during the steps at 10 s and 15 s. The PI-controller of the HP-EGR mass flow rate shows a good response to setpoint changes and also the disturbances from the charge-air pressure controller are compensated well.

**Semi-Physical Feedforward Control with PI(D)-Controllers**

Fig. 7.16 presents the model-inversion model-follow up control with PI(D)-controllers. The charge-air pressure is mainly controlled by the feedforward control, which is indicated by the small deviations between the modelled reference value $p_{2\mathrm{i,rsf}}$ and the measured pressure $p_{2\mathrm{i}}$. The PID-controller only has to compensate the deviations between these quantities. It can be clearly seen, that the reference action of the control loop and the disturbance rejection are much better than the control results without a feedforward control in Fig. 7.15. The reference signal $p_{2\mathrm{i,rsf}}$ for the underlying PID-controller also contains the non-minimum phase coupling between HP-EGR mass flow rate and charge-air pressure. Consequently, the controller is not irritated by this coupling and no misdirected control action tries to compensate the non-minimum phase course of $p_{2\mathrm{i}}$. The VGT-actuator plot also gives an indication about the quality of the feedforward control. The feed-

forward control signal $s_{t,ffc}$ shows only small deviations to the overall control signal $s_{t,ffc} + s_{t,ctl}$, which acts as setpoint for the underlying proportional position controller of the VGT-actuator. This controlled position $s_t$ follows its setpoint well. Compared to the $\dot{m}_{hp-egr}$ PI-controllers, the two degree of freedom structure with feedforward control follows its reference values slightly faster but shows small overshoots for the steps at 10 s and 25 s. Especially for these two steps the manipulated $s_{hp-egr}$ variable is actuated stronger. In the control signal of the HP-EGR-valve, there are small deviations between the feedforward control signal $s_{hp-egr,ffc}$ and the overall control signal $s_{hp-egr,ffc} + s_{hp-egr,ctl}$. In comparison to the VGT-actuator, the proportional position controller of the HP-EGR-valve has a larger deviation between its setpoint (the overall control signal $s_{hp-egr,ffc} + s_{hp-egr,ctl}$) and the measured position $s_{hp-egr}$.

**Semi-Physical Internal Model Control**

In Fig. 7.17 the semi-physical internal model control structure of Fig. 7.14 is implemented at the engine test bench. In this control structure $p_{2i}$ shows a good response to setpoint changes and disturbance rejection. The additional signal $p_{2i,rsf}$ represents a measure for the quality of the internal model and its deviation from the measured pressure $p_{2i}$ is the feedback proportion of the controller. The HP-EGR mass flow rate shows a fast reference action of the control loop and less overshoots than the model-inversion model-follow-up control scheme. Also for HP-EGR-path the quantity $\dot{m}_{hp-egr,rsf}$ represents the working principle of the internal model control, compare to Fig. 7.14. The charge-air pressure control delivers comparable results to the two degree of freedom structure with feedforward control and PID-control.

All feedforward controllers and the IMC-controllers have been parameterised by the filtered reference value $p_{2i,des,fil}$ for a moderate reference action of the control loop (Eq. (7.21) with $T_{p2i,rsf} = 0.45$ s). However, a feedforward control can also be designed with a high-performance reference action. In Fig. 7.18 the reference value $p_{2i,des,fil}$ of the semi-physical model inversion is unfiltered ($T_{p2i,rsf} = 0$ s). Consequently, the feedforward control utilises all potential in the VGT-actuator and controls $p_{2i}$ close to time optimality with a hard switching on and switching off. As a result $p_{2i}$ rises in a ramp and shows a small overshoot at $\approx 6$ s. This overshoot is caused by the reopening dynamics of the VGT-actuator ($s_t \rightarrow 0$). Furthermore, the VGT-actuator becomes dynamical very slow, if the actuator is almost fully closed ($s_t \rightarrow 1$) at a time of 6 s, see also Fig. 4.4b). This lack in dynamics leads to a large deviation between control signal $s_{t,ffc}$ and actuator position $s_t$. The stronger VGT-control action leads to stronger couplings with $\dot{m}_{hp-egr}$, which especially can be seen for the rising step of $\dot{m}_{hp-egr,rsf}$ at a time of 5 s. At these sequences, the control performance of the semi-physical internal model controller can be rated as fully satisfying. However, for the change in reference values at 25 s some disturbances can be observed in the VGT-actuation. These couplings can result from an insufficiently modelled HP-EGR dynamics, a too large bandwidth of the HP-EGR feedback signal, side effects of the simultaneously fed back signals $p_{2i}$ and $\dot{m}_{hp-egr}$ and need further investigations. One solution can be to feed back each controlled variable ($\dot{m}_{hp-egr}$, $p_{2i}$) to a separate model, or to feed back only one variable, e.g. $p_{2i}$. Since, two separate models are computationally too demanding, only the charge air pressure is fed back for an internal model control in the following. In this selected control concept the HP-EGR is controlled by the semi-

physical feedforward control from the model of the $p_{2i}$ internal model control with subsequent PI-Controllers.

### Selected Control Concept with $p_{2i}$ Internal Model Control and Semi-Physical Feedforward Control with PI-Controllers for $\dot{m}_{hp-egr}$

Consequently, the complete series of steps to setpoint changes is implemented as IMC to control $p_{2i}$ and as a semi-physical feedforward control with subsequent PI-controller for the control of $\dot{m}_{hp-egr}$. It is illustrated in Fig. 7.19 with moderate reference action of the control loop ($T_{p2i,rsf} = 0.45\,s$) and in Fig. 7.20 with fastest response to setpoint changes ($T_{p2i,rsf} = 0\,s$). In Fig. 7.19 the charge-air pressure follows its reference value $p_{2i,des,fil}$ well and the couplings of $\dot{m}_{hp-egr}$ are mainly limited to the non-minimum phase influences. Also the HP-EGR mass flow rate follows its reference value well and is only little disturbed by the VGT-actuation. Only at the step at 45 s a small overshoot is observable in $\dot{m}_{hp-egr}$. In Fig. 7.20 $p_{2i}$ is controlled with fast response to setpoint changes. This high-performance control shows a good response to setpoint changes and some couplings to $\dot{m}_{hp-egr}$. At the times of 45 s and 55 s the actuation limitation $s_{t,ffc,lim}$ from Sect. 7.4.5 is active. This pressure limitation obtains the differential pressure above the HP-EGR-valve, so that the demanded HP-EGR mass flow rate can be delivered with an almost opened HP-EGR-valve. Its effects can be seen in the ramp-shaped $s_t$ signal, compare to Fig. 7.12, and in the almost fully opened HP-EGR-valve. With moderate response to setpoint changes in Fig. 7.19 this pressure limitation is not active for the given sequence, since the VGT-actuator is opened slower. In summary the semi-physical internal model controller is capable to deliver good response to setpoint changes and disturbance rejection for the quantities $p_{2i}$ and $\dot{m}_{hp-egr}$. The feedforward control allows a fast response to setpoint changes and the model-based limitation of the VGT-actuator opening allows to keep $\dot{m}_{hp-egr}$ controllable.

### Comparison of Concepts for the Control of $\dot{m}_{hp-egr}$ and $p_{2i}$

In Tab. 7.1 the control concepts are rated with regard to the objective of function development for a modern combustion engine with more than 10 operation modes and up to 100 engine variants for different markets (Hadler et al., 2008; Zimmermann et al., 2015). In this context, the application effort for classical PI(D)-controllers can not be handled anymore, since due to the nonlinear engine process, see Sect. 4.1, a separate controller calibration for each engine operation point, engine operation mode, engine variant and changes of the ambient conditions seems to be necessary to achieve a sufficient control quality. Furthermore, the achievable control quality of PI(D)-controllers for nonlinear processes is improvable.

Both the semi-physical model follow-up control, as a combination of semi-physical feedforward control and PI(D)-controllers and the semi-physical internal model control show an outstanding control quality. For the model follow-up control a set of simple PI(D)-controllers is necessary to compensate deviations between feedforward control and engine process. These controllers also account for disturbances and can be designed rather simple, since the reference action of the

**Table 7.1:** Comparison of control concepts for control of $\dot{m}_{hp-egr}$ and $p_{2i}$ with regard to control quality, overall application effort and the manageability of engine variants. Evaluation: positive ++ neutral 0 and negative – –

|  |  | control quality | overall application effort | manageability of engine variants |
|---|---|---|---|---|
| PI(D)-controllers | Sect. 7.3 | o | – | – – |
| Semi-physical model follow-up control | Sect. 7.4 | ++ | + | + |
| Semi-physical internal model control | Sect. 7.5 | ++ | ++ | ++ |

control loop is given by the feedforward control. The internal model controller is directly given by a parameterised mean-value engine model and needs no more additional controllers. Thus, its overall application effort and the manageability of engine variants is favourable to the model-follow up control structure.

**Summary**

In summary, the simplest control concept with PI(D)-controllers delivers the worst results. Especially the response to setpoint changes and disturbance rejection of $p_{2i}$ is not satisfying. The PI-control of $\dot{m}_{hp-egr}$ can be considered as good. A combination of a semi-physical feedforward control and PI(D)-controllers is relative complex, since both the feedforward control and the closed-loop control have to be designed. However, it delivers very good control results and the couplings between $p_{2i}$ and $\dot{m}_{hp-egr}$ can almost be compensated. As a further advantage the response to setpoint changes of the $p_{2i}$-controller can be tuned close to a time optimal control. The semi-physical internal model controller is easier to implement, but shows some weaknesses at the engine test bench, if the two quantities $p_{2i}$ and $\dot{m}_{hp-egr}$ are controlled simultaneously. As long as the charge-air pressure is controlled as single controlled variable in the internal model controller and $\dot{m}_{hp-egr}$ is controlled in a semi-physical feedforward control, it delivers fully satisfactory results. Consequently, a combination of a $p_{2i}$ IMC and a semi-physical $\dot{m}_{hp-egr}$ feedforward control with PI-controllers is the suggested choice for control. Further control results at different engine operation points are given in Fig. 7.23, Fig. 7.25, Fig. 7.31 and Fig.7.32 by subsequently embedding the $p_{2i}$ and $\dot{m}_{hp-egr}$ control in the overall control structure of Fig. 7.1. In order to complete this overall control structure, the controller for LP-EGR-control is derived next.
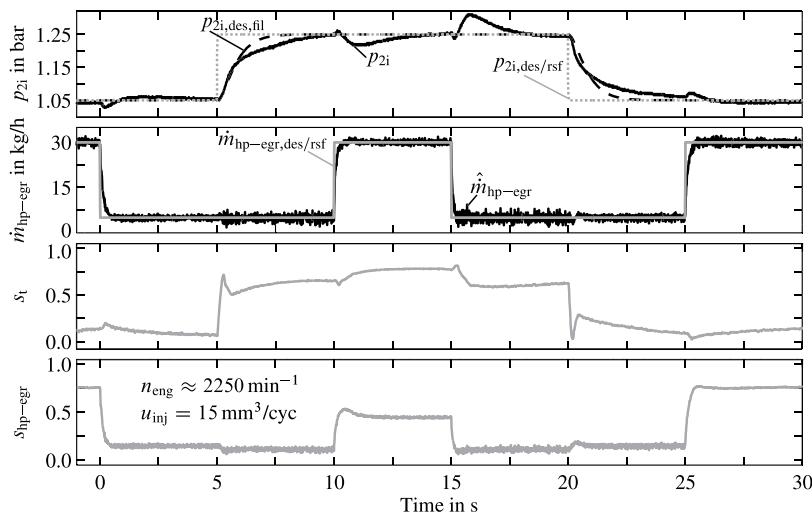
**Figure 7.15:** Test bench measurements for the control of $p_{2i}$ and $\dot{m}_{hp-egr}$ with decentralised PI(D)-controllers and steps of $p_{2i,des}$ and $\dot{m}_{hp-egr,des}$
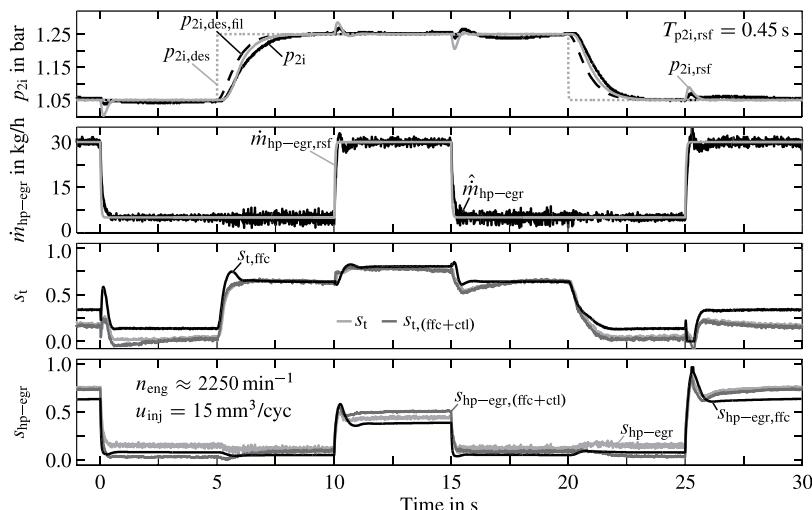


**Figure 7.16:** Test bench measurements for the control of $p_{2i}$ and $\dot{m}_{hp-egr}$ with semi-physical model-inversion model-follow up control with PI(D)-controllers and steps of $p_{2i,des}$ and $\dot{m}_{hp-egr,des}$
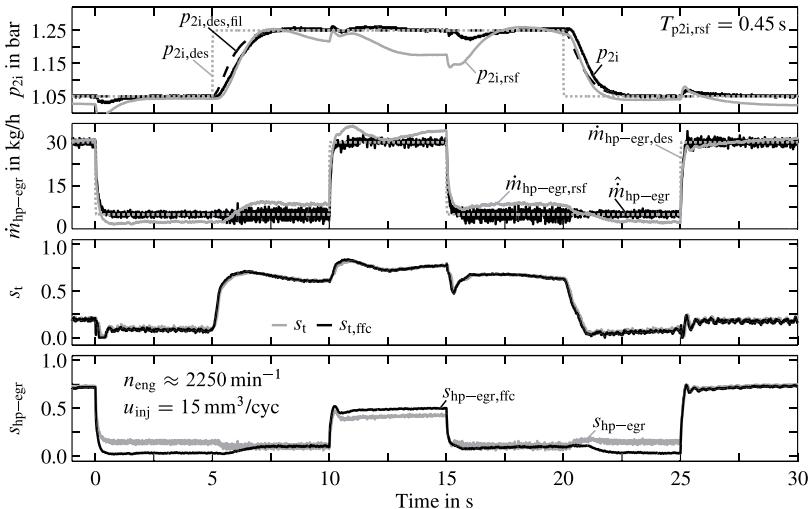
**Figure 7.17:** Test bench measurements for the control of $p_{2i}$ and $\dot{m}_{hp-egr}$ with internal model control and steps of $p_{2i,des}$ and $\dot{m}_{hp-egr,des}$
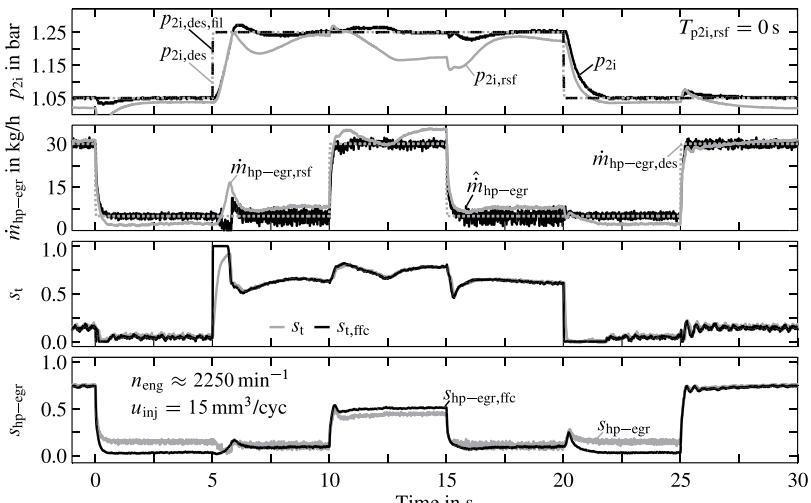


**Figure 7.18:** Test bench measurements for the control of $p_{2i}$ and $\dot{m}_{hp-egr}$ with internal model control and fast response to setpoint changes for steps of $p_{2i,des}$, $\dot{m}_{hp-egr,des}$
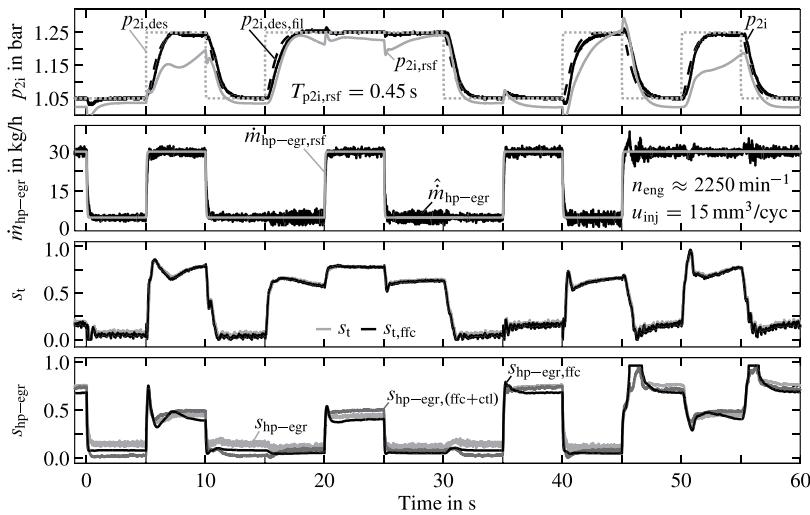
**Figure 7.19:** Measurements for the control of $p_{2i}$ (IMC) and semi-physical feedforward control with PI-controller for steps of $p_{2i,des}$, $\dot{m}_{hp-egr,des}$
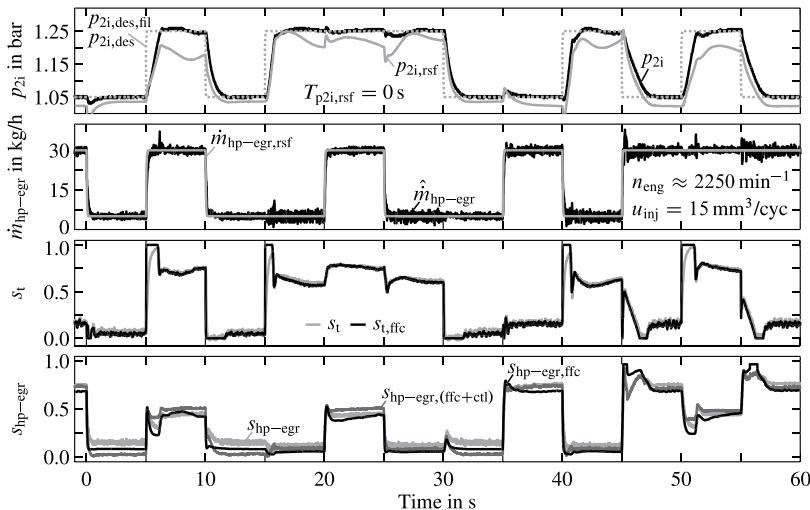


**Figure 7.20:** Measurements for the control of $p_{2i}$ (IMC) and semi-physical feedforward control with PI-controller for $\dot{m}_{hp-egr}$ with fast response to setpoint changes for steps of $p_{2i,des}$, $\dot{m}_{hp-egr,des}$

## 7.7 Semi-Physical Control for the LP-EGR Path

After the control schemes for the quantities charge-air pressure and HP-EGR mass flow rate have been derived in the previous sections, the control for the LP-EGR path is presented. The investigation of the system properties of the LP-EGR system showed, that an additional EGR loop has only minor couplings to the charge-air pressure and the HP-EGR mass flow rate, while there are significant couplings of charge-air pressure and HP-EGR, respectively air mass flow rate to the LP-EGR mass flow rate, see Sect. 4.1.3. In Sect. 4.2.1 it is further shown, that the LP-EGR-rate $r_{lp-egr}$ mainly depends on the position of the LP-EGR-actuator and is fairly invariant from the engine operation point and the actuation of the other air path actuators. Hence, this coherence will be utilised in the following to derive a control scheme for the quantity $\dot{m}_{lp-egr}$, which also considers the couplings of the charge-air pressure and the HP-EGR mass flow rate control. This novel control scheme is a further extension of the newly derived feedforward control from Mrosek and Isermann (2011). In this dissertation the control law is derived with respect to an intake throttle valve with LP-EGR-valve $s_{lp-egr/ith}$, it also can be applied to a configuration with exhaust throttle valve by replacing $s_{lp-egr/ith}$ by $s_{lp-egr/eth}$.

According to the investigations in Sect. 4.2.1, the LP-EGR-rate (4.9) is fairly invariant to the engine operation point, engine operation mode, position of other air path actuators and essentially depends on the position of the LP-EGR-actuator. Thus, it can be reasonably approximated as a function of the LP-EGR-actuator opening.

$$r_{lp-egr} \approx f\left(s_{lp-egr/ith}\right) \tag{7.28}$$

Then the control deviation of the LP-EGR mass flow rate $\Delta\dot{m}_{lp-egr}$ follows as the difference between the demanded LP-EGR mass flow rate $\dot{m}_{lp-egr,des}$ and the measured quantity $\dot{m}_{lp-egr}$

$$\Delta\dot{m}_{lp-egr} = \dot{m}_{lp-egr,des} - \dot{m}_{lp-egr}. \tag{7.29}$$

At a constant mass flow rate through the compressor (7.13), this control deviation can only be compensated by a rise of $\dot{m}_{lp-egr}$ for $\Delta\dot{m}_{lp-egr}$, which results in a decrease for the same mass flow rate in $\dot{m}_{air}$.

$$\dot{m}_c := \text{const} \Rightarrow \dot{m}_c = \underbrace{\left(\dot{m}_{air} - \Delta\dot{m}_{lp-egr}\right)}_{\tilde{\dot{m}}_{air,des}} + \underbrace{\left(\dot{m}_{lp-egr} + \Delta\dot{m}_{lp-egr}\right)}_{\dot{m}_{lp-egr,des}} \tag{7.30}$$

Thus, with Eq. (4.9) and Eq. (7.30) a desired LP-EGR-rate can be derived from the relationships for $\tilde{\dot{m}}_{air,des}$ and $\dot{m}_{lp-egr,des}$ as

$$r_{\text{lp-egr,des}} = \frac{\dot{m}_{\text{lp-egr,des}}}{\dot{m}_{\text{lp-egr,des}} + \tilde{\dot{m}}_{\text{air,des}}} = \frac{\dot{m}_{\text{lp-egr}} + \Delta \dot{m}_{\text{lp-egr}}}{\left(\dot{m}_{\text{lp-egr}} + \Delta \dot{m}_{\text{lp-egr}}\right) + \left(\dot{m}_{\text{air}} - \Delta \dot{m}_{\text{lp-egr}}\right)}$$
$$= \frac{\dot{m}_{\text{lp-egr}} + \Delta \dot{m}_{\text{lp-egr}}}{\dot{m}_{\text{lp-egr}} + \dot{m}_{\text{air}}}. \tag{7.31}$$

With this desired LP-EGR-rate, the relationship (7.28) can be inverted to

$$s_{\text{lp-egr/ith,ffc}} = f^{-1}\left(r_{\text{lp-egr,des}}\right) \tag{7.32}$$

and delivers the control signal for the feedforward control. A further underlying $r_{\text{lp-egr}}$ controller $G_{\text{C33}}$ with proportional and integral action compensates the deficits of the feedforward control. This controller has only a single set of parameters and is sufficient for the whole engine operation range. A reference shaping filter (RSF) further filters the controller's reference value, so that the feedforward control actions are settled before the controller acts on changes in the reference values. The complete scheme for the LP-EGR control is depicted in Fig. 7.21, where the control loop is transformed into an outer $\dot{m}_{\text{lp-egr}}$ and an inner $r_{\text{lp-egr}}$ control loop.
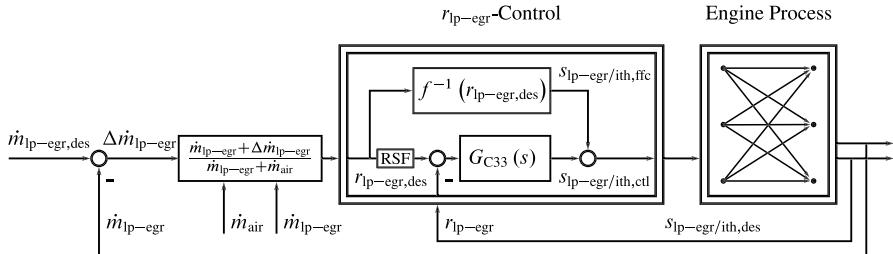


**Figure 7.21:** Transformation of the $\dot{m}_{\text{lp-egr}}$ control into a $r_{\text{lp-egr}}$ control with feedforward control, which is almost invariant to the actual engine operation point and further considers the couplings with $s_{\text{t}}$ and $s_{\text{hp-egr}}$

This transformation has the large advantage, that contrary to the strongly engine operation point and operation mode dependent gain between $\dot{m}_{\text{lp-egr}}$ and $s_{\text{lp-egr/ith}}$ from Fig. C.3, this transformed $r_{\text{lp-egr}}$ control is fairly invariant to changes in engine operation, see also Fig. 4.7. Consequently, the software calibration and testing effort can be drastically reduced, since only the curve of the feedforward signal and the inner LP-EGR-rate controller need to be calibrated and tested. Note that for a smooth operation of the $r_{\text{lp-egr}}$ control without glitches it is necessary, that the quantities $\dot{m}_{\text{air}}$ and $\dot{m}_{\text{lp-egr}}$ have the same measurement dynamics and should not dynamical be shifted against each other.

Fig. 7.22 illustrates the working principle of the semi-physical control for the LP-EGR path with measurements from the engine test bench. In the topmost plots the course of the directly controlled

variable $\dot{m}_{\text{lp}-\text{egr}}$, the transformed LP-EGR-rate and the air mass flow rate are shown. The bottom plots present the actuator signals. On the left side the contributions from the feedforward control $s_{\text{lp}-\text{egr/ith,ffc}}$ and the controller $s_{\text{lp}-\text{egr/ith,ctl}}$ to the overall control signal $s_{\text{lp}-\text{egr/ith,des}}$ are shown. In the right bottom plot, the virtually combined actuator position $s_{\text{lp}-\text{egr/ith}}$ is divided into the physical positions of the LP-EGR-valve $\tilde{s}_{\text{lp}-\text{egr}}$ and the intake throttle valve $\tilde{s}_{\text{ith}}$.
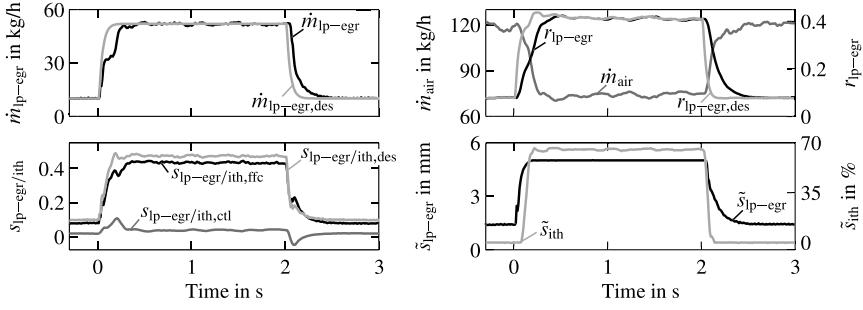


**Figure 7.22:** Test bench results of the transformation of the $\dot{m}_{\text{lp}-\text{egr}}$ control into a $r_{\text{lp}-\text{egr}}$ control to be invariant of engine operation point and operation mode $\left(n_{\text{eng}} \approx 2250\,\text{min}^{-1},\ u_{\text{inj}} = 15\,\text{mm}^3/\text{cyc}\right)$

The response to setpoint changes of the LP-EGR control has a good performance and the quantity $\dot{m}_{\text{lp}-\text{egr}}$ reaches its reference value $\dot{m}_{\text{lp}-\text{egr,des}}$ within 200 ms for rising and falling setpoints. Also the intermediate control variable $r_{\text{lp}-\text{egr}}$ reaches its reference value $r_{\text{lp}-\text{egr,des}}$ in the same time. It can be further noticed that the air mass flow rate shows approximately the opposite course as the LP-EGR mass flow rate. The control signals display, that the major control action is achieved by the feed-forward control $s_{\text{lp}-\text{egr/ith,ffc}}$, while only a minor part is contributed by the controller $s_{\text{lp}-\text{egr/ith,ctl}}$. The major controller action can be observed during setpoint changes and try to compensate deviations between the reference value $r_{\text{lp}-\text{egr,des}}$ and the controlled quantity $r_{\text{lp}-\text{egr}}$. However, these control actions are only of minor magnitude and can be tolerated. On condition less control action is demanded, a better filtering of the reference value $r_{\text{lp}-\text{egr,des}}$ for the controller $G_{\text{C33}}$ can adjust the reference signal better to the intervention of the feedforward control and reduce the remaining control action. As a final remark the measured quantity $\dot{m}_{\text{lp}-\text{egr}}$ shows a minor step at a time of $\approx 100\,\text{ms}$. This step is caused by the limited adjustment rate of the intake throttle valve actuator $s_{\text{ith}}$ and the small influence on the quantity $\dot{m}_{\text{lp}-\text{egr}}$ for positions of $s_{\text{ith}}$ below 40 %, see Fig. C.3. During the increasing step of $\dot{m}_{\text{lp}-\text{egr}}$ the intake throttle has to close from a fully opened position ($s_{\text{ith}} = 0\,\%$) to a position of $s_{\text{ith}} \approx 70\,\%$, after the LP-EGR-valve has been closed. Consequently, there is only a small influence on $\dot{m}_{\text{lp}-\text{egr}}$ during the time the throttle valve passes this adjusting range and a small step occurs.

So far only the response to setpoint changes of the LP-EGR control has been investigated. In Fig. 7.23 the LP-EGR control is combined with the charge-air pressure control (IMC) and the HP-EGR mass flow rate control (PI) to show the control performance with all controlled air path
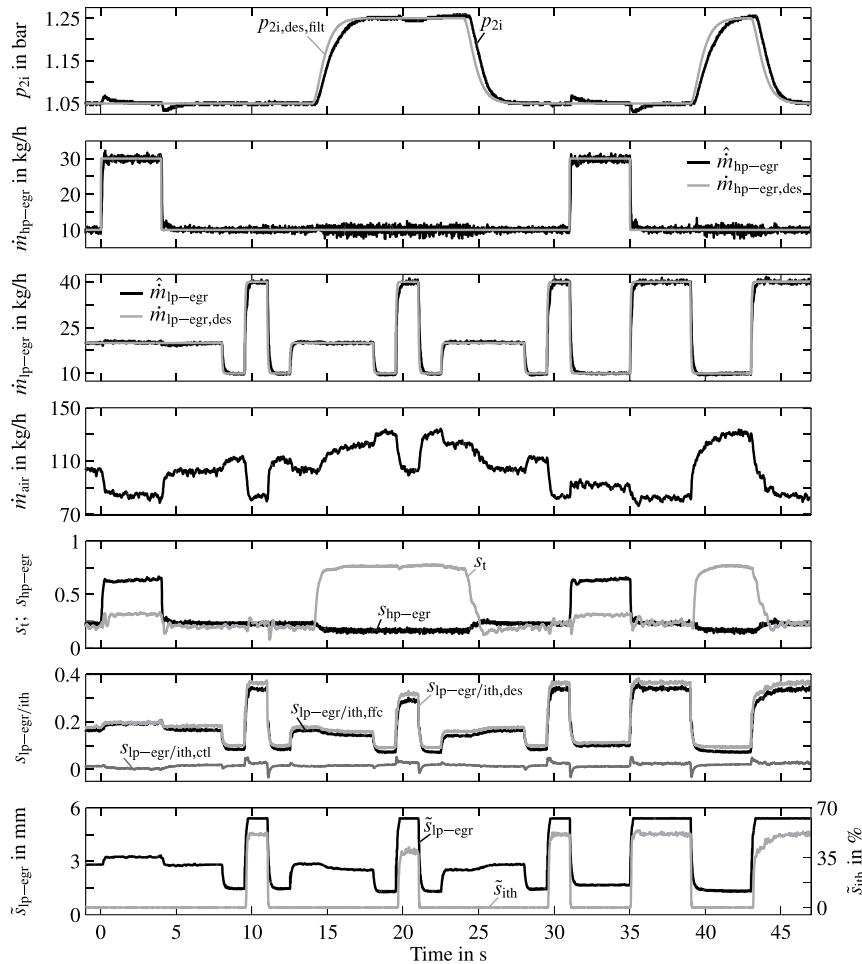
**Figure 7.23:** Test bench results of the multivariable control of $p_{2i}$ (IMC), $\dot{m}_{hp-egr}$ (PI) and $\dot{m}_{lp-egr}$ with the corresponding control and actuator signals for changes in the reference values of $p_{2i}$, $\dot{m}_{hp-egr}$ and $\dot{m}_{lp-egr}$ $\left(n_{eng} \approx 2250 \, \text{min}^{-1}, \; u_{inj} = 15 \, \text{mm}^3/\text{cyc}\right)$

variables and the occurring couplings. In the topmost plots the reference values and the controlled variables for charge-air pressure, HP-EGR mass flow rate and LP-EGR mass flow rate are illustrated. Then follow the air mass flow rate and the actuator positions $s_{hp-egr}$ and $s_t$ to indicate the manipulated variables of the HP-EGR and charge-air pressure controllers. The manipulated variables for the semi-physical LP-EGR mass flow rate control are displayed more detailed in the both

bottommost plots. In the first plot the contribution of the feedforward control $s_{lp-egr/ith,ffc}$ and the closed-loop control $s_{lp-egr/ith,ctl}$ to the overall control signal $s_{lp-egr/ith,des}$ are shown. The last plot is more of informative nature and presents the division of the control signal into the LP-EGR-valve $\tilde{s}_{lp-egr}$ and the intake throttle valve $\tilde{s}_{ith}$ positions.

During the first 30 s only the reference value of a single quantity is changed at a time, while in the last part two reference values are changed instantaneous. It can be seen that all quantities follow their reference values well and furthermore the controllers show a good disturbance rejection of the coupling effects. Only in the charge-air pressure minor couplings can be observed for the two reference value excitations of $\dot{m}_{hp-egr}$. The actuator signals $s_{hp-egr}$ and $s_t$ confirm the previous investigations about the system couplings and depict that there are only small influences from the LP-EGR loop to the other air path quantities. In the actuator signal $s_{lp-egr/ith,des}$ it can be noticed that there are some small couplings of $\dot{m}_{hp-egr}$ and $p_{2i}$. This plot further shows, that transformation to an intermediate $r_{lp-egr}$ control with semi-physical feedforward control is well suited to control the quantity $\dot{m}_{lp-egr}$, since the control signal $s_{lp-egr/ith,ctl}$ remains small.

In summary, the system analysis from Sect. 4.2.1 showed, that the LP-EGR-rate is mostly dependent from the actuator position and fairly invariant from engine operation point, operation mode, other air path actuators and ambient conditions. This allows to design a simple semi-physical control scheme based on the relationship between actuator position and LP-EGR-rate with a well suiting response to setpoint changes and disturbance rejection. A further controller compensates minor deviations in the modelled relationship between LP-EGR-actuator position and LP-EGR-rate. This approach allows to design and calibrate a control of the additional LP-EGR-path with a minimal effort for all engine operation points and modes. Next, the reference values for HP-EGR and LP-EGR are derived with regard to the air content dynamics in the intake and exhaust system.

## 7.8 Dynamical Reference Value Generation for HP- and LP-EGR

After the air path control structure and the control design of the quantities $p_{2i}$, $\dot{m}_{hp-egr}$ and $\dot{m}_{lp-egr}$ have been successfully validated with test bench measurements, the last missing fragment between the stationary and dynamical optimised reference values from Chap. 6 and the air path control will be given in this section, see Fig. 7.1.

The investigated dynamical system properties in Sect. 4.3 showed, that a major difference between the HP-EGR system and the LP-EGR system lies hidden in the gas propagation delays of the short and the long route exhaust gas recirculation. These inherent system dynamics with their abrupt stepwise changes in the single storages' air contents are modelled and successfully validated with measurements from the engine test bench in Sect. 4.4. In order to always provide an optimal cylinder charge for a low-emission combustion process and to suppress the gas propagation effects of both EGR paths, an optimal air content in the intake manifold $x_{2i}$ should be maintained during the engine operation.

**Dynamical Setpoint Optimisation**

$n_{eng}$
$u_{inj}$

$J$ → $x_{eng,out,opt}$

$\hat{T}_{2i}$ $p_{2i}$ $\varphi_{mi}$

$x_{eng,out,opt}$ ⟹ $\dot{m}_{air,des,opt}$

$$\frac{x_{eng,out,des}\left(\hat{\dot{m}}_{eng,in}+\hat{\dot{m}}_f\right)+L_{st}\hat{\dot{m}}_f}{\hat{\dot{m}}_{eng,in}}$$ → $x_{2i,des}$

$$\frac{(x_{2i,des}-\hat{x}_{1/2c})\hat{\dot{m}}_{eng,in}}{\hat{x}_3-\hat{x}_{1/2c}}$$ → $\dot{m}_{hp-egr,des}$

→ $x_{eng,out,des}$

**Charging Pressure**

$n_{eng}$
$u_{inj}$
$\ldots$
→ $p_{2i,des}$

$$\frac{\dot{m}_{air,des}-L_{st}\hat{\dot{m}}_f}{\dot{m}_{air,des}+\hat{\dot{m}}_f}$$

**Air Mass Flow Rate**

$n_{eng}$
$u_{inj}$
$\ldots$
→ $\dot{m}_{air,des}$

$$\left(\frac{T_{2i,des}-T_{2ic}}{T_{hp-egr}-T_{2ic}}\right)\frac{\hat{\dot{m}}_{eng,in}}{\hat{\dot{m}}_{eng,in}-\dot{m}_{air,des}}$$

$$\frac{(x_{2i,des}-1)\hat{\dot{m}}_{eng,in}}{\hat{x}_5-1}$$

$\xi_{hp-egr}$

$\dot{m}_{lp-egr,des,max}$

**Intake Temperature**

$n_{eng}$
$u_{inj}$
$\ldots$
→ $T_{2i,des}$

$$(1-\xi_{hp-egr})\left(\hat{\dot{m}}_{eng,in}-\dot{m}_{air,des}\right)$$ → $\dot{m}_{lp-egr,des,unlim}$ → min → $\dot{m}_{lp-egr,des}$

**Figure 7.24:** Dynamical reference value generation for the air path controllers. In order to cope for gas propagation effects, it converts stationary reference value maps for $\dot{m}_{air,des}$ and $T_{2i,des}$ under consideration of the current air content and temperatures in the intake and exhaust system into reference values for HP-EGR and LP-EGR. As extension dynamical optimised reference values according to Sect. 6.2 can be utilised for the reference value generation.

This optimised air content can be achieved by a closed-loop control of the measured or modelled quantity $x_{2i}$. However, such a pure closed-loop control shows generally a more or less reactive behaviour in disturbance rejection and is characterised by the trade-off between control performance and robustness. For a $x_{2i}$ closed-loop control there are two major aspects which have to be considered in the control design. First the long route and the short route EGR path introduce stepwise changes in the intake air content which act as disturbances for the closed-loop control. Furthermore, the process gains for the recirculated exhaust gas control paths vary suddenly with the inherent air contents in the single storages, see Fig. 4.10. Hence, these two aspects have to be incorporated into a air content control scheme with a good disturbance rejection and robustness.

Alternatively to a rather complex closed-loop control of the air content, it is possible to separate the control problem into an open-loop control of $x_{2i}$ with a reference value transformation for an underlying $\dot{m}_{hp-egr}$ and $\dot{m}_{lp-egr}$ control (Mrosek and Isermann, 2010a). This reference value generation comprises the air content model from Sect. 4.4 and governs the complex knowledge about the inherent system states and the varying process gains to deliver setpoints for the rather simple $\dot{m}_{hp-egr}$ and $\dot{m}_{lp-egr}$ controllers. Contrary to a reactive closed-loop control this reference value generation considers the process states and acts preemptive.

### 7.8.1  Reference Value Generation Scheme

Fig. 7.24 summarises the reference value generation, which will be derived in the following. In a nutshell this reference value generation transforms setpoints of the air mass flow rate $\dot{m}_{air,des}$ into setpoints of the intermediate control variable $x_{2i,des}$, which is further transformed into a reference value $\dot{m}_{hp-egr,des}$ for the HP-EGR mass flow rate control. In this control strategy, the dynamical fast HP-EGR governs the air content in the intake manifold. A further transformation converts setpoints of the intake temperature $T_{2i,des}$ into a desired value of the LP-EGR mass flow rate controller $\dot{m}_{lp-egr,des}$. The charge-air pressure setpoint is not affected by these setpoint transformations and controlled separately via its characteristic map. The untransformed setpoints $\dot{m}_{air,des}$, $T_{2i,des}$ and $p_{2i,des}$ are stored in characteristic maps depending on engine speed and desired injection quantity. Further expansions to special engine operation modes like Diesel particulate filter regeneration and others can be considered as additional map inputs and are denoted with dots. As an alternative to the stationary reference values for $\dot{m}_{air,des}$ also the dynamical optimised setpoints $x_{eng,out,opt}$ from Sect. 6.2 can be utilised in this reference value generation scheme.

After the main ideas for this reference value generation have been given, the single transformations to obtain the controller setpoints $\dot{m}_{hp-egr,des}$ and $\dot{m}_{lp-egr,des}$ out of the characteristic maps $\dot{m}_{air,des}$ and $T_{2i,des}$ are deduced in the following. First, the reference value of the air mass flow rate is transformed into a reference value for an intermediate control variable, which considers the long gas propagation times in the intake and exhaust system. This intermediate control variable is the air content in the intake manifold $x_{2i}$. Generally, there are two options to derive reference values for this quantity from the given setpoint maps. A first approach results in a control of the intake air content ($x_{2i,ctl}$), while the second approach results in an air mass flow rate control ($\dot{m}_{air,ctl}$), which also considers the air contents, see Sect. 6.2.1. A control of the intake air content reaches its stationary calibrated air mass flow rate, when $p_{2i}$ and $T_{2i}$ have reached their steady-state condition, compare to Fig. 4.8 and Fig. 6.3. Whenever deviations between the calibrated reference values and the controlled variables $p_{2i}$ and $T_{2i}$ occur, e.g. at ambient conditions where either temperature or pressure are not reachable, the calibrated air mass will also not be reached. Further, the summed emissions of the intake air content control ($x_{2i,ctl}$) are worse than the emissions of the air mass flow rate control ($\dot{m}_{air,ctl}$), see Tab. 6.2. Hence, reference values for the intermediate control variable $x_{2i}$ are derived according to an air mass flow rate control scheme.

Next, $\dot{m}_{air,des}$ is transformed via the relationship between air mass and $x_{eng,out}$ into a reference value for $x_{2i,des}$. In an engine air path with no significant gas propagation dynamics like a HP-EGR-system, both $\dot{m}_{air}$ and $x_{eng,out}$ show a similar characteristic during transients in $p_{2i}$ and $T_{2i}$, see Fig. 6.3. Thus, maintaining a constant air content at the exhaust valve, corresponds to a constant air mass in the cylinder, when the injection quantity stays constant. In order to maintain a fixed air content after the combustion process $x_{eng,out}$, the air mass flow rate reference value can be transformed via Eq. (3.33) into its reference value.

$$x_{eng,out,des} = \frac{\dot{m}_{air,des} - L_{st}\hat{\dot{m}}_f}{\dot{m}_{air,des} + \hat{\dot{m}}_f} \qquad (7.33)$$

This reference value of $x_{\mathrm{eng,out,des}}$ can be further transformed into a desired air content in the intake manifold

$$x_{2\mathrm{i,des}} = \frac{x_{\mathrm{eng,out,des}} \left( \hat{\dot{m}}_{\mathrm{eng,in}} + \hat{\dot{m}}_{\mathrm{f}} \right) + L_{\mathrm{st}} \hat{\dot{m}}_{\mathrm{f}}}{\hat{\dot{m}}_{\mathrm{eng,in}}} \qquad (7.34)$$

by rearranging Eq. (3.32) and using the estimated quantities for $\hat{\dot{m}}_{\mathrm{eng,in}}$ and $\hat{\dot{m}}_{\mathrm{f}}$ from Sect. 4.4. In this reference value generation, the setpoint for the air content $x_{2\mathrm{i,des}}$ acts as an intermediate control variable. When the fast dynamics in the intake system are neglected, the estimated air content $\hat{x}_{2\mathrm{i}}$ can be approximated by the air contents and the amounts of the inflowing mass flow rate through the throttle valve $\hat{\dot{m}}_{\mathrm{th}}$ and $\hat{\dot{m}}_{\mathrm{hp-egr}}$ as

$$\hat{x}_{2\mathrm{i}} \approx \frac{\hat{x}_3 \hat{\dot{m}}_{\mathrm{hp-egr}} + \hat{x}_{1/2\mathrm{c}} \hat{\dot{m}}_{\mathrm{th}}}{\hat{\dot{m}}_{\mathrm{hp-egr}} + \hat{\dot{m}}_{\mathrm{th}}} \qquad (7.35)$$

and can be rewritten by substituting $\hat{\dot{m}}_{\mathrm{th}}$ with the stationary form of Eq. (4.14) as

$$\hat{x}_{2\mathrm{i}} \approx \frac{\hat{x}_3 \hat{\dot{m}}_{\mathrm{hp-egr}} + \hat{x}_{1/2\mathrm{c}} \left( \hat{\dot{m}}_{\mathrm{eng,in}} - \hat{\dot{m}}_{\mathrm{hp-egr}} \right)}{\hat{\dot{m}}_{\mathrm{eng,in}}}. \qquad (7.36)$$

Afterwards $\hat{x}_{2\mathrm{i}}$ can be replaced by its setpoint and Eq. (7.36) can be rearranged for the desired HP-EGR mass flow rate, which then yields the reference value

$$\dot{m}_{\mathrm{hp-egr,des}} = \frac{\left( x_{2\mathrm{i,des}} - \hat{x}_{1/2\mathrm{c}} \right) \hat{\dot{m}}_{\mathrm{eng,in}}}{\hat{x}_3 - \hat{x}_{1/2\mathrm{c}}}. \qquad (7.37)$$

This setpoint $\dot{m}_{\mathrm{hp-egr,des}}$ implicitly includes all gas propagation dynamics, which are included in the modelled states $\hat{x}_{1/2\mathrm{c}}$ and $\hat{x}_3$. Anymore, also sudden changes in the inherent gas system states are covered by this setpoint transformation.

In the next transformation the setpoints $\dot{m}_{\mathrm{air,des}}$ and $T_{2\mathrm{i,des}}$ are converted into a reference value for the LP-EGR mass flow rate. For this purpose first the total demanded EGR mass flow rate can be expressed as

$$\dot{m}_{\mathrm{egr,des}} = \dot{m}_{\mathrm{lp-egr,des,unlim}} + \dot{m}_{\mathrm{hp-egr,des}}^{*}, \qquad (7.38)$$

which in stationary form can be rearranged via (4.13) and the reference value $\dot{m}_{\mathrm{air,des}}$ to

$$\dot{m}_{\mathrm{egr,des}} = \hat{\dot{m}}_{\mathrm{eng,in}} - \dot{m}_{\mathrm{air,des}}. \qquad (7.39)$$

This desired total EGR mass flow rate demand can be divided by $\xi_{\text{hp}-\text{egr}}$ into a HP-EGR proportion

$$\dot{m}^*_{\text{hp}-\text{egr,des}} = \xi_{\text{hp}-\text{egr}}\dot{m}_{\text{egr,des}} \tag{7.40}$$

and an unlimited LP-EGR proportion

$$\dot{m}_{\text{lp}-\text{egr,des,unlim}} = \left(1 - \xi_{\text{hp}-\text{egr}}\right)\dot{m}_{\text{egr,des}}. \tag{7.41}$$

In which the quantity $\dot{m}^*_{\text{hp}-\text{egr,des}}$ is an intermediate variable for the derivation of the unlimited setpoint $\dot{m}_{\text{lp}-\text{egr,des,unlim}}$ and does not correspond to the setpoint in (7.37). On assumption that $\hat{\dot{m}}_{\text{th}}$ can be stationary approximated as $\hat{\dot{m}}_{\text{eng,in}} - \hat{\dot{m}}_{\text{hp}-\text{egr}}$ from Eq. (4.14), it can be substituted in (4.16). Furthermore, the HP-EGR mass flow rate in (4.16) can be substituted by (7.39) and (7.40) and finally yields the desired proportion of HP-EGR $\xi_{\text{hp}-\text{egr}}$ for a temperature setpoint $T_{2\text{i,des}}$ and an air mass flow rate setpoint $\dot{m}_{\text{air,des}}$.

$$\xi_{\text{hp}-\text{egr}} = \left(\frac{T_{2\text{i,des}} - T_{2\text{ic}}}{T_{\text{hp}-\text{egr}} - T_{2\text{ic}}}\right)\frac{\hat{\dot{m}}_{\text{eng,in}}}{\hat{\dot{m}}_{\text{eng,in}} - \dot{m}_{\text{air,des}}} \tag{7.42}$$

In doing so, $\xi_{\text{hp}-\text{egr}}$ is limited between 0 and 1. This proportion $\xi_{\text{hp}-\text{egr}}$ finally delivers with the relationships (7.39) and (7.41) the unlimited setpoint $\dot{m}_{\text{lp}-\text{egr,des,unlim}}$ for the LP-EGR mass flow rate controller.

$$\dot{m}_{\text{lp}-\text{egr,des,unlim}} = \left(1 - \xi_{\text{hp}-\text{egr}}\right)\left(\hat{\dot{m}}_{\text{eng,in}} - \dot{m}_{\text{air,des}}\right) \tag{7.43}$$

In this reference value generation scheme the control of the air content in the intake manifold $x_{2\text{i,des}}$ is superior to the resulting intake temperature $T_{2\text{i}}$, which is implicitly controlled by the demanded distributions of HP- and LP-EGR. Hence, the LP-EGR mass flow rate can be regarded as a disturbance for the superior air content control. Only when all gas transport dynamics are settled, the intake temperature will reach its calibrated setpoint. During transients the air content control leads to an arbitrary intake temperature. This favouring of the air content control over the desired intake temperature is permissible, since the air content has a stronger influence on the emission formation than the inferior intake temperature, see Fig. 5.5. On condition the intake temperature shall be controlled with priority, one obtains the appropriate reference values by controlling the HP-EGR mass flow rate with the reference value (7.40) and the LP-EGR mass flow rate by (7.43). In this configuration the air mass flow rate and the intake temperature are the controlled quantities and the internal gas propagation effects are neglected.

However, in some special cases of the air content control, the reference value generation for $\dot{m}_{\text{lp}-\text{egr,des,unlim}}$ can dynamical result in an intake air content $\hat{x}_{1/2\text{c}}$ which is lower than the demanded reference value $x_{2\text{i,des}}$. In that case the superior air content control has no chance to rise the intake air content with fresh air and the engine is choked. Hence, the LP-EGR mass flow rate

demand has to be limited, so that the air content control is always capable to react and further lower the air content of the inflowing gas mass flow rate. This can be achieved by the inequality

$$\hat{\dot{m}}_{\text{eng,in}} x_{2i,\text{des}} \leq \dot{m}_{\text{air,des}} + \hat{x}_5 \dot{m}_{\text{lp−egr,des,max}}, \tag{7.44}$$

which expresses that the desired equivalent fresh air mass flow rate into the cylinder $\hat{\dot{m}}_{\text{eng,in}} x_{2i,\text{des}}$ is smaller or equal than the equivalent air mass flow rate passing the compressor. This yields such conditions in the intake system, that additional HP-EGR can be mixed with the inflowing gas mass flow rate to further reduce the portion of fresh air. In Eq. (7.44) $\dot{m}_{\text{air,des}}$ can be substituted by (7.38) and (7.39). Further $\dot{m}^*_{\text{hp−egr,des}}$ is set to zero, so that the desired intake air content will not fall below its setpoint without any HP-EGR mass flow rate and results in

$$\hat{\dot{m}}_{\text{eng,in}} x_{2i,\text{des}} \leq \hat{\dot{m}}_{\text{eng,in}} - \dot{m}_{\text{lp−egr,des,unlim}} + \hat{x}_5 \dot{m}_{\text{lp−egr,des,max}}. \tag{7.45}$$

Then the maximal allowed LP-EGR mass flow rate, which satisfies (7.45) is given with $\dot{m}_{\text{lp−egr,des,unlim}} = \dot{m}_{\text{lp−egr,des,max}}$ as

$$\dot{m}_{\text{lp−egr,des,max}} = \frac{x_{2i,\text{des}} - 1}{\hat{x}_5 - 1} \hat{\dot{m}}_{\text{eng,in}}, \tag{7.46}$$

where it shall be noted that the denominator $\hat{x}_5 - 1$ is negative. Finally, the setpoint for the LP-EGR mass flow rate controller can be derived as the minimum between the temperature dependent demand (7.43) and the air content related limitation (7.46) as

$$\dot{m}_{\text{lp−egr,des}} = \min\left(\dot{m}_{\text{lp−egr,des,unlim}}, \dot{m}_{\text{lp−egr,des,max}}\right). \tag{7.47}$$

At some operation points with low injection quantities, like the engine overrun state, the denominator of Eqs. (7.37), (7.42) and (7.46) can turn to zero. Hence, in a practical implementation some precautions have to be undertaken to avoid this division by zero and the air content control should be switched to a temperature control with the reference values (7.40) and (7.43).

Finally, also the dynamical optimised reference values from Sect. 6.2 can be easily introduced into the reference value generation by opening the switches in Fig. 7.24 and replacing $x_{\text{eng,out,des}}$ in Eq. (7.34) by $x_{\text{eng,out,opt}}$ and by substituting $\dot{m}_{\text{air,des}}$ in Eq. (7.42) by $\dot{m}_{\text{air,des,opt}}$ from Eq. (6.9). After a short investigation of the influence of modelling and measurement uncertainties follow the test bench results for the given reference value generation.

### 7.8.2 Invariance to Modelling and Measurement Uncertainties

After the detailed investigations of the modelling and measurement uncertainties in Mrosek et al. (2010b) and Mrosek (2017), the question of the practical relevance for the control of a modelled

quantity $\hat{x}_{2i}$ and the reference value generation with many modelled quantity arises. Contrary to the control of a directly measured quantity, this reference value generation scheme seems to accumulate the measurement and modelling uncertainties of each single submodel. However, as it will be proved in the following the special form of the air content model in conjunction with the reference value generation is invariant to modelling and measurement uncertainties.

In stationary engine conditions the air contents in the exhaust manifold are settled ($\hat{x}_5 = \hat{x}_3$) and the air content in the intake manifold can be expressed analogue to Eq. (3.10) as the ratio of remaining fresh air mass flow rate and total mass flow rate.

$$\hat{x}_{2i}\left(\Delta\hat{\dot{m}}_{\text{lp-egr}}, \Delta\hat{\dot{m}}_{\text{hp-egr}}, \dots\right) = \frac{\dot{m}_{\text{air}} + \hat{x}_3\left(\hat{\dot{m}}_{\text{lp-egr}} + \Delta\hat{\dot{m}}_{\text{lp-egr}} + \hat{\dot{m}}_{\text{hp-egr}} + \Delta\hat{\dot{m}}_{\text{hp-egr}}\right)}{\dot{m}_{\text{air}} + \hat{\dot{m}}_{\text{lp-egr}} + \Delta\hat{\dot{m}}_{\text{lp-egr}} + \hat{\dot{m}}_{\text{hp-egr}} + \Delta\hat{\dot{m}}_{\text{hp-egr}}} \quad (7.48)$$

In this context $\Delta\hat{\dot{m}}_{\text{lp-egr}}$ and $\Delta\hat{\dot{m}}_{\text{hp-egr}}$ are the summarised modelling and measurement uncertainties for both EGR mass flow rates. A substitution of the LP-EGR mass flow rate and its uncertainty with the stationary form of Eq. (4.13) eliminates both EGR mass flow rates and their uncertainties. Instead the modelled mass flow rate entering the engine with its uncertainty $\Delta\hat{\dot{m}}_{\text{eng,in}}$ has to be considered now.

$$\hat{x}_{2i}\left(\Delta\hat{\dot{m}}_{\text{eng,in}}, \dots\right) = \frac{\dot{m}_{\text{air}} + \hat{x}_3\left(\hat{\dot{m}}_{\text{eng,in}} + \Delta\hat{\dot{m}}_{\text{eng,in}} - \dot{m}_{\text{air}}\right)}{\hat{\dot{m}}_{\text{eng,in}} + \Delta\hat{\dot{m}}_{\text{eng,in}}} \quad (7.49)$$

In stationary engine condition counts $\hat{x}_{\text{eng,out}} = \hat{x}_3$ and Eq. (3.32) can be inserted into Eq. (7.49), whereas the uncertainties for $\hat{\dot{m}}_{\text{eng,in}}$ are also introduced in (3.32). This elimination of all air contents then yields

$$\hat{x}_{2i}\left(\Delta\hat{\dot{m}}_{\text{eng,in}}, \dots\right) = \frac{\dot{m}_{\text{air}}\left(\hat{\dot{m}}_{\text{f}} + L_{\text{st}}\hat{\dot{m}}_{\text{f}}\right) + \left(\hat{\dot{m}}_{\text{eng,in}} + \Delta\hat{\dot{m}}_{\text{eng,in}}\right)\left(\dot{m}_{\text{air}} - L_{\text{st}}\hat{\dot{m}}_{\text{f}}\right)}{\left(\hat{\dot{m}}_{\text{eng,in}} + \Delta\hat{\dot{m}}_{\text{eng,in}}\right)\left(\dot{m}_{\text{air}} + \hat{\dot{m}}_{\text{f}}\right)}. \quad (7.50)$$

Similar to the air content estimation also the reference value generation of $x_{2i,\text{des}}$ can be expressed with measurement uncertainties $\Delta\hat{\dot{m}}_{\text{eng,in}}$ and delivers with (7.33) and (7.34)

$$x_{2i,\text{des}}\left(\Delta\hat{\dot{m}}_{\text{eng,in}}, \dots\right) = \frac{\frac{\dot{m}_{\text{air,des}} - L_{\text{st}}\hat{\dot{m}}_{\text{f}}}{\dot{m}_{\text{air,des}} + \hat{\dot{m}}_{\text{f}}}\left(\hat{\dot{m}}_{\text{eng,in}} + \Delta\hat{\dot{m}}_{\text{eng,in}} + \hat{\dot{m}}_{\text{f}}\right) + L_{\text{st}}\hat{\dot{m}}_{\text{f}}}{\left(\hat{\dot{m}}_{\text{eng,in}} + \Delta\hat{\dot{m}}_{\text{eng,in}}\right)}. \quad (7.51)$$

After the influences of measurement uncertainties to the intermediate control variable (7.50) and the reference value (7.51) have been defined, it can be claimed that no control deviation shall exist between these quantities

$$x_{2i,des}\left(\Delta\hat{\dot{m}}_{eng,in}, \ldots\right) - \hat{x}_{2i}\left(\Delta\hat{\dot{m}}_{eng,in}, \ldots\right) = 0. \tag{7.52}$$

A substitution of (7.50) and (7.51) in (7.52) then results in

$$\dot{m}_{air,des} = \dot{m}_{air} \tag{7.53}$$

and proves that the combination of the dynamical reference value generation in conjunction with the special form of the air content model of Sect. 4.4 stationary results in an air mass flow rate control, which is not affected by measurement and modelling uncertainties in the intermediate quantities. A main reason for this invariance lies in the determination of the LP-EGR mass flow rate by the balance equation (4.13). This balance equation compensates all uncertainties in the EGR mass flow rate estimation and reduces the uncertainty influence to $\Delta\hat{\dot{m}}_{eng,in}$ which is later compensated by the form of the reference value generation. Contrary to this approach a direct control of a modelled quantity $\hat{x}_{2i}$ would suffer from the apparent measurement uncertainty and deliver a falsified air content to the engine.

### 7.8.3  Engine Test Bench Measurements

After the theoretical foundation is laid, the dynamical reference value generation is applied to the engine at the test bench. The implementation of the air content model in conjunction with the reference value generation demands some minor modifications of the air content model from Sect. 4.4. This air content model can be modelled by a lumped parameter approach and by a pipe receiver model. The pipe receiver model showed better model validation results, since it could describe the plug like flow effects in the intake and exhaust system more detailed, while the lumped parameter model smoothed the sudden changes in the air content more. When it comes to the implementation of the reference value generation, the transport delays $T_{d,p,1/2/c}$ and $T_{d,p,hp}$ in Fig. 4.9 complicate a precise control of $\hat{x}_{2i}$, since on the one hand these delays determine the chronological sequence of the inflowing air contents and on the other hand these delays are directly dependent from the controlled variable $\dot{m}_{hp-egr}$, respectively $\dot{m}_{th}$. These couplings result in fast stepwise changes in the reference value for the HP-EGR controller which cannot be controlled fast enough, so that the HP-EGR controller is always delayed and the control results are unsatisfying and fast varying. Hence, in the following a mixed model structure is utilised for the control of the air content. In this model the intake air content is modelled by the lumped parameter approach and the transport delays $T_{d,p,1/2/c}$ and $T_{d,p,hp}$ are set to zero. All other gas transport delays are modelled by the pipe receiver approach.

Fig. 7.25 presents the implementation of reference value generation at the engine test bench. The topmost plot contains the reference value for the air mass flow rate $\dot{m}_{air,des}$ and the measured air mass flow rate. Then follow the desired values for the intake temperature $T_{2i,des}$ and the intermediate control variable $x_{2i,des}$ with their corresponding modelled quantities. The next two plots

illustrate the directly controlled variables $\hat{\dot{m}}_{\text{hp-egr}}$ and $\hat{\dot{m}}_{\text{lp-egr}}$ and their reference values. In this engine configuration the measured air fuel ratio $\lambda$ is the most suitable quantity which can be utilised to evaluate the performance of the air content control scheme. In the next plot the measured air fuel ratio (meas.), the equivalent air fuel ratio of the air content model ($\hat{x}$-model) and the estimated air fuel ratio of the air mass flow rate measurement and the injection quantity (3.11) are presented. Finally, the course of the actuator positions $s_{\text{hp-egr}}$ and $s_{\text{lp-egr/ith}}$ complete the regarded quantities.

In the illustrated sequence first the reference value for the air mass flow rate is decreased stepwise from 72 kg/h to 47 kg/h at a time of 0 s. This demand is transformed into a demand for the intermediate control variable $x_{2i,\text{des}}$ and further delivers the setpoint for the HP-EGR mass flow rate controller. At the step time the exhaust system contains a fairly air content and the desired intake air content demands a huge amount of recirculated exhaust gas $\hat{\dot{m}}_{\text{hp-egr}}$ after the first second of the setpoint change. However, due to the systems limitations the demanded HP-EGR mass flow rate cannot be delivered, since $s_{\text{hp-egr}}$ is already fully opened. Then the recirculated exhaust gas circles around the intake and exhaust system and is recirculated via the short route EGR and the long route EGR. These gas propagation effects are included in the reference value $\dot{m}_{\text{hp-egr,des}}$ and can be further noticed in the steps of $\dot{m}_{\text{air}}$ and $\hat{\dot{m}}_{\text{hp-egr}}$. Approximately 3.5 s after the reference value step all internal gas propagation dynamics are settled and $\dot{m}_{\text{air}}$ reaches its reference value. During this rather long dwell time the intermediate control variable $\hat{x}_{2i}$ reached its reference value already after 1.2 s. Whereas some portion of this long dwell time is caused by the systems inability to deliver the demanded HP-EGR mass flow rate. A comparison between the modelled ($\hat{x}$-model) and the measured air fuel ratio $\lambda$ confirms the effectiveness of the reference value generation, since the measured and modelled air fuel show only minor differences. In contrast to the air content model, the air fuel ratio model based on the air mass flow rate sensor is largely affected by the internal gas transport dynamics and dynamically does not match the measurement.

During the reference value step in $\dot{m}_{\text{air,des}}$ at a time of 0 s also the reference value generation for the intake temperature is involved. This reference value generation considers the increased total EGR demand and adjusts the reference value $\dot{m}_{\text{lp-egr,des}}$ to a larger value. In the engine system the intake temperature cannot be controlled independently from the air content, since either the LP-EGR and HP-EGR mass flow rate ratio can be adjusted in order to meet a desired temperature or a given air content. In this reference value generation the air content control objective has the larger priority, since it has a stronger influence on the emission formation. This prioritisation can be seen in the temperature course $\hat{T}_{2i}$, which only meets its reference value after all air content dynamics are settled. In this configuration, the reference value $\dot{m}_{\text{lp-egr,des}}$ can be seen as a disturbance for the air content control and forces it to meet the given temperature in stationary conditions.

During the next setpoint change at 5 s the desired temperature changes from 27 °C to 42 °C. This demand for an increased intake temperature results in an almost instantaneous decrease of $\hat{\dot{m}}_{\text{lp-egr}}$ and the formerly by the large LP-EGR mass flow rate occupied proportion of intake volume is flushed with fresh air. This results in the overshoot in $\dot{m}_{\text{air}}$. Shortly after the LP-EGR effects have passed the intake system, also the HP-EGR mass flow rate reference value reacts on the changed intake states and a larger demand is set for $\dot{m}_{\text{hp-egr,des}}$. A similar behaviour can be observed for the opposite setpoint change at a time of 10 s. For this setpoint change $\hat{\dot{m}}_{\text{lp-egr}}$ increases and the
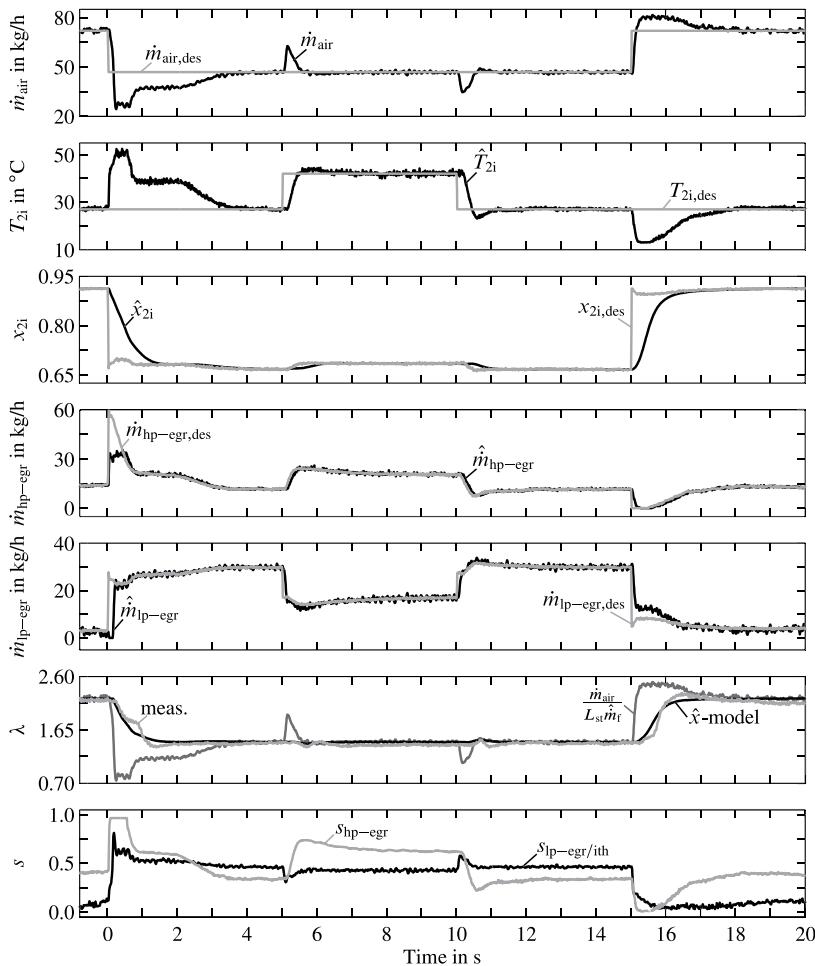
**Figure 7.25:** Test bench measurement for the dynamical reference value generation for changes of the reference values $m_{air,des}$ and $T_{2i,des}$ according to Fig. 7.24 $\left(n_{eng} \approx 1500\,min^{-1},\ u_{inj} = 15\,mm^3/cyc\right)$

intake system is flushed with exhaust gas, which results in the undershoot in $\dot{m}_{air}$. Shortly after the LP-EGR intervention also the reference value generation adjusts $\dot{m}_{hp-egr,des}$. For both setpoint changes the desired temperature is reached and the superior air content reference value generation ensures that the air content after the combustion process stays rather constant, as it can be seen in the measured air fuel ratio $\lambda$. Finally, the setpoint $\dot{m}_{air,des}$ is set back to its initial value at 15 s and

the intake and exhaust system are flushed with fresh air, so that the HP-EGR-valve is fully closed. This results in the undershoot in $\hat{T}_{2i}$ and after all air content dynamics are settled the setpoint $\hat{T}_{2i,des}$ is met. This fully closed HP-EGR-valve results in a sudden shift of the modelling error of $\hat{\dot{m}}_{lp-egr}$ in (4.13), so that this additional deviation has to be adjusted by the integral part of the LP-EGR controller from Fig. 7.21. However, this integral proportion is calibrated too weak, so that the deviations between $\hat{\dot{m}}_{lp-egr}$ and $\dot{m}_{lp-egr,des}$ are compensated only slow.

In summary, the combination of the air content model, the reference value transformation and the rather simple mass flow rate controllers for $\hat{\dot{m}}_{hp-egr}$ and $\hat{\dot{m}}_{lp-egr}$ is capable to supply the combustion process with a calibrated air content. This gets evident when the modelled air fuel ratio is compared to the measured air fuel ratio, which agree well, while the reconstructed air-fuel ratio from the $\dot{m}_{air}$ measurement emphasises the dynamical effects of the internal air contents. In order to supply the combustion process with a defined air content, the air content in the whole gas system has to be considered preemptively in the setpoint generation for the HP-EGR mass flow rate controller. This can result in fast and largely varying HP-EGR mass flow rate demands and is an indicator for the strongly varying process gain of a air content control. Furthermore, it can be seen, that the combination of the air content model with the reference value transformation is invariant to measurement and modelling uncertainties because the modelled air fuel ratio ($\hat{x}$-model) stationary meets the modelled air fuel rate from $\dot{m}_{air}$ and $\hat{\dot{m}}_f$. Hence, comparable to a classical air mass flow rate control scheme this reference value transformation is only dependent on the measurement uncertainty of the air mass flow rate sensor and the injection quantity. In contrast to this classical control scheme the novel reference value generation is capable to handle the inherent process dynamics of the air contents in the intake and exhaust system and transiently delivers the demanded oxygen concentration to the combustion process. A quantitative comparison between the stationary emissions, an intake temperature control without consideration of gas propagation dynamics and the reference value generation is given in the subsequent Sect. 7.9.2.

## 7.9 Dynamical Driving Cycle Emissions of Different Control Concepts

In order to rate the different control concepts for HP-EGR and dual EGR-path configuration, they are compared with regard to emissions and engine work $W_{eng}$ (6.1) during simulations of the NEDC. Base for this comparison are the stationary series calibration for the HP-EGR control concepts and the optimised engine maps for the dual EGR-path configuration from Sect. 6.1. All control concepts are simulated with the mean value engine model and the dynamical emission models from Chap. 5. Considered control concepts for HP-EGR operation are a $\dot{m}_{air}$-control scheme, a $r_{egr}$-control scheme and according to Sect. 6.2 dynamically optimised reference values with regard to the emissions ($x_{opt}$-control). In dual EGR-path operation the dynamical reference value generation from Sect. 7.8 is compared to a control of the intake temperature and dynamically optimised reference values ($x_{opt}$-control) from Sect. 6.2.
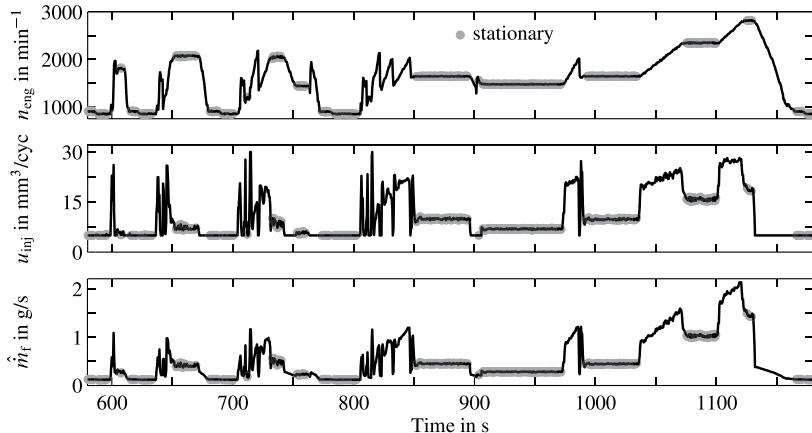
**Figure 7.26:** The NEDC can be separated into 62.1 % dynamical proportion and 37.9 % stationary proportion of time, while 69.9 % of the fuel quantity is injected in the dynamical part and 30.1 % in the stationary part.

In this dissertation the NEDC is the benchmark driving cycle to rate different control concepts. It consist of parts with stationary and dynamical engine operation and their proportions are illustrated in Fig. 7.26. A stationary driving cycle part is defined by derivations of both engine speed and injection quantity close to zero. Consequently, the driving cycle time can be separated in 62.1 % dynamical proportion and 37.9 % stationary proportion. As it can be seen in the injected fuel quantity $\hat{m}_f$, there is more fuel injected during the dynamical parts of the driving cycle. Hence, 69.9 % of the total fuel quantity is injected during the dynamical part, while only 30.1 % is injected in stationary operation. Furthermore, the driving cycle emissions are usually rated in emission quantity per km. Thus, the NEDC covers a distance of 6.68 km in dynamical driving mode and 4.33 km at constant velocity. In the following investigations, the driving cycle emissions are given as overall distance related emissions during the driving cycle and emission proportions of the stationary and dynamical driving cycle parts. All control concepts are compared with regard to the dynamical cylinder charge, which is determined by simulations of the pipe receiver air content model from Sect. 4.4. A transformation of the differential form of (3.10) gives the dynamical air mass equivalent

$$\hat{m}_{air,dyn} = \frac{\hat{x}_{eng,out}\hat{m}_f + \hat{m}_f L_{st}}{1 - \hat{x}_{eng,out}} \tag{7.54}$$

in air mass per working cycle for all control concepts. For a solely HP-EGR configuration the deviations between the measured quantity $m_{air}$ and $\hat{m}_{air,dyn}$ are small, while they have to be considered with additional LP-EGR. Note, that in case of no injection quantity, Eq. (7.54) is not capable to simulate the dynamical air mass equivalent.

### 7.9.1 Dynamical Emissions of the HP-EGR Series Calibration

In this section, the results of a $\dot{m}_{\text{air}}$-control, a $r_{\text{egr}}$-control and quasi-stationary simulations are compared for the series calibration of the investigated DTH-Z19 engine, since this is the reference for the dual path EGR system. The $\dot{m}_{\text{air}}$-control and $r_{\text{egr}}$-control are realised with operation point dependent decentralised PI-controllers and are parameterised according to Sect. 7.3 by replacing the HP-EGR-quantities by the appropriate control variables and their reference values. The charge-air pressure is controlled in two degrees of freedom with semi-physical feedforward control and operation point dependent decentralised PID-controllers. In order to achieve a semi-physical feedforward control, as given in Sect. 7.4, its reference value $\dot{m}_{\text{hp-egr,des}}$ has to be approximated with (7.9) as

$$\dot{m}_{\text{hp-egr,des,(mair-ctl)}} = \dot{m}_{\text{eng,in,des}} - \dot{m}_{\text{air,des}} \tag{7.55}$$

for the $\dot{m}_{\text{air}}$-control and

$$\dot{m}_{\text{hp-egr,des,(regr-ctl)}} = \dot{m}_{\text{eng,in,des}} \cdot r_{\text{egr,des}} \tag{7.56}$$

for the $r_{\text{egr}}$-control. These approximations do not cover the air mass storage effects in the intake system and can consequently not be utilised to generate a feedforward signal $s_{\text{hp-egr,ffc}}$.

In Fig. 7.27 the air path control is simulated in the urban part of the NEDC. The controlled quantities $\dot{m}_{\text{air,dyn}}$, $r_{\text{egr}}$ and $p_{2i}$ are shown for both control concepts $\dot{m}_{\text{air}}$-control and $r_{\text{egr}}$-control and compared to their quasi stationary reference values, which result from the reference value map outputs of a given $n_{\text{eng}}$ and $u_{\text{inj}}$ profile. For both control concepts the actuator positions $s_{\text{t}}$ and $s_{\text{hp-egr}}$ are presented. In the bottom plots the emission quantities $\dot{m}_{\text{nox}}$ and $\dot{m}_{\text{mss}}$ as well as the engine torque $M_{\text{eng}}$ are illustrated for the two control concepts and the quasi-stationary simulation of the engine maps (quasi-stat.).

In the air mass flow rate plot it can be seen, that the $\dot{m}_{\text{air}}$-control follows its reference value $m_{\text{air,des}}$ well, while the corresponding air mass flow rate of the $r_{\text{egr}}$-control scheme dynamically follows a different trajectory. At some points (614 s, 650 s, 680 s 735 s), the $\dot{m}_{\text{air}}$-control is not capable to follow its reference values, since the HP-EGR-valve is saturated. Similar investigations can be made for the quantity $r_{\text{egr}}$. In this plot the $r_{\text{egr}}$-controller follows its reference value $r_{\text{egr,des}}$, while there are dynamical variations of the $\dot{m}_{\text{air}}$-control. In the charge-air pressure $p_{2i}$ there are no significant deviations between both control schemes, while both controllers follow the reference values delayed by the relative slow turbocharger dynamics. In the emission quantities there are some deviations between the control schemes and the quasi-stationary simulations. These deviations are apparent during the acceleration phases, e.g. in the zoomed section. At these peaks the $\dot{m}_{\text{air}}$-control shows larger NO$_x$ emissions than the $r_{\text{egr}}$-control, while vice versa the particulate emissions are larger for the $r_{\text{egr}}$-control, see Sect. 6.2.1. During the dynamical phases the quasi-stationary emissions are often smaller than the emissions of both control concepts. In the engine torque $M_{\text{eng}}$, there are no significant deviations between the different control concepts.

Fig. 7.28 highlights the same quantities in the extra urban part of the NEDC. Alike in the urban part it can be noticed, that both control concepts follow their reference values well, while there are dynamical deviations in the uncontrolled quantity. In this part the $NO_x$ emissions for the $r_{egr}$-control are smaller than the emissions of the $\dot{m}_{air}$-control and the quasi-stationary simulations, while especially at times between $1110\,s$ and $1120\,s$ the particulate emissions of the $r_{egr}$-control are larger. Generally, the $NO_x$ emissions of the $\dot{m}_{air}$-control fit the quasi-stationary emissions in the sections with low dynamics well, while there are some deviations in the emissions of the $r_{egr}$-control. One reason for these deviations is the interpolation of the reference value maps for $m_{air,des}$ and $r_{egr,des}$. At the supporting points, a given air mass flow rate can be directly transformed into the corresponding $r_{egr}$-rate. However, between these supporting points both reference values are bilinear interpolated. Due to the nonlinear relationship between the two quantities $m_{air}$ and $r_{egr}$, the achieved air mass flow rate resulting from a $m_{air,des}$-map and a $r_{egr}$-map differ in the interpolation range.

This fact gets obvious at the time range between $1078\,s$ and $1100\,s$, where both the $r_{egr}$-control and the $\dot{m}_{air}$-control are settled to their reference value, but deviate in $\dot{m}_{air,dyn}$. Furthermore, the achieved air mass flow rate from a $r_{egr}$-control strongly varies at fixed $p_{2i}$ with changes in the ambient temperature, since at changed ambient temperatures the intake temperature changes and according to (3.28) the mass flow rate entering the engine. Thus, at varying engine mass flow rates and fixed EGR-rate the resulting quantity $\dot{m}_{air}$ varies.

Dynamically there are some differences between the control concepts. Hence, the zoomed load steps at $1101\,s$ and $1120\,s$ are discussed in the following. As analysed in Sect. 6.2.1, the first zoomed step at $1101\,s$ represents an acceleration activity, compare to Fig. 7.26, with a rise in injection quantity. During this transient the $\dot{m}_{air}$-control rises the air mass flow rate fast to meet its reference value, while the air mass flow rate resulting from the $r_{egr}$-control follows delayed. For the $\dot{m}_{air}$-control this increase of air mass flow rate results in a $NO_x$ peak, but lowered particulate emissions. In comparison to the quasi-stationary emissions, the $\dot{m}_{nox}$ emissions are larger, while the particulate emissions $\dot{m}_{mss}$ are lowered for this transient. The $r_{egr}$-control has lower $NO_x$ emissions, while the particulate emissions are similar to the quasi-stationary course. In the second zoomed section at $1120\,s$ a deceleration is investigated. In this transient $\dot{m}_{nox}$ shows an undershoot for the air mass flow rate control, while $\dot{m}_{mss}$ is in the same range as the particulate emissions of the $r_{egr}$-control. For the $r_{egr}$-control the $NO_x$ emissions are at a level with the quasi-stationary simulations and larger than the $NO_x$ emissions of the other control scheme.

As conclusion, a $\dot{m}_{air}$-control has dynamical enlarged $NO_x$ emissions for load steps of rising injection quantity, but compensates it with decreased $NO_x$ emissions for load steps of falling injection quantity. In respect of particulate emissions the $\dot{m}_{air}$-control benefits from the increased air mass at rising load steps and is not penalised for missing air at falling load steps. Consequently, the dynamical $NO_x$ balance for the $\dot{m}_{air}$-control is rather neutral, while there are some advantages with respect to the particulate emissions. The $NO_x$ balance for the $r_{egr}$-control benefits from rising loads and is neutral with respect to falling loads. With respect to the particulate emissions a rising injection quantity results in dynamical increased particulate emissions, which cannot be compensated

by decreased particulate emissions for falling injection quantities. Thus, a $r_{egr}$-control achieves its favourable $NO_x$ emissions on the cost of larger particulate emissions.
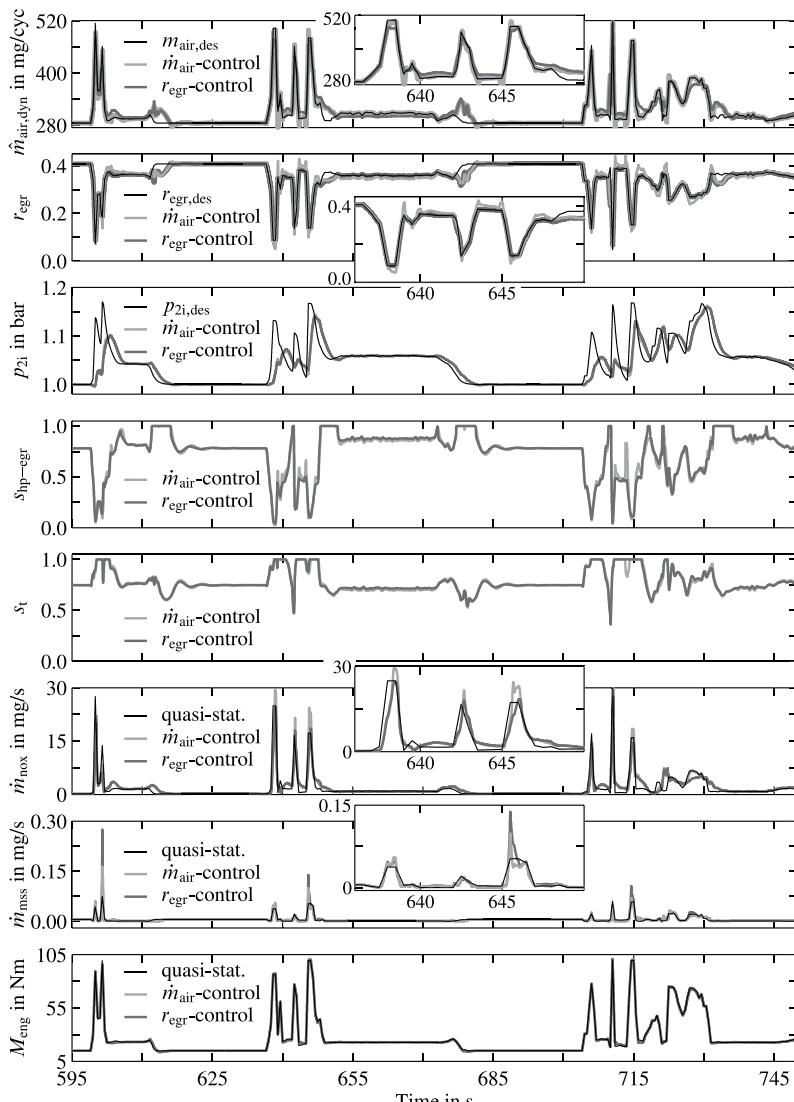


**Figure 7.27:** Simulated comparison of an air mass flow rate and EGR-rate control scheme with regard to the dynamical emissions in the urban part of the NEDC (HP-EGR configuration)
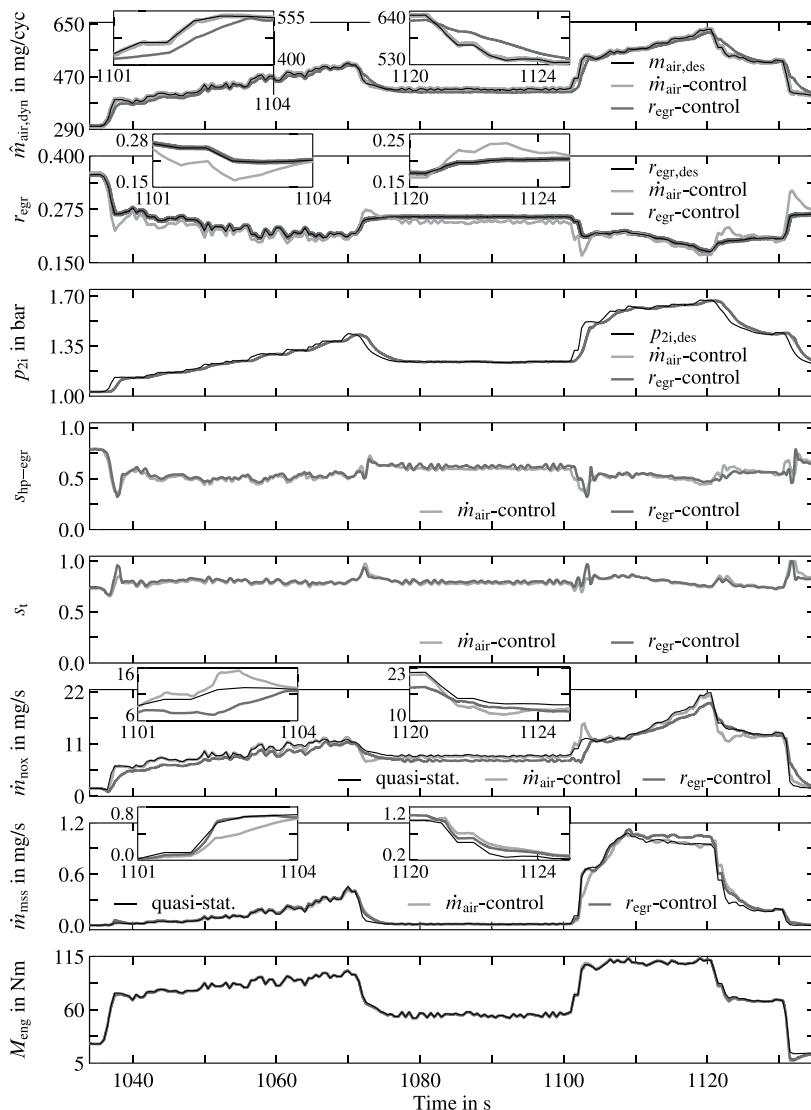
**Figure 7.28:** Simulated comparison of an air mass flow rate and EGR-rate control scheme with regard to the dynamical emissions in the extra-urban part of the NEDC (HP-EGR configuration)

These characteristics of both control concepts can be visualised in Fig. 5.5a), where the $NO_x$ emissions and the particulate emissions are plotted over the air mass flow rate. It can be seen, that $\hat{c}_{nox}$ forms a relative straight line, while $\hat{c}_{mss}$ rises exponentially with decreasing $\dot{m}_{air}$. A $\dot{m}_{air}$-control concept dynamically avoids the exponential particulate peak of a rising load step, by delivering more $\dot{m}_{air}$. During a falling load step less air is delivered, which is not penalised, since at small injection quantities, respectively large air mass flow rates, the course of $\hat{c}_{mss}$ is rather flat. Due to the straight course of $\hat{c}_{nox}$ the dynamical benefits and drawbacks with regard to the $NO_x$ emissions are virtually compensated. A $r_{egr}$-control hits the exponential particulate increase during rising injection quantities and cannot compensate it with significantly lower emissions at falling injection quantities.
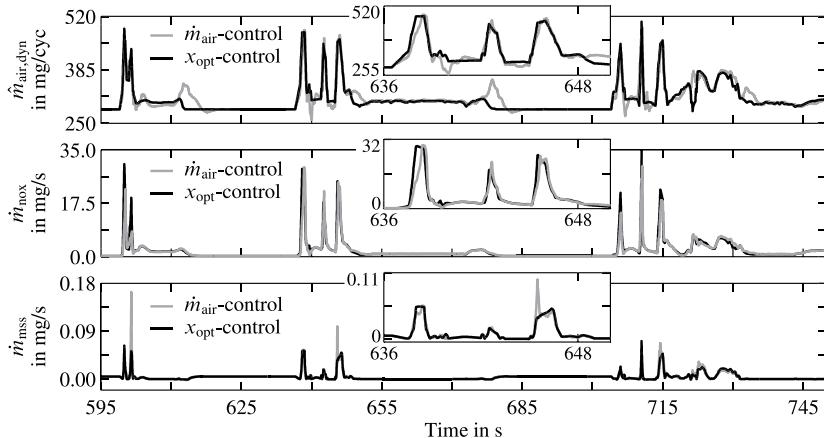


**Figure 7.29:** Simulated comparison of an air mass flow rate control and dynamical optimised reference values with regard to the dynamical emissions in the urban part of the NEDC (HP-EGR configuration)

Next, the results of the $\dot{m}_{air}$-control are compared with the trajectories of dynamically optimised reference values ($x_{opt}$-control), as given in Sect. 6.2.2. Fig. 7.29 compares these control concepts in the urban part of the NEDC and shows the quantities $\hat{m}_{air,dyn}$, $\dot{m}_{nox}$ and $\dot{m}_{mss}$. It can be noted, that the optimised air mass flow rate trajectory dynamically slightly differs from the $\dot{m}_{air}$-control. These deviations result in larger $\dot{m}_{nox}$ emission peaks, while the $\dot{m}_{mss}$ emissions peaks are smaller. A further comparison of the extra urban part of the NEDC is given in Fig. 7.30. During this section at times between 1077 s and 1100 s the dynamically optimised air mass flow rate favours the $NO_x$ emissions without significant increase in the particulate emissions. At the load step at 1103 s the dynamical optimisation avoids the $\dot{m}_{nox}$-peak from the $\dot{m}_{air}$-control. In the further course at the times between 1110 s and 1130 s the optimised reference values shift the $NO_x$ particulate tradeoff towards lower particulate emissions and larger $NO_x$ emissions.
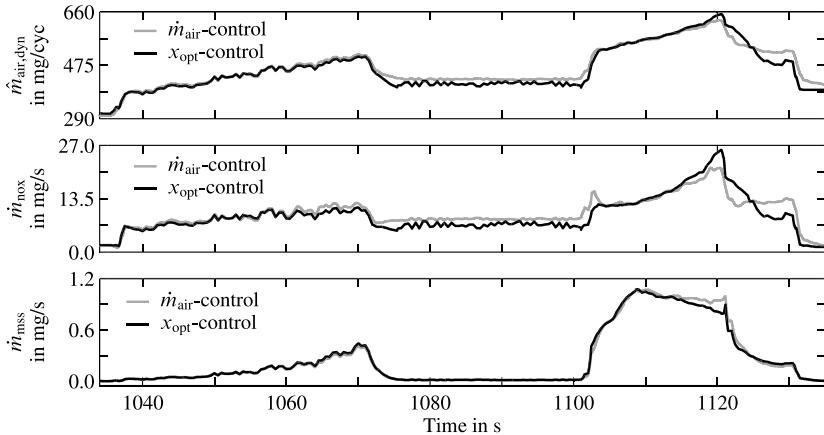
**Figure 7.30:** Simulated comparison of an air mass flow rate control and dynamical optimised reference values with regard to the dynamical emissions in the extra-urban part of the NEDC (HP-EGR configuration)

A quantitative comparison of the different investigated control concepts is given in Tab. 7.2 with respect to the overall distance related driving cycle emissions (over.), the distance related emissions at stationary sections (stat.), and the distance related emissions during the dynamical phases of the driving cycle (dyn.). It can be noted, that a great proportion of the quasi-stationary emissions is contributed during the dynamical driving cycle proportions with large injection quantities. This emission increase is independent from the air path dynamics and results from the calibrated engine maps at these injection quantities and engine speeds. With the different control concepts, the air path dynamics are considered in the emission quantities. The air mass flow rate control results in emissions, which only vary slightly from the quasi-stationary emissions. The $r_{egr}$-control lowers the $NO_x$ emissions on the cost of larger particulate emissions, while the optimised reference values $x_{opt}$-control slightly move the quasi-stationary $NO_x$ particulate tradeoff in direction of lower particulate emissions. As conclusion for the HP-EGR-configuration it can be stated, that a large part of the emissions is contributed in the dynamical part of the driving cycle. A reason for these increased emissions are larger injection quantities, while the air path dynamics and the choice of the control concept have only minor impact on the distance related emissions. An air mass flow rate control delivers distance related emissions, which agree in their magnitude well with the stationary calibrated engine maps. The $r_{egr}$-control scheme can be utilised, if lower $NO_x$ emissions are demanded on the cost of larger particulate emissions. Dynamical optimised reference values have no significant advantage over a $\dot{m}_{air}$-control. It is shown, that dynamical optimised reference values have only a small potential to further lower the emissions of the HP-EGR configuration with series calibration, but are optimal with regard to the quality criterion.

**Table 7.2:** Overall, stationary and dynamical distance related emissions of the HP-EGR series calibration during the NEDC for different controlled variables

| | quasi-stationary | | | $\dot{m}_{air}$-control | | | $r_{egr}$-control | | | $x_{opt}$-control | | |
|---|---|---|---|---|---|---|---|---|---|---|---|---|
| in | $m_{nox}$ mg/km | $m_{mss}$ mg/km | $W_{eng}$ kWh | $m_{nox}$ mg/km | $m_{mss}$ g/km | $W_{eng}$ kWh | $m_{nox}$ mg/km | $m_{mss}$ mg/km | $W_{eng}$ kWh | $m_{nox}$ mg/km | $m_{mss}$ mg/km | $W_{eng}$ kWh |
| over. | 244.8 | 2.74 | 1.53 | 244.1 | 2.74 | 1.54 | 228.6 | 2.91 | 1.54 | 245.5 | 2.71 | 1.54 |
| stat. | 139.5 | 0.29 | 0.44 | 135.9 | 0.29 | 0.44 | 130.5 | 0.29 | 0.44 | 128.5 | 0.30 | 0.44 |
| dyn. | 313.0 | 4.33 | 1.09 | 314.1 | 4.32 | 1.09 | 292.1 | 4.61 | 1.09 | 321.3 | 4.27 | 1.10 |

deviations between quasi-stationary and controlled engine operation in dynamical related emissions (dyn.)

| | | | | +0.4% | -0.02% | $\pm$0% | -7.2% | +6.5% | $\pm$0% | +2.7% | -1.4% | +0.9% |

### 7.9.2 Dynamical Emissions of the Dual EGR-Path Calibration

In this section, the dynamical emissions of the dual EGR-path calibration are analysed for quasi-stationary reference values, the air content control $x$-control from Sect. 7.8, the intake temperature control $T_{2i}$-control from Sect. 7.8 and dynamically optimised reference values ($x_{opt}$-control) from Sect. 6.2. In order to achieve the control objective, reference values for the intermediate control variables $\dot{m}_{hp-egr}$ and $\dot{m}_{lp-egr}$ are controlled according to (7.40) and (7.43) for the $T_{2i}$-control, respectively according to (7.37) and (7.47) for the $x$-control. Stationary reference values for the dual EGR-path configuration are given in Sect. 6.1. The quantities $\dot{m}_{hp-egr}$ and $p_{2i}$ are controlled with the semi-physical internal model control from Sect. 7.5, while the semi-physical control from Sect. 7.7 controls the LP-EGR mass flow rate. In order to determine the emission and combustion quantities dynamically correct, the air content pipe-receiver model from Sect. 4.4 is utilised to determine the cylinder charge. For visualisation the dynamical air mass equivalent (7.54) $\hat{m}_{air,dyn}$ is utilised.

Fig. 7.31 compares the quasi-stationary driving cycle results with the air content control and intake temperature control in the urban part of the NEDC. The control results are given for the primarily controlled variables air mass flow rate, respectively dynamical air mass equivalent $\hat{m}_{air,dyn}$, intake temperature and charge-air pressure. It can be seen, that the control results of the $x$-control meet the demanded air mass flow rates $m_{air,des}$ dynamical well, while the $T_{2i}$-control scheme shows some deviations in $\hat{m}_{air,dyn}$. This gets obvious in the zoomed section. The $T_{2i}$-control scheme has not the objective to meet the dynamical air mass equivalent. Its objective is to follow the demanded intake temperature trajectory, which is met well in the $T_{2i}$ plot. In the $x$-control scheme $T_{2i}$ is the inferior control variable and it dynamically has deviations to the reference values $T_{2i,des}$. However, in stationary condition both control concepts show no deviations between the controlled quantity and the reference value of the inferior control variables. The last controlled quantity $p_{2i}$ is controlled equally well in both control concepts. For completeness, also the actuator positions $s_{hp-egr}$, $s_{lp-egr/ith}$ and $s_t$ are given for both control concepts.
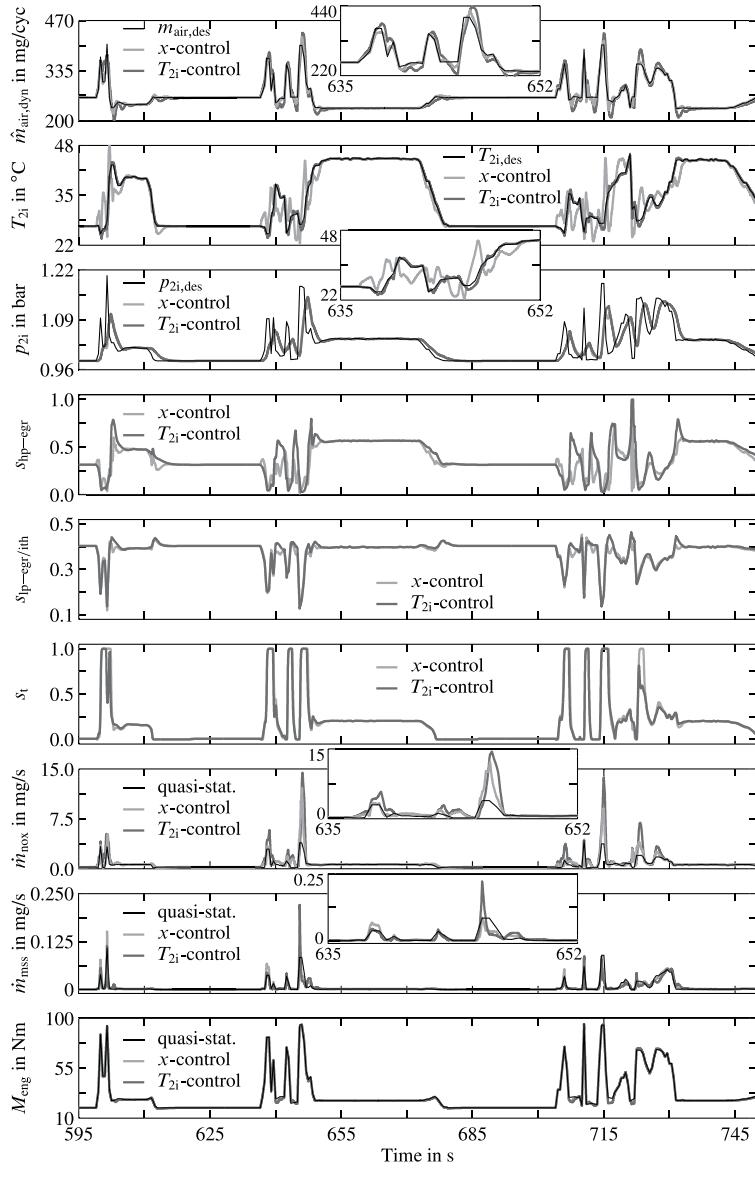
**Figure 7.31:** Simulated comparison of a $x$-control, a $T_{2i}$-control with regard to the dynamical emissions in the urban part of the NEDC (HP-EGR and LP-EGR configuration)
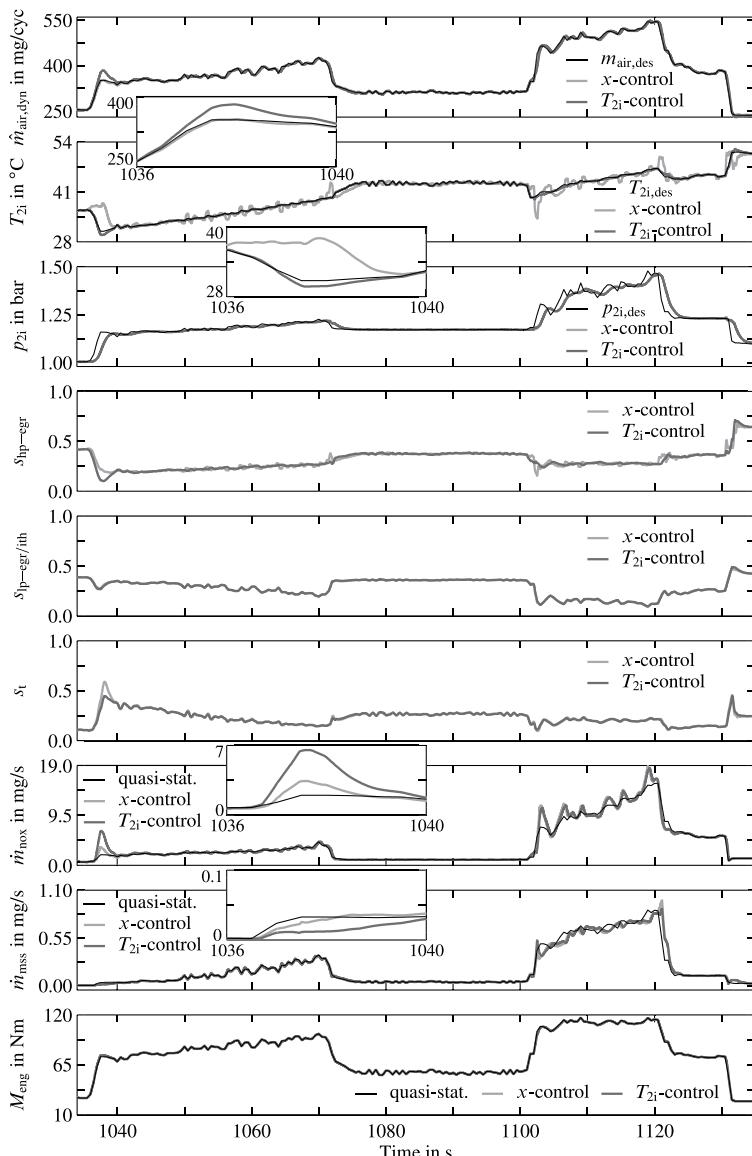
**Figure 7.32:** Simulated comparison of a $x$-control, a $T_{2i}$-control with regard to the dynamical emissions in the extra-urban part of the NEDC (HP-EGR and LP-EGR configuration)

With respect to the $NO_x$ emissions, there are dynamical significant deviations between the quasi-stationary emissions and the emissions of both control concepts. While the $\dot{m}_{nox}$-peaks of the $x$-control are significantly smaller, there are larger peaks for the $T_{2i}$-control. The particulate emissions $\dot{m}_{mss}$ show a rather mixed characteristics, which does neither favour the $x$-control nor the $T_{2i}$-control. Though, both control schemes have dynamical larger emissions than the quasi-stationary simulation, these short emission peaks contribute only minor to the overall driving cycle emissions. The resulting engine torque shows almost no deviation between all investigated control concepts.

In Fig. 7.32 the control concepts are compared in the extra-urban part of the NEDC. Significant deviations between the $x$-control and the $T_{2i}$-control can be only observed in the zoomed section, where the $x$-control scheme prevents a $\dot{m}_{nox}$ peak. Furthermore, there are some minor differences in the emission quantities between the control concepts and the quasi-stationary simulation results at the acceleration part at the time range from 1100 s to 1120 s. In the rest of this section no notably deviations can be observed between the two control concepts and the quasi-stationary simulations.
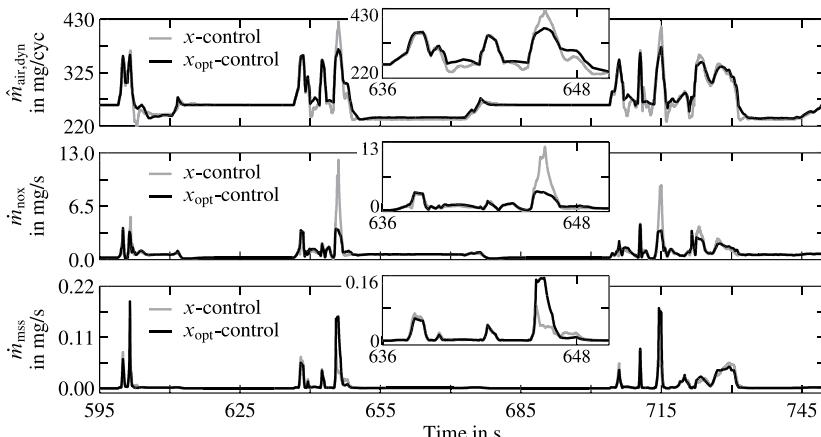


**Figure 7.33:** Simulated comparison of a air content control and dynamical optimised reference values with regard to the dynamical emissions in the urban part of the NEDC (HP-EGR and LP-EGR configuration)

Next, in Fig. 7.33 dynamical optimised reference values ($x_{eng,opt}$-control), according to Sect. 6.2, are compared to the results of the $x$-control scheme during the urban part of the NEDC. It can be noted, that the dynamically optimised reference values, result in a dynamical air mass equivalent, which differs from the results of the $x$-control. These optimised trajectories especially avoid $\dot{m}_{nox}$ emission peaks on the cost of increased particulate emissions. A comparison to Fig. 7.31 shows, that the benefits of optimised reference values get effective at transients where $p_{2i}$ follows its reference value delayed by the inherent process dynamics.

Fig. 7.34 compares the potential of the $x_{opt}$-control to the $x$-control for the extra-urban part of the NEDC. It can be seen, that there is only minor room for improvement in this section. A small $\dot{m}_{nox}$ peak is optimised at 1037 s and the course of the emissions during the acceleration part between 1100 s and 1120 s is smoothed with optimised reference values. In comparison to Fig. 7.32, dynamically optimised reference values deliver an emission course, which follows the quasi-stationary emissions closer.
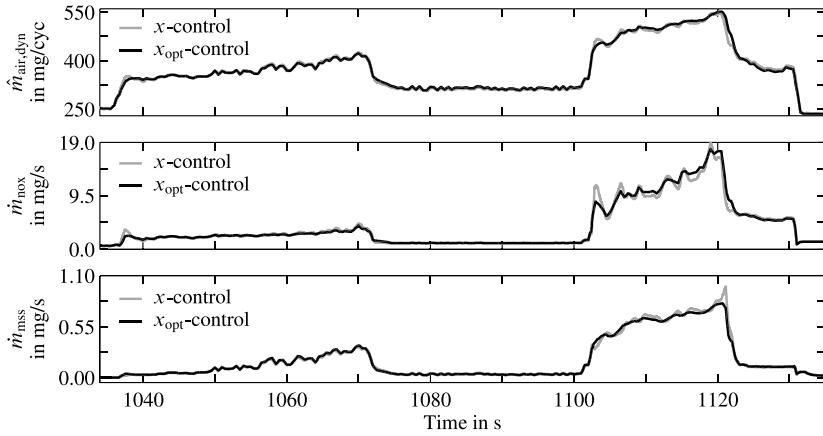


**Figure 7.34:** Simulated comparison of a air content control and dynamical optimised reference values with regard to the dynamical emissions in the extra-urban part of the NEDC (HP-EGR and LP-EGR configuration)

Finally, in Tab. 7.3 the investigated control concepts are quantitatively evaluated with regard to the distance related emissions and the delivered engine work during the overall driving cycle (over.), the stationary proportions (stat.) and the dynamical proportions (dyn.). The $T_{2i}$-control scheme can be applied without significant effort and shows the largest $NO_x$ emissions. Its overall particulate emissions are lower than the emissions of the quasi-stationary simulation.

At this point the additional effort for the air content model and the dynamical reference value generation from Sect. 7.8 pays off. The $NO_x$ emissions are significantly lower than the emissions of the $T_{2i}$-control scheme, while there is only a tiny increase in the particulate emissions. However, these quantities of $m_{mss}$ are still smaller than the quasi-stationary emission level. The largest effort is needed for dynamically optimised reference values and it delivers $NO_x$ emission, which are closest to the quasi-stationary simulations, while the particulate emissions are slightly better. With regard to the engine work, all control concepts have comparable results. In stationary engine operation there are no notable emission deviations between the different control concepts, while most deviations are contributed during the dynamical proportions of the driving cycle. As conclusion it can be stated that the effort for a $x$-control scheme and dynamical optimised reference values pays off and delivers lower $NO_x$ emissions than the $T_{2i}$-control at almost no rise in partic-

ulate emissions. A further decrease in the dynamical emissions can be achieved with additional effort by the $x_{opt}$-control scheme. These $x$-control and $x_{opt}$-control concepts aim at the dynamical part of driving cycles and their benefit will probably be larger for driving cycles with a greater dynamical engine excitation. Thus, in future research these control concepts could be evaluated in respect to driving cycles having larger proportions of dynamics.

**Table 7.3:** Overall, stationary and dynamical distance related emissions of the LP-EGR calibration during the NEDC for different controlled variables

| | quasi-stationary | | | $T_{2i}$-control | | | $x$-control | | | $x_{opt}$-control | | |
|---|---|---|---|---|---|---|---|---|---|---|---|---|
| in | $m_{nox}$ mg/km | $m_{mss}$ mg/km | $W_{eng}$ kWh | $m_{nox}$ mg/km | $m_{mss}$ mg/km | $W_{eng}$ kWh | $m_{nox}$ mg/km | $m_{mss}$ mg/km | $W_{eng}$ kWh | $m_{nox}$ mg/km | $m_{mss}$ mg/km | $W_{eng}$ kWh |
| over. | 79.3 | 2.32 | 1.64 | 98.4 | 2.25 | 1.64 | 88.3 | 2.26 | 1.64 | 84.5 | 2.28 | 1.64 |
| stat. | 42.1 | 0.34 | 0.50 | 42.0 | 0.34 | 0.50 | 42.3 | 0.34 | 0.50 | 41.3 | 0.31 | 0.50 |
| dyn. | 103.5 | 3.61 | 1.14 | 134.9 | 3.48 | 1.14 | 118.2 | 3.50 | 1.14 | 112.5 | 3.56 | 1.14 |
| deviations between quasi-stationary and controlled engine operation in dynamical related emissions (dyn.) | | | | | | | | | | | | |
| | | | | +30.3% | -3.7% | ±0% | +14.2% | -3.1% | ±0% | +8.7% | -1.4% | ±0% |

## 7.9.3  Essential Findings of Sect. 7.9

In a nutshell, stationary and dynamical proportions of a driving cycle are defined. The example of the NEDC shows, that this driving cycle can be separated into 62.1 % of dynamical proportion and 37.9 % of stationary proportion, while 69.9 % of the fuel quantity is injected in the dynamical part and 30.1 % in the stationary part. Due to larger injection quantity and longer time, the emissions of the dynamical driving cycle part are larger than the emissions of the stationary part.

In the reference engine calibration with only a HP-EGR, the quasi-stationary emissions of the driving cycle are compared to the emission level of a dynamical simulation with two air path control concepts $\dot{m}_{air}$-control and $r_{egr}$-control, see Fig. 7.29 and Fig. 7.30. Interestingly, the emission level of the dynamical engine operation differs only slightly from the quasi-stationary driving cycle emissions. In which the $\dot{m}_{air}$-control shows slight benefits in the dynamical $NO_x$ emissions at unvaried particulate emissions, while the $r_{egr}$-control shows 7.2 % decreased dynamical $NO_x$ emissions with a 6.5 % increase in the particulate emissions. Further, dynamical optimised reference values show a decrease of 1.4 % in the particulate emissions with an increase of 2.7 % in the $NO_x$ emissions.

Two control structures for HP- and LP-EGR are compared with regard to the quasi-stationary emissions of the driving cycle. A simple control of air mass flow rate and intake temperature without consideration of air content dynamics ($T_{2i}$-control) and a control structure with a dynamical reference value generation to consider gas propagation times in the in- and exhaust system ($x$-control), see Fig. 7.31 and Fig. 7.32. Compared to the quasi-stationary emission level, the simple $T_{2i}$-control shows a 30.3 % increase in the dynamical $NO_x$ emissions, while the particulate emissions sink for 3.7 %. As results of the $x$-control, the dynamical $NO_x$ emissions are 14.2 % increased, while the particulate emissions decrease for 3.1 %. Dynamical optimised reference values show the best results and have 8.7 % increased $NO_x$ emissions and 1.4 % lowered particulate emissions.

Interestingly, the postulated strong deviations between emission of a stationary and dynamical engine operation can not be shown with the given combination of engine, air path control, engine calibration and driving cycle. Generally, the investigated emission level of a dynamical engine operation only slightly differs from the stationary engine operation. Thus, there is only a small potential for an improved emission level with for dynamical optimised reference values for the air path control, with the given test conditions. Though, recent legislative matters tend to driving cycles like the worldwide harmonized light-duty vehicles test procedure (WLTP) or real driving emissions (RDE), which incorporate more dynamics in engine speed and injection quantity than the NEDC. These novel driving cycles and tighter emission limits give the demand to on-line optimise reference values for arbitrary driving situations.

Finally, the investigations of the $T_{2i}$-control showed, that gas propagation times in the intake and exhaust system have a negative influence on the emission formation. These gas propagation effects are considered by the dynamical reference value generation from Sect. 7.8 and deliver good results for the dynamical emission formation. Finally, in comparison to the $\dot{m}_{air}$-control with only a HP-EGR configuration, the derived control concept $x$-control with additional LP-EGR is capable to lower the overall $NO_x$ emissions to 36.2 % and the particulate emissions to 82.5 %, while the delivered engine work $W_{eng}$ rises to 107.2 %.

## 7.10   Summary

In this chapter different control concepts for the air path of engines with dual EGR are presented. The quantities HP-EGR mass flow rate and charge-air pressure are controlled decentralised from the LP-EGR mass flow rate. For the classical HP-EGR mass flow rate and charge-air pressure control problem, a two degree of freedom control concept with semi-physical feedforward control, reference shaping filters and decentralised PI(D)-controllers is presented. For this control, the PI(D)-controllers are automatically calibrated by a linearisation of the mean-value engine model and a subsequent internal model control design with model reduction to PI(D)-controllers.

The semi-physical feedforward control is based upon a model inversion of the semi-physical air path model. This model inversion allows a control design with minor calibration effort, since parameterised engine models are usually available. The feedforward control further decouples the air path quantities and implicitly considers the side effects of different engine operation modes, LP-EGR operation and changes in the ambient conditions. Further, its modularity is well suited for a modern engine development process by construction kits. The two degree of freedom control concept allows to fulfil both common control objectives having simultaneously a good response to setpoint changes and a well suiting disturbance rejection. Anymore, the semi-physical feedforward control is extended to a semi-physical internal model control, which makes additional PI(D)-controllers superfluous.

The different control concepts are compared with test bench measurements. A solely control with decentralised PI(D)-controllers shows moderate reference following and strong couplings in the charge-air pressure. The control of the quantity HP-EGR mass flow rate shows better control results. The two degree of freedom structure as combination of a semi-physical feedforward control and subsequent PI(D)-control have a very good reference following and couplings are damped to a minimum. Similar results could be achieved by the semi-physical internal model control. One large benefit of the semi-physical feedforward control is the potential to speed up the reference following of the charge-air pressure close to the results of a time optimal control.

A decentralised semi-physical control is utilised to control the LP-EGR mass flow rate. This control applies the invariance of the LP-EGR-rate to the LP-EGR-actuator position at all engine operation points to generate a control signal. Further, the control is validated at the engine test bench and shows good control results with the simultaneous control of the other air path quantities $\hat{\dot{m}}_{hp-egr}$ and $p_{2i}$.

The reference values for the HP- and LP-EGR mass flow rate controllers are derived from stationary maps for air mass flow rate and intake temperature by a dynamical reference value generation with the intake air content as intermediate control variable. This reference value generation considers the inherent dynamics of gas propagation in the intake and exhaust system to supply the cylinders with the proper amount of fresh air. Test bench results validate this reference value generation and show, that it is capable to handle the inherent gas propagation effects of the LP-EGR system. In this control scheme the intake air content is the primary control variable, while the intake temperature is controlled inferior. It is proven, that the combination of the air content model

and the reference value generation is stationary invariant to modelling and measurement uncertainties and stationary delivers the desired air mass flow rate. Alternatively, the reference value generation can be modified, so that the intake temperature is controlled as primary control variable. Consequently, in this configuration the intake air content is controlled with minor priority.

Finally, different control concepts for a solely HP-EGR operation and a dual EGR configuration are simulated and compared with regard to the emissions and the delivered engine work. For the HP-EGR series calibration the air mass flow rate control yielded emissions, which were close to the quasi-stationary emissions of the engine calibration. The $r_{egr}$-control delivered favourable $NO_x$ emissions, while the particulate emissions were enlarged. Dynamically optimised reference values (Sect. 6.2) almost reached the quasi-stationary $NO_x$ emission level and could further reduce the particulate emissions. All control concepts delivered comparable results with respect to the engine work. In the dual EGR configuration the simple intake temperature control had the largest increase in the $NO_x$ emissions. These emissions could be reduced by the more complex air content control (Sect. 7.8) and the dynamically optimised reference value concept (Sect. 6.2), which yielded the lowest $NO_x$ emissions of all investigated control concepts. The particulate emissions of all investigated control concepts were slightly lower than the emissions of the quasi-stationary simulations, while the engine work was almost equal for all control concepts.

# 8 Conclusions

The objective of this dissertation is to derive a modern model-based framework for engine control development and calibration considering the exemplary process of a turbocharged Diesel engine with HP- and LP-EGR. The Diesel engine is a complex process and many facts are not known, but necessary to understand the whole system. Thus, there is an extended version of this dissertation in Mrosek (2017), which gives more details and especially covers the approach of model parameterisation.

Well fitting engine and emission models are the essential basis to optimise reference values for engine control, to determine controlled variables and to develop, calibrate and rate controllers for the air path quantities. Based upon a semi-physical mean value engine model the system properties of the engine air path with HP- and LP-EGR are analysed and modular model-based controllers to master the rising complexity and variance of future engine configurations are developed. Finally, the performance of different control concepts is quantitatively rated by a comparison of the stationary calibrated emission level with the emission output of an engine operation during a dynamical driving cycle.

**System Properties**

As a first step in control development the system properties are analysed by step responses to the relevant air path actuators HP-EGR-valve, LP-EGR-actuator and VGT-actuator. Besides the known effects of HP-EGR-valve and VGT-actuator, new effects are introduced by the LP-EGR system. There are strong influences from HP-EGR and VGT to the LP-EGR quantities, while there are only small influences resulting from the LP-EGR system. An analysis shows, that the LP-EGR rate is mainly dependent from its actuator position and not from the engine operation point. This allows to derive a simple control law for the LP-EGR quantities. A main difference between a HP-EGR and a LP-EGR are the gas transportation dynamics in the intake and exhaust system. These dynamics can be modelled by a control oriented pipe receiver air content model. Suitable control variables for the dual EGR system are the air content in the intake system and the intake temperature. According to the emission modelling this air content is a strong indicator for the particulate emissions.

**Emission and Combustion Models**

The legislative emission limitations are a main driver of Diesel engine development and many control functionalities are benchmarked by their resulting emissions. Consequently, models are necessary, to optimise and evaluate the stationary and dynamical engine operation.

It is shown, that the emission formation can be simplified to a batch process, whose output is determined by the cylinder filling at intake valve closing and the injection characteristics. Most of the resulting dynamics result from the air path dynamics in the cylinder filling and the emission measurement dynamics. These measurement dynamics are composed of gas propagation times and sensors dynamics. A closed loop control of the relevant model inputs for stationary emission models allows a fast stationary measurement design. Stationary $NO_x$ and particulate emissions as well as the engine torque are modelled with a global-local modelling approach, consisting of local polynomial models which are globally superimposed weighted by the engine operation point. A combination of a air content model describing the cylinder filling dynamics, stationary emissions models and emission measurement dynamics models allows the simulate the dynamical emission formation.

### Optimisation of the Emissions

A calibration for a system with HP- and LP-EGR shows large emission benefits compared to the series calibration with only HP-EGR. A comparison of different controlled variables ($\dot{m}_{air}$, $r_{egr}$, $x_{2i}$) shows strong deviations between the stationary and dynamical emissions during operation point changes. These deviations are caused by the multi-variable control problem and the different dynamics in the engine air path. The compared quantities can be controlled relatively fast to their setpoint, while the charge-air pressure follows delayed by the turbocharger dynamics. This yields different trajectories in the cylinder charge and either $NO_x$ or particulate emissions are favoured. A novel real-time capable optimisation utilises a multi-criteria loss function of weighted polynomial emission models. Its weights are derived from a stationary engine calibration. The optimum of this superimposed loss function can be determined analytically. As a result, the dynamical optimised reference values for the controller neither favour $NO_x$ or particulate emissions during an engine transient.

### Reference Value Generation

A reference value generation transforms reference values for the air mass flow rate into the intermediate control variable intake air content and the directly controlled variable HP-EGR mass flow rate. A desired intake temperature is transformed to a LP-EGR mass flow rate demand. Contrary to an air content control, this reference value generation is not affected by suddenly changing process gains of the air content in the intake and exhaust system. It is proven, that the reference value transformation is invariant from measurement and modelling uncertainties and stationary results in an air mass flow rate control.

### Semi-Physical Air Path Control

A semi-physical air path control is the key to master the rising demand for controller performance and to handle variants of engines at a low calibration effort. It is applied to control the HP-EGR

mass flow rate and the charge-air pressure. Changing engine operation modes and the influence of ambient conditions, particulate filter loading are implicitly incorporated into the control concept. Its modularity allows to interchange single submodels during the engine development process and to adapt for engine variants without recalibrating the complete controller maps. Further, it is well suited for a modern engine development process by construction kits and allows the reuse of parameterised submodels. A semi-physical feedforward control in conjunction with simple PI(D)-controllers delivers a very good response to setpoint changes, decoupling of controlled variables and good disturbance rejection. Further it can be tuned to achieve an almost time optimal response to setpoint changes. This control scheme can be further transformed into a semi-physical IMC. Also the LP-EGR mass flow rate is controlled by a semi-physical relationship, which utilises the system property that the LP-EGR rate mainly depends on its actuator position and is fairly independent from the other engine states.

**Dynamical Emissions of Different Control Concepts**

Finally, the dynamical emissions of different control concepts are evaluated during the NEDC. The NEDC can be separated into proportions with dynamical and stationary engine operation. Given that a large proportion of the driving cycle is of dynamical nature, also the proportion of dynamical emission formation is relatively large. Considering the injected fuel mass, there is no significant emission increased during the dynamical parts of the driving cycle. In series calibration with HP-EGR an air mass flow rate control is compared to a EGR rate control and to dynamical optimised reference values. The overall driving cycle emissions of the air mass flow rate control are close to the dynamical optimised reference values, while the EGR rate control has decreased $NO_x$ emissions on the cost of higher particulate emissions. Generally with the given combination of engine, air path control, engine calibration and driving cycle, the investigated emission level during dynamical engine operation only slightly differs from stationary engine operation. Thus, there is only a small potential for an improved emission level with for dynamical optimised reference values for the air path control. More room to improve the dynamical emissions by a dynamical optimisation will given with future driving cycles like the WLPT and RDE, which contain more and stronger transients. In a dual EGR configuration an intake temperature control yields the worst results. Good results can be achieved with a dynamical reference value generation, which considers the gas propagation times. Compared to a $\dot{m}_{air}$-control with and a single HP-EGR, this control concept with additional LP-EGR is capable to lower the overall $NO_x$ emissions to 36.2 % and the particulate emissions to 82.5 %, while the delivered engine work $W_{eng}$ rises to 107.2 %.

**Outlook**

Semi-physical models are a key to master current and future tasks in system understanding and function development. Their modularity makes them easy adjustable to new engine configurations. Certainly, for a well suiting engine model several submodels interact and have to be parameterised well to achieve satisfying simulation results. Currently all models have to be parameterised as best as possible and a method to achieve this is given in this thesis. However, it is not likely that each single submodel contributes equally large to the overall model quality. Consequently, a sensitivity analysis of single submodels can identify the relevant submodels for a well suiting overall model and simplify the overall model parameterisation process.

A semi-physical control concept is easy to calibrate and delivers good response to setpoint changes and disturbance rejection. Beyond the successful control of a engine with VGT turbocharger and HP-EGR, this semi-physical control concept can be further adapted to engines having waste gate or two-stage turbochargers. Furthermore, the HP-EGR mass flow rate control could be extended to handle different controlled variables like e.g. the air mass flow rate.

# A  Test Facilities

The institute of automatic control at the Technische Universität Darmstadt owns and operates a dynamical engine test bench to acquire measurements for engine modelling as well as for algorithm validation. This test bench allows to validate theoretically developed algorithms for measurement strategies, fault detection and diagnosis, engine optimisation and engine control at the real-world engine process.

All combustion engines are mounted on roll carts and are equipped with quick connectors for the external cooling circuit. Several electrical connectors allow a fast connection of test engine's sensors and the ECU to the test bench automation system. This engine setup allows a fast exchange of the investigated test engine. An inverter-fed asynchronous motor (160 kW rated power, 300 Nm nominal torque, 5000 min$^{-1}$ maximum speed) acts as dynamometer and is connected via a synchronising shaft and a resilient coupling to the combustion engine. The closed-loop controlled asynchronous machine can drive the engine independently from the injection quantity at a desired speed and it generates the necessary resistive torque with a settling time smaller than 5 ms.
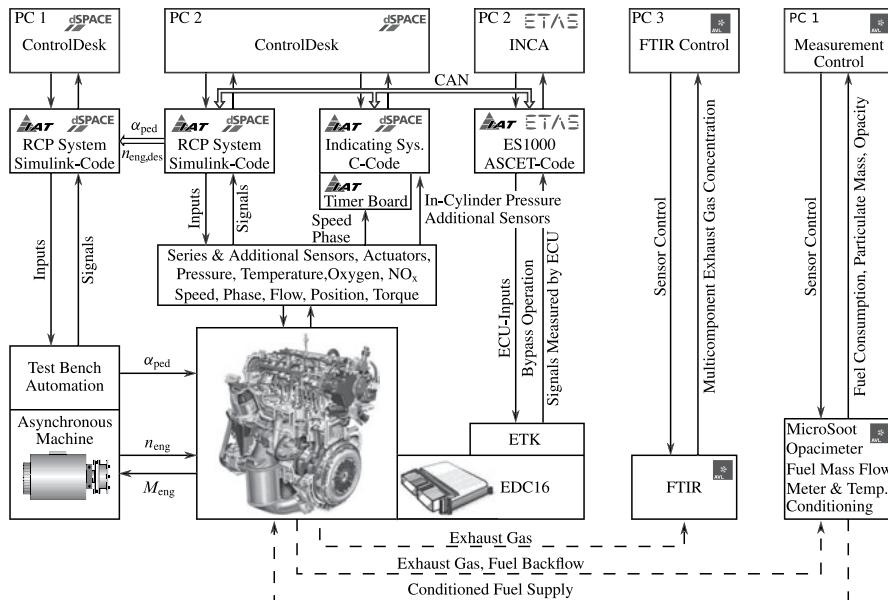


**Figure A.1:** Test bench automation scheme

Figure A.1 illustrates the test bench automation scheme and the rapid control prototyping (RCP) environment for algorithm validation and data acquisition. One rapid control prototyping system is utilised for test bench automation. It supervises test bench conditions, controls coolant flow, coolers, test cell ventilation and it delivers the engine speed setpoint $n_{eng,des}$ for the inverter and the accelerator pedal signals $\alpha_{ped}$ for the ECU. These signals can be set either via the user interface of the test bench automation system or are set via CAN-bus signals from other RCP-systems.

All other RCP-systems are used for function development and data acquisition. First the combination of an ES1000 prototyping system with an ETK (Emulatortastkopf; emulator test probe) from ETAS makes it possible to read and modify ECU-internal quantities in real-time. Further these systems allow to *bypass* some ECU-functionalities and execute prototyping software on the ES1000 system. Whereat *bypass* indicates that external measurements or ECU-quantities can be used as function inputs for a prototyping function, which writes its output back to an ECU-internal variable. In this case the original ECU-internal function outputs which usually write these variables are bypassed. The ES1000 system is programmed with ASCET (Advanced Simulation and Control Engineering Tool), and ECU-internal quantities and calibration parameters are measured and modified by the software INCA (Integrated Calibration and Acquisition System). In this dissertation the ES1000 system is mainly used for data acquisition, to modify the injection parameters and to execute a cylinder-individual closed-loop control of the location of mass fraction burned 50 %, see Kohlhase (2011).

The indicating system is based on dSPACE rapid control prototyping hardware and allows a real-time estimation of combustion quantities like the mean indicated pressure and the location of mass fraction burned 50 %. Furthermore, a crank-angle synchronous data acquisition of analogue signals is possible. This crank-angle synchronous data capturing via trigger events of an angle transmitter and phase signal demands a special timer board, which was developed at the institute of automatic control. A detailed description of combustion quantity estimation from in-cylinder pressure signals and the indicating system with the timer board is given in Kohlhase (2011).

A further RCP-system from dSPACE executes automatically generated code from MATLAB Simulink. This system is utilised to manipulate intake and exhaust system actuators, for data acquisition of series and additional sensors and for implementation of control algorithms. This RCP-system is visualised and operated with the dSPACE software ControlDesk.

Finally, the fuel consumption, the fuel conditioning and the emission measurement devices are controlled via the appropriate manufacturers' software on separate computers. The test bench is equipped with an AVL SESAM FTIR (Fourier transform infrared spectroscopy) multi component exhaust measurement system, an AVL 439 opacimeter to measure the exhaust-gas opacity, an AVL 483 microsoot-sensor to measure the soot concentration and $NO_x$-sensors from NGK. Anymore, the fuel temperature can be regulated with an AVL 753 fuel conditioning system and the fuel consumption can be measured with an AVL 735 fuel mass flow meter.

The test engine is a 1.91 Opel DTH Z19 common rail Diesel engine with cooled high-pressure exhaust gas recirculation and variable turbine turbocharger and fulfils the emission standard Euro 4. Tab. A.1 summarises the technical engine data. In order to be able to parameterise single sub-

models of the mean value engine model, the test engine was equipped with several additional pressure and temperature sensors in all relevant storage elements and ducts. For the indicating system in-cylinder pressure sensors have been mounted in the glow plug bores. Further the high-pressure EGR-actuator was replaced by a state of the art actuator with position measurement and the VGT-actuator was equipped with an external position sensor.

**Table A.1:** Technical data of the test engine

| | |
|---|---|
| Manufacturer | GM Powertrain |
| Engine type | DTH-Z19 |
| Number of cylinders | 4 |
| Displacement | $1910\,cm^3$ |
| Number of valves | 16 |
| Maximal power | $110\,kW$ |
| Maximal torque | $315\,Nm$ |
| Compression ratio | 17.5 |

The engine was extended with a low-pressure exhaust gas recirculation by the author. Consequently, a Diesel particulate filter, a low-pressure EGR-cooler, a second EGR-valve, a pneumatic actuated exhaust gas throttle valve and a conventional throttle valve in the intake system were retrofitted to the engine. All actuators are state of the art actuators with position measurement. A DPF solution with electrical regeneration system was installed with support of DES (Diesel Exhaust Systems GmbH). The LP-EGR cooler was kindly provided by Behr GmbH & Co. KG and was connected to the test bench cooling system. In comparison to the dynamically slow pneumatic exhaust gas throttle valve, the electrical intake throttle valve is capable to react dynamically fast to setpoint changes and is equipped with a sophisticated two-degree of freedom control, see Kopf (2014).

# B   Exhaust Temperature Model

The temperature after the combustion process is influenced by the cylinder charge and the rather complex combustion characteristics. For the mean value engine model the engine exhaust temperature is modelled according to Eq. (3.31) as stationary temperature increase in the cylinder group, in which the nonlinear relationship between different factors of influence and the temperature increase is modelled by a LOLIMOT-model. In this modelling approach the cylinder charge can be described by the quantities $p_{2i}$ and $x_{2i}$, while the quantities $n_{eng}$, $u_{inj}$, $\varphi_{mi}$ and $\varphi_{Q50}$ can be used as influencing variables for the combustion characteristics.

**Table B.1:** Engine exhaust temperature model quality with different model inputs

| Model structure | $R^2_{\text{train}}$ | RMSE$_{\text{train}}$ in °C | $R^2_{\text{val}}$ | RMSE$_{\text{val}}$ in °C |
|---|---|---|---|---|
| $T_{\text{eng,out}} - T_{2i} = f_{LOLIMOT}\,(\cdot)$ | | | | |
| $f_{LOLIMOT}\left(u_{\text{inj}}\right)$ | 0.939 | 28.77 | 0.938 | 29.15 |
| $f_{LOLIMOT}\left(u_{\text{inj}}, p_{2i}\right)$ | 0.958 | 23.95 | 0.958 | 24.02 |
| $f_{LOLIMOT}\left(u_{\text{inj}}, p_{2i}, n_{\text{eng}}\right)$ | 0.977 | 17.85 | 0.977 | 17.83 |
| $f_{LOLIMOT}\left(u_{\text{inj}}, p_{2i}, n_{\text{eng}}, \varphi_{\text{mi}}\right)$ | 0.984 | 14.41 | 0.985 | 14.54 |
| $f_{LOLIMOT}\left(u_{\text{inj}}, p_{21i}, n_{\text{eng}}, \varphi_{Q50}\right)$ | 0.986 | 13.64 | 0.986 | 13.83 |
| $f_{LOLIMOT}\left(u_{\text{inj}}, p_{2i}, n_{\text{eng}}, \varphi_{Q50}, x_{2i}\right)$ | 0.988 | 12.87 | 0.988 | 12.96 |

Tab. B.1 gives an overview of different model inputs' relevance and the achievable model quality on the training and validation data. The relevance of different model inputs can be exemplary interpreted with the models having only one model input. For that case the best model quality could be achieved with the model input $u_{\text{inj}}$, all other investigated model inputs ($p_{2i}$, $x_{2i}$, $n_{\text{eng}}$, $\varphi_{\text{mi}}$, $\varphi_{Q50}$) have delivered worse results on the given training and validation datasets. The training and validation datasets have consisted of stationary measurements of the turbocharger parameterisation and the stationary measurements to determine the emission models. In Tab. B.1 it can be observed that the model improved in model training and model validation with the number of model inputs. However, for the last model with the additional model input $x_{2i}$ the improvement was rather small, so that this additional model input was neglected in the mean value engine model. Anymore, it can be observed that the model input quantity location of mass fraction burned 50 % $\varphi_{Q50}$ delivered better modelling and validation results than the model input start of the main injection $\varphi_{\text{mi}}$, since it contains some information about the course of the combustion process.

The exhaust temperature model (3.31) ($T_{\text{eng,out}} - T_{2i} = f_{LOLIMOT}\left(n_{\text{eng}}, u_{\text{inj}}, p_{2i}, \varphi_{\text{mi}}\right)$) performance on the training and validation dataset is given in Fig. B.1a) in form of a measured versus predicted plot and as the error distribution in Fig. B.1b). These plots and the quality criteria in Tab. B.1 indicate that the exhaust temperature can be fully satisfactorily modelled with the given model.
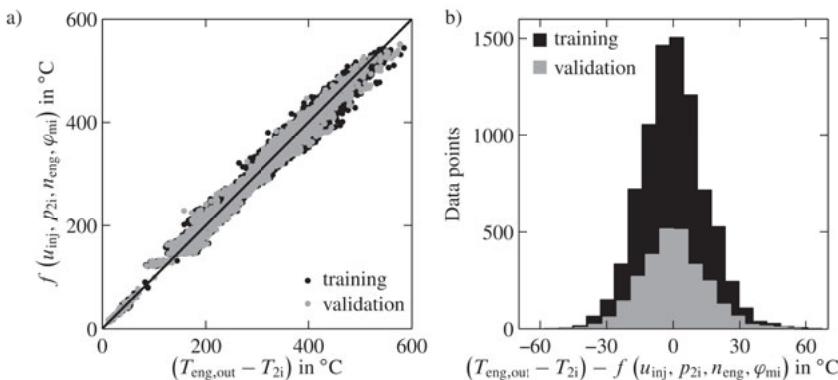
**Figure B.1:** a) Measured versus predicted combustion temperature increase model b) Error distribution for the combustion temperature increase model

# C EGR-Valve Characteristic Shaping

The position of both EGR-valves is coupled nonlinear with the air mass flow rate and the exhaust gas mass flow rate in the engine operation range. This nonlinearity determines the static gains of the control loops and can result in an unsatisfying control performance or instability of the closed-loop control. In the following, the static characteristic of both EGR-valves is shaped to achieve an almost linear coupling to the air mass flow rate and the exhaust gas mass flow rate.
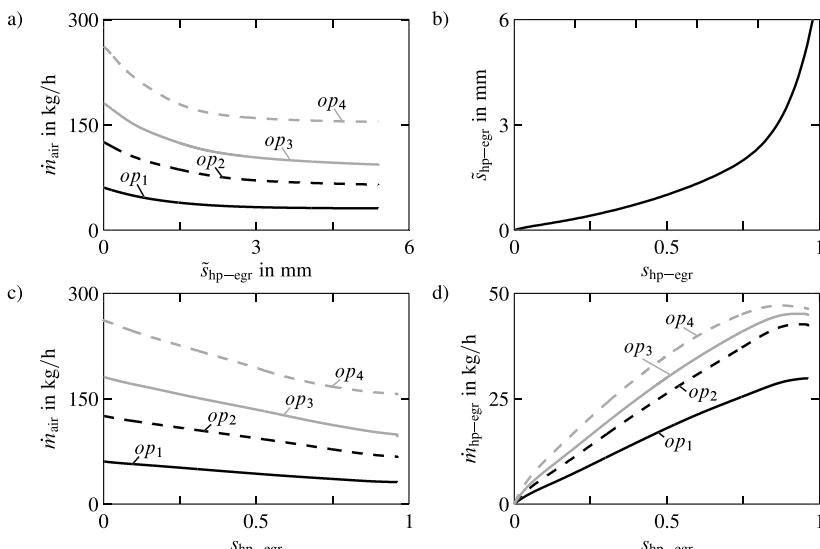


**Figure C.1:** Shaping of the HP-EGR-valve characteristics a) $\tilde{s}_{hp-egr}$ gain to the air mass flow rate b) nonlinear normalisation of the HP-EGR-valve characteristics c) gain of the normalised valve $s_{hp-egr}$ characteristics to the air mass flow rate d) gain of the normalised valve $s_{hp-egr}$ characteristics to the HP-EGR mass flow rate

Fig. C.1a) presents the simulated couplings of the valve position $\tilde{s}_{hp-egr}$ to $\dot{m}_{air}$ at four different engine operation points. The considered engine operation points $op_i$ are listed in Tab. C.1 and represent a representative cross section through the covered engine operation area in the NEDC. At all illustrated operation points the nonlinearity between $\tilde{s}_{hp-egr}$ and $\dot{m}_{air}$ has a similar shape. As long as $\tilde{s}_{hp-egr}$ is in the range of $0 \ldots 1.8\,mm$, the air mass flow rate drops steeply, then the nonlinearity becomes very flat. This nonlinearity is compensated by a polynomial, which shapes $\tilde{s}_{hp-egr}$ to the normalised actuator position $s_{hp-egr}$ in Fig. C.1b).

Fig. C.1 c) and d) reflect the couplings of the normalised actuator position $s_{hp-egr}$ to $\dot{m}_{air}$ and $\dot{m}_{hp-egr}$. In both figures an almost linear static characteristics of $s_{hp-egr}$ can be observed. Only if $s_{hp-egr}$ is almost opened at $\approx 0.95$ the curves of $s_{hp-egr}$ flatten. This is caused by the insufficient compensated small gain of the HP-EGR-valve at positions where it is almost opened. However, a complete linearisation in this operation range is not of practical relevance.

**Table C.1:** Considered engine operation points

|        | $n_{eng}$ in min$^{-1}$ | $u_{inj}$ in mm$^3$/cyc |
|--------|-------------------------|-------------------------|
| $op_1$ | 1000                    | 0                       |
| $op_2$ | 2000                    | 15                      |
| $op_3$ | 2500                    | 22.5                    |
| $op_4$ | 3000                    | 30                      |

For the LP-EGR path, the two actuators LP-EGR-valve and exhaust throttle valve have to be considered. Both actuators are treated as one combined actuator with the normalised position $s_{lp-egr/eth}$. In Fig. C.2a) the operation range of both actuators is equally divided to the signal $\overline{s}_{lp-egr/eth}$. First the LP-EGR-valve ($\tilde{s}_{lp-egr}$) opens for $\overline{s}_{lp-egr/eth} \in [0, 0.5[$. Thereafter the exhaust throttle valve ($\tilde{s}_{eth}$) increases the exhaust pressure $p_5$ for $\overline{s}_{lp-egr/eth} \in [0.5, 1]$. At the investigated engine operation points these in series connected actuators result in one combined actuator with a strongly nonlinear characteristic to the air mass flow rate. In the range of $\overline{s}_{lp-egr/eth} \in [0.35, 0.65]$ the gain of this combined actuator is very small, while it is significantly higher in the rest of the operation range. Comparable to the HP-EGR-valve, the characteristic of $\tilde{s}_{lp-egr}$ and $\tilde{s}_{eth}$ is normalised, to achieve a relative linear characteristic between the normalised actuator position $s_{lp-egr/eth}$ and the air mass flow rate, respectively the LP-EGR mass flow rate.

Fig. C.2b) represents the shaping of the normalised actuator $s_{lp-egr/eth}$ to the positions of $\tilde{s}_{lp-egr}$ and $\tilde{s}_{eth}$. With this shaping the LP-EGR-valve is actuated for $s_{lp-egr/eth} \in [0, 0.3[$ and the exhaust throttle valve is active for $s_{lp-egr/eth} \in [0.3, 1]$. At $s_{lp-egr/eth} = 0.3$ both actuators have a gain close to zero, which cannot be linearised. Thus, a small overlap between LP-EGR-valve actuation and exhaust throttle valve actuation has to be accepted. In Fig. C.2c) and d) the coupling between the normalised and shaped characteristics of $s_{lp-egr/eth}$ to $\dot{m}_{air}$ and $\dot{m}_{lp-egr}$ is revealed. For both mass flow rates the stationary coupling is mostly linear. Only some small ripples are visible during the superposition of $\tilde{s}_{lp-egr}$ and $\tilde{s}_{eth}$.

Finally, the two actuators LP-EGR-valve $\tilde{s}_{lp-egr}$ and intake throttle valve $\tilde{s}_{ith}$ can be treated similar to the combined actuator $s_{lp-egr/eth}$. For completeness the combination of these actuators to the normalised actuator $s_{lp-egr/ith}$ is illustrated in Fig. C.3a)-d). In these plots it gets obvious that this actuator coupling results in a rather linear characteristics between $s_{lp-egr/ith}$ and the quantities $\dot{m}_{air}$ and $\dot{m}_{lp-egr}$. In the body of this dissertation the actuators $s_{hp-egr}$, $s_{lp-egr/eth}$ and $s_{lp-egr/ith}$ are shown in their normalised form, otherwise the measured position is denoted by the symbols $\tilde{s}_{hp-egr}$, $\tilde{s}_{lp-egr}$, $\tilde{s}_{eth}$ and $\tilde{s}_{ith}$.
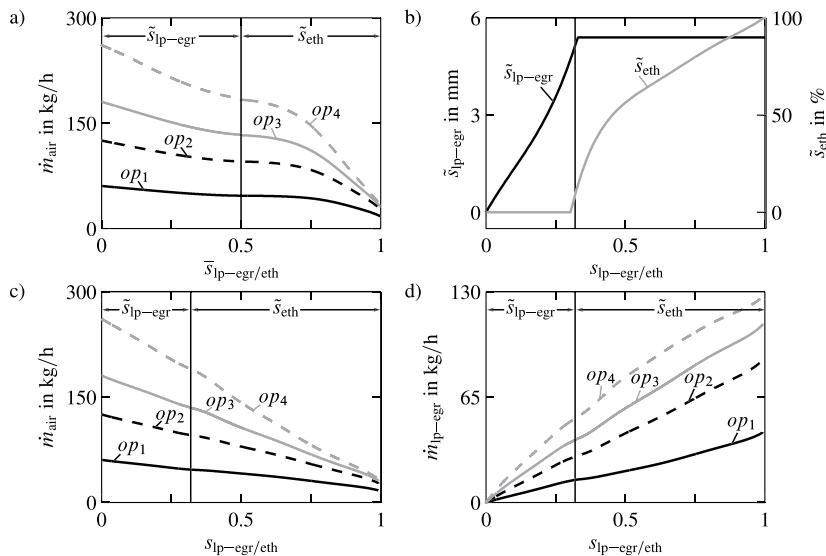
**Figure C.2:** Shaping of the characteristics of the series connected LP-EGR-valve and exhaust throttle valve a) $\overline{s}_{lp-egr/eth}$ gain to the air mass flow rate b) nonlinear normalisation of the LP-EGR-valve and the exhaust throttle valve characteristics c) gain between the normalised combined actuator characteristics and the air mass flow rate d) gain between the normalised combined actuator characteristics and the LP-EGR mass flow rate
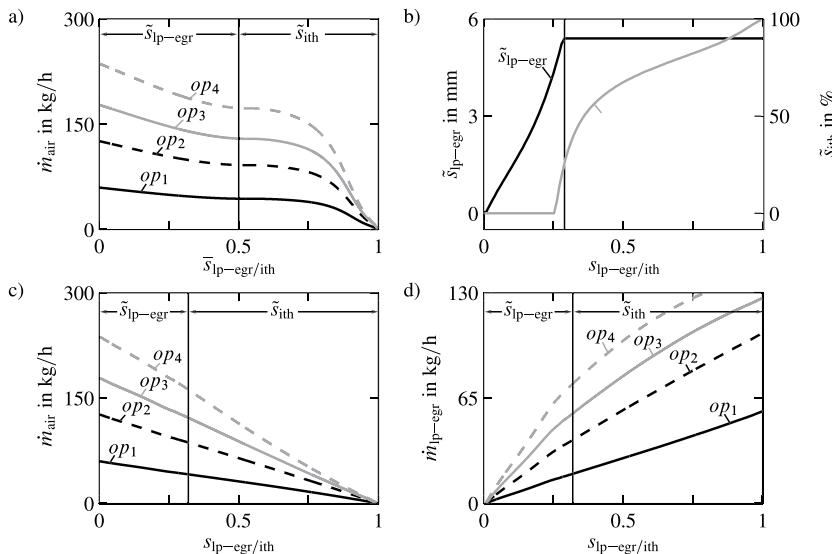
**Figure C.3:** Shaping of the characteristics for the series connected LP-EGR-valve and intake throttle valve a) $\overline{s}_{\text{lp}-\text{egr/ith}}$ gain to the air mass flow rate b) nonlinear normalisation of the LP-EGR-valve and the intake throttle valve characteristics c) gain between the normalised combined actuator characteristics and the air mass flow rate d) gain between the normalised combined actuator characteristics and the LP-EGR mass flow rate

# D   Gas Mass Storage in Intake Volumes

During transients in pressure and temperature, storages in the intake system accumulate and deliver significant gas masses. This effect should be incorporated into the following mass flow rate balance equations (4.13), (4.14) and it can be modelled as follows. Schwarte (2007) determines the dynamically accumulated gas mass in a storage by the total derivative of the ideal gas law (3.8) as

$$\frac{\mathrm{d}m_{\mathrm{st}}}{\mathrm{d}t} = \frac{\mathrm{d}}{\mathrm{d}t}\left(\frac{p_{\mathrm{st}}V_{\mathrm{st}}}{RT_{\mathrm{st}}}\right) = \frac{\mathrm{d}p_{\mathrm{st}}}{\mathrm{d}t}\frac{V_{\mathrm{st}}}{RT_{\mathrm{st}}} - \frac{\mathrm{d}T_{\mathrm{st}}}{\mathrm{d}t}\frac{p_{\mathrm{st}}V_{\mathrm{st}}}{RT_{\mathrm{st}}^2} \approx \frac{\mathrm{d}p_{\mathrm{st}}}{\mathrm{d}t}\frac{V_{\mathrm{st}}}{RT_{\mathrm{st}}} \tag{D.1}$$

and neglects the term considering changes in the intake temperature. This simplification holds, since temperature sensors possess significant measurement dynamics, so that the derivative of the measured signal is small and can be neglected. On the other hand the intake temperature can be determined dynamically fast by the modelled temperature (4.16), which is derived from the noisy ratio of mass flow rates. Thus, also the derivation of $\hat{T}_{2\mathrm{i}}$ is not advisable and the gas mass accumulation model has to be restricted to the derivation of the intake pressure.

Another way to derive the dynamical gas mass storage (D.1) can be given by the adiabatic formulation. The adiabatic formulation is given as pressure changes

$$\frac{\mathrm{d}p_{\mathrm{st}}}{\mathrm{d}t} = \frac{\kappa R}{V_{\mathrm{st}}}\left(\sum_{i=1}^{p}\dot{m}_{\mathrm{in},i}T_{\mathrm{in},i} - \sum_{j=1}^{q}\dot{m}_{\mathrm{out},j}T_{\mathrm{st}}\right) \tag{D.2}$$

and temperature changes

$$\frac{\mathrm{d}T_{\mathrm{st}}}{\mathrm{d}t} = \frac{RT_{\mathrm{st}}}{p_{\mathrm{st}}V_{\mathrm{st}}c_{\mathrm{V}}}\left(c_{\mathrm{p}}\sum_{i=1}^{p}\dot{m}_{\mathrm{in},i}T_{\mathrm{in},i} - c_{\mathrm{p}}\sum_{j=1}^{q}\dot{m}_{\mathrm{out},j}T_{\mathrm{st}} - c_{\mathrm{V}}\left(\sum_{i=1}^{p}\dot{m}_{\mathrm{in},i} - \sum_{j=1}^{q}\dot{m}_{\mathrm{out},j}\right)T_{\mathrm{st}}\right) \tag{D.3}$$

in storages, see Guzzella and Onder (2010). If the heat capacity ratio $c_{\mathrm{p}}/c_{\mathrm{V}}$ is replaced by the isentropic expansion factor $\kappa$, Eq. (D.3) is solved for

$$\kappa\left(\sum_{i=1}^{p}\dot{m}_{\mathrm{in},i}T_{\mathrm{in},i} - \sum_{j=1}^{q}\dot{m}_{\mathrm{out},j}T_{\mathrm{st}}\right) = \frac{\mathrm{d}T_{\mathrm{st}}}{\mathrm{d}t}\frac{p_{\mathrm{st}}V_{\mathrm{st}}}{RT_{\mathrm{st}}} + \left(\sum_{i=1}^{p}\dot{m}_{\mathrm{in},i} - \sum_{j=1}^{q}\dot{m}_{\mathrm{out},j}\right)T_{\mathrm{st}} \tag{D.4}$$

and then substituted in (D.2) follows with the mass balance equation for storages (3.1) eventually the relation (D.1).

# E   Emission and Combustion Models

In this section suitable model inputs for different emission and combustion models are compared more detailed than in Sect. 5.3.4. The set of possible model inputs includes three possible inputs to describe the in-cylinder oxygen mass ($m_{air}$, $\hat{x}_{2i}$, $\hat{x}_{eng,out}$), distinguishes if in-cylinder pressure measurement is available ($\varphi_{Q50}$, $\varphi_{mi}$) and includes either $\hat{T}_{2i}$ or $r_{egr}$ as additional controlled variable for the LP-EGR system. In the following tables models for the different emission and combustion quantities are presented and quantified with the coefficient of determination and the root mean square error for training data and validation data. Further the number of parameters $n$ for the particular models is given. Note that the number of parameters $n$ results from the 21 local models and the number of chosen regressors for each local polynomial model, see Sect.5.3.2. Models printed in bold are utilised for simulation of the dynamical emissions (Sect. 5.4) and stationary engine optimisation (Sect. 6.1).

In Tab. E.1 and Tab. E.2 the quality criteria for the $NO_x$ models are given. The $NO_x$ concentration $c_{nox}$ and $NO_x$ mass flow rate $\dot{m}_{nox}$ are two quantities, which can be modelled with good results on training and validation data. Between the model inputs $m_{air}$ and $\hat{x}_{2i}$ there is no significant difference in the reachable model quality, while the input $\hat{x}_{eng,out}$ delivers slightly worse results. Generally, all investigated model inputs $\varphi_{Q50}$ or $\varphi_{mi}$ and $\hat{T}_{2i}$ or $r_{egr}$ result in a good model quality.

For the particulate emissions in Tab. E.3 and E.4 the best model quality can be achieved with the model input $\hat{x}_{eng,out}$. The other two equivalents for the air mass $m_{air}$, respectively the air content in the cylinder charge $\hat{x}_{2i}$ deliver worse training and validation results. Especially for model validation the input $\hat{x}_{eng,out}$ shows its potential. In comparison to the other input quantities it contains information about the injected fuel quantity and the air content in the cylinder, see Eq. (3.32). This results in better interpolation capabilities for model validation. [1] With respect to the model quality the model inputs $\varphi_{Q50}$ and $\hat{T}_{2i}$ are advantageous compared to the model inputs $\varphi_{mi}$ and $r_{egr}$.

The engine torque in Tab. E.5 is best modelled with $m_{air}$ or $\hat{x}_{2i}$ and the quantities $p_{2i}$, $\varphi_{Q50}$ and $\hat{T}_{2i}$ as model inputs. In the following tables (Tab. E.6 – E.9) one can get a good overview about the reachable model qualities of the quantities $p_{mi,hp}$, $p_{mi,lp}$, $\varphi_{Q50}$ and $\varphi_{mi}$. These quantitative overviews for the single modelled quantities are further visualised with measured versus predicted plots and the histograms of the error distributions in Fig. E.1 and Fig. E.2.

In a nutshell this section gives an overview about reachable model qualities with different model inputs for the interested reader and further contains models for the quantities $p_{mi,hp}$, $p_{mi,lp}$, $\varphi_{Q50}$ and $\varphi_{mi}$.

---

[1]Note that the quantity $\hat{x}_{eng,out}$ can be stationary derived from the measured air mass flow rate and the desired injection quantity, respectively the injected fuel mass by substituting the air-fuel rate definition of the global engine system Eq. (3.11) into the air-fuel ratio definition of storage elements Eq. (3.13), see also Eq. (7.33). It is not affected by side-effects like cylinder-individual combustion, incomplete combustion, engine ageing and others.

**Table E.1:** $c_{\text{nox}}$ model quality

| x-regressors | | | | $R^2_{\text{train}}$ | $\text{RMSE}_{\text{train}}$ | $R^2_{\text{val}}$ | $\text{RMSE}_{\text{val}}$ | $n$ |
|---|---|---|---|---|---|---|---|---|
| $x_1$ | $x_2$ | $x_3$ | $x_4$ | | in ppm | | in ppm | |
| $m_{\text{air}}$ | $p_{2i}$ | $\varphi_{Q50}$ | $\hat{T}_{2i}$ | 0.99214 | 23.2023 | 0.97918 | 34.8799 | 392 |
| $m_{\text{air}}$ | $p_{2i}$ | $\varphi_{Q50}$ | $r_{\text{egr}}$ | 0.99222 | 23.0796 | 0.98141 | 32.9587 | 348 |
| $m_{\text{air}}$ | $p_{2i}$ | $\varphi_{mi}$ | $\hat{T}_{2i}$ | 0.99122 | 24.5258 | 0.97541 | 37.9131 | 360 |
| $m_{\text{air}}$ | $p_{2i}$ | $\varphi_{mi}$ | $r_{\text{egr}}$ | 0.99226 | 23.0223 | 0.98032 | 33.9173 | 334 |
| $\hat{x}_{2i}$ | $p_{2i}$ | $\varphi_{Q50}$ | $\hat{T}_{2i}$ | **0.99221** | **23.0945** | **0.97805** | **35.8207** | **340** |
| $\hat{x}_{2i}$ | $p_{2i}$ | $\varphi_{Q50}$ | $r_{\text{egr}}$ | 0.98804 | 28.6198 | 0.96651 | 44.2436 | 370 |
| $\hat{x}_{2i}$ | $p_{2i}$ | $\varphi_{mi}$ | $\hat{T}_{2i}$ | 0.99178 | 23.7271 | 0.97433 | 38.7345 | 336 |
| $\hat{x}_{2i}$ | $p_{2i}$ | $\varphi_{mi}$ | $r_{\text{egr}}$ | 0.98522 | 31.8107 | 0.97119 | 41.0342 | 338 |
| $\hat{x}_{\text{eng,out}}$ | $p_{2i}$ | $\varphi_{Q50}$ | $\hat{T}_{2i}$ | 0.98725 | 29.5501 | 0.95050 | 53.7884 | 345 |
| $\hat{x}_{\text{eng,out}}$ | $p_{2i}$ | $\varphi_{Q50}$ | $r_{\text{egr}}$ | 0.99040 | 25.6327 | 0.96855 | 42.8704 | 436 |
| $\hat{x}_{\text{eng,out}}$ | $p_{2i}$ | $\varphi_{mi}$ | $\hat{T}_{2i}$ | 0.98669 | 30.1912 | 0.95119 | 53.4133 | 340 |
| $\hat{x}_{\text{eng,out}}$ | $p_{2i}$ | $\varphi_{mi}$ | $r_{\text{egr}}$ | 0.98977 | 26.4689 | 0.96714 | 43.8218 | 394 |

**Table E.2:** $\dot{m}_{\text{nox}}$ model quality

| x-regressors | | | | $R^2_{\text{train}}$ | $\text{RMSE}_{\text{train}}$ | $R^2_{\text{val}}$ | $\text{RMSE}_{\text{val}}$ | $n$ |
|---|---|---|---|---|---|---|---|---|
| $x_1$ | $x_2$ | $x_3$ | $x_4$ | | in mg/s | | in mg/s | |
| $m_{\text{air}}$ | $p_{2i}$ | $\varphi_{Q50}$ | $\hat{T}_{2i}$ | **0.99572** | **1.4937** | **0.98745** | **2.2146** | **378** |
| $m_{\text{air}}$ | $p_{2i}$ | $\varphi_{Q50}$ | $r_{\text{egr}}$ | 0.99672 | 1.3080 | 0.98910 | 2.0632 | 341 |
| $m_{\text{air}}$ | $p_{2i}$ | $\varphi_{mi}$ | $\hat{T}_{2i}$ | 0.99543 | 1.5432 | 0.98667 | 2.2816 | 385 |
| $m_{\text{air}}$ | $p_{2i}$ | $\varphi_{mi}$ | $r_{\text{egr}}$ | 0.99685 | 1.2814 | 0.98834 | 2.1343 | 350 |
| $\hat{x}_{2i}$ | $p_{2i}$ | $\varphi_{Q50}$ | $\hat{T}_{2i}$ | 0.99509 | 1.6001 | 0.98651 | 2.2952 | 328 |
| $\hat{x}_{2i}$ | $p_{2i}$ | $\varphi_{Q50}$ | $r_{\text{egr}}$ | 0.99384 | 1.7930 | 0.97989 | 2.8028 | 337 |
| $\hat{x}_{2i}$ | $p_{2i}$ | $\varphi_{mi}$ | $\hat{T}_{2i}$ | 0.99512 | 1.5956 | 0.98618 | 2.3235 | 380 |
| $\hat{x}_{2i}$ | $p_{2i}$ | $\varphi_{mi}$ | $r_{\text{egr}}$ | 0.99309 | 1.8984 | 0.98039 | 2.7680 | 335 |
| $\hat{x}_{\text{eng,out}}$ | $p_{2i}$ | $\varphi_{Q50}$ | $\hat{T}_{2i}$ | 0.98727 | 2.5768 | 0.95765 | 4.0674 | 306 |
| $\hat{x}_{\text{eng,out}}$ | $p_{2i}$ | $\varphi_{Q50}$ | $r_{\text{egr}}$ | 0.99438 | 1.7121 | 0.97503 | 3.1234 | 400 |
| $\hat{x}_{\text{eng,out}}$ | $p_{2i}$ | $\varphi_{mi}$ | $\hat{T}_{2i}$ | 0.99013 | 2.2688 | 0.95986 | 3.9595 | 340 |
| $\hat{x}_{\text{eng,out}}$ | $p_{2i}$ | $\varphi_{mi}$ | $r_{\text{egr}}$ | 0.99432 | 1.7210 | 0.97805 | 2.9281 | 389 |

**Table E.3:** $c_{\text{mss}}$ model quality

| x-regressors | | | | $R^2_{\text{train}}$ | RMSE$_{\text{train}}$ | $R^2_{\text{val}}$ | RMSE$_{\text{val}}$ | $n$ |
|---|---|---|---|---|---|---|---|---|
| $x_1$ | $x_2$ | $x_3$ | $x_4$ | | in mg/m$^3$ | | in mg/m$^3$ | |
| $m_{\text{air}}$ | $p_{2\text{i}}$ | $\varphi_{\text{Q50}}$ | $\hat{T}_{2\text{i}}$ | 0.93222 | 3.3436 | 0.85556 | 2.9102 | 352 |
| $m_{\text{air}}$ | $p_{2\text{i}}$ | $\varphi_{\text{Q50}}$ | $r_{\text{egr}}$ | 0.93211 | 3.3489 | 0.80416 | 3.9458 | 320 |
| $m_{\text{air}}$ | $p_{2\text{i}}$ | $\varphi_{\text{mi}}$ | $\hat{T}_{2\text{i}}$ | 0.91159 | 4.3612 | 0.86141 | 2.7924 | 333 |
| $m_{\text{air}}$ | $p_{2\text{i}}$ | $\varphi_{\text{mi}}$ | $r_{\text{egr}}$ | 0.91982 | 3.9554 | 0.71430 | 5.7563 | 326 |
| $\hat{x}_{2\text{i}}$ | $p_{2\text{i}}$ | $\varphi_{\text{Q50}}$ | $\hat{T}_{2\text{i}}$ | 0.94978 | 2.4774 | 0.63370 | 7.3803 | 396 |
| $\hat{x}_{2\text{i}}$ | $p_{2\text{i}}$ | $\varphi_{\text{Q50}}$ | $r_{\text{egr}}$ | 0.85303 | 7.2502 | 0.36438 | 12.807 | 334 |
| $\hat{x}_{2\text{i}}$ | $p_{2\text{i}}$ | $\varphi_{\text{mi}}$ | $\hat{T}_{2\text{i}}$ | 0.91364 | 4.2600 | 0.69874 | 6.0699 | 341 |
| $\hat{x}_{2\text{i}}$ | $p_{2\text{i}}$ | $\varphi_{\text{mi}}$ | $r_{\text{egr}}$ | 0.81591 | 9.0812 | 0.18199 | 37.919 | 318 |
| $\hat{x}_{\text{eng,out}}$ | $p_{2\text{i}}$ | $\varphi_{\text{Q50}}$ | $\hat{T}_{2\text{i}}$ | **0.94958** | **2.4873** | **0.91239** | **1.7652** | **381** |
| $\hat{x}_{\text{eng,out}}$ | $p_{2\text{i}}$ | $\varphi_{\text{Q50}}$ | $r_{\text{egr}}$ | 0.95477 | 2.2311 | 0.78939 | 4.2434 | 389 |
| $\hat{x}_{\text{eng,out}}$ | $p_{2\text{i}}$ | $\varphi_{\text{mi}}$ | $\hat{T}_{2\text{i}}$ | 0.93992 | 2.9638 | 0.83194 | 3.3861 | 360 |
| $\hat{x}_{\text{eng,out}}$ | $p_{2\text{i}}$ | $\varphi_{\text{mi}}$ | $r_{\text{egr}}$ | 0.94217 | 2.8526 | 0.64964 | 7.0590 | 376 |

**Table E.4:** $\dot{m}_{\text{mss}}$ model quality

| x-regressors | | | | $R^2_{\text{train}}$ | RMSE$_{\text{train}}$ | $R^2_{\text{val}}$ | RMSE$_{\text{val}}$ | $n$ |
|---|---|---|---|---|---|---|---|---|
| $x_1$ | $x_2$ | $x_3$ | $x_4$ | | in mg/s | | in mg/s | |
| $m_{\text{air}}$ | $p_{2\text{i}}$ | $\varphi_{\text{Q50}}$ | $\hat{T}_{2\text{i}}$ | 0.94039 | 0.0034643 | 0.76638 | 0.0037988 | 324 |
| $m_{\text{air}}$ | $p_{2\text{i}}$ | $\varphi_{\text{Q50}}$ | $r_{\text{egr}}$ | 0.94783 | 0.0030318 | 0.74754 | 0.0041051 | 330 |
| $m_{\text{air}}$ | $p_{2\text{i}}$ | $\varphi_{\text{mi}}$ | $\hat{T}_{2\text{i}}$ | 0.94100 | 0.0034284 | 0.75732 | 0.0039460 | 341 |
| $m_{\text{air}}$ | $p_{2\text{i}}$ | $\varphi_{\text{mi}}$ | $r_{\text{egr}}$ | 0.93937 | 0.0035232 | 0.76008 | 0.0039012 | 310 |
| $\hat{x}_{2\text{i}}$ | $p_{2\text{i}}$ | $\varphi_{\text{Q50}}$ | $\hat{T}_{2\text{i}}$ | 0.95932 | 0.0023643 | 0.82689 | 0.0028148 | 344 |
| $\hat{x}_{2\text{i}}$ | $p_{2\text{i}}$ | $\varphi_{\text{Q50}}$ | $r_{\text{egr}}$ | 0.91005 | 0.0052270 | 0.64633 | 0.0057508 | 341 |
| $\hat{x}_{2\text{i}}$ | $p_{2\text{i}}$ | $\varphi_{\text{mi}}$ | $\hat{T}_{2\text{i}}$ | 0.94993 | 0.0029100 | 0.82746 | 0.0028055 | 354 |
| $\hat{x}_{2\text{i}}$ | $p_{2\text{i}}$ | $\varphi_{\text{mi}}$ | $r_{\text{egr}}$ | 0.90041 | 0.0057872 | 0.59884 | 0.0065229 | 342 |
| $\hat{x}_{\text{eng,out}}$ | $p_{2\text{i}}$ | $\varphi_{\text{Q50}}$ | $\hat{T}_{2\text{i}}$ | **0.96809** | **0.0018544** | **0.90223** | **0.0015898** | **393** |
| $\hat{x}_{\text{eng,out}}$ | $p_{2\text{i}}$ | $\varphi_{\text{Q50}}$ | $r_{\text{egr}}$ | 0.96275 | 0.0021646 | 0.85322 | 0.0023867 | 396 |
| $\hat{x}_{\text{eng,out}}$ | $p_{2\text{i}}$ | $\varphi_{\text{mi}}$ | $\hat{T}_{2\text{i}}$ | 0.96281 | 0.0021610 | 0.86731 | 0.0021576 | 378 |
| $\hat{x}_{\text{eng,out}}$ | $p_{2\text{i}}$ | $\varphi_{\text{mi}}$ | $r_{\text{egr}}$ | 0.95831 | 0.0024225 | 0.76488 | 0.0038232 | 388 |

**Table E.5:** $M_{\text{eng}}$ model quality

| x-regressors | | | | $R^2_{\text{train}}$ | $\text{RMSE}_{\text{train}}$ | $R^2_{\text{val}}$ | $\text{RMSE}_{\text{val}}$ | $n$ |
|---|---|---|---|---|---|---|---|---|
| $x_1$ | $x_2$ | $x_3$ | $x_4$ | | in Nm | | in Nm | |
| $m_{\text{air}}$ | $p_{2\text{i}}$ | $\varphi_{\text{Q50}}$ | $\hat{T}_{2\text{i}}$ | **0.99734** | **1.4675** | **0.97984** | **2.9366** | **189** |
| $m_{\text{air}}$ | $p_{2\text{i}}$ | $\varphi_{\text{Q50}}$ | $r_{\text{egr}}$ | 0.99664 | 1.6479 | 0.98012 | 2.9164 | 170 |
| $m_{\text{air}}$ | $p_{2\text{i}}$ | $\varphi_{\text{mi}}$ | $\hat{T}_{2\text{i}}$ | 0.99717 | 1.5126 | 0.97806 | 3.0636 | 211 |
| $m_{\text{air}}$ | $p_{2\text{i}}$ | $\varphi_{\text{mi}}$ | $r_{\text{egr}}$ | 0.99660 | 1.6584 | 0.98006 | 2.9208 | 197 |
| $\hat{x}_{2\text{i}}$ | $p_{2\text{i}}$ | $\varphi_{\text{Q50}}$ | $\hat{T}_{2\text{i}}$ | **0.99719** | **1.5072** | **0.97823** | **3.0514** | **183** |
| $\hat{x}_{2\text{i}}$ | $p_{2\text{i}}$ | $\varphi_{\text{Q50}}$ | $r_{\text{egr}}$ | 0.99546 | 1.9162 | 0.97202 | 3.4594 | 213 |
| $\hat{x}_{2\text{i}}$ | $p_{2\text{i}}$ | $\varphi_{\text{mi}}$ | $\hat{T}_{2\text{i}}$ | 0.99715 | 1.5185 | 0.96860 | 3.6646 | 208 |
| $\hat{x}_{2\text{i}}$ | $p_{2\text{i}}$ | $\varphi_{\text{mi}}$ | $r_{\text{egr}}$ | 0.99549 | 1.9094 | 0.96891 | 3.6466 | 249 |
| $\hat{x}_{\text{eng,out}}$ | $p_{2\text{i}}$ | $\varphi_{\text{Q50}}$ | $\hat{T}_{2\text{i}}$ | 0.99704 | 1.5478 | 0.95611 | 4.3327 | 265 |
| $\hat{x}_{\text{eng,out}}$ | $p_{2\text{i}}$ | $\varphi_{\text{Q50}}$ | $r_{\text{egr}}$ | 0.99576 | 1.8516 | 0.95337 | 4.4660 | 385 |
| $\hat{x}_{\text{eng,out}}$ | $p_{2\text{i}}$ | $\varphi_{\text{mi}}$ | $\hat{T}_{2\text{i}}$ | 0.99678 | 1.6148 | 0.95267 | 4.4997 | 276 |
| $\hat{x}_{\text{eng,out}}$ | $p_{2\text{i}}$ | $\varphi_{\text{mi}}$ | $r_{\text{egr}}$ | 0.99576 | 1.8509 | 0.95608 | 4.3341 | 392 |

**Table E.6:** $p_{\text{mi,hp}}$ model quality

| x-regressors | | | | $R^2_{\text{train}}$ | $\text{RMSE}_{\text{train}}$ | $R^2_{\text{val}}$ | $\text{RMSE}_{\text{val}}$ | $n$ |
|---|---|---|---|---|---|---|---|---|
| $x_1$ | $x_2$ | $x_3$ | $x_4$ | | in bar | | in bar | |
| $m_{\text{air}}$ | $p_{2\text{i}}$ | $\varphi_{\text{Q50}}$ | $\hat{T}_{2\text{i}}$ | 0.99838 | 0.08623 | 0.98780 | 0.17177 | 212 |
| $m_{\text{air}}$ | $p_{2\text{i}}$ | $\varphi_{\text{Q50}}$ | $r_{\text{egr}}$ | 0.99680 | 0.12111 | 0.98509 | 0.18992 | 205 |
| $m_{\text{air}}$ | $p_{2\text{i}}$ | $\varphi_{\text{mi}}$ | $\hat{T}_{2\text{i}}$ | 0.99820 | 0.09075 | 0.98706 | 0.17693 | 235 |
| $m_{\text{air}}$ | $p_{2\text{i}}$ | $\varphi_{\text{mi}}$ | $r_{\text{egr}}$ | 0.99663 | 0.12424 | 0.98499 | 0.19057 | 213 |
| $\hat{x}_{2\text{i}}$ | $p_{2\text{i}}$ | $\varphi_{\text{Q50}}$ | $\hat{T}_{2\text{i}}$ | **0.99839** | **0.08595** | **0.98475** | **0.19205** | **205** |
| $\hat{x}_{2\text{i}}$ | $p_{2\text{i}}$ | $\varphi_{\text{Q50}}$ | $r_{\text{egr}}$ | 0.99642 | 0.12816 | 0.98166 | 0.21064 | 229 |
| $\hat{x}_{2\text{i}}$ | $p_{2\text{i}}$ | $\varphi_{\text{mi}}$ | $\hat{T}_{2\text{i}}$ | 0.99819 | 0.09129 | 0.98601 | 0.18397 | 225 |
| $\hat{x}_{2\text{i}}$ | $p_{2\text{i}}$ | $\varphi_{\text{mi}}$ | $r_{\text{egr}}$ | 0.99649 | 0.12683 | 0.97967 | 0.22177 | 273 |
| $\hat{x}_{\text{eng,out}}$ | $p_{2\text{i}}$ | $\varphi_{\text{Q50}}$ | $\hat{T}_{2\text{i}}$ | 0.99824 | 0.08976 | 0.96531 | 0.28967 | 267 |
| $\hat{x}_{\text{eng,out}}$ | $p_{2\text{i}}$ | $\varphi_{\text{Q50}}$ | $r_{\text{egr}}$ | 0.99608 | 0.13404 | 0.96738 | 0.28091 | 353 |
| $\hat{x}_{\text{eng,out}}$ | $p_{2\text{i}}$ | $\varphi_{\text{mi}}$ | $\hat{T}_{2\text{i}}$ | 0.99789 | 0.09843 | 0.96905 | 0.27360 | 282 |
| $\hat{x}_{\text{eng,out}}$ | $p_{2\text{i}}$ | $\varphi_{\text{mi}}$ | $r_{\text{egr}}$ | 0.99589 | 0.13737 | 0.97038 | 0.26766 | 351 |

**Table E.7:** $p_{\text{mi,lp}}$ model quality

| x-regressors | | | | $R^2_{\text{train}}$ | $\text{RMSE}_{\text{train}}$ | $R^2_{\text{val}}$ | $\text{RMSE}_{\text{val}}$ | $n$ |
|---|---|---|---|---|---|---|---|---|
| $x_1$ | $x_2$ | $x_3$ | $x_4$ | | in bar | | in bar | |
| $m_{\text{air}}$ | $p_{2\text{i}}$ | $\varphi_{\text{Q50}}$ | $\hat{T}_{2\text{i}}$ | 0.97615 | 0.057324 | 0.90386 | 0.095777 | 251 |
| $m_{\text{air}}$ | $p_{2\text{i}}$ | $\varphi_{\text{Q50}}$ | $r_{\text{egr}}$ | 0.97787 | 0.055218 | 0.91537 | 0.089859 | 307 |
| $m_{\text{air}}$ | $p_{2\text{i}}$ | $\varphi_{\text{mi}}$ | $\hat{T}_{2\text{i}}$ | 0.97616 | 0.05731 | 0.90308 | 0.096164 | 269 |
| $m_{\text{air}}$ | $p_{2\text{i}}$ | $\varphi_{\text{mi}}$ | $r_{\text{egr}}$ | 0.97850 | 0.054425 | 0.91190 | 0.091683 | 319 |
| $\hat{x}_{2\text{i}}$ | $p_{2\text{i}}$ | $\varphi_{\text{Q50}}$ | $\hat{T}_{2\text{i}}$ | **0.97563** | **0.057939** | **0.90111** | **0.097136** | **251** |
| $\hat{x}_{2\text{i}}$ | $p_{2\text{i}}$ | $\varphi_{\text{Q50}}$ | $r_{\text{egr}}$ | 0.96738 | 0.067034 | 0.90126 | 0.097060 | 248 |
| $\hat{x}_{2\text{i}}$ | $p_{2\text{i}}$ | $\varphi_{\text{mi}}$ | $\hat{T}_{2\text{i}}$ | 0.97597 | 0.057534 | 0.89613 | 0.099552 | 275 |
| $\hat{x}_{2\text{i}}$ | $p_{2\text{i}}$ | $\varphi_{\text{mi}}$ | $r_{\text{egr}}$ | 0.96916 | 0.065177 | 0.90201 | 0.096694 | 280 |
| $\hat{x}_{\text{eng,out}}$ | $p_{2\text{i}}$ | $\varphi_{\text{Q50}}$ | $\hat{T}_{2\text{i}}$ | 0.97568 | 0.057880 | 0.89089 | 0.102030 | 279 |
| $\hat{x}_{\text{eng,out}}$ | $p_{2\text{i}}$ | $\varphi_{\text{Q50}}$ | $r_{\text{egr}}$ | 0.97251 | 0.061541 | 0.90931 | 0.093021 | 334 |
| $\hat{x}_{\text{eng,out}}$ | $p_{2\text{i}}$ | $\varphi_{\text{mi}}$ | $\hat{T}_{2\text{i}}$ | 0.97495 | 0.058746 | 0.90093 | 0.097225 | 285 |
| $\hat{x}_{\text{eng,out}}$ | $p_{2\text{i}}$ | $\varphi_{\text{mi}}$ | $r_{\text{egr}}$ | 0.97325 | 0.060704 | 0.90166 | 0.096865 | 321 |

Table E.8: $\varphi_{Q50}$ model quality

| x-regressors | | | | $R^2_{\text{train}}$ | RMSE$_{\text{train}}$ | $R^2_{\text{val}}$ | RMSE$_{\text{val}}$ | $n$ |
|---|---|---|---|---|---|---|---|---|
| $x_1$ | $x_2$ | $x_3$ | $x_4$ | | in °CA | | in °CA | |
| $m_{\text{air}}$ | $p_{2i}$ | $\varphi_{\text{mi}}$ | $\hat{T}_{2i}$ | 0.99012 | 0.36625 | 0.96883 | 0.65029 | 365 |
| $m_{\text{air}}$ | $p_{2i}$ | $\varphi_{\text{mi}}$ | $r_{\text{egr}}$ | 0.98794 | 0.40473 | 0.95939 | 0.74229 | 328 |
| $\hat{x}_{2i}$ | $p_{2i}$ | $\varphi_{\text{mi}}$ | $\hat{T}_{2i}$ | **0.99118** | **0.34611** | **0.96914** | **0.64702** | **361** |
| $\hat{x}_{2i}$ | $p_{2i}$ | $\varphi_{\text{mi}}$ | $r_{\text{egr}}$ | 0.98784 | 0.40631 | 0.96830 | 0.65581 | 307 |
| $\hat{x}_{\text{eng,out}}$ | $p_{2i}$ | $\varphi_{\text{mi}}$ | $\hat{T}_{2i}$ | 0.99040 | 0.36095 | 0.94369 | 0.87406 | 352 |
| $\hat{x}_{\text{eng,out}}$ | $p_{2i}$ | $\varphi_{\text{mi}}$ | $r_{\text{egr}}$ | 0.98791 | 0.40514 | 0.95826 | 0.75256 | 368 |

Table E.9: $\varphi_{\text{mi}}$ model quality

| x-regressors | | | | $R^2_{\text{train}}$ | RMSE$_{\text{train}}$ | $R^2_{\text{val}}$ | RMSE$_{\text{val}}$ | $n$ |
|---|---|---|---|---|---|---|---|---|
| $x_1$ | $x_2$ | $x_3$ | $x_4$ | | in °CA | | in °CA | |
| $m_{\text{air}}$ | $p_{2i}$ | $\varphi_{Q50}$ | $\hat{T}_{2i}$ | 0.99773 | 0.20038 | 0.98931 | 0.38763 | 361 |
| $m_{\text{air}}$ | $p_{2i}$ | $\varphi_{Q50}$ | $r_{\text{egr}}$ | 0.99710 | 0.22658 | 0.98655 | 0.43477 | 320 |
| $\hat{x}_{2i}$ | $p_{2i}$ | $\varphi_{Q50}$ | $\hat{T}_{2i}$ | **0.99791** | **0.19220** | **0.98845** | **0.40290** | **351** |
| $\hat{x}_{2i}$ | $p_{2i}$ | $\varphi_{Q50}$ | $r_{\text{egr}}$ | 0.99690 | 0.23434 | 0.98794 | 0.41170 | 319 |
| $\hat{x}_{\text{eng,out}}$ | $p_{2i}$ | $\varphi_{Q50}$ | $\hat{T}_{2i}$ | 0.99793 | 0.19134 | 0.97062 | 0.64261 | 325 |
| $\hat{x}_{\text{eng,out}}$ | $p_{2i}$ | $\varphi_{Q50}$ | $r_{\text{egr}}$ | 0.99706 | 0.22811 | 0.98503 | 0.45863 | 340 |
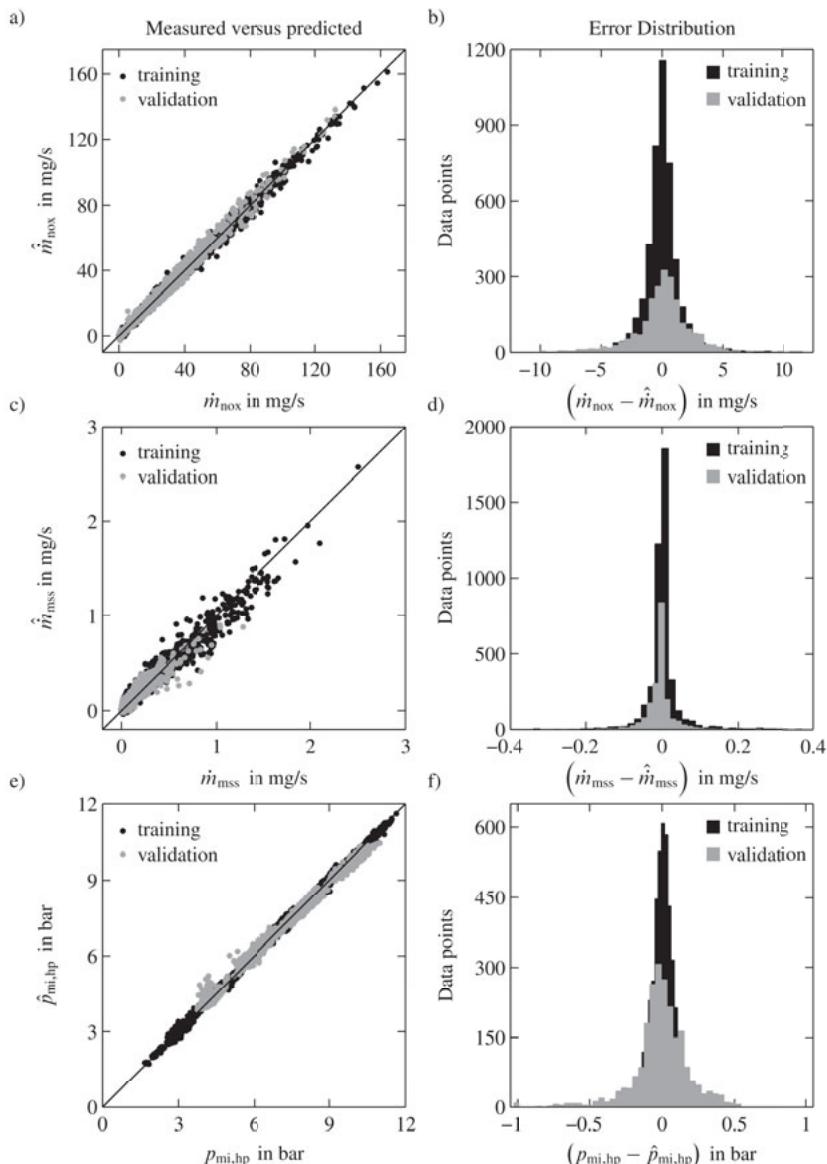
**Figure E.1:** Measured versus predicted plots and error distributions for the modelled quantities $\dot{m}_{\text{nox}}$, $\dot{m}_{\text{mss}}$ and $p_{\text{mi,hp}}$. $\hat{\dot{m}}_{\text{nox}} = f(n_{\text{eng}}, u_{\text{inj}}, m_{\text{air}}, p_{2i}, \varphi_{Q50}, \hat{T}_{2i})$;
$\hat{\dot{m}}_{\text{mss}} = f(n_{\text{eng}}, u_{\text{inj}}, \hat{x}_{\text{eng,out}}, p_{2i}, \varphi_{Q50}, \hat{T}_{2i})$; $\hat{p}_{\text{mi,hp}} = f(n_{\text{eng}}, u_{\text{inj}}, \hat{x}_{2i}, p_{2i}, \varphi_{Q50}, \hat{T}_{2i})$
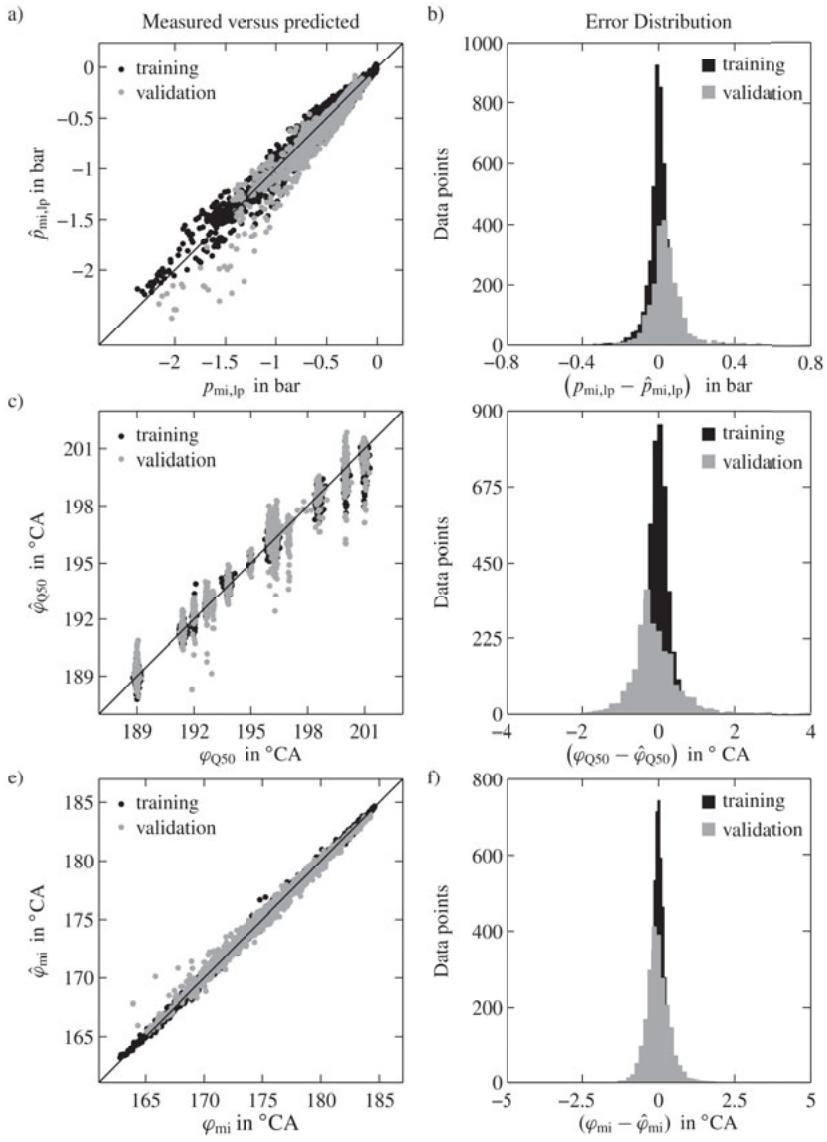
**Figure E.2:** Measured versus predicted plots and error distributions for the modelled quantities $p_{mi,lp}$, $\varphi_{Q50}$ and $\varphi_{mi}$. $\hat{p}_{mi,lp} = f(n_{eng}, u_{inj}, \hat{x}_{2i}, p_{2i}, \varphi_{Q50}, \hat{T}_{2i})$;
$\hat{\varphi}_{Q50} = f(n_{eng}, u_{inj}, \hat{x}_{2i}, p_{2i}, \varphi_{mi}, \hat{T}_{2i})$;  $\hat{\varphi}_{mi} = f(n_{eng}, u_{inj}, \hat{x}_{2i}, p_{2i}, \varphi_{Q50}, \hat{T}_{2i})$

# Bibliography

Alberer, D. and del Re, L. (2009). Optimization of the transient Diesel engine operation. In *9th International Conference on Engines & Vehicles*, number 2009-24-0113, Capri, Naples, Italy. SAE.

Alfieri, E. (2009). *Emissions-Controlled Diesel Engine*. Dissertation, Eidgenössische Technische Hochschule Zürich.

Ammann, M. (2003). *Modellbasierte Regelung des Ladedrucks und der Abgasrückführung beim aufgeladenen PKW-Common-Rail-Dieselmotor*. Dissertation, Eidgenössische Technische Hochschule Zürich. in German language.

Åström, K. J. and Hägglund, T. (2005). *Advanced PID Control*. ISA - The Instrumentation, Systems, and Automation Society.

Beatrice, C., Bertoli, C., Giacomo, N. D., and Guido, C. (2009). Experimental investigation of the benefits of cooled and extra-cooled low-pressure EGR on a light duty Diesel engine performance. In *9th International Conference on Engines & Vehicles*, number 2009-24-0138, Capri, Naples, Italy. SAE.

Benz, M. (2010). *Model-based optimal emission control of Diesel engines*. Dissertation, Eidgenössische Technische Hochschule Zürich.

Berndt, R. (2009). *Einfluss eines diabaten Turboladermodells auf die Gesamtprozess-Simulation abgasturboaufgeladener PKW-Dieselmotoren*. Dissertation, Technische Universität Berlin. in German language.

Bessai, C., Stölting, E., and Gratzke, R. (2011). Virtual oxygen sensor in the intake manifold of a Diesel engine. *MTZ worldwide edition*, 72(11):34–39.

Bischoff, M., Eiglmeier, C., Werner, T., and Zülch, S. (2012). The new 3.0-l TDI biturbo engine from Audi – Part 2: Thermodynamics and calibration. *MTZ worldwide edition*, 73(2):30–36.

Bohn, D., Heuer, T., and Kusterer, K. (2005). Conjugate flow and heat transfer investigation of a turbo charger. *Journal of Engineering for Gas Turbines and Power*, 127:663–669.

Brace, C. (1998). Prediction of Diesel engine exhaust emissions using artificial neural networks. In *Neural Networks in Systems Design - IMechE Seminar S591*, Solihull, United Kingdom. IMechE.

Brune, K.-H. (2009). *Numerische und experimentelle Untersuchung des Betriebsverhaltens eines Abgasturboladerverdichters im Niederdruckabgasrückführbetrieb*. Dissertation, Technische Universität Darmstadt. in German language.

Chauvin, J., Grondin, O., and Moulin, P. (2011). Control oriented model of a variable geometry turbocharger in an engine with two EGR loops. *Oil & Gas Science and Technology – Revue d'IFP Energies nouvelles*, 66(4):563–571.

Crabb, D., Fleiss, M., Larsson, J.-E., and Somhorst, J. (2013). New modular engine platform from Volvo. *MTZ worldwide edition*, 74(9):4–11.

DIN EN 590 (2010). Kraftstoffe für Kraftfahrzeuge - Dieselkraftstoff - Anforderungen und Prüfverfahren; Deutsche Fassung EN 590:2009+A1:2010. in German language.

Diop, S., Moraal, P., Kolmanovsky, I., and van Nieuwstadt, M. (1999). Intake oxygen concentration estimation for DI Diesel engines. In *Proceedings of the 1999 IEEE International Conference on Control Applications*, Kohala Coast-Island of Hawai'i, USA.

Drews, P., Hoffmann, K., Beck, R., Gasper, R., Vanegas, A., Peters, N., and Abel, D. (2009). Fast model predictive control for the air path of a turbocharged Diesel engine. In *European Control Conference 2009 - ECC'09*, Budapest, Hungary.

Dworschak, J., Neuhauser, W., Rechberger, E., and Stastny, J. (2009). The new BMW six-cylinder Diesel engine. *MTZ worldwide edition*, 70(2):4–10.

Eidenböck, T., Mayr, K., Neuhauser, W., and Staub, P. (2012). The new BMW six-cylinder Diesel engine with three turbochargers – Part 1: Drive unit and turbocharger system. *MTZ worldwide edition*, 73(10):18–24.

Eriksson, L. (2007). Modeling and control of turbocharged SI and DI Engines. *Oil & Gas Science and Technology*, 62(4):523–538.

Ertl, C., Kaufmann, M., and Kranawetter, E. (2009). Influence of emission legislation on the architecture of functions for electronic Diesel-engine management systems. In *7th Symposium "Powertrain control systems for motor vehicles"*, Berlin, Germany.

European Commission (2007). Regulation (EC) no 715/2007 of the European parliament and of the council. *Official Journal of the European Union L171*, 50:1–15.

Flierl, R. and Lauer, F. (2013). Mechanically fully variable valvetrain and cylinder deactivation. *MTZ worldwide edition*, 74(4):50–57.

Föllinger, O. (1994). *Regelungstechnik*. Hüthig. in German language.

Galindo, J., Climent, H., Guardiola, C., and Doménech, J. (2009). Modeling the vacuum circuit of a pneumatic valve system. *Journal of Dynamic Systems, Measurement, and Control*, 131(3):031011–1 – 031011–11.

Genieser, P., Elsässer, A., Gurney, D., and Warth, M. (2010). Systems development for future passenger car Diesel engines. *MTZ worldwide edition*, 71(10):34–39.

Greitzer, E. (1976). Surge and rotating stall in axial flow compressors - Part 1: Theoretical compression system model. *Journal of Engineering for Power*, 98:190–198.

Guzzella, L. and Amstutz, A. (1998). Control of Diesel engines. *Control Systems, IEEE*, 18(5):53–71.

Guzzella, L. and Onder, C. (2010). *Introduction to Modeling and Control of Internal Combustion Engine Systems*. Springer, Berlin Heidelberg, 2 edition.

Hadler, J., Rudolph, F., Dorenkamp, R., Kösters, M., Mannigel, D., and Veldten, B. (2008). Volkswagen's new 2.0 l TDI engine for the most stringent emission standards – part 2. *MTZ worldwide edition*, 69(6):54–59.

Hafner, M. (2002). *Modellbasierte stationäre und dynamische Optimierung von Verbrennungsmotoren am Motorenprüfstand unter Verwendung neuronaler Netze*. Number 482 in Fortschrittberichte VDI: Reihe 12, Verkehrstechnik, Fahrzeugtechnik. VDI-Verlag, Düsseldorf, Germany. in German language.

Hafner, M., Schüler, M., Nelles, O., and Isermann, R. (2000). Fast neural networks for Diesel engine control design. *Control Engineering Practice*, 8:1211–1221.

Hastie, T., Tibshirani, R., and Friedman, J. (2011). *The Elements of Statistical Learning: Data Mining, Inference, and Prediction*. Springer, 2nd edition.

Herceg, M., Raff, T., Findeisen, R., and Allgöwer, F. (2006). Nonlinear model predictive control of a turbocharged Diesel engine. In *Computer Aided Control System Design, 2006 IEEE International Conference on Control Applications, 2006 IEEE International Symposium on Intelligent Control*, Munich, Germany. IEEE.

Herrmann, O. (2005). *Emissionsregelung bei Nutzfahrzeugmotoren über den Luft- und Abgaspfad*. Dissertation, Rheinisch-Westfälische Technische Hochschule Aachen. in German language.

Heuck, M., Feldt, M., Eichhorn, M., and Horn, A. (2008). Modellgestütztes AGR-Management für zukünftige Luftsysteme aufgeladener Dieselmotoren. In *Steuerung und Regelung von Fahrzeugen und Motoren - AUTOREG*, Baden-Baden, Germany. in German language.

Heywood, J. B. (1988). *Internal Combustion Engine Fundamentals*. McGraw-Hill, 1. edition.

Hippe, P. (2006). *Windup in Control: Its Effects and Their Prevention*. Springer, London.

Hirsch, M. and del Re, L. (2009). Sequential identification of engine subsystems by optimal input design. In *9th International Conference on Engines & Vehicles*, number 2009-24-0132, Capri, Naples, Italy. SAE.

Horowitz, I. M. (1963). *Synthesis of Feedback Systems*. Academic Press, New York.

Huang, H.-P., Jeng, J.-C., Chiang, C.-H., and Pan, W. (2003). A direct method for multi-loop PI/PID controller design. *Journal of Process Control*, 13:769–786.

Isermann, R. (1991). *Digital Control Systems Volume 2: Stochastic Control, Multivariable Control, Adaptive Control, Applications*. Springer, 2nd edition.

Isermann, R., editor (2010). *Elektronisches Management motorischer Fahrzeugantriebe: Elektronik, Modellbildung, Regelung und Diagnose für Verbrennungsmotoren, Getriebe und Elektroantriebe*. Vieweg+Teubner Verlag, 1 edition. in German language.

Isermann, R., Jost, O., and Schwarte, A. (2000). Modellgestützte Reglerentwicklung für einen Abgasturbolader mit variabler Turbinengeometrie an einem DI-Dieselmotor. *MTZ Motortechnische Zeitschrift*, 3(3):184 – 193. in German language.

Isermann, R. and Münchhof, M. (2011). *Identification of Dynamic Systems*. Springer.

Jankovic, M., Jankovic, M., and Kolmanovsky, I. (2000). Constructive Lyapunov control design for turbocharged diesel engines. *IEEE Transactions on Control Systems Technology*, 8(2):288–299.

Jung, M. (2003). *Mean-Value Modelling and Robust Control of the Airpath of a Turbocharged Diesel Engine*. Dissertation, University of Cambridge.

Justi, E. W. (1938). *Spezifische Wärme - Enthalpie, Entropie und Dissoziation technischer Gase*. Springer, Berlin. in German language.

Kecman, V. (2001). *Learning and Soft Computing: Support Vector Machines, Neural Networks, and Fuzzy Logic Models*. The MIT Press.

Knapp, T. (1993). *Parameteradaptive Regelung zeitvarianter und komplexer Prozesse*. Number 331 in Fortschrittberichte VDI: Reihe 8, Mess-, Steuerungs- und Regelungstechnik. VDI-Verlag, Düsseldorf, Germany. in German language.

Kohlhase, M. (2011). *Brennraumdruckbasiertes Motormanagement für Otto- und Dieselmotoren zur Verbrauchs- und Emissionsreduktion*. Number 760 in Fortschrittberichte VDI: Reihe 12, Verkehrstechnik, Fahrzeugtechnik. VDI-Verlag, Düsseldorf, Germany. in German language.

Kolmanovsky, I., Moraal, P., van Nieuwstadt, M., and Stefanopoulou, A. G. (1997). Issues in modelling and control of intake flow in variable geometry turbocharged engines. In *Proceedings of 18th IFIP Conference on System modeling and Optimization*, Detroit, USA.

Kopf, S. (2014). *Modellbasierte Lageregelung mechatronischer Aktuatoren im Luftpfad von Verbrennungsmotoren*. Dissertation, Technische Universität Darmstadt. in German language.

Kortwittenborg, T. and Walter, F. (2013). Strategy to control the cylinder deactivation. *MTZ worldwide edition*, 74(2):18–22.

Kreisselmeier, G. (1999). Two-degree-of-freedom control structure. *at - Automatisierungstechnik*, 47:266–269. in German language.

Lee, J. and Edgar, T. F. (2004). ISE tuning rule revisited. *Automatica*, 40:1455–1458.

Lückert, P., Busenthür, D., Arndt, S., and Sass, H. (2013). The Mercedes-Benz OM 651 four cylinder Diesel engine for worldwide use. In 22$^{nd}$ *Aachen Colloquium Automobile and Engine Technology*, Aachen, Germany.

Lutz, O. and Wolf, F. (1938). *IS-Tafel für Luft und Verbrennungsgase*. Springer, Berlin. in German language.

Maiboom, A., Tauzia, X., Shah, S. R., and Hétet, J.-F. (2009). Experimental study of an LP EGR system on an automotive Diesel engine, compared to HP EGR with respect to PM and NOx emissions and specific fuel consumption. In *9th International Conference on Engines & Vehicles*, number 2009-24-0138, Capri, Naples, Italy. SAE.

Malobabic, M. (1989). *Das Betriebsverhalten Leitschaufel- und Bypassgeregelter PKW-Abgasturbolader*. Dissertation, Universität Hannover. in German language.

Mayne, D. Q. (1973). The design of linear multivariable systems. *Automatica*, 9:201–207.

Merker, G. P., Schwarz, C., Stiesch, G., and Otto, F. (2006). *Simulating Combustion: Simulation of combustion and pollutant formation for engine-development*. Springer.

Mhatre, S. and Brosilow, C. (2000). Multivariable model state feedback: Computationally simple, easy-to-tune alternative to MPC. *AIChE Journal*, 46(8):1566–1580.

Middendorf, H., Theobald, J., Lang, L., and Hartel, K. (2012). The 1.4-l TSI gasoline engine with cylinder deactivation. *MTZ worldwide edition*, 73(3):5–8.

Mollenhauer, K. and Tschöke, H., editors (2010). *Handbook of Diesel Engines*. Springer, 1st edition.

Moraal, P. and Kolmanovsky, I. (1999). Turbocharger modeling for automotive control applications. In *SI Engine Modeling*, number 1999-01-0908, Detroit, Michigan, USA. SAE.

Moraal, P., Kolmanovsky, I., and van Nieuwstadt, M. (1999). Modeling and identification of a current to vacuum transducer and VNT actuator. In *Proceedings of the 1999 IEEE/ASME International Conference on Advanced Intelligent Mechatronics*, Atlanta, USA.

Morari, M. and Zafiriou, E. (1989). *Robust Process Control*. Prentice Hall.

Moulin, P. and Chauvin, J. (2011). Modeling and control of the air system of a turbocharged gasoline engine. *Control Engineering Practice*, 19(3):287–297.

Moulin, P., Grondin, O., and Chauvin, J. (2010). Impact of EGR on turbocharger control on a Diesel engine with two EGR loops. In *6th IFAC Symposium Advances in Automotive Control*, Munich, Germany.

Mueller, V., Christmann, R., Muenz, S., and Gheorghiu, V. (2005). System structure and controller concept for an advanced turbocharger/EGR system for a turbocharged passenger car Diesel engine. In *Powertrain & Fluid Systems Conference & Exhibition*, number 2005-01-3888, San Antonio, TX, USA. SAE.

Münz, S., Römuss, C., Schmidt, P., Brune, K.-H., and Schiffer, H.-P. (2008). Diesel engines with low-pressure exhaust-gas recirculation - Challenges for the turbocharger. *MTZ worldwide edition*, 69(2):20–26.

Naber, D., Motz, S., Krüger, M., and Gerhardt, J. (2011). Approaches for optimising the transient behaviour of Diesel engines in terms of emissions and fuel consumption. In *11th Stuttgart International Symposium "Automotive and Engine Technology"*, Stuttgart, Germany.

Nakayama, S., Fukuma, T., Matsunaga, A., Miyake, T., and Wakimoto, T. (2003). A new dynamic combustion control method based on charge oxygen concentration for Diesel engines. In *SAE Powertrain & Fluid Systems Conference & Exhibition*, Pittsburgh, PA, USA. SAE 2003-01-3181.

Nam, K., Yu, J., and Cho, S. (2011). Improvement of fuel economy and transient control in a passenger diesel engine using LP(Low Pressure)-EGR. In *SAE 2011 World Congress & Exhibition*, number 2011-01-0400, Detroit, Michigan, United States.

Nelles, O. (2000). *Nonlinear System Identification*. Springer.

Neusser, H.-J., Kahrstedt, J., Dorenkamp, R., and Jelden, H. (2013). The Euro 6 engines in the modular Diesel engine system of Volkswagen. *MTZ worldwide edition*, 74(6):4–10.

Nitzke, H.-G. and Rebohl, T. (2000). *Simulation und Realisierung von Abgasrückführkonzepten für Dieselmotoren*. Verlag Mainz, Aachen. in German language.

Ortner, P. and del Re, L. (2007). Predictive control of a Diesel engine air path. *IEEE Transactions on Control Systems Technology*, 15(3):449 – 456.

Pischinger, R., Klell, M., and Sams, T. (2009). *Thermodynamik der Verbrennungskraftmaschine: Der Fahrzeugantrieb*. Springer, 3rd edition. in German language.

Rajamani, R. (2005). Control of a variable-geometry turbocharged and wastegated Diesel engine. *Proceedings of the Institution of Mechanical Engineers, Part D: Journal of Automobile Engineering*, 219(11):1361–1368.

Rautenberg, M., Mobarak, A., and Malobabic, M. (1983). Influence of heat transfer between turbine and compressor on the performance of small turbochargers. In *International Gas Turbine Congress*, Tokyo, Japan.

Reif, K., editor (2012). *Dieselmotor-Management: Systeme, Komponenten, Steuerung und Regelung*. Vieweg+Teubner Verlag, 5 edition. in German Language.

Renninger, P., Weirich, M., von Pfeil, K., and Isermann, R. (2006). Optimization strategies for the transient operation of Diesel engines within the smoke limitation. In *ATZ/MTZ Konferenz Motorenentwicklung auf dynamischen Prüfständen*, Wiesbaden, Germany. in German language.

Richert, F. (2006). *Objektorientierte Modellbildung und Nichtlineare Prädiktive Regelung von Dieselmotoren*. Number 1092 in Fortschrittberichte VDI: Reihe 8, Mess-, Steuerungs- und Regelungstechnik. VDI-Verlag, Düsseldorf, Germany. in German language.

Rinolfi, R. (2008). Die Zukunft der Dieseltechnik. *ATZextra*, 13(1):38–43. in German language.

Romagnoli, A. and Martinez-Botas, R. (2012). Heat transfer analysis in a turbocharger turbine: An experimental and computational evaluation. *Applied Thermal Engineering*, 38:58–77.

Röpke, K., Nessler, A., Haukap, C., Baumann, W., Köhler, B., and Schaum, S. (2009). Model-based methods for engine calibration - Quo vadis. In *3rd International Symposium on Development Methodology*, Wiesbaden.

Roppenecker, G. (2009). State feedback control of linear systems – A renewed approach. *at – Automatisierungstechnik*, 57(10):491–498. in German language.

Rückert, J. (2004). *Modellgestützte Regelung von Ladedruck- und Abgasrückführrate beim Dieselmotor*. Number 1064 in Fortschrittberichte VDI: Reihe 8, Mess-, Steuerungs- und Regelungstechnik. VDI-Verlag, Düsseldorf, Germany. in German language.

Schaffnit, J. (2002). *Simulation und Control Prototyping zur Entwicklung von Steuergerätefunktionen für aufgeladene Nutzfahrzeug-Dieselmotoren*. Number 497 in Fortschrittberichte VDI: Reihe 12, Verkehrstechnik, Fahrzeugtechnik. VDI-Verlag, Düsseldorf, Germany. in German language.

Schilling, A. (2008). *Model-Based Detection and Isolation of Faults in the Air and Fuel Paths of Common-rail DI Diesel Engines Equipped with a Lambda and a Nitrogen Oxides Sensor*. Dissertation, Eidgenössische Technische Hochschule Zürich.

Schloßer, A. (2000). *Modellbildung und Simulation zur Ladedruck- und Abgasrückführregelung an einem Dieselmotor*. Number 860 in Fortschrittberichte VDI: Reihe 8, Mess-, Steuerungs- und Regelungstechnik. VDI-Verlag, Düsseldorf, Germany. in German language.

Schommers, J., Zygan, A., Binz, R., Eckert, D., Paule, M., Reichel, S., and Kempka, K.-H. (2008). Bluetec – the concept for Diesel engines with lowest emissions. *MTZ worldwide edition*, 69(5):4–10.

Schopp, G., Burkhardt, T., Dingl, J., Schwarz, R., and Eisath, C. (2009). Function development and calibration for charged engines - model based from concept to mass production. In *7th Symposium "Powertrain Control Systems for Motor Vehicles"*, Berlin. in German language.

Schöppe, D., Geurts, D., Balland, J., Schreuers, B., and Peters, M. (2009). Delphi Diesel structured engine control to achieve most stringent emission legislation. In *7th "Powertrain Control Systems for Motor Vehicles" Symposium*, Berlin, Germany.

Schüler, M. (2001). *Stationäre Optimierung der Motorsteuerung von PKW-Dieselmotoren mit Abgasturbolader durch Einsatz schneller neuronaler Netze*. Number 461 in Fortschrittberichte VDI: Reihe 12, Verkehrstechnik, Fahrzeugtechnik. VDI-Verlag, Düsseldorf, Germany. in German language.

Schwarte, A. (2007). *Modellbasierte Fehlererkennung und Diagnose des Ansaug- und Abgassystems von Dieselmotoren*. Number 634 in Fortschrittberichte VDI: Reihe 12, Verkehrstechnik, Fahrzeugtechnik. VDI-Verlag, Düsseldorf, Germany. in German language.

Schwarte, A., Schneider, D., Nienhoff, M., Kopold, R., Kornienko, A., Koops, I., and Birkner, C. (2007). Physical model based control of the airpath of Diesel engines for future requirements. *at - Automatisierungstechnik*, 55(7):346 – 351. in German language.

Schwarzmann, D. (2008). *Nonlinear Internal Model Control with Automotive Applications*. Logos Verlag, Berlin.

Sequenz, H. (2013). *Emission Modelling and Model-Based Optimisation of the Engine Control*. Number 1222 in Fortschrittberichte VDI: Reihe 8, Mess-, Steuerungs- und Regelungstechnik. VDI-Verlag, Düsseldorf, Germany.

Sequenz, H., Schreiber, A., and Isermann, R. (2009). Identification of nonlinear static processes with local polynomial regression and subset selection. In *15th IFAC Symposium on System Identification*, Saint-Malo, France.

Shaaban, S. (2004). *Experimental investigation and extended simulation of turbocharger non-adiabatic performance*. Dissertation, Universität Hannover.

Sidorow, A., Isermann, R., Cianflone, F., and Landsmann, G. (2011). Comparison of a turbocharger model based on isentropic efficiency maps with a parametric approach based on Euler's turbo-machinery equation. In *IFAC Worldcongress*, Milano, Italy.

Stiesch, G. (2003). *Modeling Engine Spray and Combustion Processes*. Springer.

Stodola, A. (1945). *Steam and Gas Turbines*. McGraw-Hill, New York, USA. reprinted by Peter Smith.

Stölting, E., Seebode, J., Gratzke, R., and Behnk, K. (2008). Emission-based engine management for heavy-duty applications. *MTZ worldwide edition*, 69(12):30–35.

Thompson, G. J., Atkinson, C. M., Clark, N. N., Long, T. W., and Hanzevack, E. (2000). Neural network modelling of the emissions and performance of a heavy-duty Diesel engine. *Proceedings of the Institution of Mechanical Engineers, Part D: Journal of Automobile Engineering*, 214(2):111–126.

Tschanz, F. (2012). *Control of particulate matter and nitrogen oxide emissions in Diesel engines*. Dissertation, Eidgenössische Technische Hochschule Zürich. No. 20785.

Tschanz, F., Amstutz, A., Onder, C., and Guzzella, L. (2010). A real-time soot model for emission control of a Diesel engine. In *IFAC Symposium Advances in Automotive Control*, Munich, Germany.

Uesugi, Y., Kouzuki, M., Mori, T., Naito, M., Morinaga, S., Yasuda, H., Yamauchi, M., Tanimura, K., and Kunz, J. (2009). The new 2.2 l Diesel engine from Mazda. *MTZ worldwide edition*, 70(6):22–28.

van Nieuwstadt, M. J., Kolmanovsky, I., Moraal, P. E., Stefanopoulou, A., and Janković, M. (2000). EGR-VGT control schemes: Experimental comparison of a high-speed Diesel engine. *IEEE Control Systems Magazine*, 20(3):63–79.

VDI-Gesellschaft Verfahrenstechnik und Chemieingenieurwesen, editor (2010). *VDI Heat Atlas*. Springer, second edition.

Vogt, M. (2008). *Support Vector Machines for Identification and Classification Problems in Control Engineering*. Number 1138 in Fortschrittberichte VDI: Reihe 8, Mess-, Steuerungs- und Regelungstechnik. VDI-Verlag, Düsseldorf, Germany.

von Pfeil, K. (2011). *Ladedruck- und Luftmassenregelung von aufgeladenen Dieselmotoren mit lokal linearen Modellen und Optimierung des dynamischen Emissionsverhaltens im Rauchbetrieb*. Number 744 in Fortschrittberichte VDI: Reihe 12, Verkehrstechnik, Fahrzeugtechnik. VDI-Verlag, Düsseldorf, Germany. in German language.

Wahlström, J. (2009). *Control of EGR and VGT for Emission Control and Pumping Work Minimization in Diesel Engines*. PhD thesis, Linköping University. No. 1256.

Wahlström, J. and Eriksson, L. (2007). Performance gains with EGR-flow inversion for handling non-linear dynamic effects in EGR VGT CI engines. In *Fifth IFAC Symposium on Advances in Automotive Control*, Monterey, CA, USA.

Wang, J. (2009). Air fraction estimation for multiple combustion mode Diesel engines with dual-loop EGR systems. *Control Engineering Practice*, 16(12):1479–1486.

Wartha, J., Westin, F., Leu, A., and De Marco, M. (2012). Opel 2.0-l biturbo Diesel engine with two-stage intercooling. *MTZ worldwide edition*, 73(7-8):28–233.

Weber, O., Jörgl, V., Shutty, J., and Keller, P. (2005). Future breathing system requirements for clean Diesel engines. In *14. Aachener Kolloquium Fahrzeug- und Motorentechnik*.

Wei, X. (2006). *Advanced LPV Techniques for Diesel Engines*. PhD thesis, Johannes Kepler Universität, Linz, Austria.

Wenzel, S. (2006). *Modellierung der Ruß- und $NO_x$-Emissionen des Dieselmotors*. Dissertation, Otto-von-Guericke-Universität Magdeburg. in German language.

Werner, P., Schommers, J., Breitbach, H., and Spengel, C. (2011). The new V6 Diesel engine from Mercedes-Benz. *MTZ worldwide edition*, 72(5):22–28.

Wright, R. A. and Kravaris, C. (2000). Two-degree-of-freedom output feedback controllers for nonlinear processes. In *Proceedings Of The 2000 American Control Conference*, pages 3636 – 3640.

Wurmthaler, C. and Kühnlein, A. (2009). Model based feed forward control for measurable disturbances. *at – Automatisierungstechnik*, 57(7):328–331. in German language.

Youssef, B., Moulin, P., and Grondin, O. (2007). Model based control of turbochargers: Application to a Diesel HCCI engine. In *16th IEEE International Conference on Control Applications*, Singapore.

Zahn, S. (2012). *Arbeitsspielaufgelöste Modellbildung und Hardware-in-the-Loop-Simulation von Pkw-Dieselmotoren mit Abgasturboaufladung*. Number 760 in Fortschrittberichte VDI: Reihe 12, Verkehrstechnik, Fahrzeugtechnik. VDI-Verlag, Düsseldorf, Germany. in German language.

Zahn, S. and Isermann, R. (2008). Crank angle synchronous modelling and real-time simulation of Diesel engines for ECU function development and testing. In *9th International Symposium On Advanced Vehicle Control*, Kobe, Japan.

Zimmermann, M., Bleile, T., Heiber, F., and Henle, A. (2015). Mastering the complexity of engine control functions. *MTZ worldwide edition*, 76(01):38–41.

## Own Publications

Mrosek, M. (2017). *Mean Value Modelling, Optimisation and Control of Turbocharged Diesel Engines with High- and Low Pressure Exhaust Gas Recirculation*. Internal Report, Technische Universität Darmstadt.

Mrosek, M. and Isermann, R. (2009a). Aufgeladene Dieselmotoren mit zweistufiger Abgasrückführung - Systemeigenschaften, Regelungsstruktur und automatisierter Reglerentwurf. In *7. Symposium „Steuerungssysteme für den Antriebsstrang von Kraftfahrzeugen"*, Berlin. in German language.

Mrosek, M. and Isermann, R. (2009b). System properties and control of turbocharged Diesel engines with high- and low-pressure EGR. In *IFAC Workshop on Engine and Powertrain Control, Simulation and Modeling*, Rueil-Malmaison, France.

Mrosek, M. and Isermann, R. (2010a). Dynamic reference value generation for the control of a Diesel engine with HP- and LP-EGR. In *Proceedings of the ASME 2010 Dynamic Systems and Control Conference*, Cambridge, Massachusetts, USA. ASME.

Mrosek, M. and Isermann, R. (2010b). Model-based estimation and control of the intake gas composition for turbocharged Diesel engines with high- and low-pressure-EGR. In *10th Stuttgart International Symposium*, Stuttgart, Germany.

Mrosek, M. and Isermann, R. (2010c). On the parametrisation of turbocharger power and heat transfer models. In *IFAC Symposium Advances in Automotive Control*, Munich, Germany.

Mrosek, M. and Isermann, R. (2011). System properties and control of turbocharged Diesel engines with high-and low-pressure EGR. *Oil & Gas Science and Technology – Revue d'IFP Energies nouvelles*, 66(4):587–598.

Mrosek, M., Sequenz, H., and Isermann, R. (2010a). Control oriented $NO_x$ and soot models for Diesel engines. In *IFAC Symposium Advances in Automotive Control*, Munich, Germany.

Mrosek, M., Sequenz, H., and Isermann, R. (2011a). Diesel engine air path control in transient operation - A model based approach for optimised reference values. In *2. Automobiltechnisches Kolloquium*, Munich, Germany. in German language.

Mrosek, M., Sequenz, H., and Isermann, R. (2011b). Identification of emission measurement dynamics for Diesel engines. In *IFAC Worldcongress*, Milano, Italy.

Mrosek, M., Sequenz, H., and Isermann, R. (2011c). Modellbasierte Optimierung der Luftpfadregelung von Dieselmotoren bezüglich der dynamischen Emissionen. In *5. Fachtagung Steuerung und Regelung von Fahrzeugen und Motoren - AUTOREG2011*, Baden-Baden, Germany. in German language.

Mrosek, M., Zahn, S., and Isermann, R. (2009). Parameter estimation for physical based air path models of turbocharged Diesel engines - an experience based guidance. In *9th International Conference on Engines & Vehicles*, number 2009-24-0134, Capri, Naples, Italy. SAE.

Mrosek, M., Zahn, S., and Isermann, R. (2010b). Parameter estimation for physical based air path models of turbocharged Diesel engines - an experience based guidance. *SAE International Journal of Engines*, 2:570–583.

Sequenz, H., Mrosek, M., and Isermann, R. (2010a). A global-local emission-model for NO$_x$ and soot emissions of turbocharged CR-Diesel engines. In *ASME Dynamic Systems and Control Conference*, Cambridge, Massachusetts, USA.

Sequenz, H., Mrosek, M., and Isermann, R. (2010b). Stationary global-local emission models of a CR-Diesel engine with adaptive regressor selection for measurements of airpath and combustion. In *IFAC Symposium Advances in Automotive Control*, Munich, Germany.

Sequenz, H., Mrosek, M., and Isermann, R. (2011a). Model based smoke limitation for the control of turbocharged CR-Diesel engines. In *11th Stuttgart International Symposium "Automotive and Engine Technology"*, Stuttgart, Germany.

Sequenz, H., Mrosek, M., Zydek, S., and Isermann, R. (2011b). Model based optimisation of a step in acceleration for a CR-Diesel engine. In *18th World Congress of the International Federation of Automatic Control*, Milano, Italy.

# Lebenslauf

## Persönliche Daten

| | |
|---|---|
| Name | Matthias Patrick Alexander Mrosek |
| Geburtsdatum | 8. Februar 1978 |
| Geburtsort | Frankfurt am Main |
| Nationalität | deutsch |

## Schulausbildung

| | |
|---|---|
| 1984–1988 | Grundschule (Linden-Schule, Kriftel) |
| 1987–1997 | Gymnasium (Main-Taunus-Schule, Hofheim) |

## Hochschulausbildung

| | |
|---|---|
| 2000–2006 | Studium der Elektrotechnik an der Technischen Universität Darmstadt, Vertiefungsrichtung Allgemeine Elektrotechnik |

## Berufstätigkeit

| | |
|---|---|
| 1997–2000 | Berufsausbildung zum Prozessleitelektroniker bei der Hoechst AG und Provadis GmbH |
| 2000–2000 | Prozessleitelektroniker bei der Clariant Deutschland GmbH |
| 2007–2011 | Wissenschaftlicher Mitarbeiter am Institut für Automatisierungstechnik der TU Darmstadt bei Prof. Dr.-Ing. Dr. h. c. Rolf Isermann |
| seit 2011 | Entwicklungsingenieur bei der Linde Material Handling GmbH |

# Online-Buchshop für Ingenieure

## Die Reihen der Fortschritt-Berichte VDI:

1 Konstruktionstechnik/Maschinenelemente
2 Fertigungstechnik
3 Verfahrenstechnik
4 Bauingenieurwesen
5 Grund- und Werkstoffe/Kunststoffe
6 Energietechnik
7 Strömungstechnik
8 Mess-, Steuerungs- und Regelungstechnik
9 Elektronik/Mikro- und Nanotechnik
10 Informatik/Kommunikation
11 Schwingungstechnik
12 Verkehrstechnik/Fahrzeugtechnik
13 Fördertechnik/Logistik
14 Landtechnik/Lebensmitteltechnik
15 Umwelttechnik
16 Technik und Wirtschaft
17 Biotechnik/Medizintechnik
18 Mechanik/Bruchmechanik
19 Wärmetechnik/Kältetechnik
20 Rechnerunterstützte Verfahren (CAD, CAM, CAE CAQ, CIM ...)
21 Elektrotechnik
22 Mensch-Maschine-Systeme
23 Technische Gebäudeausrüstung

ISBN 978-3-18-380312-5